Final Technical Report of a NIAC Phase 2 Study

December 9, 2014

NASA Grant and Cooperative Agreement Number: NNX12AQ60G

NIAC Phase 2 Study Period: 09/10/2012 – 09/09/2014

An Innovative Solution to NASA's NEO Impact Threat Mitigation Grand Challenge and Flight Validation Mission Architecture Development

PI: Dr. Bong Wie, Vance Coffman Endowed Chair Professor
Asteroid Deflection Research Center
Department of Aerospace Engineering
Iowa State University, Ames, IA 50011
email: bongwie@iastate.edu
(515) 294-3124

Co-I: Brent Barbee, Flight Dynamics Engineer
Navigation and Mission Design Branch (Code 595)
NASA Goddard Space Flight Center
Greenbelt, MD 20771
email: brent.w.barbee@nasa.gov
(301) 286-1837

Graduate Research Assistants: Alan Pitz (M.S. 2012), Brian Kaplinger (Ph.D. 2013), Matt Hawkins (Ph.D. 2013), Tim Winkler (M.S. 2013), Pavithra Premaratne (M.S. 2014), Sam Wagner (Ph.D. 2014), George Vardaxis, Joshua Lyzhoft, and Ben Zimmerman

NIAC Program Executive: Dr. John (Jay) Falker
NIAC Program Manager: Jason Derleth
NIAC Senior Science Advisor: Dr. Ronald Turner
NIAC Strategic Partnerships Manager: Katherine Reilly

Contents

List of Figures

List of Tables

Abstract

This final technical report describes the results of a NASA Innovative Advanced Concept (NIAC) Phase 2 study entitled "An Innovative Solution to NASA's NEO Impact Threat Mitigation Grand Challenge and Flight Validation Mission Architecture Development." This NIAC Phase 2 study was conducted at the Asteroid Deflection Research Center (ADRC) of Iowa State University in 2012–2014. The study objective was to develop an innovative yet practically implementable solution to the most probable impact threat of an asteroid or comet with short warning time ($<$5 years). The technical materials contained in this final report are based on numerous technical papers, which have been previously published by the project team of the NIAC Phase 1 and 2 studies during the past three years. Those technical papers as well as a NIAC Phase 2 Executive Summary report can be downloaded from the ADRC website (www.adrc.iastate.edu).

Chapter 1

Hypervelocity Asteroid Intercept Vehicle (HAIV) Mission Concept

This chapter describes a planetary defense strategy that exploits the innovative concept of blending a hypervelocity kinetic impactor with a subsurface nuclear explosion for mitigating the most probable impact threat of near-Earth objects (NEOs) with a warning time shorter than 5 years.

1.1 Introduction

Despite the lack of a known immediate impact threat from an asteroid or comet, historical scientific evidence suggests that the potential for a major catastrophe created by an asteroid or comet impacting Earth is very real. Humankind must be prepared to deal with such an event that could otherwise cause a regional or global catastrophe. There is now growing national and international interest in developing a global plan to protect the Earth from a catastrophic impact by a hazardous near-Earth object (NEO). This growing interest was recently spurred by the Chelyabinsk meteorite impact event that occurred in Russia on February 15, 2013 and a near miss by asteroid 367943 Duende (2012 DA14), approximately 40 m in size, on the same day.

A variety of NEO deflection/disruption technologies, such as nuclear explosions, kinetic impactors, and slow-pull gravity tractors (GTs), have been investigated by planetary defense researchers during the past two decades [1–10]. To date, however, there is no consensus on how to reliably deflect or disrupt hazardous NEOs in a timely manner. All of the non-nuclear techniques will require mission lead times much longer than 10 years, even for a relatively small NEO. When the time-to-impact with the Earth exceeds a decade, the velocity perturbation needed to alter the orbit of a target asteroid sufficiently to deflect it away from Earth impact is relatively small (approximately 1 to 2 cm/s). Thus, most non-nuclear options as well as a nuclear standoff explosion can be employed for deflection missions when we have sufficiently long warning times. It is emphasized that any NEO deflection effort must produce an actual orbital change much larger than predicted orbital perturbation uncertainties from all sources. Likewise, any NEO deflection/disruption approach must be robust against the unknown material properties of a target NEO.

Kinetic impactors and nuclear explosions may be considered as the most mature technologies for asteroid deflection or disruption, as concluded in the 2010 NRC report [10]. Both approaches are impulsive and energy-rich, in that the final momentum change can be considerably more than that present in the original impactor, or in the expanded vaporization layer (from a nuclear standoff explosion). Both methods are expected to eject some debris, and the amount depends on surface material properties. High porosity affects the ability to convert the excess energy into additional momentum. Some asteroids like Itokawa have been determined to have densities (and thus porosities) comparable to terrestrial material with well-characterized shock propagation. Others appear to have very low porosity that may absorb excess energy without the hydrodynamic rebound that can amplify the original impulse.

Because nuclear energy densities are nearly a million times higher than those possible with chemical bonds, a nuclear explosive device is the most mass-efficient means for storing energy with today's technology. Deflection methods with sufficiently high energy density are often preferred over a nuclear disruption approach. One of these deflection methods utilizes a nuclear explosion at a specified standoff distance from the target NEO, to effect a large velocity change by ablating and blowing off a thin layer of the NEO's surface. Nuclear standoff explosions are thus assessed to be much more effective than any other non-nuclear alternatives, especially for larger asteroids. The precise outcome of a NEO deflection attempt using a nuclear standoff explosion is dependent on myriad variables. Shape and composition of the target NEO are critical factors. These critical properties, plus others, would need to be characterized, ideally by a separate mission, prior to a successful nuclear deflection attempt. Other techniques involving the use of surface or subsurface nuclear explosives are assessed to be more efficient than the nuclear standoff explosion, although they may cause an increased risk of fracturing the target asteroid [10].

Nuclear standoff explosions require an optimal standoff distance for imparting maximum velocity change to the target asteroid. Therefore, we have to determine how close the nuclear explosion must be to effectively change the orbital trajectories of asteroids of different types, sizes, and shapes. A simple model that can be used to assess the effectiveness of a nuclear standoff explosion approach is developed in [9]. Geometric principles and basic physics are used in [9] to construct a simple model which can be augmented to account for icy bodies, anisotropic ejecta distributions, and effects unique to the nuclear blast model. Use of this simple model has resulted in an estimation of NEO velocity change of approximately 1 cm/s on the same order as other complex models,

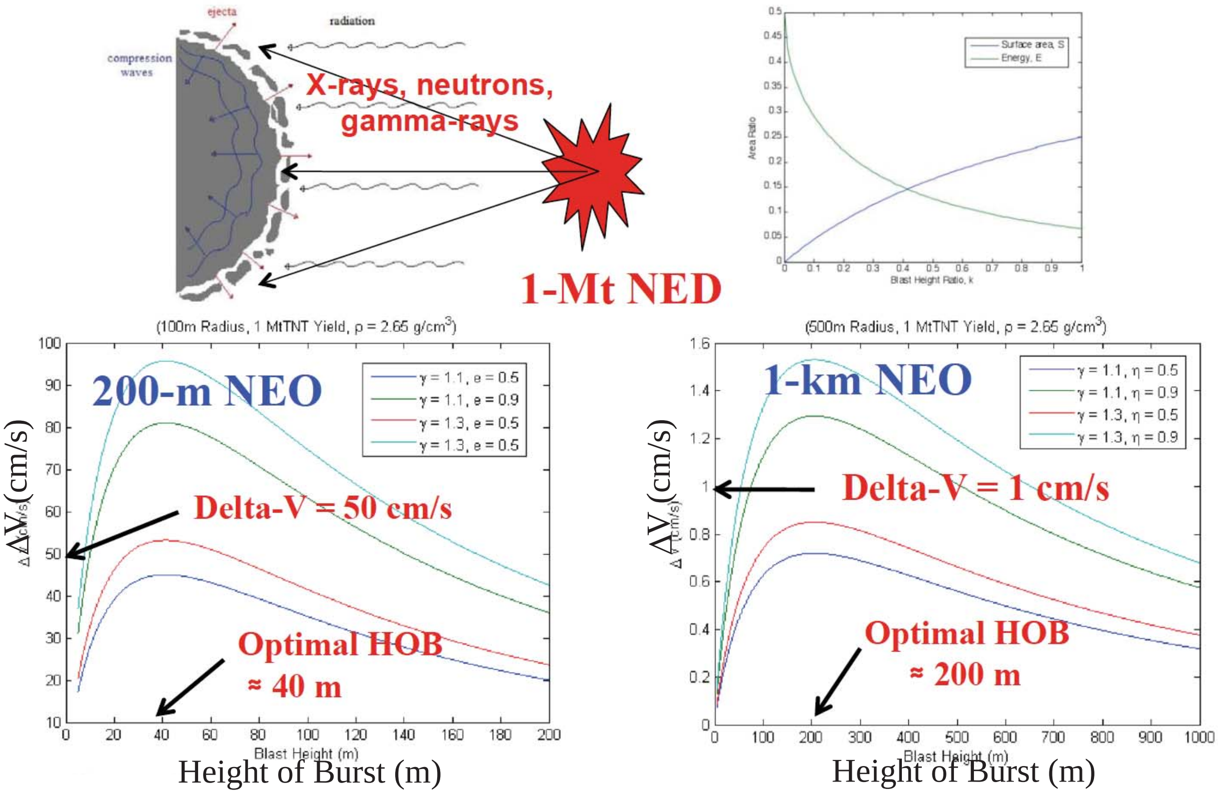

Figure 1.1: A summary of the ideal deflection ΔV performance characteristics of nuclear standoff explosions [9].

and data correlation suggests an optimal standoff distance of about 200 m for an ideal spherical model of a 1-km diameter NEO. The deflection ΔV performance characteristics of nuclear standoff explosions are provided in Fig. 1.1. However, more rigorous physical modeling and simulation, including hydrodynamic codes and other forms of computer modeling, are necessary to account for changes in material properties under the realistic conditions of the nuclear blast. Possible fracturing of the asteroid and other anticipated outcomes of a nuclear blast must also be assessed in further study. More details of the physical fundamentals of such nuclear standoff explosions can be found in [1, 2, 4].

Due to various uncertainties and constraints in asteroid detection and tracking, the warning time or mission lead time can be very short. An 18-m diameter meteor exploded with the energy of 30 Hiroshima nuclear bombs 30 km above the city of Chelyabinsk, Russia on February 15, 2013, with no warning at all. Asteroid 367943 Duende (2012 DA14), which had a near miss of the Earth on the same day as the Chelyabinsk event, was initially discovered on February 23, 2012. That is, we would have had only one year of warning time if the 40 m DA14 was going to collide with Earth. Another recent example is asteroid 2014 RC, which had a close encounter with Earth on September 7, 2014. This 20-m asteroid was initially discovered on August 31, 2014 by the Catalina

Sky Survey near Tucson, Arizona, and independently detected the next night by the Pan-STARRS 1 telescope, located on the summit of Haleakala on Maui, Hawaii. We would have had only one week of warning time if 2014 RC was going to collide with Earth.

If a NEO on an Earth-impacting course is detected with a short warning time (e.g., much less than 5 years), the challenge becomes how to mitigate its threat in a timely manner. For a small asteroid impacting in a sufficiently unpopulated region, mitigation may simply involve evacuation [10]. However, for larger asteroids, or asteroids impacting sufficiently developed regions, the threat may be mitigated by either disrupting the asteroid (i.e., destroying or fragmenting with substantial orbital dispersion), or by altering its trajectory such that it will either avoid impacting the predicted impact location, or miss the Earth entirely. When the time to impact with Earth is short, the velocity change required to deflect an NEO becomes extremely large. Thus, for the most probable mission scenarios, in which the warning time is shorter than 5 years, the use of high-energy nuclear explosives in space will become inevitable [10]. A scenario in which a small (e.g., 50 to 150 m) Earth-impacting NEO is discovered with short warning time is considered the most probable scenario because smaller NEOs greatly outnumber larger NEOs, and smaller NEOs are more difficult to detect. Most direct intercept missions with a short warning time will result in arrival closing velocities of 10 to 30 km/s with respect to a target asteroid. A rendezvous mission to a target asteroid that requires such an extremely large arrival ΔV of 10 to 30 km/s is not feasible.

A subsurface nuclear explosion is the most efficient use of nuclear explosives [10, 11]. The nuclear subsurface explosion, even with shallow burial to a depth of 3 to 5 m, can deliver a large amount of energy into the target asteroid, so that there is a likelihood of totally disrupting the target asteroid. Such subsurface nuclear explosions are known to be at least 20 times more effective than a nuclear contact burst (a nuclear explosion very close to the surface) [11]. The momentum/energy transfer created by a shallow subsurface nuclear explosion is at least 100 times larger than that of an optimal standoff nuclear explosion. However, state-of-the-art nuclear subsurface penetrator technology limits the impact velocity to no more than about 300 m/s because higher impact velocities prematurely destroy the fusing mechanisms/electronics of nuclear explosive devices [11]. An increased impact speed limit of 1.5 km/s may be technically feasible as mentioned in [11] for nuclear Earth-Penetrator Weapons (EPWs). Neither a precision standoff explosion at an optimal height of burst near an irregularly shaped, smaller NEO, with intercept velocities as high as 30 km/s, nor a surface contact burst, is a trivial engineering task.

Despite the uncertainties inherent to the nuclear disruption approach, disruption can become an effective strategy if most fragments disperse at speeds in excess of the escape velocity of an asteroid so that a very small fraction of fragments impacts the Earth. When the warning time

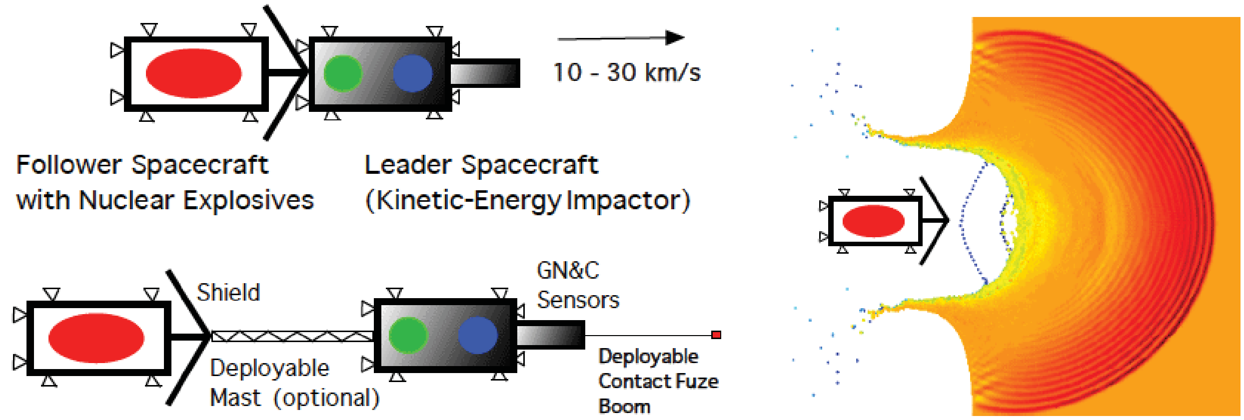

Figure 1.2: Initial conceptual illustration of a two-body hypervelocity asteroid intercept vehicle (HAIV) system, which was proposed for a NIAC Phase 1 Study in 2011 [12].

is very short, disruption is likely to become the only feasible strategy, especially if all other deflection approaches were to fail, as was concluded in the 2010 NRC report [10]. However, it is again emphasized that non-nuclear techniques should be preferred for non-destructive deflection of hazardous NEOs whenever we have sufficient mission lead times (>10 years).

This chapter will describe a planetary defense strategy that exploits the innovative concept of blending a hypervelocity kinetic impactor with a subsurface nuclear explosion for mitigating the most probable impact threat of NEOs with a warning time shorter than 5 years [12–15]. Initial conceptual design of a hypervelocity asteroid intercept vehicle (HAIV) will be presented in this chapter. The HAIV concept has been developed through NASA Innovative Advanced Concept (NIAC) Phase 1 & 2 Studies (2011–2014). The HAIV is a two-body space vehicle consisting of a leading kinetic impactor and a trailing body carrying nuclear explosives, as illustrated in Figs. 1.2 through 1.4. Its flight demonstration mission design as well as target asteroid selection for a planetary defense flight validation mission will be presented in this chapter. Various key enabling technologies required for the HAIV mission of optimally intercepting and disrupting a target asteroid will also be discussed.

1.2 Overview of the HAIV Mission Concept

Most direct intercept missions with a short warning time will result in arrival closing velocities of 10 to 30 km/s (relative to a target asteroid). A rendezvous mission to a target asteroid, requiring such an extremely large arrival ΔV of 10 to 30 km/s, is not practically feasible. A nuclear subsurface explosion, even with shallow burial to a depth of 3 to 5 m, can deliver a large amount of energy into the target asteroid, so that there is a likelihood of totally disrupting the target asteroid. Such subsurface nuclear explosions are known to be at least 20 times more effective than a nuclear contact burst [11]. However, state-of-the-art nuclear subsurface penetrator technology limits

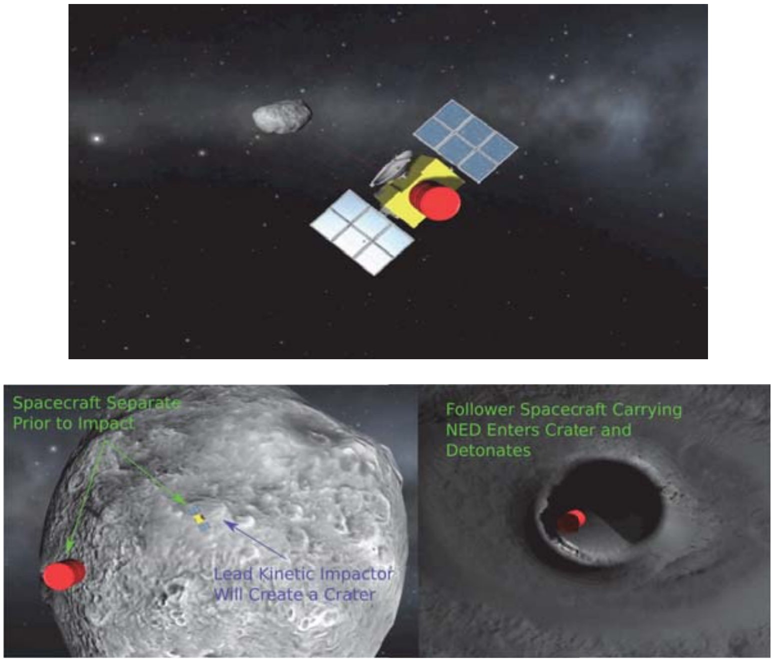

Figure 1.3: A notional depiction of the HAIV mission concept further investigated for a NIAC Phase 2 Study in 2012–2014.

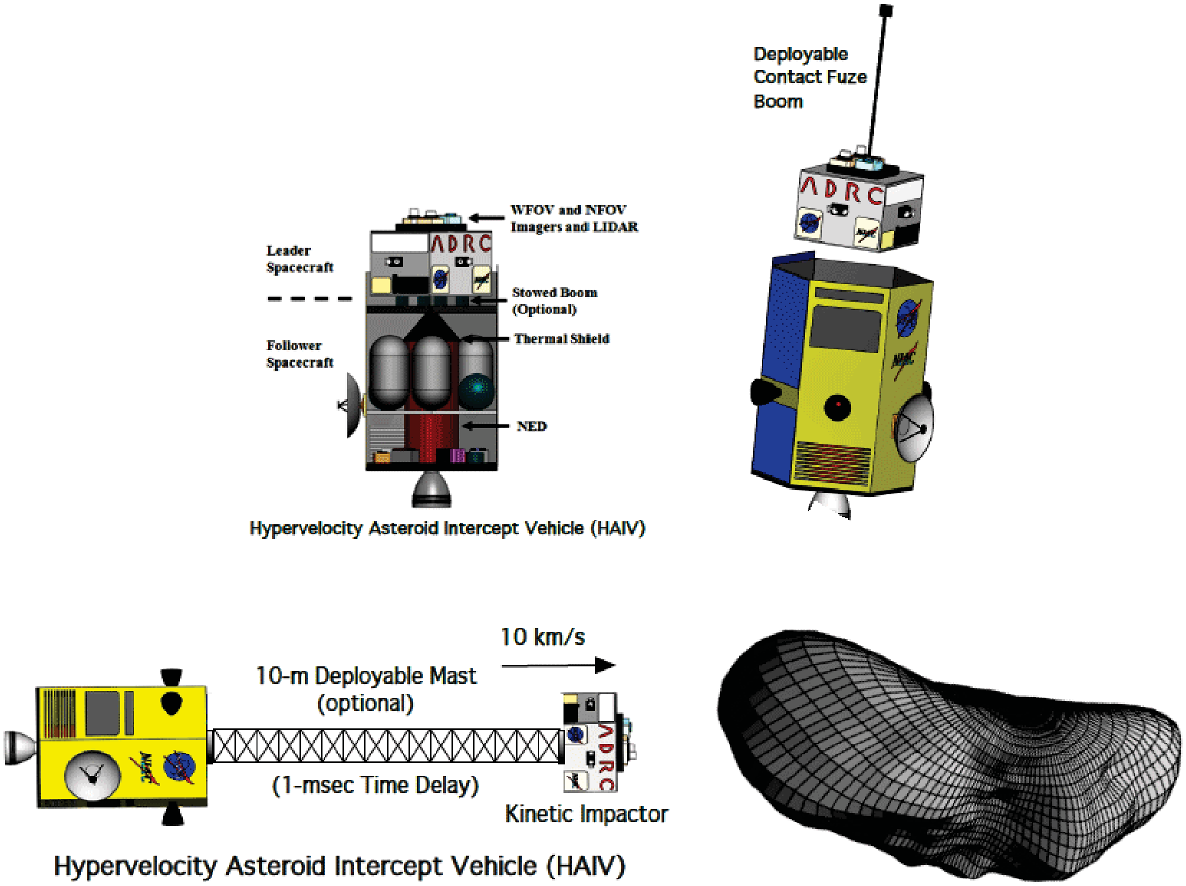

Figure 1.4: HAIV configuration options [13].

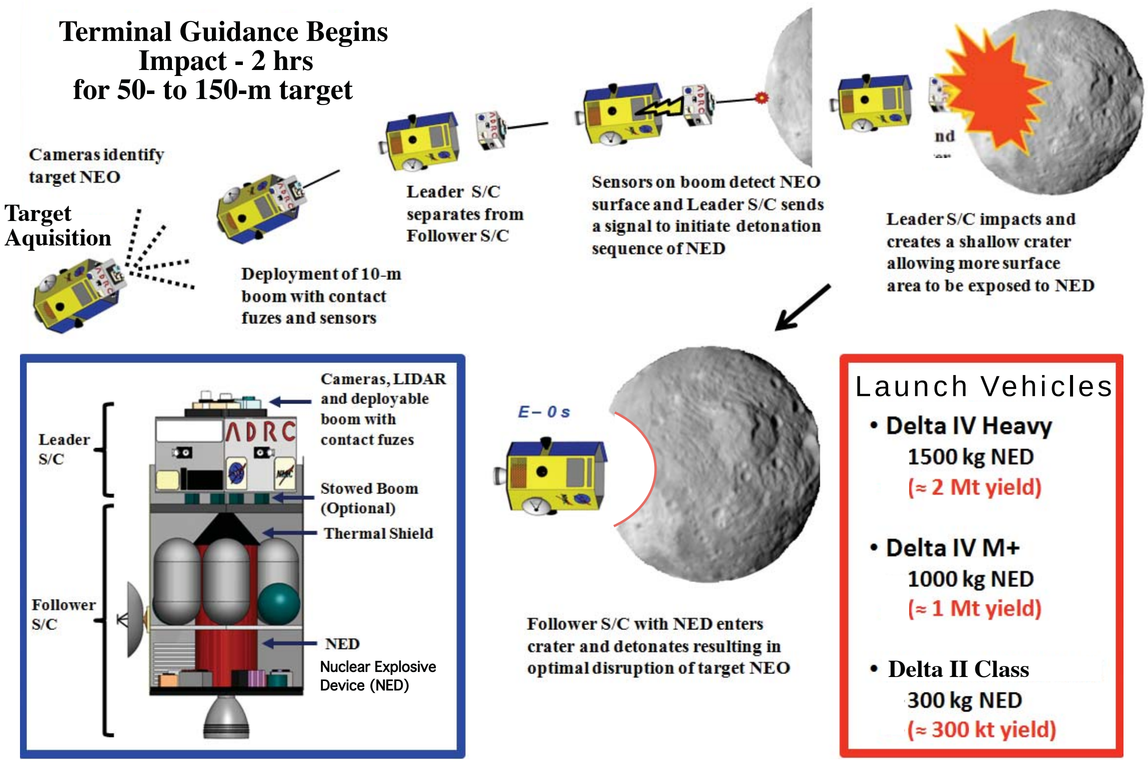

Figure 1.5: A reference HAIV flight system and its terminal guidance operational concept [13].

the impact velocity to less than about 300 m/s because higher impact velocities prematurely destroy the fusing mechanisms/electronics of nuclear explosive devices [11]. That said, an increased impact speed limit of 1.5 km/s may be technically feasible as mentioned in [11] for nuclear Earth-Penetrator Weapons (EPWs).

In order to overcome such practical constraints on the penetrated subsurface nuclear explosion, a hypervelocity asteroid intercept vehicle (HAIV) system concept has been developed. The HAIV system will enable a last-minute, nuclear disruption mission with intercept velocities as high as 30 km/s. The HAIV is a two-body space vehicle consisting of a fore body (leader) and an aft body (follower), as illustrated in Figs. 1.2 through 1.4. The leader spacecraft creates a kinetic-impact crater in which the follower spacecraft carrying nuclear explosive devices (NEDs) makes a robust and effective explosion below the surface of the target asteroid body. Surface contact burst or standoff explosion missions will not require such a two-body vehicle configuration. However, for a precision standoff explosion at an optimal height of burst, accurate timing of the nuclear explosive detonation will be required during the terminal guidance phase of hypervelocity intercept missions.

A reference HAIV mission architecture and its terminal guidance phase are illustrated in Fig. 1.5. For a small (50 to 150 m) target asteroid, the terminal guidance phase may begin 2 hrs prior to the final intercept collision. The nuclear fuzing system may be activated, arming the NED payload, much earlier in the terminal phase operations timeline. Instruments located on the leader spacecraft detect the target NEO, and a terminal guidance subsystem on-board the HAIV becomes active. Measurements continue through optical/IR cameras located on the leader spacecraft and an intercept impact location is identified on the target asteroid body. The high-resolution optical/IR cameras provide successive images of the NEO to the terminal guidance system for a few trajectory correction maneuvers (TCMs). Separation must occur between the leader spacecraft and the follower spacecraft before the leading kinetic impactor collides with the target.

A variety of existing launch vehicles, such as Delta II class, Atlas V, Delta IV, and Delta IV Heavy, can be used for the HAIV mission carrying a variety of NED payloads ranging from 300-kg (with approximately 300-kt yield) to 1,500-kg (with approximately 2-Mt yield). Conceptual design of an interplanetary ballistic missile (IPBM) system architecture for launching the HAIV system can be found in [16].

Because the hypervelocity kinetic impact and nuclear subsurface explosion simulations rely heavily on energy transmission through shocks, the simulation research work conducted for the HAIV mission concept study [17–19] used Adaptive Smoothed Particle Hydrodynamics (ASPH) to mitigate some of the computational and fidelity issues that arise in more complex, high-fidelity hydrocode simulations. The propagation of the nuclear explosive shock can be seen for an illustrative benchmark test case shown in Fig. 1.6. The shock propagation process dissipates some energy due to interactions with the rebounding shock front. In the center area of deeper regolith, the seeding process naturally results in a much more porous material, absorbing energy from the shock. Upon reaching the second core at the far side, some large chunks escape the disruption process in some cases (even with lower material strengths). An improved ASPH code, implemented on a modern low-cost GPU (Graphics Processing Unit) desktop computer, has been developed for the HAIV mission study [17–19] using the research results of Owen et al. [20]. However, a more computationally efficient, modern GPU-based hydrodynamics code needs to be further developed by incorporating more accurate physical models of a nuclear subsurface explosion [21, 22]. Details of nuclear subsurface explosion modeling and simulations will be presented in Chapter 4.

The orbital dispersion problem of a fragmented asteroid in an elliptic orbit, for assessing the effectiveness of an asteroid disruption mission, is illustrated in Fig. 1.7 [23]. Various approaches have been employed in [23] to be computationally efficient and accurate for several examples with a large number of fragments (e.g., 500,000). An N-body orbit simulation code was also used for orbital dispersion simulation and analysis in [23, 24]. To assess the degree of mitigation, the code includes the gravitational focusing effect of the Earth on those fragments that pass near the Earth, and provides a census of those that hit the Earth (i.e., those fragment with a minimum distance to Earth of <1 Earth radius). The code then has two modes of use as described as [23, 24]:

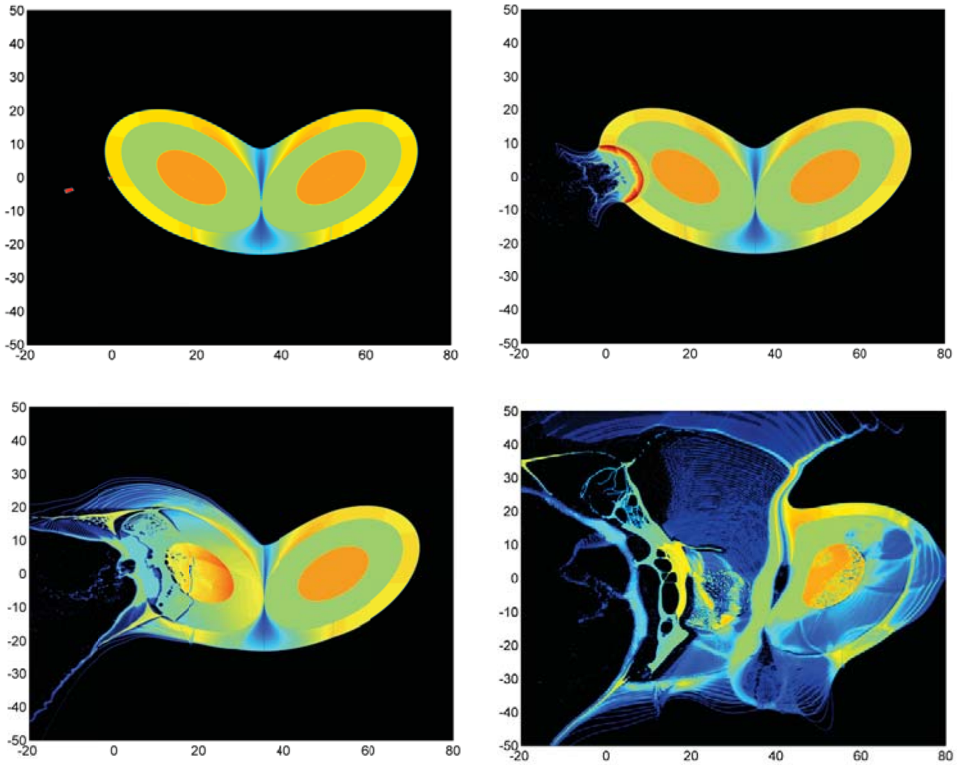

Figure 1.6: A 70-m asymmetric asteroid model disrupted by a 10-km/s kinetic impact and a subsequent 70-kt nuclear subsurface explosion of the HAIV system [17–19].

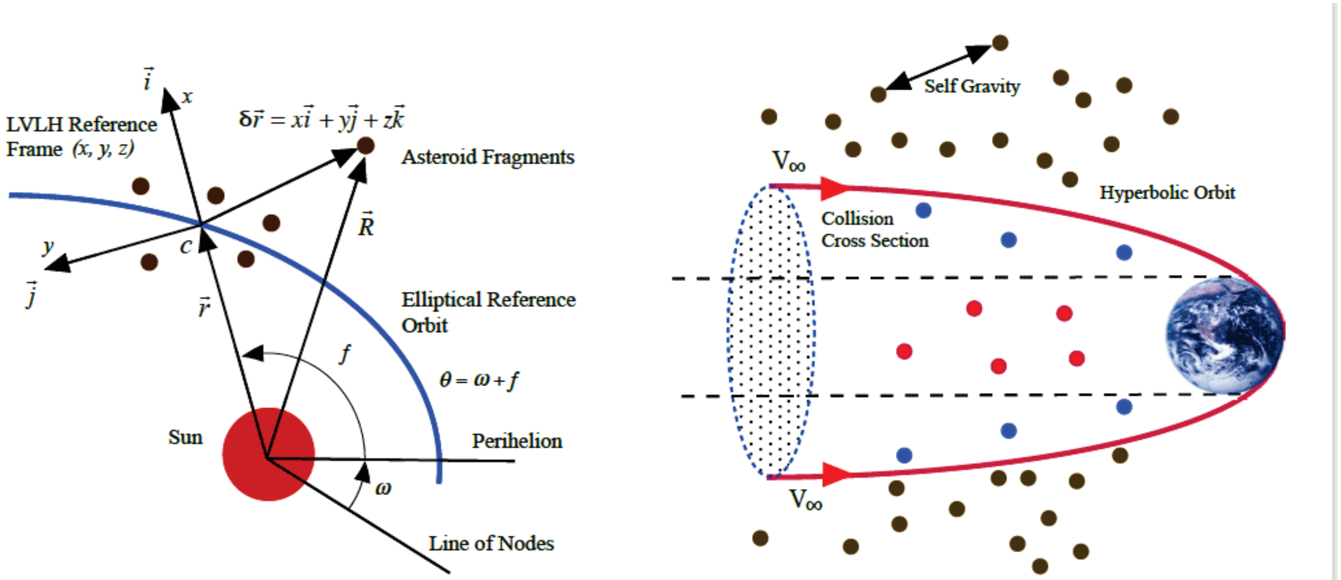

Figure 1.7: Illustration of the disruption modeling and simulation problem [23].

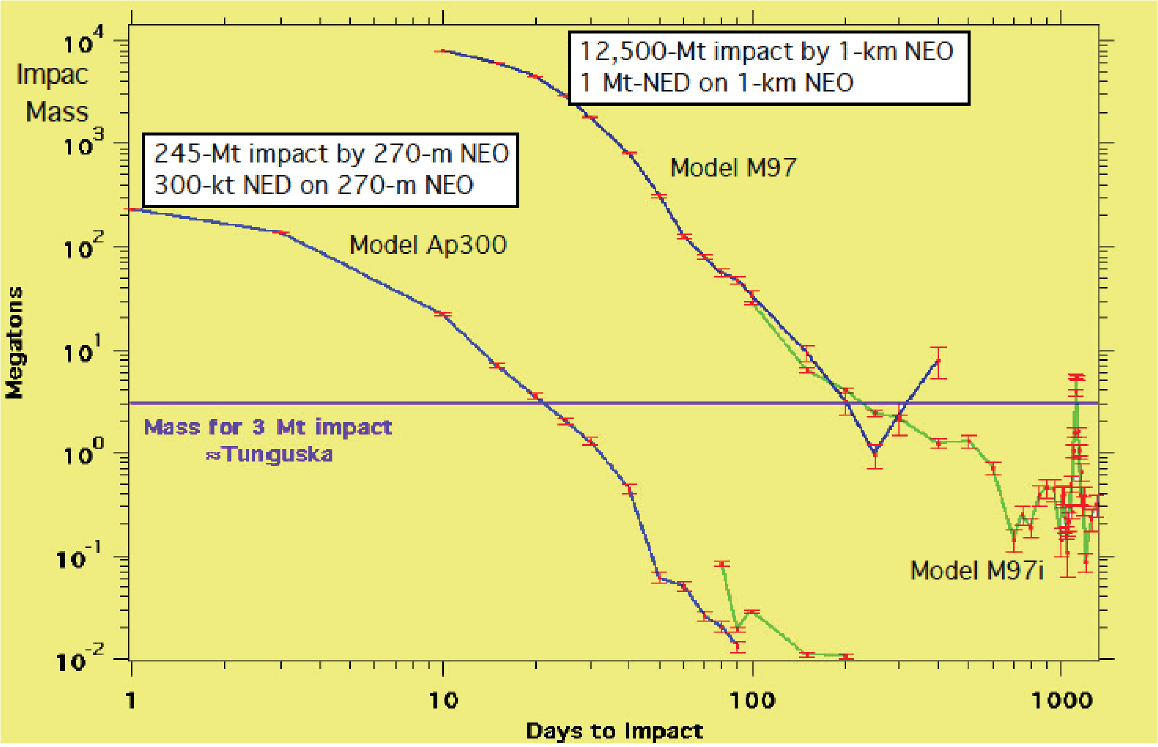

Figure 1.8: A summary of orbital dispersion simulation study results for nuclear subsurface explosions [23, 24].

- Orbital elements are evaluated for each fragment and the code is used to project the fragment forward in time. This is used to show the debris cloud evolution over the whole time from intercept to impact time.

- The orbital elements of each fragment are used to define its position and velocity at a time just prior to the original impact date. Times ranging from 5 days to 6 hours prior to the nominal impact time can be selected. A subset of the fragments that will pass within about 15 Earth radii is selected. These fragments are directly integrated, accounting for the gravity of the Earth and moon. Those fragments that pass within 1 Earth radius are impacts.

After the analytic step places the debris field near the Earth, the relative velocity of each fragment with respect to the Earth is used to calculate its closest approach. All fragments that pass within 15 Earth radii are selected for integration.

A summary of the effectiveness of nuclear subsurface explosions is presented in Fig. 1.8 [23, 24]. The mass that impacts the Earth is converted to energy in units of Mt using an Earth approach hyperbolic excess speed, V_∞. of 9.98 km/s. From Fig. 1.8, we notice that a 1-Mt nuclear disruption mission for a 1-km NEO requires an intercept-to-impact time of 200 days if we want to reduce the impact mass to that of the Tunguska event. A 270-m NEO requires an intercept-to-impact time of 20 days for its 300-kt nuclear disruption mission to reduce the impact mass to that of the Tunguska event. Therefore, it can be concluded that under certain conditions, disruption (with large orbital dispersion) is the only feasible strategy providing considerable impact threat mitigation for some representative, worst-case scenarios. An optimal interception can further reduce the impact mass percentage shown in Fig. 1.8. However, further study is necessary for assessing the effects of inherent physical modeling uncertainties and mission constraints.

1.3 Enabling Space Technologies for the HAIV Mission

Key enabling technologies, which need to be further considered in developing a HAIV flight system are described here.

1.3.1 Two-Body HAIV Configuration Design Tradeoffs

Partitioning options between the leader and follower spacecraft to ensure the follower spacecraft enters the crater opening safely need further tradeoffs. A baseline HAIV configuration uses no mechanical connection between the two spacecraft (after separation). This separated/fractionated configuration depends on the accuracy and measurement rates of the instruments, communication, flight computer, and guidance and tracking algorithms to carry out the terminal guidance phase. Another option includes the use of a deployable mast between the two spacecraft. Figure 1.4 shows these two optional configurations. As the mast is deployed and separation distance increases, the center of mass moves from the center towards the front of the follower spacecraft. This new configuration is still treated as a single body but achieves a two-body arrangement. Divert thrusters are pre-positioned at the expected new center of mass location to control the new system as a single body. These large divert thrusters need to be gimbaled to achieve the desirable thrust directions. This configuration reduces mission complexity and operations, but is limited to the length of the boom.

The deployable mast must be sufficiently rigid to avoid oscillatory motion of the two bodies. A robust deployable mechanism is required. A 10-m deployable mast employed by NASA's Nuclear Spectroscopic Telescope Array (NuSTAR) scientific satellite is applicable to the HAIV system. Essential to the NuSTAR satellite, launched in June 2012, is a deployable mast that extends to 10 meters after launch. This mast separated the NuSTAR X-ray optics from the detectors, necessary to achieve the long focal length required by the optics design. The articulated mast, built by ATK-Goleta, is low-risk, low-weight, compact, and has significant flight heritage. It provides a stiff, stable, and reliable structure on which the optics are mounted. It is based on a design used to establish a 60-meter separation between the two antennae of the the Shuttle Radar Topography

Mission (SRTM), which flew on the Space Shuttle Endeavor in February 2000 and made high-resolution elevation (topographic) maps of most of our planet. A hinged deployable mast consists of a hinged truss structure that is collapsible in storage and, when deployed, locks into place and is held firm. ATK, the manufacturer of such trusses, reports 12.4 m and 6.2 m length trusses, both with ending stiffness of 1.5×10^6 Nm^2, although mechanical properties are dependent on component materials.

1.3.2 Terminal Guidance Sensors/Algorithms

One of the key enabling technologies required for the HAIV mission architecture is precision terminal GNC (Guidance, Navigation, and Control) technology. NASA's Deep Impact mission, successfully accomplished in 2005, has validated some basic capabilities of a terminal GNC system for a large, 5-km target body at an impact speed of 10 km/s in very favorable lighting conditions [25–27]. Precision impact targeting of a smaller, 50 to 150 m class target with an impact speed of 30 km/s in worst-case circumstances is a much more technically challenging problem and, therefore, must be further studied and flight validated.

A terminal GNC system to be further developed and flight validated is briefly described here. A baseline HAIV system requires optical/IR cameras on the leader spacecraft to accurately identify and track the target NEO and initiate fuzing for the nuclear explosive device (NED). The HAIV mission may utilize the instruments used by the Deep Impact mission [25–27], which included a Medium Resolution Instrument (MRI) or Wide Field of View (WFOV) Imager and a High Resolution Instrument (HRI) or Narrow Field of View (NFOV) Imager. The MRI of the Deep Impact mission located the target NEO at the start of the terminal guidance phase. It is a small telescope with a diameter of 12 cm. The field of view of the MRI Imager is approximately $10^\circ \times 10^\circ$, which allows it to observe more stars and, therefore, provide better navigation information to the HAIV during its coasting flight phase. Immediately after acquisition of the target NEO, the MRI passes information to the HRI, which has a field of view of $2.3^\circ \times 2.3^\circ$. It is comprised of a 30-cm diameter telescope that delivers light to both an infrared spectrometer and a multispectral camera. These imagers should be located on the front face of the leading kinetic impactor portion of the HAIV spacecraft.

All of these critical terminal guidance system hardware as well as terminal guidance algorithms for achieving a precision targeting accuracy of <10 m (3σ), which is an order of magnitude better than the 300-m (3σ) targeting accuracy of NASA's Deep Impact mission, will need to be further developed and flight validated.

1.3.3 Thermal Protection and Shield Issues

A GPU-based hydrodynamics code [17–19], which has been developed for studying the effects of a nuclear disruption mission, is also used to estimate the thermal and structural limits experienced by the two-body HAIV [21]. The hydrodynamic code helps to establish a shield design and configuration on the follower spacecraft. Several different geometries include a flat cylindrical plate, conical shape, spherical cap, and an ogive nose cone.

The hydrodynamics code described in [17–19] is based on a meshless model. The initial kinetic impact is generated by a spherical shell matching the mass of the leading body, resulting in a field of hot gas and ejecta through which the follower spacecraft must survive. It is assumed that most standard NED designs will experience melting or exceed the maximum allowable structural load in this region. Therefore, a shield design is desirable to mitigate the effects of incident vaporized rock from the leader spacecraft, substantially protect the payload from micrometeorites ejected from the kinetic impact, and allow for the maximum depth of burst. Some preliminary results for thermal protection and shield design can be found in [13, 21], which show the peak specific internal energy due to thermal loading of a 0.7 m diameter cylindrical aluminum payload shield as a function of depth for various nominal thicknesses. A minimal thickness for this shield is shown to be about 10 cm. Above this value, little additional penetration is observed, given the thermal gradient in this region. A complicating factor is the acceleration of the payload. The 10 km/s initial relative speed greatly exceeds the speed of sound in the shield structure, resulting in the equivalent of a standing shock along the shield. Ahead of this shock, the payload measures only minimal interruption. Some initial acceleration due to ejecta impacts and interaction with the gas environment is measurable, but shortly thereafter the maximum structural load is reached. Thickness of the shield has almost no effect on the maximum depth reached before structural failure, making overly thick shields a hindrance rather than a benefit.

The study results for minimum thicknesses and masses (of aluminum) of the flat, conical, spherical, and ogive nose cone can also be found in [13]. These thicknesses are chosen to allow survival of the payload until the shield experiences structural failure. A further study found these thicknesses to depend very little on the material chosen, other than the mass of the resulting system, as the shape of the shield and the leader spacecraft tend to govern the achievable depth. Also discussed in [13] is the maximum achieved depth of burst (DOB). Reduced performance can be achieved by using thinner shields, and lowering the required DOB would result in benefits for timing the detonation of the payload. Based on such initial study, the following conclusions can be drawn for the design of the payload thermal shield. First, the primary variables in achievable DOB are the shape, mass, and timing of the kinetic-impact leader spacecraft. Additional analysis must be done to optimize this portion of the mission. Second, given a particular environment, a discontinuous shock to the payload presents challenges in determining how far to allow penetration before detonation. The nuclear payload cannot survive a direct impact at this speed, so it must be triggered using a combination of sensor and optical data at an appropriate data rate. Third, geometry of the shield seems to present a greater influence on DOB than any other variable. Adding thickness to the thermal shield in excess of the minimums presented do not result in further penetration, since both shields experience high structural loads at the maximum DOB. Finally, these results appear to be independent of the materials tested, as the limiting factor is the acceptable structural loads on the payload. However, significant mass can be saved by utilizing lighter alloys or materials for the thermal shield as discussed in [13].

1.3.4 Nuclear Fuzing Mechanisms

The nuclear explosive device (NED) was treated as a black-box payload to be delivered safely and reliably to a target asteroid in our NIAC Phase 1 & 2 studies [12–15]. However, it is emphasized that the NED triggering system is an integral part of the HAIV system and is one of the key enabling technologies required for the HAIV flight system.

In general, a standard fuzing mechanism ensures optimum NED effectiveness by detecting that the desired conditions for its detonation have been met, and providing an appropriate command signal to the firing set to initiate nuclear detonation. Fuzing generally involves devices to detect the location of the NED with respect to the target, signal processing and logic, and an output circuit to initiate firing. Without the proper selection of a reliable triggering or fuzing mechanism, there is a high risk that the mission can be unsuccessful. Current terrestrial triggering systems such as salvage fuzes, timing, contact, and radar (proximity) fuzes will need to be further examined for the HAIV. These fuzes act on the instantaneous time scale of approximately 1 milliseconds [13].

The salvage fuze acts as a contingency fuze that is employed as a failsafe detonation. The fuze "salvages" the NED and explodes when all other fuzes fail. The salvage fuze serves as a countermeasure to a terminal defense interceptor system and initiates after a detected collision possibility. The NED then explodes as soon as a target comes within a certain range of the NED. Sometimes radar and contact fuzes operate as the failsafe triggers and must function after withstanding extreme deceleration forces and delivery vehicle deformation. In an asteroid intercept scenario, the salvage fuze comprised of several contact and radar fuzes becomes activated. The contact and radar fuzes provide one option for arming and detonating the NED.

As discussed in [13], another option for triggering the NED is a timing fuze. The timing fuze operates by using time-to-go, estimated intercept distance, and the rate of the intercept distance. This information is provided to the triggering mechanism by the GNC instruments and flight computer. The computer activates the timing fuze once the guidance parameters meet specific conditions. The timing fuze is the most appropriate as the entire terminal-phase GNC process will be autonomous. However, if the timing fuze proves to be inaccurate, the salvage fuzes (contact and radar fuzes) can restore the arming mechanism of the NED. A salvage fuze is always present to resume the arming of the NED in the presence of any such triggering problems.

Proper fuzing systems and operations need to be further developed and flight validated. For a standoff burst disruption mission, radar acts as part of the primary fuzing system. For the subsurface or contact burst option, timing and radar fuzes may represent part of the primary detonation system, and contact fuzes are used as a failsafe detonation. The selection and sequencing of these fuzing options are chosen autonomously and are not dependent on additional hardware or configurations. Contact and radar fuzes can be located on top (front) of the follower spacecraft and in the thermal shield. However, the timing fuze and NED remain protected by the thermal shield.

It is important to note that such nuclear fuzing mechanisms have never been designed and tested to be used in space. One of the key enabling technologies to be flight validated during a flight validation mission for the HAIV system is sensors/electronics for NED fuzing mechanisms capable of handling a hypervelocity intercept with a speed of 10 to 30 km/s.

Chapter 2

Planetary Defense Flight Validation (PDFV) Mission Design

This chapter describes a reference PDFV mission architecture designed by the Mission Design Lab (MDL) of NASA Goddard Space Flight Center (GSFC) and target selection results for such a HAIV flight demonstration mission [15, 28].

2.1 The Need for a PDFV Mission

To help understand the mission requirements and constraints of a PDFV mission, it is useful to examine past and current robotic missions to NEOs. Between 1986 and 2011, a total of eleven science spacecraft have performed flybys of six comets and seven asteroids, and rendezvoused with two asteroids. Although there has been no space mission for directly demonstrating or validating planetary defense technologies, space agencies such as NASA, ESA, and JAXA have had several successful missions that demonstrate technology and mission capabilities that are somewhat relevant to a PDFV mission. Some of the most notable missions to NEOs are the Hayabusa Mission by JAXA, and the NEAR-Shoemaker and Deep Impact missions by NASA.

The Hayabusa spacecraft, formerly known as MUSES-C, was sent to the asteroid 25143 Itokawa, which is 535 × 294 × 209 m in size. While at the asteroid, the spacecraft attempted two landings for the purpose of collecting surface samples, which were subsequently returned to Earth in June 2010. However, problems with the sample collection mechanism resulted in only tiny grains of asteroid material being returned. The spacecraft also had a small lander onboard, called MINERVA, that was to be guided to the surface of the asteroid. Unfortunately, the lander drifted into space and was unable to complete its mission.

The NEAR-Shoemaker mission was designed to study the asteroid 433 Eros, which is one of the largest NEOs at 34.4 × 11.2 × 11.2 km in size. This spacecraft was the first to orbit an asteroid as well as the first to land on one. While the Hayabusa mission was designed to softly touch down

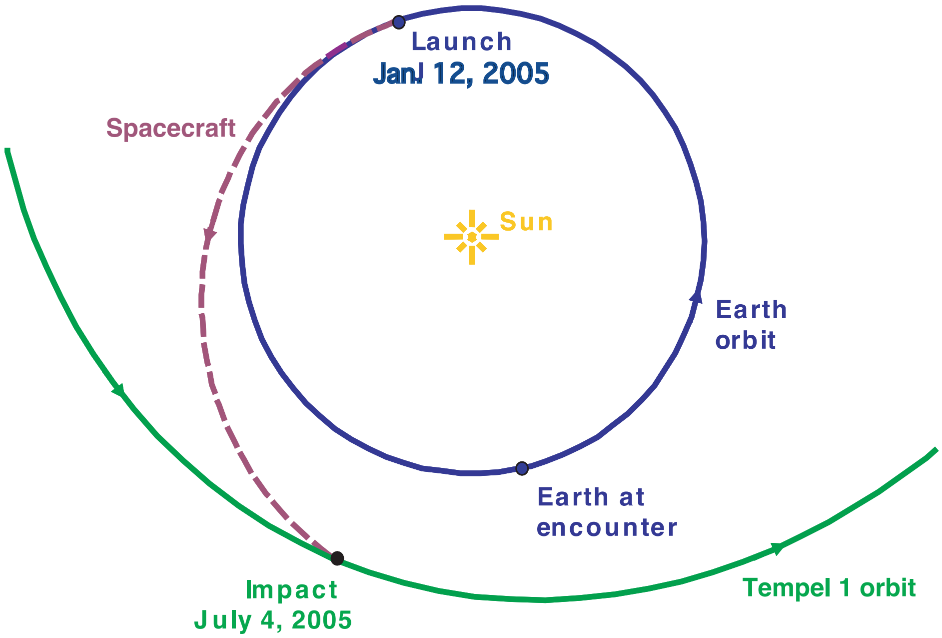

Figure 2.1: The Deep Impact mission trajectory [25–27].

on the surface of Itokawa, the Deep Impact mission in 2005 was designed to collide with its target at high speed [25–27]. Approximately 24 hours prior to impact with the comet 9P/Tempel 1, which is 7.6 × 4.9 km in size, the impactor was separated from the flyby spacecraft and autonomously navigated to ensure a hypervelocity impact at a relative speed of 10.3 km/s [25–27]. The Deep Impact mission trajectory is illustrated in Fig. 2.1.

The Rosetta spacecraft of ESA, which was launched on 2 March 2004, subsequently flew past the asteroids 2867 Steins in 2008 and 21 Lutetia in 2010. It successfully rendezvoused with comet 67P/Churyumov-Gerasimenko in August 2014. On 12 November 2014, Rosetta's lander, named Philae, attempted a soft landing on the comet surface at a relative speed of around 1 m/s; but, it bounced twice and ultimately ended up sideways in the shadow of a cliff.

NASA is currently developing the OSIRIS-REx mission, which will launch in 2016 to rendezvous with asteroid 101955 Bennu (1999 RQ36) and return samples of the asteroid material to Earth in 2023. This mission will utilize large deep space maneuvers, an Earth gravity assist, rendezvous and proximity operations maneuvers, and an asteroid departure maneuver. In early December of 2014, Japan's JAXA launched an asteroid sample return mission known as Hayabusa 2 with the goal of returning samples from the NEA 162173 (1999 JU3).

In the mid 2000s, ESA considered a demonstration mission for a kinetic impactor called the Don Quijote mission. The mission concept called for two separate spacecraft to be launched at the same time but follow different interplanetary trajectories. Sancho, the orbiter spacecraft, would be the first to depart Earth's orbit, and rendezvous with a target asteroid approximately 500 m in diameter. Sancho would measure the position, shape, and other relevant characteristics before and after a hypervelocity impact by Hidalgo, the impactor spacecraft. After Sancho studied the target for some months, Hidalgo would approach the target at a relative speed of approximately 10 km/s. Sancho then observes any changes in the asteroid and its heliocentric orbit after the kinetic impact to assess the effectiveness of this deflection strategy. However, this mission concept was never realized due to higher than expected mission costs.

Most NEO science missions required at least several years, in some cases 5 to 6 years or more, for mission concept development and spacecraft construction prior to launch. It is also important to note that quite a few of these missions originally targeted different asteroids or comets than those that were actually visited. This is because the mission development schedules slipped and launch windows for particular asteroids or comets were missed. Additionally, several of these missions experienced hardware or software failures or glitches that compromised the completion of mission objectives. None of those things would be tolerable for a planetary defense mission aimed at deflecting or disrupting an incoming NEO, especially with relatively little advance warning. Thus, while the successful scientific missions that have been sent to asteroids and comets thus far have certainly provided future planetary defense missions with good heritage on which to build, we are clearly not ready to respond reliably to a threatening NEO scenario.

It is also important to note that most of these missions visited asteroids or comets that range in size from several kilometers to several tens of kilometers. Furthermore, the flyby distances ranged from several tens of kilometers to several thousand kilometers. The sole exception to this is the Deep Impact mission [25–27], which succeeded in delivering an impactor to the target. However, the mission was aided by the fact that comet 9P/Tempel 1 is 7.6×4.9 km in size and, therefore, provided a relatively large target to track and intercept. The Deep Impact mission was not intended to be a PDFV mission. For planetary defense missions requiring NEO intercept, the requirements will be far more stringent: NEO targets with diameters as small as several tens to several hundreds of meters will have to be reliably tracked and intercepted at hypervelocity speeds, with impact occurring within mere meters of the targeted point on the NEO's surface. This will require significant evolution of the autonomous GNC technology currently available for spacecraft missions to NEOs.

Furthermore, none of the potential planetary defense mission payloads (e.g., nuclear explosives) to deflect or disrupt NEOs have ever been tested on NEOs in the space environment. Significant work is therefore required to appropriately characterize the capabilities of those payloads, particularly the ways in which they physically couple with NEOs to transfer energy or alter momentum, and ensure robust operations during an actual emergency scenario.

2.2 Preliminary PDFV Mission Design by the MDL of NASA GSFC

2.2.1 Overview

The primary objective of the one-week MDL design study conducted for our NIAC Phase 2 study in 2012 [15] was to assess the technical feasibility of deploying a spacecraft to intercept a small (50 to 150 m) NEO within 10 m of its center with 3σ confidence at high relative velocity ($>$10 km/s) in order to provide a viable planetary defense solution for short warning time scenarios. The MDL performed this assessment by developing a preliminary spacecraft systems concept for the HAIV capable of reliably delivering a notional NED payload to a target NEO and transmitting adequate telemetry for validation of system performance. In addition to the conceptual spacecraft design, the MDL created associated plans for the supporting mission and ground operations in order to provide an overall mission architecture.

The MDL worked to design a fully capable HAIV (rather than a simplified test platform) and apply the fully capable design to a suitable practice target NEO. The MDL endeavored to make the flight validation mission affordable through judicious mission design rather than via a scaled-down, less expensive flight demonstration platform. The primary design drivers are the high relative velocity at impact and the precision timing required for detonation of the NED in the shallow crater excavated by the leading kinetic impactor portion of the vehicle. The MDL carefully considered what systems equipment should be placed on the lead portion (kinetic impactor) of the HAIV and what should be placed on the follower portion (NED payload carrier). Additionally, high reliability is required because there will only be one opportunity to successfully strike the target NEO. These considerations make it clear that the HAIV will need to be a highly responsive system with onboard autonomous control because of the latency inherent in ground commanding and the highly dynamic environment of the terminal approach phase.

Yet another challenging aspect of this mission is that the size, shape, and rotational state of the NEO will generally not be known in advance of the intercept mission. Design, selection, fuzing, and so on for the NED was purposely placed outside the scope of the MDL study. For the purposes of the study, it was assumed that a dummy mass proxy for the NED payload is installed in the HAIV for the flight validation mission. The NED proxy is modeled as a cylinder 1 m in length with a 0.5 m face diameter and a mass of 300 kg.

2.2.2 HAIV System and Mission Design

The overall configuration/system design of an experimental HAIV system is illustrated in Fig. 2.2. This reference HAIV system consists of the leading impactor portion of the vehicle, the trailing

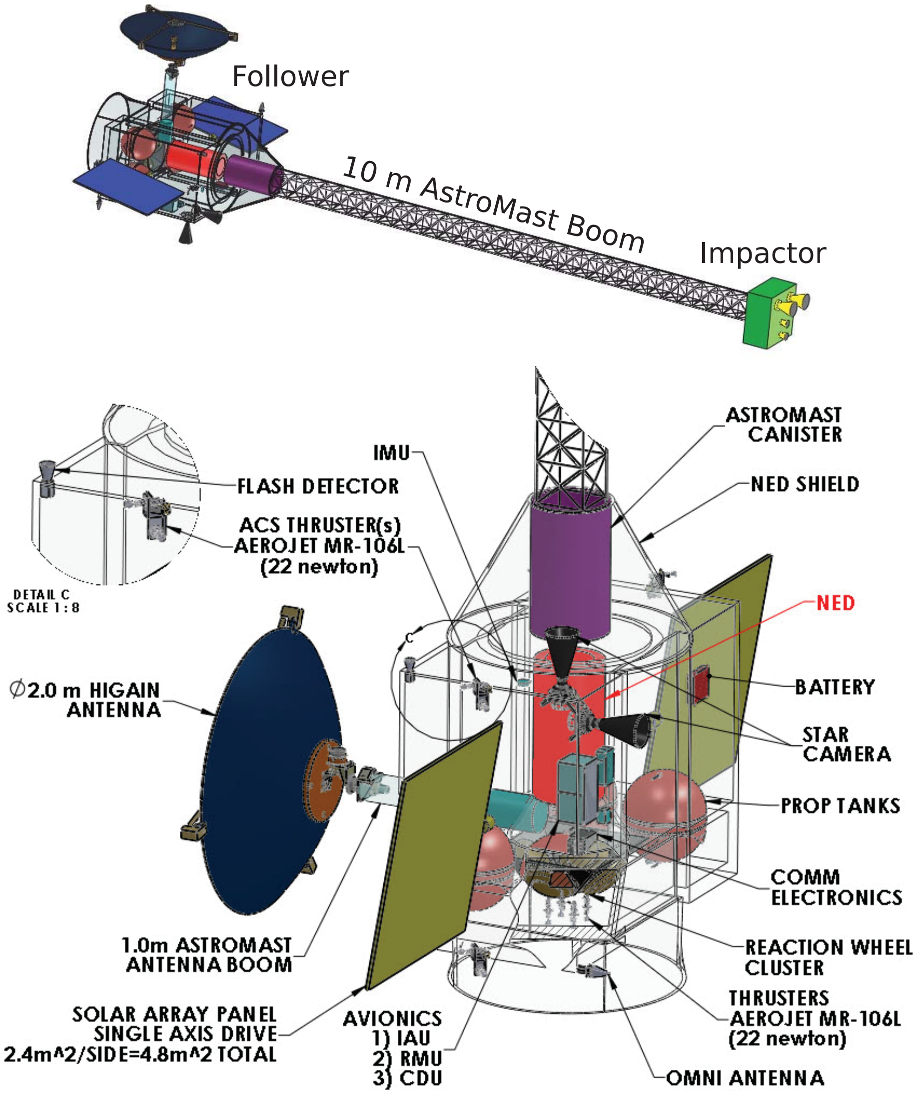

Figure 2.2: An experimental HAIV flight system designed by the MDL of NASA GSFC [15].

follower portion of the vehicle (carrying the dummy mass proxy for the NED), and the 10-m AstroMast extendable boom that provides the necessary separation between the impactor and follower during NEO impact. This optional configuration employing a deployable boom ensures that the two parts of the vehicle remain collinear during impact. The length of the boom is customized for the particular mission scenario at hand such that the boom length provides an appropriate delay time between when the impactor creates the crater on the NEO and when the follower arrives in the crater and detonates the NED. The appropriate delay time is of course dependent on the terminal approach profile, which is chiefly dominated by the HAIV velocity relative to the NEO at impact.

For launch vehicles, the MDL considered the United Launch Alliance (ULA) Atlas V 400/500 Evolved Expendable Launch Vehicle (EELV) Series, the SpaceX Falcon 9, and the Boeing Delta IV series. All of these launch vehicles provide sufficient mass capability at the desired Earth departure

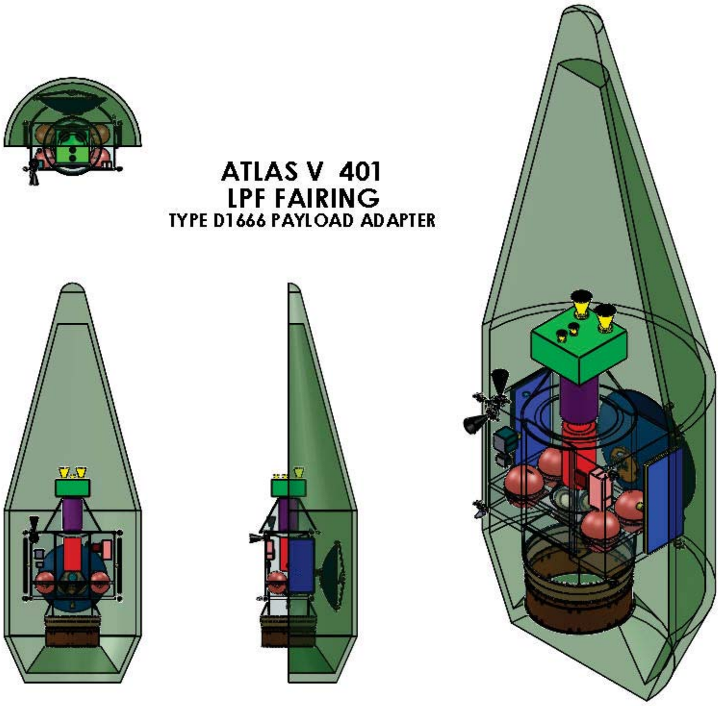

Figure 2.3: A reference HAIV launch configuration with Atlas V 401 [15].

C_3 but the Atlas V is the only EELV currently covered under the NASA Launch Services Program II contract. As such, the Atlas V 401 with a 4 m fairing was selected as the primary launch vehicle for the MDL study. The HAIV launch configuration in the Atlas V 401 payload fairing is shown in Fig. 2.3. Accordingly, the HAIV flight demo mission will launch from Cape Canaveral Air Force Station (CCAFS).

After analyzing several candidate asteroids for a PDFV mission, asteroid 2006 CL9 was chosen as a reference target of the conceptual flight validation mission design by the MDL. The physical and orbit properties of 2006 CL9 are presented in Table 2.1. The orbital elements of 2006 CL9 listed in this table are heliocentric ecliptic J2000 orbital elements at epoch JD 2456400.5 (2013-04-18.0) TDB (JPL Orbit ID 26).

An important consideration in target selection for the MDL study was how well the orbit of the NEO is known. If there is too much uncertainty in our knowledge of the NEO's orbit it may not be possible to guide the HAIV to a precision intercept with the NEO. The quality of NEO orbit knowledge is usually expressed by the Orbit Condition Code (OCC), which is an integer scale describing the amount of along-track uncertainty in the NEO orbit knowledge. The size, shape, and orientation of NEO orbits are generally easier to estimate than the position of the NEO along its orbital path, and the location of the NEO on its orbit is therefore usually the least well known aspect of the NEO's orbit. The OCC scale ranges from 0 (a very well known orbit) to 9 (very

Table 2.1: Physical and orbital properties of a reference target (asteroid 2006 CL9) [15]

Parameters	Values
Absolute magnitude H	22.73
Estimated diameter ($w/p = 0.13$)	104 m
Estimated diameter ($w/p = 0.25$)	75 m
Rotation period	0.145 ± 30% hours
Semi-major axis a	1.34616 AU
Eccentricity e	0.23675
Inclination i	2.93551 deg
Longitude of Ascending Node Ω	139.313 deg
Argument of Perihelion ω	9.94912 deg
Mean Anomaly at Epoch M_0	209.664 deg
OCC	5
Earth MOID	0.03978 AU

Table 2.2: Notional flight validation mission selected for 2006 CL9 [15]

Parameters	Values
Earth departure date	2019-08-02
Earth departure C_3	11.99 km^2/s^2
Flight time to intercept	121.41 days
NEO Relative velocity at intercept	11.5 km/s
Approach phase angle	3.04 deg
Max. distance from Earth	0.36 AU
Max. distance from Sun	1.28 AU

poor orbit knowledge), and NEOs with OCC $>$5 are generally considered "lost" for the purposes of locating them in the sky during future observing opportunities.

Note that two estimated diameter values for 2006 CL9 are presented in Table 2.1 based on the parameter p, which is the geometric albedo of the NEO (a measure of how optically reflective its surface is). The albedos of NEOs vary widely and are very difficult to ascertain from ground based observations. This leads to significant uncertainty in the physical size of most known NEOs. The problem can be summarized as: small shiny objects can have the same brightness in the sky as large dull objects. The intrinsic brightness of the NEOs, expressed by the absolute magnitude H, is much better constrained (because it is directly observed) than albedo.

A reference mission trajectory selected for 2006 CL9 is summarized in Table 2.2. The reference trajectory design is based on patched conics with Lambert targeting applied to high-fidelity ephemerides for the Earth and NEO, and, therefore, no deterministic ΔV is required on the part of the spacecraft in this initial trajectory design.

A reference orbital trajectory of a PDFV mission to asteroid 2006 CL9 is shown in Fig. 2.4,

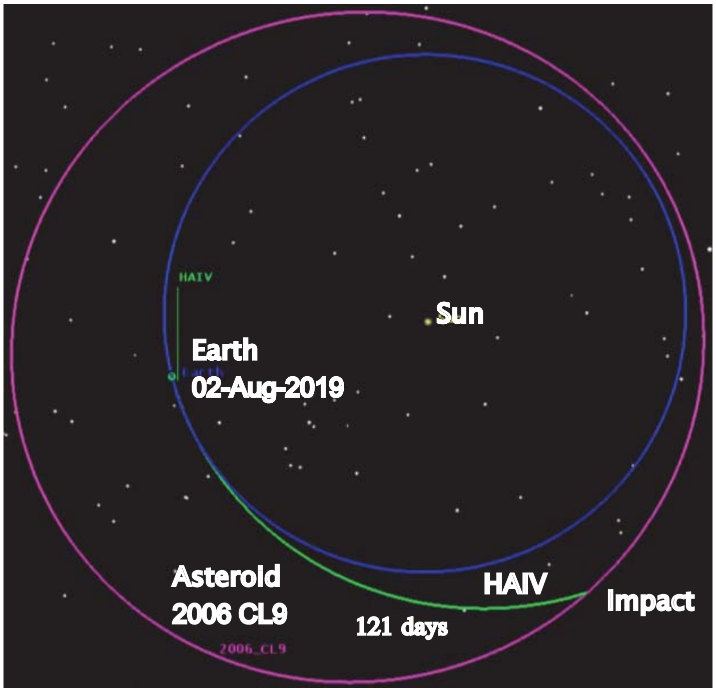

Figure 2.4: A reference PDFV mission trajectory for a target asteroid (2006 CL9) [15].

which is similar to the Deep Impact mission trajectory shown in Fig. 2.1 due to the fact that both missions are intended to directly intercept and impact the target object. For the Atlas V 401, the dispersion on the Earth departure C_3 is 0.15 km^2/s^2, which leads to a ΔV for launch dispersion correction of approximately 26 m/s, including maneuver execution errors. The Declination of the Launch Asymptote (DLA) and Right ascension of the Launch Asymptote (RLA) are $-12.0°$ and $52.4°$, respectively. The time of injection into the outbound Earth departure hyperbola is 2019-08-02, 08:47:26.443 UTC. The flight time to NEO intercept is 121.41 days, which leads to a time of intercept of 2019-12-01, 18:37:50.443 UTC. The velocity relative to the target at intercept is 11.5 km/s and the approach phase angle is 3 deg. The maximum distance from the Earth is 0.36 AU and the maximum distance from the Sun is 1.28 AU. This particular trajectory design was assumed to be the middle of the launch window. The total post-launch ΔV budget for the mission is 37.1 m/s.

Figure 2.5(a) presents the overall mission timeline, beginning with launch on August 2, 2019. Launch is followed by two weeks of on-orbit checkout (during the Earth departure trajectory), which leads into approximately 121 days of outbound cruise towards the target NEO. Although the flight validation mission only carries a simple mass proxy for the NED, we will treat it as if it were a live explosive payload and go through the same steps that we would with the live payload. Thus, the dummy nuclear payload is “armed” 30 days prior to NEO impact (I-30 days). The onboard targeting system is engaged at I-48 hours and images of the NEO (still very small in the camera Field Of View (FOV) begin to be transmitted to the ground. The boom is then extended to

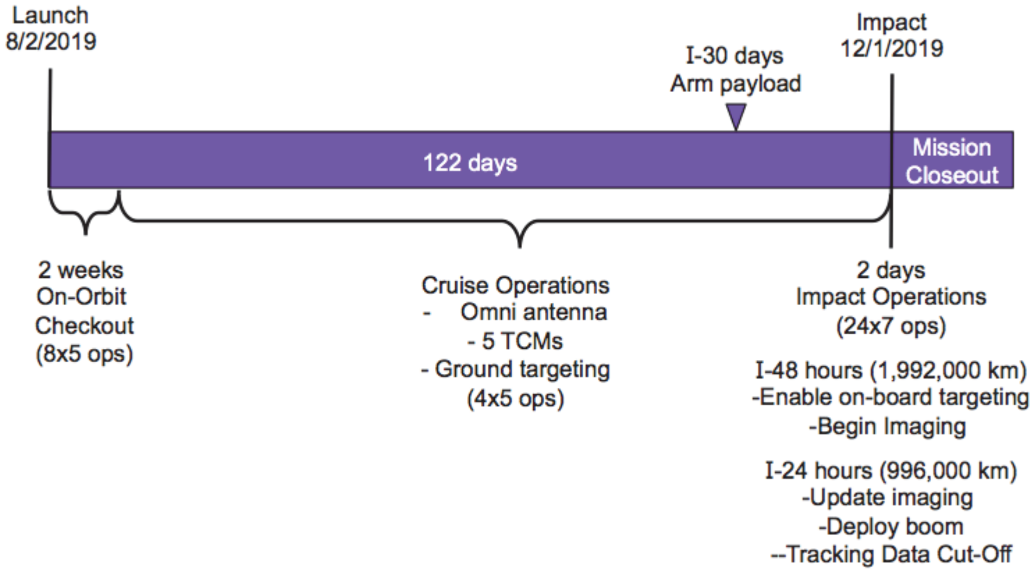

(a) Overall mission timeline.

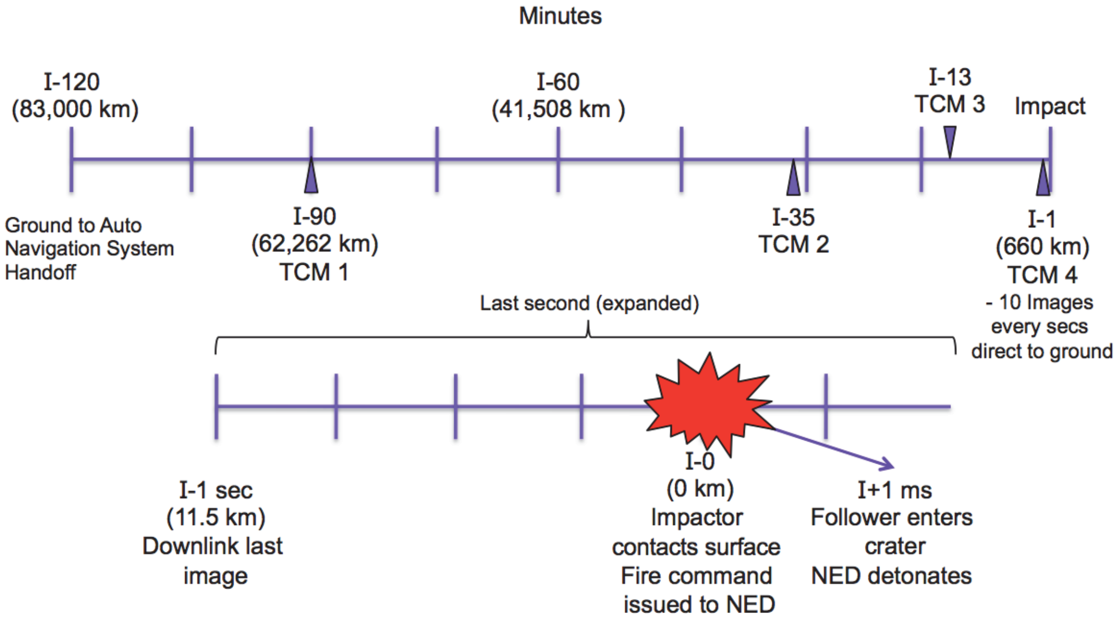

(b) Mission timeline for the final 2 hours.

Figure 2.5: HAIV flight validation mission timeline by the MDL of NASA GSFC [15].

deploy the impactor at I-24 hours. Figure 2.5(b) shows the mission timeline for the final 2 hours. At I-2 hours the ground relinquishes control to the space vehicle and the Trajectory Correction Maneuvers (TCMs) begin. At the final 60 seconds before impact the HAIV is 660 km away from the NEO and is transmitting 10 images per second to the ground, with the final image downlinked at I-1 second. At I-0 the impactor contacts the surface of the NEO (creating a shallow crater) and that event causes the fire command to be issued to the NED mass proxy (which is instrumented with the same circuitry that would be used with an actual NED). At I+1 millisecond the follower portion of the vehicle enters the crater and the NED would detonate at this time (due to the fire command having been issued at the proper time 1 millisecond prior to crater entry).

2.2.3 Terminal Guidance, Navigation, and Control Subsystem

One of key subsystems of the HAIV is the terminal Guidance, Navigation, and Control (GNC) subsystem, which is briefly described here. The MDL performed a complete navigation simulation of the terminal approach phase beginning at I-2 hours. The navigation simulation included a linear covariance analysis and a Monte Carlo error analysis. The navigation simulation utilized a sequential Kalman filter with observations derived from the asteroid centroid location in the sensor CCD (Charge-Coupled Device). The navigation filter is solving for the inertial position and velocity of the spacecraft with respect to the asteroid. The simulation software utilized is the Orbit Determination Toolbox (ODTBX), which is an advanced mission simulation and analysis tool used for concept exploration, early design phases, and rapid design center environments. ODTBX is developed by the Navigation and Mission Design Branch at NASA Goddard Space Flight Center. The software is released publicly under the NASA Open Source Agreement and is available on SourceForge at http://sourceforge.net/projects/odtbx/.

The optical navigation sensors modeled in the simulations are based on the Deep Impact mission's Impactor Targeting Sensor (ITS), which has a Field Of View (FOV) of $0.6°$, a focal length of 2101 mm, and a resolution of 1024×1024. The navigation relies on identification of the target body centroid in the sensor field of view. The acquisition requirement is to be able to detect a 13th apparent magnitude object with a signal-to-noise ratio of at least 10 within a 5-second exposure.

Figure 2.6 presents a block diagram for the Autonomous Navigation System (ANS) that is modeled in simulation to perform navigation and compute TCMs. TCM targeting is based on the latest estimate of spacecraft state from the Kalman filter, which encapsulates both navigation and maneuver execution errors. Four TCMs are performed after optical acquisition to correct for navigation and execution errors. TCMs 1 through 3 are targeted using full three-dimensional differential correction while TCM 4 is targeted using two-dimensional B-plane targeting. This

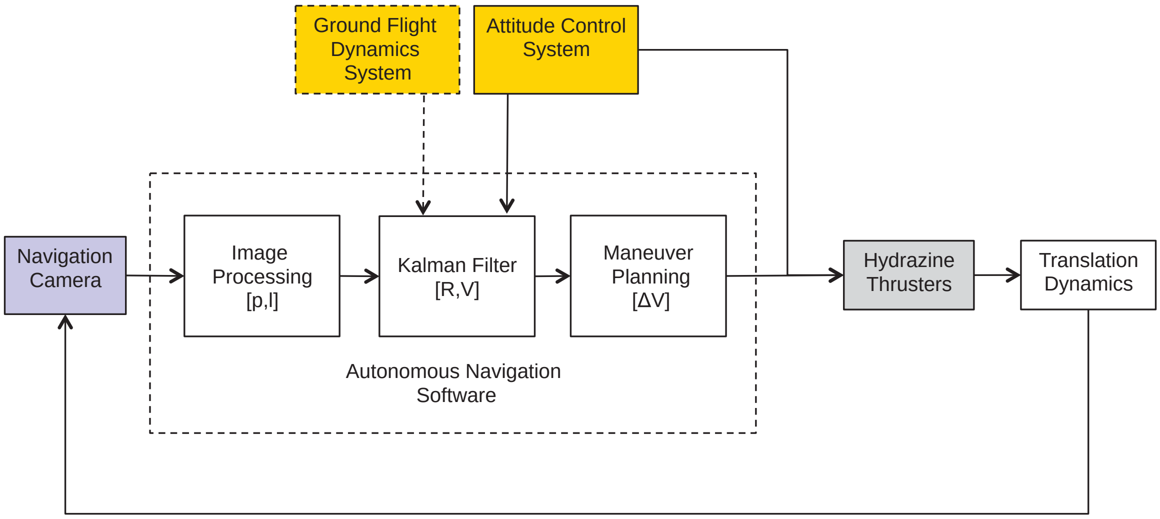

Figure 2.6: Block diagram of the Autonomous Navigation System (ANS) of an experimental HAIV [15].

was found to be the most robust targeting scheme after initial experimentation because the range between the HAIV and the target NEO is not very observable and that compromises targeting schemes that rely solely on full three-dimensional position targeting. The ground-to-ANS handoff occurs at I–2 hours, at which time the flight dynamics system on the ground provides a final state update to the HAIV and hands over translational control to the ANS. The ANS computes and executes TCMs at I–90 minutes, I–35 minutes, I–12 minutes, and I–1 minute. The ANS was exercised for our target NEO scenario with a Monte Carlo simulation to characterize performance in terms of impact accuracy.

The HAIV Attitude Control System (ACS), illustrated in Fig. 2.7, is designed to provide stable pointing throughout all mission phases from launch to NEO impact. After launch the ACS will null residual tip-off motion and acquire the appropriate mission attitude, with the solar array panels facing the Sun. During outbound cruise, up until the terminal approach phase begins, the ACS will facilitate solar array pointing to the Sun (the arrays are able to rotate completely about the +Y spacecraft body axis). The ACS will also facilitate pointing of the high-gain antenna to the Earth with a pointing accuracy of 0.1°. The antenna can be slewed in two axes over a restricted angular range. The ACS will also keep the cold side of the spacecraft pointed away from the Sun for appropriate thermal control. For maneuvers, the ACS will point the thruster centerlines within 0.5° of the designated inertial coordinates. During the terminal approach phase the ACS will nominally hold the +X spacecraft body axis parallel to the spacecraft's velocity vector. That pointing will be maintained by using thrusters to translate transversely. Additionally, the star camera may be provided as a backup to the impact sensors. The ACS for this mission requires a standard three-axis

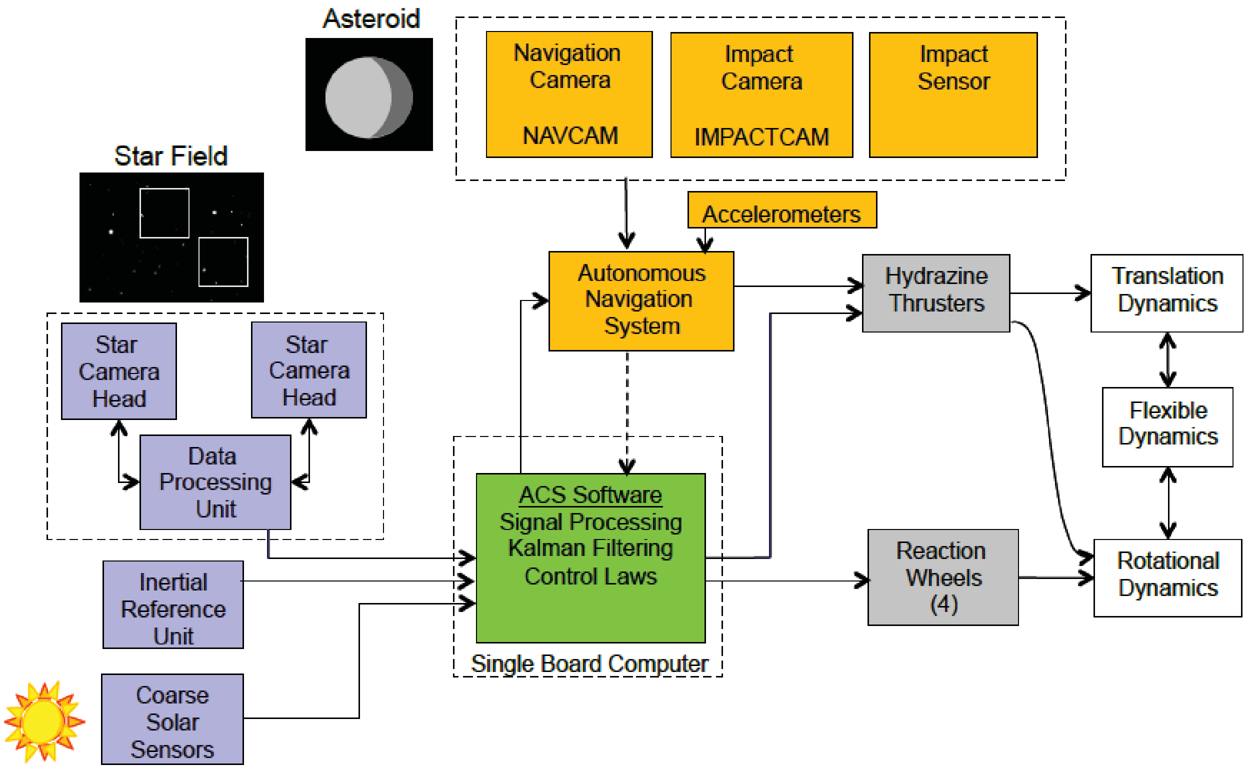

Figure 2.7: Block diagram of the Attitude Control System (ACS) of an experimental HAIV [15].

stabilized system. The attitude sensors include two star cameras and an inertial reference unit (gyros and possibly an accelerometer package). While two camera heads are baselined in the design, the data processing unit can accommodate up to four camera heads if needed. The attitude actuators include four reaction wheels arranged in a pyramid to provide mutual redundancy along with hydrazine thrusters. The following attitude control modes are defined for this mission: acquisition, cruise, terminal phase, and safe hold. The ACS will be operating continuously using the reaction wheels, and the attitude control thrusters will be used at discrete times for momentum unloading. The attitude control thrusters may also be needed during any “turn-and-burn” maneuvers. During the terminal phase, the ACS software will provide the inertial-to-body frame quaternion to the ANS.

The terminal guidance system performance was evaluated for our target NEO scenario with a Monte Carlo simulation to characterize performance in terms of impact accuracy. Due to study time constraints only 100 Monte Carlo cases were executed to produce the preliminary results shown in Fig. 2.8. Figure 2.8(a) shows the impact locations in the B-plane while Fig. 2.8(b) shows the corresponding impact locations on the body of the target NEO. Note that the area of brightness on the surface of the spherical NEO model shown in Fig. 2.8(b) accurately depicts the solar illumination in the reference mission scenario for 2006 CL9. Further detailed studies on the

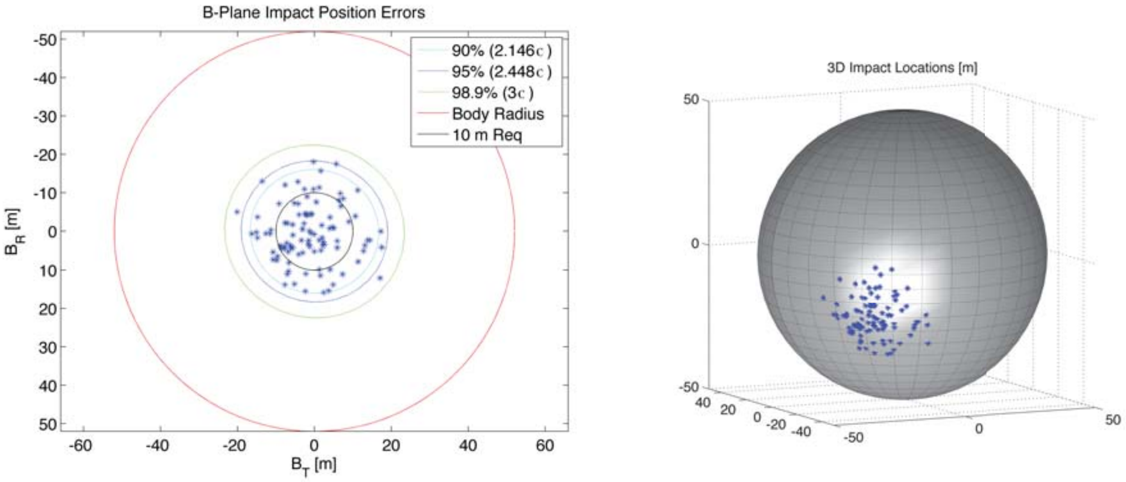

(a) Simulated HAIV impact locations in the B-plane. (b) Simulated HAIV impact locations on the target NEO body.

Figure 2.8: Monte Carlo simulation results for intercepting an ideal 100-m target asteroid using the B-plane targeting method [15].

effects of various additional uncertainties in orbit determination, navigation, spacecraft attitude control, sensor noise, etc. will be needed to finish preparing the design for flight implementation. A terminal guidance system design study utilizing optical and infrared seekers for an irregular-shaped asteroid will be presented in Section 19.4.

2.2.4 Future Work for HAIV Mission Design

Technologies and algorithms must be developed and validated to create sensors capable of accurately and reliably detecting the hypervelocity collision of the impactor with the target NEO. These sensors could be hypervelocity electromechanical contact sensors, some form of LIDAR or radar, a visible flash detector, or some other type of device. The number of sensors and the manner of their operation must be such that robust hypervelocity impact detection is provided, i.e., false positives and false negatives must both be prevented with adequate confidence. The appropriate number of sensors will be informed by the type of sensors used, and reliability is a key factor.

Additional sensors and/or multiple sensor types may be necessary if an adequate confidence of successful fire commanding cannot be provided with a given set of sensors. The design of the hypervelocity impact sensors will be informed by rigorous high-fidelity computational modeling of the hypervelocity kinetic impact event, and ground validation of some candidate sensor types may be possible, e.g., using hypervelocity impact facilities in terrestrial laboratories. Such ground test campaigns could utilize scale models of the HAIV instrumented with candidate impact detection sensors. Another aspect of the design that would benefit tremendously from ground testing is the NED shield. The behavior of the boom during the hypervelocity impact is another key area that must be studied through both high-fidelity computer simulations and possibly ground testing. We must be certain that the size, shape, and materials used to construct the boom fail during the hypervelocity impact in a manner that does not threaten the NED payload, the impact sensors, or the production and reception of the NED fire command signal. At the same time, during the process of advancing the design for actual implementation, it will be necessary to further assess the feasibility, advantages, and disadvantages of having the impactor and follower be physically separated free-flying vehicles rather than connected by a boom.

Another key area of analysis is the final approach timeline. The results presented herein demonstrate that the final approach timeline depends on the target NEO diameter and albedo, as well as the approach phase angle relative to the NEO and the relative velocity at impact. Developing parametric models for the approach timeline as a function of these and other key driving parameters will facilitate refinement of the onboard optical systems to ensure acquisition of the target sufficiently far in advance of the impact for the ANS to be able to operate robustly and achieve a precise and accurate impact with high confidence. We can also adjust our trajectory optimization algorithms to attempt to minimize the intercept velocity within the constraints that the crater excavated on the NEO is of sufficient depth and that the additional maneuver required for intercept velocity control is within our available ΔV budget.

One of the driving requirements of the HAIV system is the requirement that the flight experiment must be able to be fully validated in ground post-processing of the HAIV telemetry. While this requirement actually leads to a robust design, it would clearly be beneficial to have an observer spacecraft present near the target NEO before and after the impact to more directly observe and characterize the HAIV performance. As such, subsequent to the MDL study we developed new algorithms to perform trajectory scans that identify mission opportunities in which an observer and HAIV spacecraft can be both transported to the NEO (at different times) for low ΔV. The results of these new mission opportunity searches may reveal affordable options for having both an observer and a HAIV in the mission simultaneously. Another alternative worth considering is having the HAIV deploy a free-flying observer that could also serve as calibration target during the cruise to the NEO. The difficulty with this option is that the deployed free-flying system would need to be capable of high bandwidth communications with Earth and would therefore probably be so large that the it cannot reasonably treated as a small deployable add-on; in that case we return to the aforementioned alternative of deploying a fully capable observer as a separate spacecraft. The final variation on this option is to have another entity supply the observer spacecraft since it is fully decoupled from the HAIV. For example, NASA could build, deploy, and operate the HAIV, while another agency, e.g., ESA, could build, deploy, and operate the observer spacecraft. This scenario is advantageous from the perspective of addressing the international nature of planetary defense.

The MDL study identified other areas of beneficial forward work, some of which have been addressed during our NIAC phase 2 work. These include improvement of ANS performance and robustness for NEO targeting accuracy and maneuver magnitude management, using the GNC algorithms to process synthetic imagery for realistic cases including irregularly shaped rotating NEOs of various sizes, and assessment of the effects of NEO density on the cratering performance of the kinetic impactor portion of the HAIV.

2.2.5 Summary

This section has presented the results of a NASA/Goddard Space Flight Center (GSFC) Mission Design Lab (MDL) study for the conceptual design of the HAIV flight validation mission as part of our NIAC Phase 2 study [15]. The MDL study provided a feasible and detailed conceptual design for the HAIV flight validation mission and identified a number of key topics for further research. These research topics include high-fidelity computational modeling of hypervelocity impact physics, detailed development of advanced GNC algorithms for precision hypervelocity intercept of small (50 to 150 m size) NEOs, and design and development of test plans for robust hypervelocity impact sensors. In our subsequent research we continued to refine, deepen, expand, and advance the design of the HAIV system and its flight validation mission.

The estimated cost of an experimental HAIV flight demonstration mission described in this section is approximately \$530M, including the launch vehicle [15]. An approximate cost of \$150M is assumed for the notional launch vehicle, which is the Atlas V 401. The cost estimate is comprehensive and includes the complete design, construction, integration, and testing of the spacecraft itself, launch vehicle integration and test, project management, mission operations, ground system, systems integration and test, education and public outreach, and project reserves. More details of the HAIV flight validation mission design by the MDL of NASA GSFC can be found in [15].

When a hazardous NEO on a collision course with Earth is discovered, we will not have the luxury of designing, testing, and refining our systems and plans. We will need to be prepared to take effective action on relatively short notice with a high probability of succeeding on the first try because we may not have a second chance. That level of preparedness can only be achieved through proper design and testing of systems so that we are comfortable with carrying out planetary defense test and practice missions before we need to deploy such a mission in response to an actual threat.

2.3 Target Selection for the PDFV Mission

In [15, 28], a simple direct intercept mission trajectory, as illustrated in Fig. 2.4, similar to the Deep Impact mission trajectory shown in Fig. 2.1, was found to be the best option for the PDFV

Table 2.3: Target selection criteria for the Don Quijote mission study [29]

Orbit Characteristics	Preferred Range
Rendezvous ΔV	$<$ 7 km/s
Orbit type	Amor
MOID	large and increasing
Orbit accuracy	well determined orbits
Physical Characteristics	**Preferred Range**
Size	$<$ 800 m
Density	$\sim$1.3 g/cm^3
Absolute magnitude	20.4 - 19.6
Shape	not irregular
Taxonomic type	C-type
Rotation period	$<$ 20 hours
Binarity	not binary

mission. The direct intercept mission has the largest number of feasible candidate target asteroids, requires a minimal total post-launch ΔV, and is a representative of the most probable worst-case asteroid mitigation mission scenario with short warning time. More advanced missions, which enable an observer spacecraft to arrive at the asteroid prior to the main spacecraft impact, have also been analyzed in [28]. The results generally show that allowing the impactor spacecraft to perform multiple gravity assists lowers the total required ΔV for each mission considered as well as increases the impactor arrival velocity. Several feasible gravity-assist rendezvous missions are presented in [28]. There are several possible target asteroids which require a total ΔV of 1.5 km/s or less, with the most efficient combined rendezvous/impact mission requiring only approximately 600 m/s of ΔV.

2.3.1 Reference Targets of the Don Quijote Mission Study

Although the Don Quijote mission was never realized and launched by ESA, it is useful to review the target selection process once considered for the Don Quijote mission [29–31]. Its target selection criteria were based on a set of NEO characteristics defined by ESA's NEOMAP summarized in Table 2.3. A preliminary selection resulted in the asteroids 2002 AT4 and 1989 ML. As seen in Table 2.4, asteroid 2002 AT4 is roughly half the size of 1989 ML, but intercepting it requires more ΔV.

2.3.2 Target Selection Problem Formulation

A comparison of NEA orbit families is shown in Fig. 2.9. For a PDFV mission, NEAs in the Atira and Amor orbit groups are preferred as target candidates. NEAs in these groups all have perihelion

Table 2.4: Properties of candidate targets formerly considered for the Don Quijote mission study [29]

	2002 AT4	1989 ML
Orbital period (yrs)	2.549	1.463
e	0.447	0.137
i (deg)	1.5	4.4
ΔV (km/s)	6.58	4.46
Orbit type	Amor	Amor
MOID	large	large
Absolute magnitude	20.96	19.35
Taxonomic type	D-type	E-type
Diameter (m)	380	800
Rotational period (hrs)	6	19

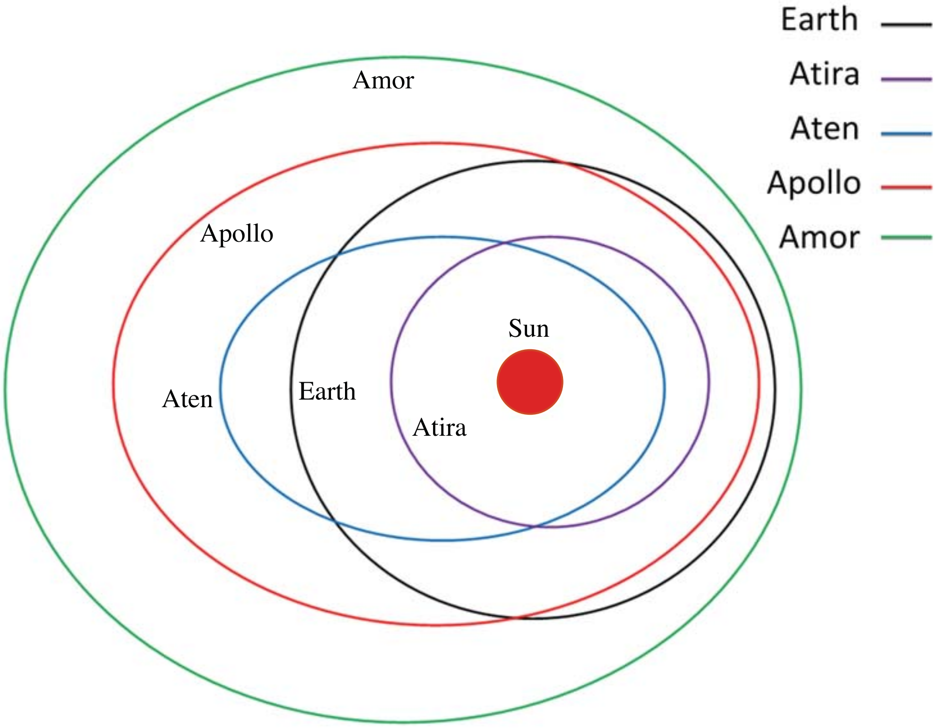

Figure 2.9: Typical orbits of Amor, Apollo, Aten, and Atira asteroids.

distances < 1.3 AU, and many of them also cross the Earth's orbit at some point. The proximity of NEA orbits to Earth's orbit means that the ΔV required for intercept is usually small. As such, we expect that a number of NEAs will prove to be viable candidates for a NEA deflection/disruption flight validation mission. Apollo and Aten NEA orbits cross Earth's orbit, and in some cases this leads to lower mission ΔV requirements as compared to Atiras or Amors. On the other hand, this same fact means that any significant perturbation to the NEA's orbit could cause it to impact the Earth later. Such unintended consequences must not occur. This is the reason why ESA considered asteroids 2002 AT4 and 1989 ML from the Amor group for the Don Quijote mission [29–31].

To preclude the possibility of inadvertently perturbing a previously harmless NEA onto an Earth collision course, only Atira and Amor NEAs are considered for a PDFV mission in [15, 28]. The Amor asteroid group is characterized by asteroids that approach the Earth, but do not actually cross its orbit. By definition the perihelion distances of these asteroids lie between 1.017 and 1.3 AU. As of July 21, 2012, there were 3398 Amor and Atira asteroids listed in NASA's NEO Program database. Only 10 of those are Atira asteroids; because their orbits are entirely inside Earth's orbit and we currently have no space-based NEO survey, it is very difficult to discover Atiras. Amor asteroid orbits are entirely outside of the Earth's orbit. Because the orbits of Atiras and Amors are entirely interior or exterior to Earth's orbit, respectively, disturbances to the orbits of those asteroids due to human activity are not likely to cause those asteroids to move onto Earth-impacting orbits after the PDFV mission.

A mission design software tool capable of performing advanced mission analysis for thousands of potential target asteroids is described in [28]. Due to the large number of design parameters in this type of mission design, an exhaustive search of all 3398 asteroids would be impractical. Consequently, all mission design computation is performed using an evolutionary genetic algorithm in [28]. A combination of evolutionary algorithms, modular mission design software, and modern GPUs (Graphics Processing Units) allows computationally efficient design of multiple possible mission architectures for thousands of possible target asteroids.

The first constraint imposed ensures that the HAIV will be able to communicate with Earth ground stations during the final impact phase of the mission. This is achieved by penalizing any mission where the impact would occur on the opposite side of the sun from the Earth. The exact angle limitations for the impact Earth-Asteroid angle are: the angle must be $<175^\circ$ from the Earth and $>185^\circ$ from the Earth, as illustrated in Fig. 2.10. The second main constraint is a guidance and navigation constraint such that the impactor approaches from the sunward side of the asteroid. This constraint ensures proper lighting conditions for the terminal guidance phase of the mission.

The purpose of a PDFV mission is to demonstrate the feasibility of the HAIV system for the purpose of planetary defense. The HAIV is designed for the hypervelocity impacts that are likely

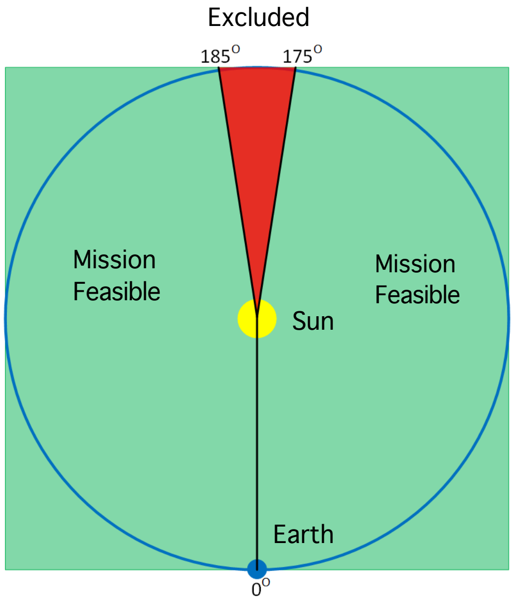

Figure 2.10: Illustration of the Earth-Sun-Asteroid line-of-sight communication angle excluded for the PDFV mission [28].

to be required by planetary defense missions executed with short warning time. Therefore, the PDFV mission must have a minimum impact velocity of 5 km/s. Due to anticipated technological limitations, impact velocities over 30 km/s are penalized as well. However, it should be noted that none of the missions analyzed have had an impact velocity above 30 km/s, meaning the HAIV impactor never has to decrease its approach velocity. All other major mission constraints are provided in Table 2.5. The exact penalty functions are also discussed in [28]. It is worth noting that limitations on NEA orbit group and absolute magnitude reduce the number of asteroids that must be searched from approximately 3,500 to 1,500.

2.3.3 Direct Intercept PDFV Mission

For the direct intercept mission, an appropriate launch vehicle is used to inject the HAIV into an interplanetary orbit that directly intercepts the target asteroid. This is the simplest mission type analyzed in [28], with only two variables to optimize (launch date and time-of-flight to the asteroid), and yields the largest number of feasible target asteroids. For direct intercept missions a relatively low C_3 limit of 12.5 km^2/s^2 is used. By limiting missions to low C_3 it may be possible to use a less capable (and therefore less expensive) launch vehicle than for missions that include both an impactor and rendezvous (observer) spacecraft.

Table 2.5: The PDFV mission constraints [28]

Parameters	Values
Asteroid types	Amor, Atira
Earliest launch date	1-Jan-2018
Latest launch date	31-Dec-2022
Minimum impact velocity	5 km/s
Maximum impact velocity	30 km/s
H magnitude range	20.75-23.62
Communication LOS constraints	$<175°$ and $>185°$
Impact angle constraint	penalized if approach isn't from the sunward side
Impactor limitations	For dual missions the impact must occur after rendezvous S/C arrival
Maximum departure C_3	12.5 km^2/s^2 for single S/C mission, 30 km^2/s^2 for dual S/C missions

Table 2.6: Top 3 target asteroid candidates for a simple direct intercept PDFV mission [28]

Asteroid	2006 CL9	2009 QO5	2004 BW18
a (AU)	1.35	1.59	1.37
e	0.24	0.24	0.25
Diameter (m)	104	105	97
Departure C_3 (km^2/s^2)	11.99	12.50	12.49
S/C ΔV (km/s)	0.0	0.0	0.0
LOS angle)	349°	349°	333°
Sun phase angle	3	28°	34°
Departure date	2-Aug-2019	27-Mar-2019	7-Apr-2019
TOF (days)	121.41	124.38	268.45
OCC	5	1	5
Impact velocity (km/s)	11.53	9.22	6.57

With the low C_3 limit, hundreds of potential target asteroids were found during the search in [28]. These asteroid require no ΔV from the HAIV impactor, other than minor trajectory corrections during the terminal guidance phase of the mission. The results presented in Table 2.6 represent the top 3 candidate asteroids. These asteroids were chosen because their orbits are fairly well known (or future observations of them will be possible prior to the mission launch dates).

Another consideration in the target search is how well the orbit of the target NEO is known. If there is too much uncertainty in our knowledge of the NEO's orbit, it may not be possible to guide the HAIV to a precision intercept with the NEO. The quality of NEO orbit knowledge is usually expressed by the Orbit Condition Code (OCC), which is an integer scale describing the amount of along-track uncertainty in the NEO orbit. The OCC is also known as the Minor Planet Center (MPC) "U" parameter (http://www.minorplanetcenter.net/iau/info). The size, shape, and orientation of NEO orbits are generally easier to estimate than the position of the NEO along its orbital path, and the location of the NEO on its orbit is therefore usually the least well known aspect of the NEO's orbit. The OCC scale ranges from 0 (a very well known orbit) to 9 (very poor orbit knowledge), and NEOs with OCC >5 are generally considered "lost" for the purposes of locating them in the sky during future observing opportunities [15].

A filter of OCC smaller than 5 is considered in [15, 28] for NEO target search. The trajectory scans were applied to Amor and Atira NEOs with estimated diameter near 100 m and OCC smaller than 5. The trajectory scan constraints included Earth departure characteristic energy $C_3 <12.5$ km^2/s^2, Earth departure date between 2018 and 2020, Sun-Spacecraft-Earth (SSE) angle at the time of intercept $>3°$, and sun phase angle at intercept $<90°$. The SSE angle is measured between the vector that points from the spacecraft to the Sun and the vector that points from the spacecraft to the Earth. If the SSE angle is too small then the Sun may interfere with communications between the spacecraft and Earth, and we require a good communications link with the spacecraft, especially at the time of NEO intercept, in order to collect the telemetry needed to confirm the success of the flight experiment [15].

The sun phase angle at intercept is measured between the velocity vector of the spacecraft relative to the NEO and the heliocentric position vector of the NEO at the time of intercept. A phase angle of zero places the spacecraft directly between the Sun and the NEO at the time of intercept, while a phase angle of $90°$ means that the spacecraft approaches the NEO orthogonal to the NEO-Sun line. Designing the trajectory so that a small value of the phase angle obtains provides a situation in which the Sun is naturally illuminating the full face of the NEO, or nearly so, from the spacecraft's perspective during terminal approach, which is highly advantageous for optical acquisition of the NEO with the spacecraft's onboard cameras and especially important for small NEOs that are optically faint even under such ideal circumstances.

After analyzing the trajectory scan results, the asteroid 2006 CL9 was selected as the notional target for the conceptual flight validation mission in [15, 28]. Another factor in the selection of 2006 CL9 is that while its OCC value of 5 would present navigation challenges for the PDFV mission, there may be opportunities to gather more ground-based observations of this NEA within the next couple of years, which may improve our knowledge of its orbit and thus reduce the OCC. It happens that this NEA meets the criteria for NASA's Near-Earth Object Human Space Flight Accessible Targets Study (NHATS) [32] and the next upcoming observing opportunity is among the NHATS data published for the NEAs.

A reference PDFV mission trajectory for asteroid 2006 CL9 has been shown previously in Fig. 2.4, which is similar to the Deep Impact mission trajectory shown in Fig. 2.1 due to the fact

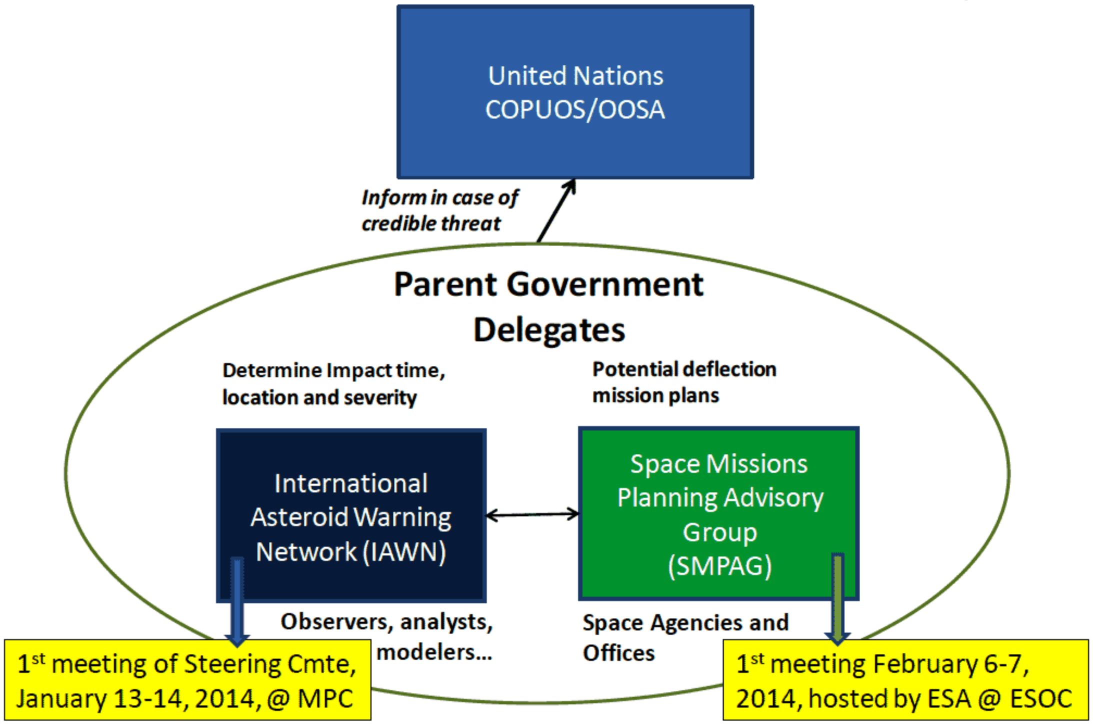

Figure 2.11: International efforts in preparing for a planetary defense mission. Image courtesy of Lindley Johnson at NASA/NEOO.

that both missions are intended to directly intercept and impact the target object. More detailed description of this reference PDFV mission can be found in [15]. Advanced PDFV mission design for accommodating both rendezvous spacecraft and direct intercept spacecraft is also presented in [28]. A complex orbital trajectory optimization algorithm, developed in [33, 34] for combined multiple gravity-assist maneuvers and impulsive ΔV maneuvers, is utilized in [28].

2.4 Recommendations for Planetary Defense

With a mandate from the U.N. Committee on the Peaceful Uses of Outer Space (COPUOS), the Space Mission Planning and Advisory Group (SMPAG) has been established in 2013 to coordinate a global response should a threatening asteroid be found heading toward Earth, as illustrated in Fig. 2.11. The NEO Observation (NEOO) Program Office of NASA has been coordinating all efforts related to NEO survey, detection, and impact warning.

However, no agency of the U.S. federal government has been officially designated for planning and/or preparing for planetary defense actions prior to detection of a real impact threat (the warning time for which, as noted previously, may be quite short). Therefore, we recommend that a U.S. government agency be formally designated by the Congress for the coordination of all R&D activities of preparing for all planetary defense options, prior to detecting any impact threat.

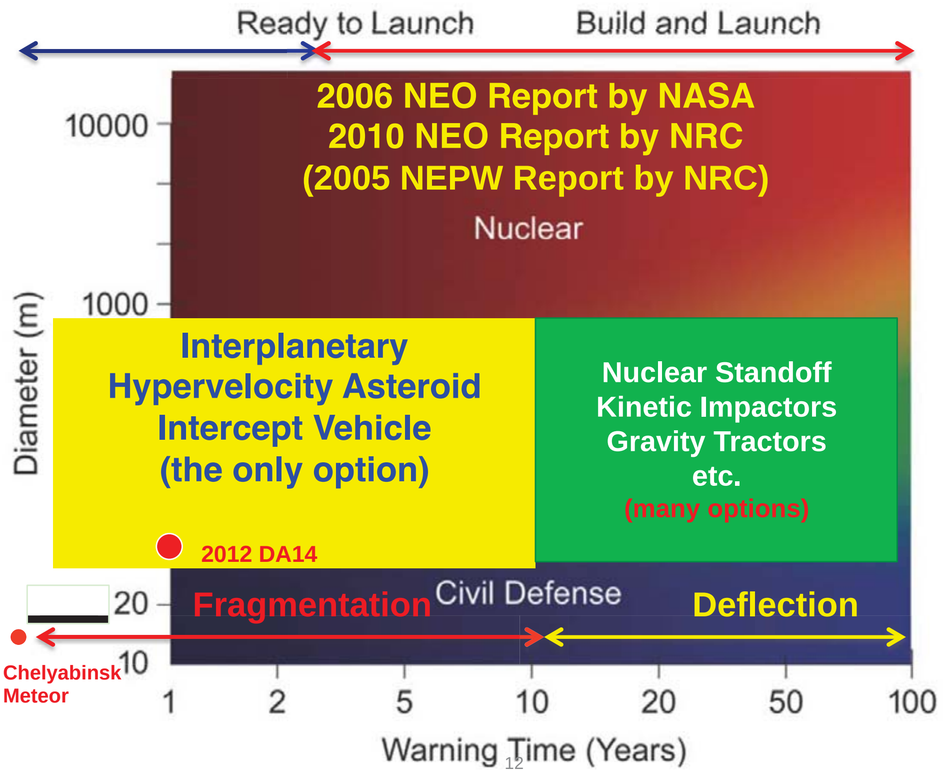

Figure 2.12: A summary of various mitigation options for planetary defense.

If we have sufficient warning time (>10 years), then various options, including kinetic impactors, gravity tractors, and nuclear standoff explosions, can be employed for a non-destructive deflection mission. For the more probable impact threat scenario, in which the warning time is less than 5 years, a disruption/dispersion mission employing nuclear explosions is likely to become the only option (other than evacuation of the area affected by the impact on Earth, assuming the impacting NEO is not large enough to be globally catastrophic). Various mitigation options for a wide range of warning times (1 week to 20 years) are summarized in Figs. 2.12 and 2.13.

The mission effectiveness of the proposed HAIV system can be further enhanced by exploiting an asteroid warning system, which is being developed at the University of Hawaii with $5 million funding from NASA. Once this system, called the ATLAS (Asteroid Terrestrial-impact Last Alert System), becomes fully operational in early 2016, it is expected that it will offer a one-week warning for a 45-m asteroid and three weeks for a 140-m asteroid. Provided that such one-week warning from the ATLAS can be assured, a target asteroid >45 m in size can be intercepted and disrupted far outside of Earth's gravitational sphere of influence and, consequently, avoid a potentially troublesome suborbital intercept. It is emphasized that a suborbital intercept may become inevitable for situations with ultra-short warning times of only 1 to 24 hrs (to be further discussed in Chapter 5).

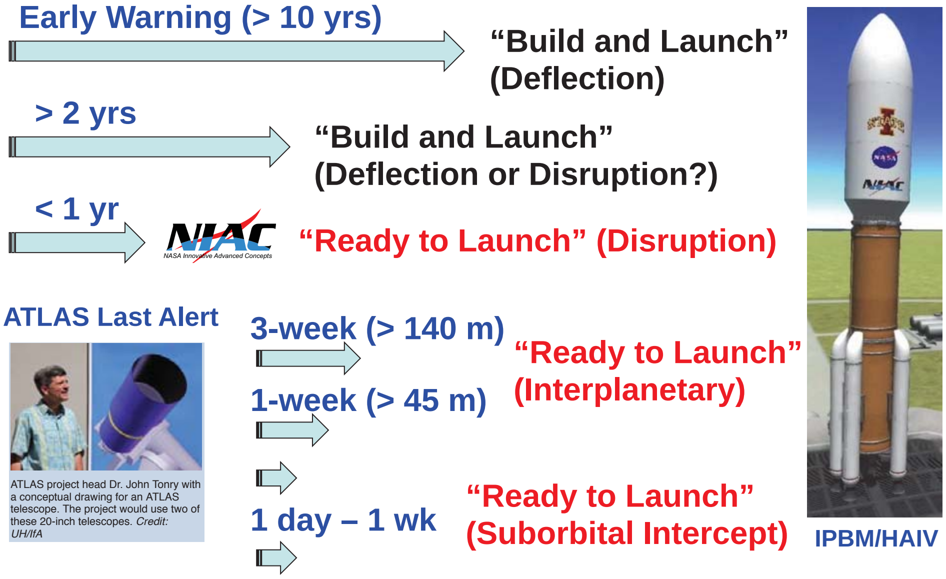

Figure 2.13: Applicability of the HAIV mission concept to various mission scenarios.

Most NEO science missions required at least several years, in some cases 5 to 6 years or more, for mission concept development and spacecraft construction prior to launch. It is also important to note that quite a few of these missions originally targeted different asteroids or comets than those that were actually visited. This is because the mission development schedules slipped and launch windows for particular asteroids or comets were missed. Additionally, several of these missions experienced hardware or software failures or glitches that compromised the completion of mission objectives. None of those things would be tolerable for a planetary defense mission aimed at deflecting or disrupting an incoming NEO, especially with relatively little advance warning. Thus, while the successful scientific missions that have been sent to asteroids and comets thus far have certainly provided future planetary defense missions with good heritage on which to build, we are clearly not ready to respond reliably to a threatening NEO scenario.

It is also important to note that most of these missions visited asteroids or comets that range in size from several kilometers to several tens of kilometers. Furthermore, the flyby distances ranged from several tens of kilometers to several thousand kilometers. The sole exception to this is the Deep Impact mission, which succeeded in delivering an impactor to the target in 2007. However, the mission was aided by the fact that comet 9P/Tempel 1 is 7.6 × 4.9 km in size and, therefore, provided a relatively large target to track and intercept. The Deep Impact mission was not intended to be a PDFV mission. For planetary defense missions requiring NEO intercept, the requirements will be far more stringent: NEO targets with diameters as small as several tens to hundreds of meters will have to be reliably tracked and intercepted at hypervelocity speeds, with impact occurring within mere meters of the targeted point on the NEO's surface. This will require significant evolution of the autonomous guidance and control technology currently available for science missions to NEOs.

Furthermore, none of the potential planetary defense mission payloads (e.g., kinetic impactors, nuclear explosives) to deflect or disrupt NEOs have ever been tested on NEOs in the space environment. Significant work is, therefore, required to appropriately characterize the capabilities of those payloads, particularly the ways in which they physically couple with NEOs to transfer energy or alter momentum, and ensure robust operations during an actual emergency scenario.

With regard to the need for planetary defense spacecraft system testing, it is important to note that there is currently no solicitation for planetary defense flight validation mission proposals. Such missions are necessarily similar in cost to science missions (e.g., Discovery or New Frontiers), yet there is no established mechanism for funding planetary defense flight validation missions. So, there is a need for planetary defense flight validation mission funding. It is worth pointing out that such missions will naturally, by their intrinsic nature, return significant amounts of science data even though they are not primarily science missions.

Finally, the very nature of the HAIV design (and the motivation for its design) underscores the need for a dedicated space-based NEO survey telescope located far from Earth's vicinity. Such a telescope would be an affordable and cross-cutting system that simultaneously serves the planetary defense, science, and exploration communities. Completing the NEO population survey as soon as possible is the best way to maximize the amount of warning time available to us should we find a NEO on an Earth-impacting trajectory. That cannot be done using Earth-based telescopes, and such telescopes will always be blind to the sunward direction (from which the Chelyabinsk impactor approached); a space-based NEO survey will not have the same blind spot. Although we are designing the HAIV to address short warning time situations because they are the most stressing cases and there will always be a risk of such a case occurring, we want to emphasize that doing our best to avoid short warning time scenarios by deploying a space-based NEO survey telescope is the most prudent course of action. Unfortunately, as with planetary defense flight validation missions, the NEO survey telescope cannot seem to find a funding source within NASA. Therefore, we recommend that NASA make the funding of a dedicated space-based NEO survey telescope a top priority, followed by funding for planetary defense flight validation missions.

In summary, it is time to initiate a planetary defense flight validation program, mandated by the Congress, for demonstrating, validating, and refining planetary defense technologies in space, so that we will be properly prepared to respond effectively when a near-Earth object (NEO) on a collision course with Earth is discovered. It will require at least 5 years of further development and space flight validation testing before operational planetary defense technologies could be *employed in a real short warning time situation. Now is the time to initiate such preparations. Waiting until a threatening NEO is discovered will be far, far too late. In addition, it is time to build and launch a dedicated space-based NEO survey telescope stationed far from Earth's vicinity. Such a system will be a key asset that simultaneously benefits planetary defense, fundamental solar system science, and space exploration.*

Chapter 3

Terminal Intercept Guidance with Optical and Infrared Seekers

The terminal intercept GNC (Guidance, Navigation, and Control) is one of the key enabling technology areas critical for a successful HAIV mission. On July 4, 2005, the performance of a closed-loop terminal guidance system employing strapdown optical navigation was flight demonstrated by NASA's Deep Impact mission for impacting a large, 5-km comet at an impact speed of 10 km/s [25–27]. However, a reliable and accurate intercept of a smaller (50 to 150 m) target NEO with an impact speed of 30 km/s in worst-case circumstances will be a technically challenging problem. To study the feasibility of a HAIV mission for intercepting a small NEO, a closed-loop terminal guidance simulator has been developed by utilizing a polyhedron shape model of asteroid 433 Eros as well as GPU (Graphics Processing Units) computation. This chapter describes a new terminal guidance system architecture employing a strapdown IR (Infrared) seeker, to be employed for a HAIV mission [35–39].

3.1 Introduction

As was illustrated in Fig. 1.5 of Chapter 1, the HAIV mission will end with a terminal intercept guidance phase during which corrective TCMs (Trajectory Correction Maneuvers) are executed to compensate for errors in orbital navigation toward the target asteroid. The terminal intercept guidance phase begins some time after the on-board sensors acquire the target. For a small (50 m) target asteroid, the terminal phase may begin 2 hours prior to intercept, while the Deep Impact mission initiated its terminal guidance 24 hours prior to its final impact with a larger (5 km) comet.

Orbital navigation during a terminal phase of the intercept mission will have to be autonomous, as computing and commanding accelerations via a communications link with Earth will be too time-consuming. The interceptor must be able to issue autonomous guidance commands based solely upon on-board measurements. Various options for on-board GNC measurements as well

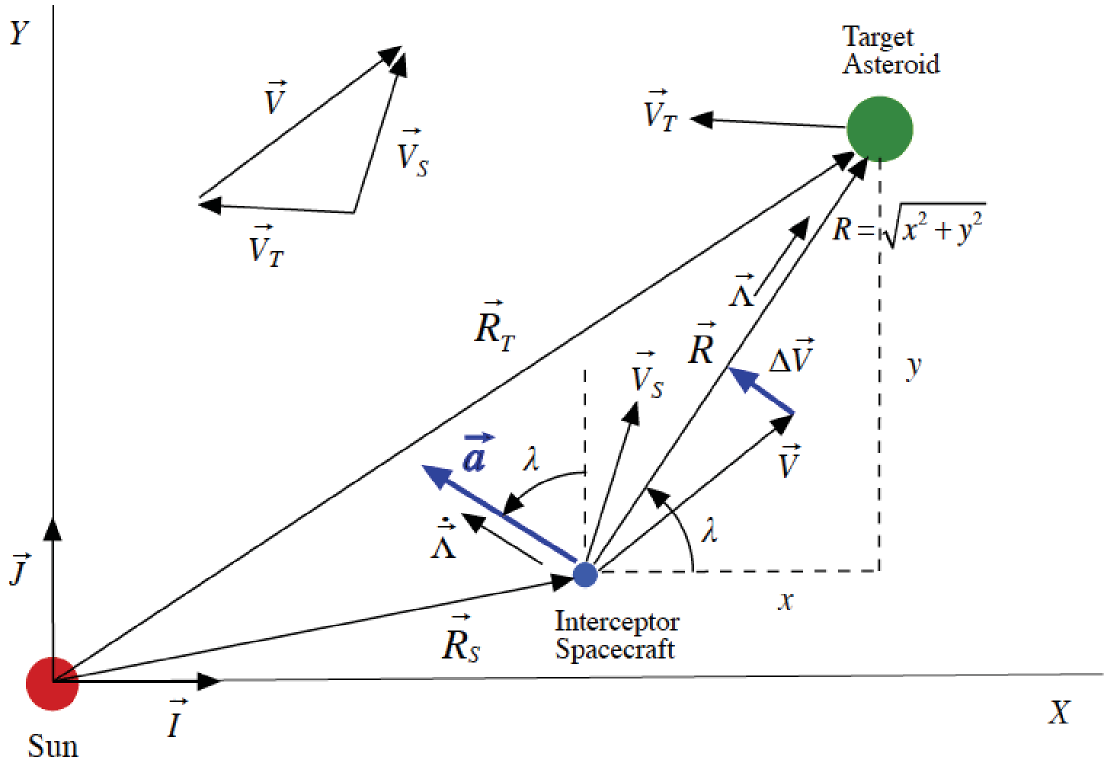

Figure 3.1: Two-dimensional geometry illustration of the terminal intercept guidance problem [35, 36].

as terminal guidance algorithms are discussed in [40, 41]. The conventional seekers for tactical missiles or interceptors include: optical, laser, IR, and radar seekers [42]. There are two types of seekers employed for a terminal phase of tactical missiles or interceptors. They are: strapdown (or body-fixed) seekers and gimbaled seekers. The strapdown seekers are directly attached to the vehicle, and their measurements of the target information are relative to the body-fixed coordinate system. The field-of-view (FOV) limitations of such strapdown seekers can be avoided by using gimbaled seekers, which can directly measure the line-of-sight (LOS) angle and the LOS rate of a target body. The seekers are also categorized by semiactive (or passive) and active seekers depending on the location of their signal sources [42].

Traditional terminal guidance algorithms often require continuous (proportional or throttleable) accelerations. However, most divert thrusters are not throttleable; i.e., they are on-off thrusters. The classical proportional navigation (PN) guidance scheme and its numerous variations [42] are certainly applicable to the terminal intercept guidance of an asteroid impactor.

The practicality of a pulsed PN guidance algorithm applied to the asteroid intercept problem has been investigated in [35, 36]. The geometry of a terminal intercept guidance problem is illustrated in Fig. 3.1. The reader is referred to [35, 36, 42] for detailed discussions of the terminal intercept guidance problem as illustrated in Fig. 3.1, and an illustrative example of the pulsed PN guidance law applied to an ideal asteroid intercept problem is briefly described herein.

A fictitious 300-m asteroid is assumed to be in a circular orbit with a radius of one astronomical unit. An interceptor with closing velocity of 10.4 km/s is displaced 350 km out radially. It is displaced 24 hours travel time ahead of the target in the tangential direction. In the absence of guidance commands, the assumed initial conditions will result in a miss distance of 88.29 km. A 1,000-kg interceptor with two 10-N on-off thrusters is assumed. Simulation results summarized in Figs. 3.2 and 3.3 indicate that the pulsed PN guidance system performed well for a reference terminal guidance problem investigated in [35, 36].

The effectiveness of a predictive guidance scheme based on orbital perturbation theory has also been examined in [35, 36]. Predictive guidance law calculates impulsive velocity corrections at pre-determined times to eliminate the final miss distance. Advanced terminal intercept guidance algorithms developed in [43, 44] can also be employed for the HAIV mission. The use of both optical and IR seekers have been further studied for the HAIV mission in [37–39].

This chapter describes the preliminary development of a GPU-based optical navigation and guidance system simulator utilizing a polyhedron shape model of asteroid scaled 433 Eros shown in Fig. 3.4. Data for this polyhedron shape model has been obtained from the NEAR collected shape database [45,46]. Scaling this model by a factor of 333 generates a reference asteroid model having a 50-m diameter. Adding lighting effects to the asteroid model illuminates the asteroid figure and create realistic simulated camera images, as can be seen in Fig. 3.5. From this lit target, the center-of-brightness (COB) of the figure will be determined for the guidance and navigation purposes. The COB will be calculated from light intensity of each camera pixel. The intercept is accomplished by estimating the LOS and LOS rate relative to the COB, then using this information in the desired guidance scheme. Along with optical image processing, the plausibility of an asteroid impact for a two-body HAIV separating at 60 seconds before the final impact occurs has been studied in [37, 38]. This separation concept is taken from the Deep Impact mission, where the impactor separated from the flyby spacecraft at a relative speed of approximately 36 cm/s. Once the fore and aft body separation occurs at 60 seconds before the final impact for the HAIV mission, no additional control effort is applied.

In this chapter, a new terminal guidance system architecture for the HAIV mission is also described. Most previous terminal guidance system studies for an asteroid intercept problem [35, 40, 41] have considered mainly optical cameras due to their cost-effective nature and acceptable target tracking performance as was demonstrated by Deep Impact mission [25–27]. However, similar to the case of Raytheon's Exoatmospheric Kill Vehicle (EKV), an IR seeker may need to be considered for the HAIV mission requiring reliable and accurate target tracking and intercept of small asteroids. The EKV is a kinetic impact interceptor launched by the Ground Based Interceptor (GBI) missile, the launch vehicle of the Ground-Based Midcourse Defense System of

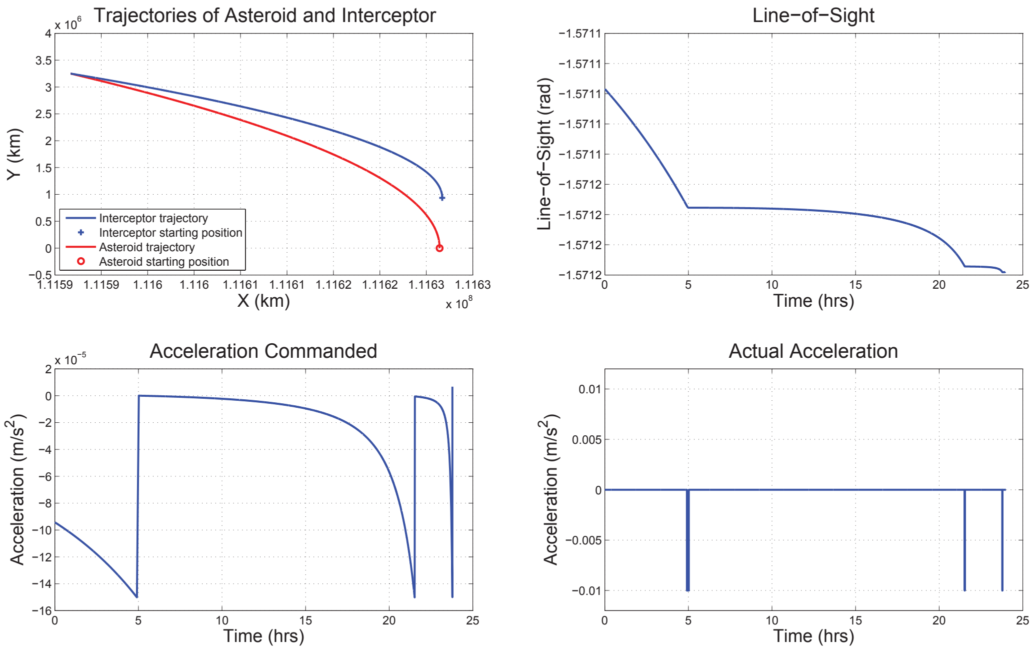

Figure 3.2: Trajectories, line-of-sight angle, commanded acceleration, and applied acceleration of the pulsed PN guidance law applied to an ideal asteroid intercept problem [35, 36].

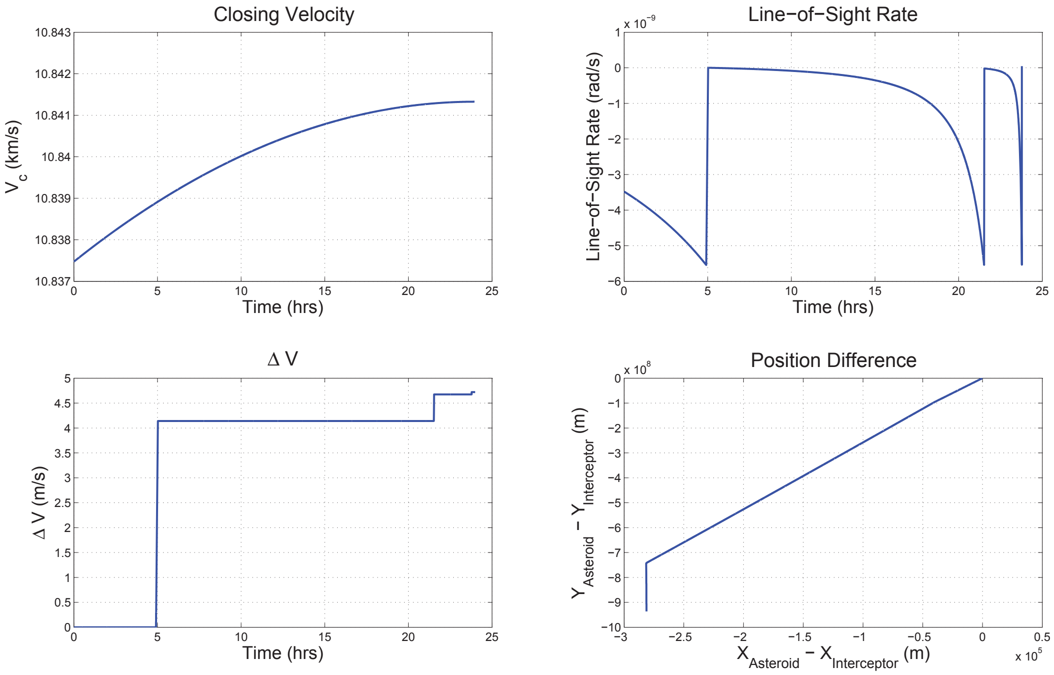

Figure 3.3: Closing velocity, line-of-sight rate, ΔV usage, and position error of the pulsed PN guidance law applied to an ideal asteroid intercept problem [35, 36].

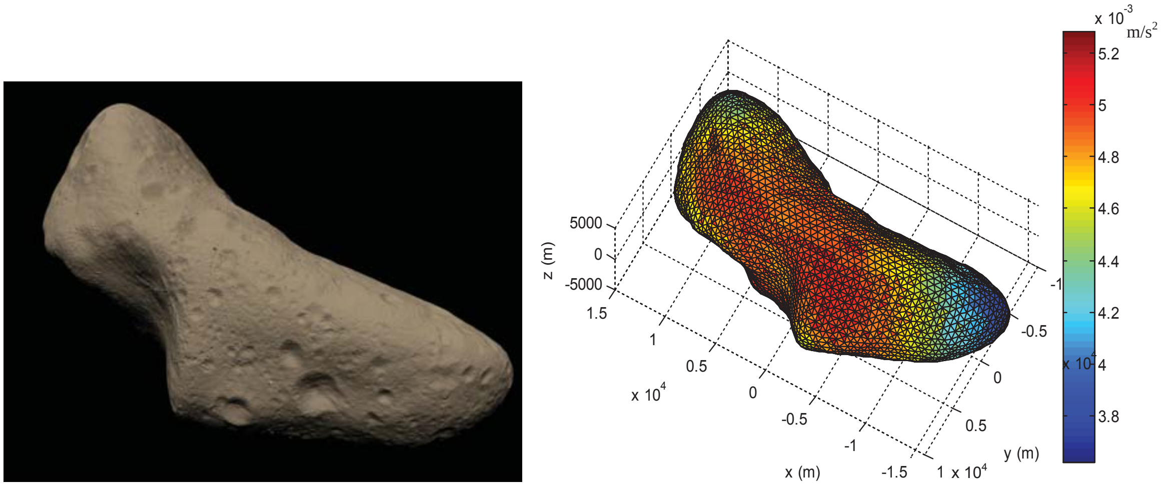

Figure 3.4: A 3D model of asteroid 433 Eros generated using NEAR's laser rangefinder measurements (left) and the surface gravitational acceleration of Eros computed using its polyhedron shape model (right) [37].

the United States. An EKV is boosted to a terminal intercept trajectory by a GBI missile. The closed-loop terminal guidance system of the EKV (after separated from the GBI missile) utilizes a strapdown electro-optical IR seeker to precisely hit the nuclear warhead of target ballistic missiles with a closing impact speed of approximately 6 to 10 km/s (http://www.raytheon.com/capabilities/products/ekv/).

The terminal guidance system employing optical cameras tracks the COB of a target asteroid. As can be seen in Fig. 3.5, an optical terminal guidance system may become ineffective if the target asteroid is not sufficiently illuminated by the sun, or if the sun-asteroid-spacecraft phase angle is near 180 degrees. However, an IR seeker will be able to provide target information required for onboard guidance algorithms even when optical cameras cannot. An IR seeker, with proper wavelength band of the target asteroid, will be able to detect and track, reliably and accurately, the target asteroid. A blended optical and IR sensor system will allow for targeting of the center-of-figure (COF), which for some cases is near to the center-of-mass (COM) of the target body.

A comparison of an optical image and a fictive IR image (without heat radiation blur) of the Eros polyhedron shape model is provided in Fig. 3.5. In this figure, a plus sign indicates the estimated COB of the optical image and the estimated COF of the IR image while the COM of the target body is indicated by a circle. In can be seen that for the IR image, the COF is estimated to be much closer to the COM. A similar comparison of optical and infrared images of asteroids with different sizes and albedos is provided in Fig. 3.6.

Figure 3.5: Comparison of an optical image (left) and an ideal fictive IR image (right) of a scaled Eros polyhedron shape model [38, 39].

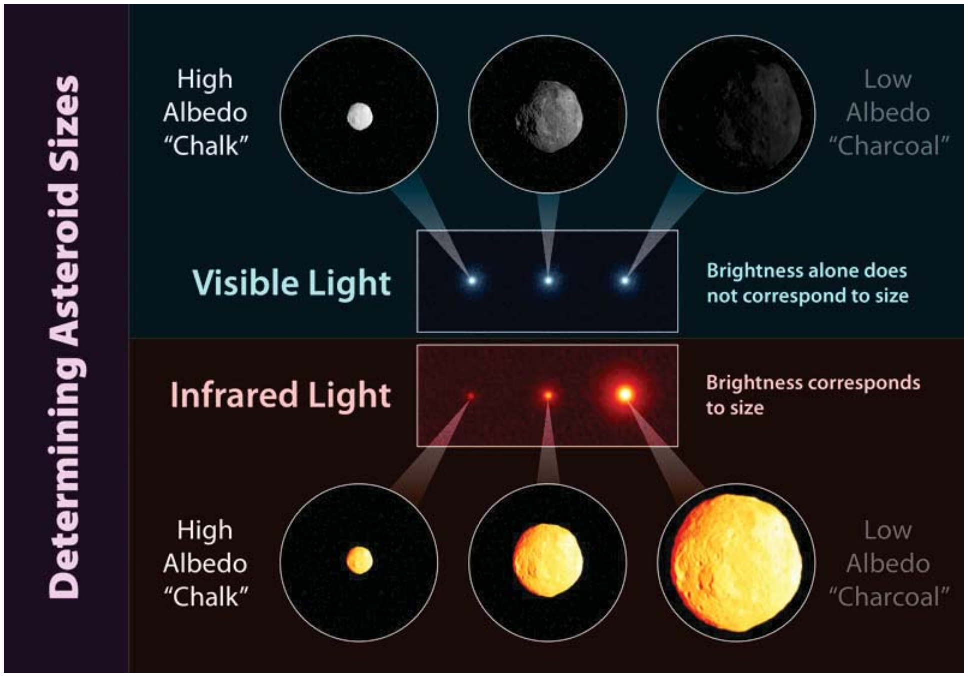

Figure 3.6: An illustration for comparing optical and infrared images of asteroids with different sizes and albedos (Image courtesy of NASA/JPL).

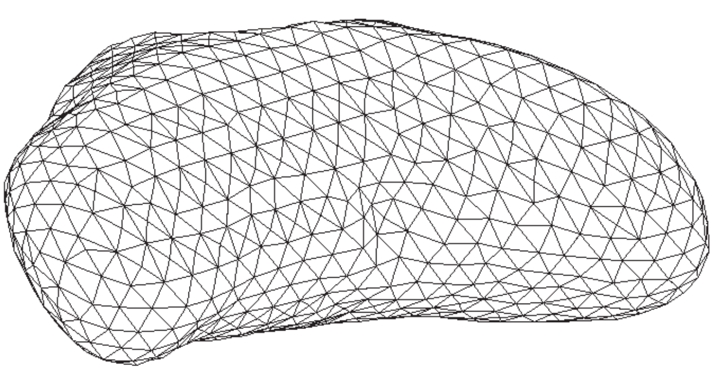

Figure 3.7: A triangulated shape model of asteroid 433 Eros.

3.2 Optical Image Rendering

This section introduces the rendering of optical (visual) images that are utilized by a closed-loop terminal guidance system simulator [37–39].

3.2.1 3D Polyhedron Optical Model for an Irregularly Shaped Asteroid

Consider a triangulation of surface points represented as a 3D wireframe polygon model, as illustrated in Fig. 3.7 for asteroid Eros. A reference shape model of asteroid Eros, shown in Figs. 3.4 and 3.5, has 200,700 faces [45,46]. This number of faces corresponds to the variable n_f of a computer shape model. Generally, the number of vertices needed to fill out the model, n_v, is strictly less than n_f, so it is more computationally efficient to do calculations on the vertices whenever possible. However, much of the shape information depends in some sense on an orientation of the body surface, for which each face element needs to be properly defined. A connectivity array stores the relationships between each set of vertex data.

Let $\vec{R}_1$, $\vec{R}_2$, and $\vec{R}_3$ be the position vectors of the three vertices of a face element from the origin of a target asteroid body-fixed reference frame A, as shown in Fig. 3.8. Then, we introduce three vectors $\vec{X}_i$, $\vec{Y}_i$, and $\vec{Z}_i$ associated with the ith surface element, as follows:

$$\vec{X}_i = \vec{R}_2 - \vec{R}_1, \qquad \vec{Y}_i = \vec{R}_3 - \vec{R}_1, \qquad \vec{Z}_i = \left(\vec{R}_1 + \vec{R}_2 + \vec{R}_3 \right)/3 \tag{3.1}$$

It is assumed that the origin of this reference frame is located at the center of mass of the target asteroid. The unit normal vectors of each face are then determined and stored as

$$\vec{N}_i = \vec{X}_i \times \vec{Y}_i \qquad \text{if} \quad \vec{N}_i \cdot \vec{Z}_i > 0 \quad \text{for} \quad i = 1, ..., n_f \tag{3.2}$$

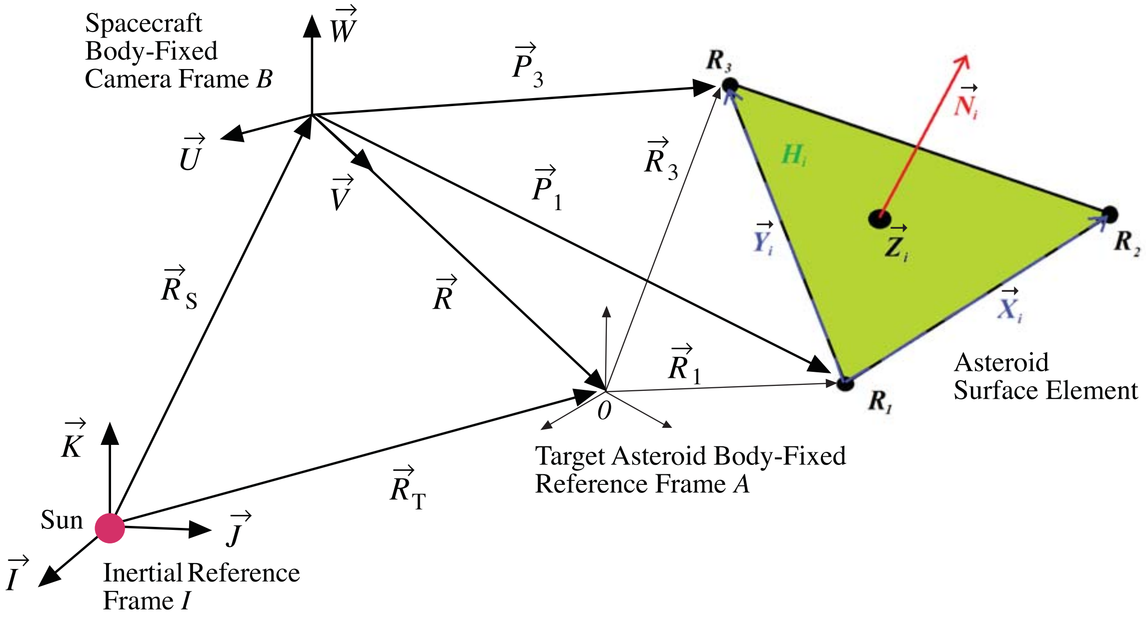

Figure 3.8: Geometry illustration for optical image rendering and triangulation of surface points.

The wireframe model uses a known rotational orientation of the target asteroid. A rotation matrix $\mathbf{C}^{A/I}$ is used to describe a simulated "real" orientation (e.g., a spinning body) for the 3D wireframe polygon model.

3.2.2 Camera Focal Plane

In order to decouple the attitude and translational motions of the interceptor spacecraft in the simulator, a "perfect" pointing of the camera is assumed. Thus, the choice of estimated center of mass or previously computed center of brightness is at the center of the camera focal plane, with the camera needing zero time to adjust to the new settings. The camera focal plane distance was chosen arbitrarily as the distance from the spacecraft to the target.

We choose a set of orthogonal unit vectors, $\{\vec{U}, \vec{V}, \vec{W}\}$, for a spacecraft body-fixed camera frame B such that

$$\vec{U} = \vec{V} \times \vec{W}, \qquad \vec{V} = \frac{\vec{R}}{|\vec{R}|}, \qquad \vec{W} = \frac{\vec{R} \times \vec{R}_T}{|\vec{R} \times \vec{R}_T|} \tag{3.3}$$

where $\vec{R} = \vec{R}_T - \vec{R}_S$ is the position vector of the target asteroid from the spacecraft, $\vec{R}_T$ is the position vector of the target asteroid from the sun, $\vec{R}_S$ is the position vector of the spacecraft from the sun, as illustrated in Figs. 3.1 and 3.8. It is assumed that the camera is located at the center of mass of the spacecraft.

The basis vectors $\{\vec{U}, \vec{V}, \vec{W}\}$ can be expressed in an inertial reference frame I with a set of basis vectors, $\{\vec{I}, \vec{J}, \vec{K}\}$, as follows:

$$\vec{U} = \quad \vec{I} \;\; \vec{J} \;\; \vec{K} \quad \mathbf{U} \tag{3.4a}$$

$$\vec{V} = \quad \vec{I} \;\; \vec{J} \;\; \vec{K} \quad \mathbf{V} \tag{3.4b}$$

$$\vec{W} = \quad \vec{I} \;\; \vec{J} \;\; \vec{K} \quad \mathbf{W} \tag{3.4c}$$

where $\mathbf{U}$, $\mathbf{V}$, and $\mathbf{W}$ are column vectors. We also have a coordinate transformation to the spacecraft body-fixed camera frame B from the inertial reference frame I, as follows:

$$\begin{bmatrix} \vec{U} \\ \vec{V} \\ \vec{W} \end{bmatrix} = \mathbf{C}^{B/I} \begin{bmatrix} \vec{I} \\ \vec{J} \\ \vec{K} \end{bmatrix} = \big[\; \mathbf{U} \quad \mathbf{V} \quad \mathbf{W} \;\; {}^{T}_{3\times 3} \begin{bmatrix} \vec{I} \\ \vec{J} \\ \vec{K} \end{bmatrix} \tag{3.5}$$

As shown in Fig. 3.8, the position vector of each vertex of a surface element from the spacecraft is described by

$$\vec{P}_j = \vec{R} + \vec{R}_j \qquad \text{for} \quad j = 1, 2, 3 \tag{3.6}$$

where $\vec{R}$ is the position vector of the origin of the target-fixed reference frame B from the spacecraft. To save computational time and storage space, a condensed array of these values are computed only for the faces satisfying $\vec{N}_i \cdot \vec{V} < 0$. This results in only the faces visible to the spacecraft. Due to the decoupling of the camera dynamics, a direct orientation of this plane is not possible given the currently available information. Thus, a direction for camera “up” must be chosen.

For the spacecraft body-fixed camera frame B defined as Eq. (3.3), the sunlight will always come into this reference frame from a horizontal direction, and “up” will always be orthogonal to the plane containing the target, the sun, and the spacecraft. The coordinates of each vertex in this (u, w) image plane can be computed as

$$\begin{bmatrix} u_j \\ w_j \end{bmatrix} = \begin{bmatrix} \vec{P}_j \cdot \vec{U} \\ \vec{P}_j \cdot \vec{W} \end{bmatrix} \qquad \text{for} \quad j = 1, 2, 3 \tag{3.7}$$

At this location of (u_j, w_j), what is visible to the spacecraft depends on camera parameters that interpret the “real” system. The resolution and field of view for the reference cameras considered for the HAIV mission are listed in Table 3.1. At each time step, these camera data are used to compute the half resolution of the image plane, denoted as R_h, as

$$R_h = |\vec{R}| \tan \quad \frac{1}{2} f_v \tag{3.8}$$

where f_v represents the field of view in radians (assumed isotropic) and $\vec{R}$ is the position vector of the target from the spacecraft body-fixed frame B. If (u_r, w_r) represent the (u, w) resolutions in the camera 2D pixel frame, then the information represented by each pixel corresponds to a size of $2R_h/u_r$ in the horizontal direction and $2R_h/w_r$ in the vertical direction.

Table 3.1: Parameters of reference optical cameras [37]

	High Resolution	Medium Resolution	Infrared
Resolution (u_r, w_r) (pixels)	1024×1024	1024×1024	512×512
Field of View, f_v (radians)	2.05e-3	10.0e-3	10.0e-3
Pixel Size at 1,000 km (m)	2.0	9.8	19.5

3.2.3 Lighting Conditions

A simple flat shading model is used to calculate the brightness of the target surface. Given a diffuse lighting coefficient, k_d, and an ambient lighting coefficient, k_a, the corresponding brightness attributed to each face of the 3D model is determined as

$$C_i = \begin{cases} k_d \quad \vec{N}_i \cdot \vec{S} \quad + k_a & \text{if } \vec{N}_i \cdot \vec{S} < 0 \\ 0 & \text{if } \vec{N}_i \cdot \vec{S} \geq 0 \end{cases} \tag{3.9}$$

where $\vec{S} = \vec{R}_T / |\vec{R}_T|$ is a unit sun vector, and a value C_i of 1 corresponds to perfect reflectivity of the incident sunlight at that distance. A grayscale colormap is used for visualization. The diffuse coefficient works closely in line with the albedo, and is chosen to be 0.25 for the simulations. Since the cameras may have very little time to resolve detail of the body shape, we assume that their lower threshold for brightness is very low and we choose k_a = 0. This computational process is very fast, and can be computed completely in parallel for each face.

When additional lighting detail is desired, the following interpolation model as described in [47] is employed. Let each vertex have a normal vector $\vec{N}_1$, $\vec{N}_2$, and $\vec{N}_3$ computed as an average of the adjacent faces, found from inverting the connectivity array. Then, a corresponding value for brightness at each vertex $\widetilde{C}_1, \widetilde{C}_2$, and $\widetilde{C}_3$ is computed using the flat shading model equation. If a pixel representing the image plane at (u, w) is calculated to intercept this triangle, then an inverse squared weighted average is assigned to the pixel as follows:

$$C(u, w) = \frac{\alpha_1}{\alpha_T}\widetilde{C}_1 + \frac{\alpha_2}{\alpha_T}\widetilde{C}_2 + \frac{\alpha_3}{\alpha_T}\widetilde{C}_3 \tag{3.10}$$

where $\alpha_T = \alpha_1 + \alpha_2 + \alpha_3$ and

$$\alpha_j = \frac{1}{(u - u_j)^2 + (w - w_j)^2} \qquad \text{for } \ j = 1, 2, 3 \tag{3.11}$$

3.2.4 Pixel Value Assignment

For either the flat or interpolated shading models, the facet at which a pixel intercepts the target projection must be determined. This is done on the GPU computer in parallel to reduce computa-

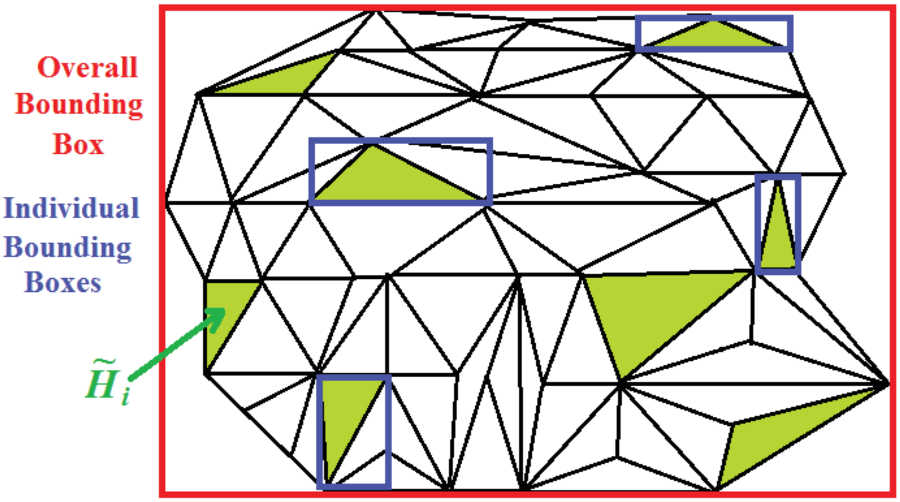

Figure 3.9: Illustration of a parallel trim reduction technique [37, 38].

tional time, especially using a higher fidelity target model. Each pixel has its assigned coordinates in the (u, w) plane representing the center of the box over which the pixel is integrated. This works well when the size of a pixel is on the scale of the surface facets, but an averaged value needs to be used at greater distances. To determine the intercepted triangle, we first compute the upper and lower bounds of each visible triangle in parallel. Then, a reduction is performed to get the outer limits of the target in the (u, w) plane. This process is illustrated in Fig. 3.9. Pixels outside of this range can automatically be assigned a value of 0. In fact, only the location and value of nonzero image components are stored in the present computational model.

The arrays containing the limits of each facet are sorted, and then a scan of these arrays is completed. This process assigns a vector of possible intersections for each pixel. This vector contains the identification of all facets through which the pixel passes through the bounding box. This is generally a low number. For each candidate intersection, the convex hull of the triangle, H_i, is identified, as shown in Fig. 3.8. This is projected onto the (u, w) plane, forming the set $\widetilde{H}_i$ shown in Fig. 3.9.

If $\widetilde{\mathbf{X}}_i$ and $\widetilde{\mathbf{Y}}_i$ are the projections of $\vec{X}_i$ and $\vec{Y}_i$ in the (u, w) plane, then the coordinates of the ith pixel in the (u, w) plane can be expressed as

$$\begin{matrix} u_i \\ w_i \end{matrix} = \widetilde{\mathbf{P}}_1 + d_1 \widetilde{\mathbf{X}}_i + d_2 \widetilde{\mathbf{Y}}_i \tag{3.12}$$

where

$$\widetilde{\mathbf{P}}_1 = \begin{matrix} \vec{P}_1 \cdot \vec{U} \\ \vec{P}_1 \cdot \vec{W} \end{matrix} , \quad \widetilde{\mathbf{X}}_i = \begin{matrix} \vec{X}_i \cdot \vec{U} \\ \vec{X}_i \cdot \vec{W} \end{matrix} , \quad \widetilde{}_i = \begin{matrix} \vec{Y}_i \cdot \vec{U} \\ \vec{Y}_i \cdot \vec{W} \end{matrix} \tag{3.13}$$

The ith pixel location (u_i, w_i) lies within the triangle if $d_1 > 0$, $d_2 > 0$, and $d_1 + d_2 < 1$. This assigns a single facet as the possibility for intersection. However, at pixels near the boundary of the target asteroid, several potential intersection may occur.

3.2.5 Line-of-Sight Vector

The line-of-sight (LOS) vector from the spacecraft to the center-of-brightness (COB) of the target asteroid needs to be determined for the purpose of terminal intercept guidance. If $I_i(u, w)$ is the brightness value of each pixel, then the centroid of the image array (or the COB) is computed using an weighted average as follows:

$$\bar{u} = \frac{I_i(u, w) u_i}{\sum I_i(u, w)}, \qquad \bar{w} = \frac{I_i(u, w) w_i}{\sum I_i(u, w)} \tag{3.14}$$

The LOS vector of the target asteroid's COB then becomes

$$\vec{\Lambda} = \vec{R} + \vec{d} \tag{3.15}$$

where $\vec{d}$ is the COB location on the camera (u, w) focal plane and

$$\begin{aligned} \vec{\Lambda} &= \Lambda_x \vec{I} + \Lambda_y \vec{J} + \Lambda_z \vec{K} \\ \vec{R} &= X \vec{I} + Y \vec{J} + Z \vec{K} \\ \vec{d} &= \bar{u}\, \vec{U} + \bar{w}\, \vec{W} \end{aligned}$$

Finally, we have the LOS vector of the COB, expressed in an inertial reference frame I, as follows:

$$\begin{bmatrix} \Lambda_x \\ \Lambda_y \\ \Lambda_z \end{bmatrix} = \begin{bmatrix} X \\ Y \\ Z \end{bmatrix} + \mathbf{C}^{I/B} \begin{bmatrix} \bar{u} \\ 0 \\ \bar{w} \end{bmatrix} \tag{3.16}$$

where

$$\mathbf{C}^{I/B} = \quad \mathbf{U} \quad \mathbf{V} \quad \mathbf{W} \quad {}_{3\times 3} \tag{3.17}$$

The relative target position vector (X, Y, Z) needs to be determined by a spacecraft onboard navigation system, and the rotation matrix $\mathbf{C}^{I/B}$ needs to be determined by a spacecraft attitude determination system.

3.3 Terminal Intercept Guidance with Optical Cameras

Figure 3.10 shows some illustrative target images used for the optical terminal guidance prior to impacting a 150-m target. The image seen at 5 minutes before impact may cause a concern because of its small image size, which is due to a target asteroid assumed herein as 120 times smaller than the original 433 Eros model. Figure 3.11 compares the optical camera images of 50-m and 450-m asteroids at I–2 seconds. In Fig. 3.11(b), it can be seen that there are more pixels that have an intensity greater that zero than in Fig. 3.11(a). All parameters of the asteroids are kept constant except for the size.

Optical terminal guidance simulation results are provided in Figs. 3.12 and 3.13. It can be seen that a predictive (three-pulse) terminal guidance law employing simulated optical images performs well for intercepting a small 50-m target asteroid as well as a large 450-m target asteroid, despite the noisy estimated LOS rates when the interceptor becomes very close to the target. The LOS rates shown in Figs. 3.12 and 3.13 are the estimated LOS rates based on the estimated LOS angle, using simulated optical images shown Fig. 3.11. Detailed discussions of the analysis and simulation of an optical terminal guidance system studied for the HAIV mission can be found in [35–41].

3.4 IR Telescope/Seeker Characterization

Most terminal guidance system studies for an asteroid intercept problem [35, 40, 41] have considered mainly optical cameras due to their cost-effective nature and acceptable target tracking performance as was demonstrated by NASA's Deep Impact mission [25–27]. However, similar to the case of Raytheon's EKV, a strapdown infrared seeker may need to be considered for the HAIV mission requiring reliable and accurate target tracking and intercept of small asteroids, as illustrated in Fig. 3.5.

3.4.1 IR Telescope/Seeker

As an example of infrared space telescopes, consider the Wide-field Infrared Survey Explorer (WISE) spacecraft equipped with a 40-cm diameter infrared telescope, as illustrated in Fig. 3.14. The WISE spacecraft is a NASA infrared-wavelength astronomical space telescope launched into a low-Earth orbit in December 2009. It has successfully completed an all-sky astronomical survey with images in 3.4, 4.6, 12, and 22 μm wavelength range bands, over ten months. After its hydrogen coolant depleted in September 2010, a four-month extended mission (renamed NEOWISE) was conducted to search for small solar system bodies close to Earth's orbit using the two shortest wavelength detectors (http://neowise.ipac.caltech.edu/). The NEOWISE was able to detect a 250-m diameter size object at approximately 0.5 AU [48].

3.4.2 Classical Cassegrain Telescope Optics

For the purpose of preliminary initial design of an IR seeker system for the HAIV mission, we consider a classical Cassegrain telescope configuration illustrated in Fig. 3.15. This basic telescope

(a) I–30 minutes (b) I–5 minutes

(c) I–2 seconds (d) I–0.125 seconds

Figure 3.10: Simulated camera images during terminal guidance for intercepting a 150-m asteroid [37, 38].

(a) 50-m target (b) 450-m target

Figure 3.11: Comparison of optical images at I–2 seconds for 50-m and 450-m asteroids [37, 38].

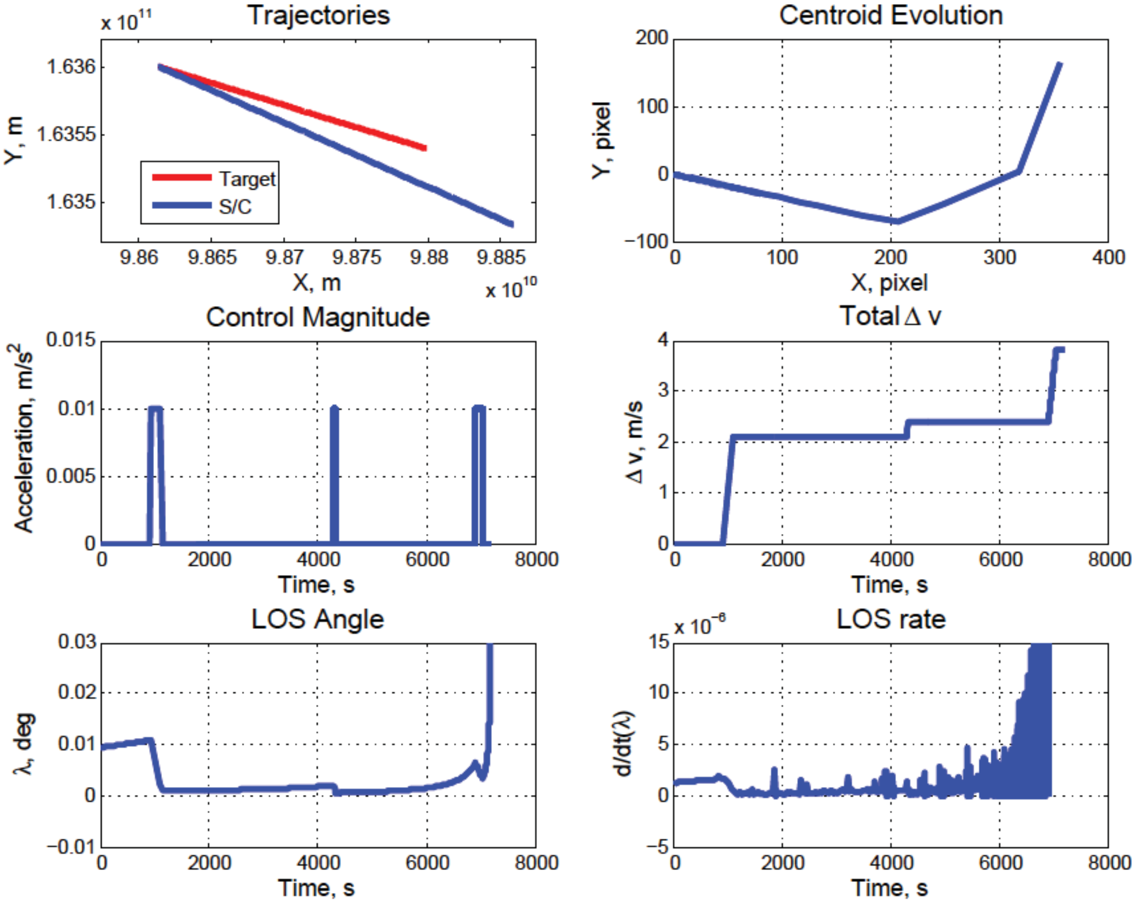

Figure 3.12: Optical terminal guidance simulation results for a 450-m target asteroid [37, 38].

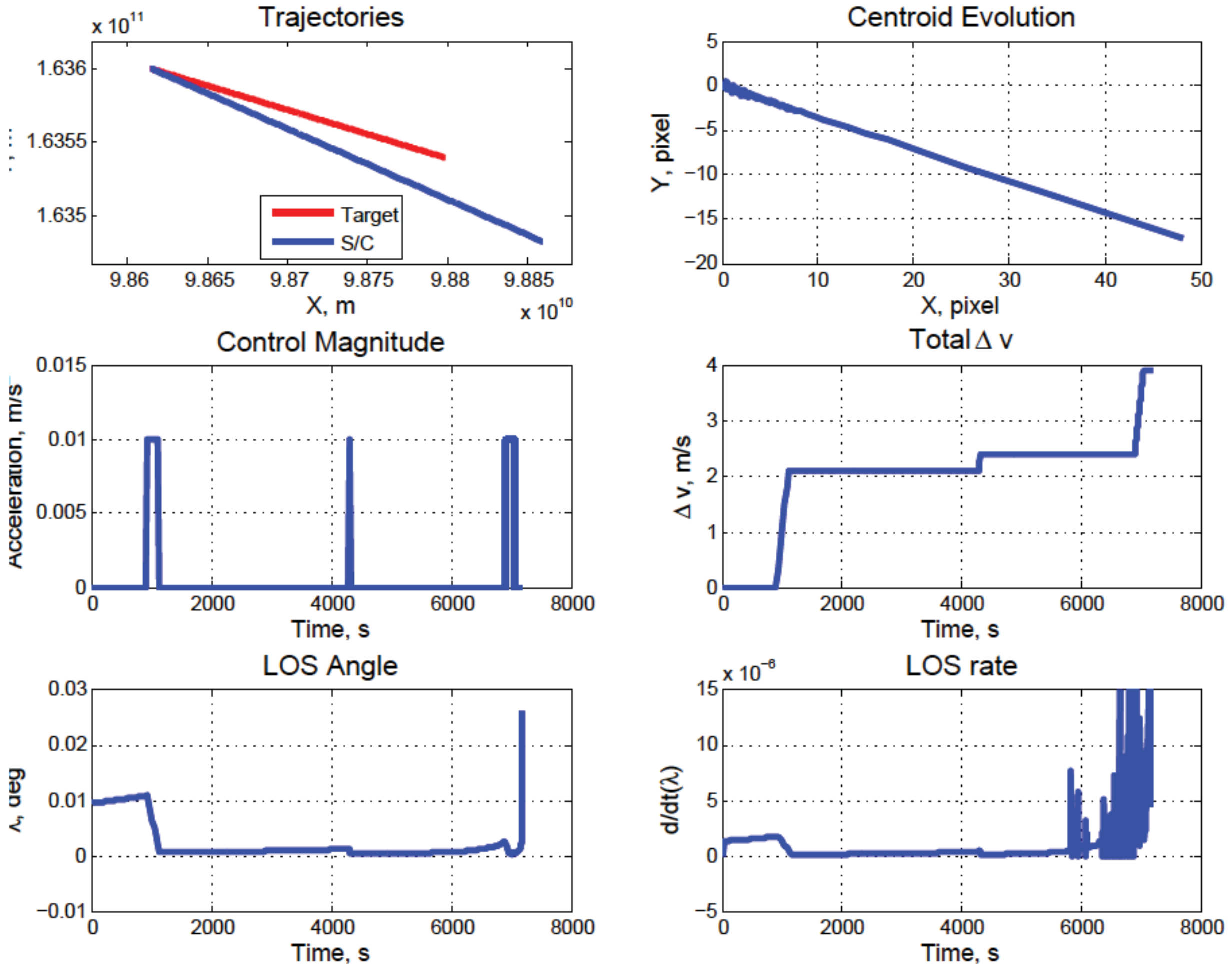

Figure 3.13: Optical terminal guidance simulation results for a 50-m target asteroid [37, 38].

configuration is chosen due to its simplicity and similarity to the WISE infrared telescope design shown in Fig. 3.14. Various configuration parameters of the Cassegrain telescope are shown in Fig. 3.15. These parameters are to be selected, given an effective focal length, primary mirror focal length, diameter, and back focus distance. Baffling and glare stops are not taken into account herein.

The magnification of the telescope is determined first. This is simply done by dividing the focal length of the system, F, by the primary mirror's focal length, f_1, as follows:

$$M = \frac{F}{f_1} \tag{3.18}$$

Once magnification is calculated, other parameters of this system can be selected. Given the back focus (distance from the primary mirror to the focal plane), b_*, the primary mirror focus intercept point is selected as

$$p = \frac{F + b_*}{M + 1} \tag{3.19}$$

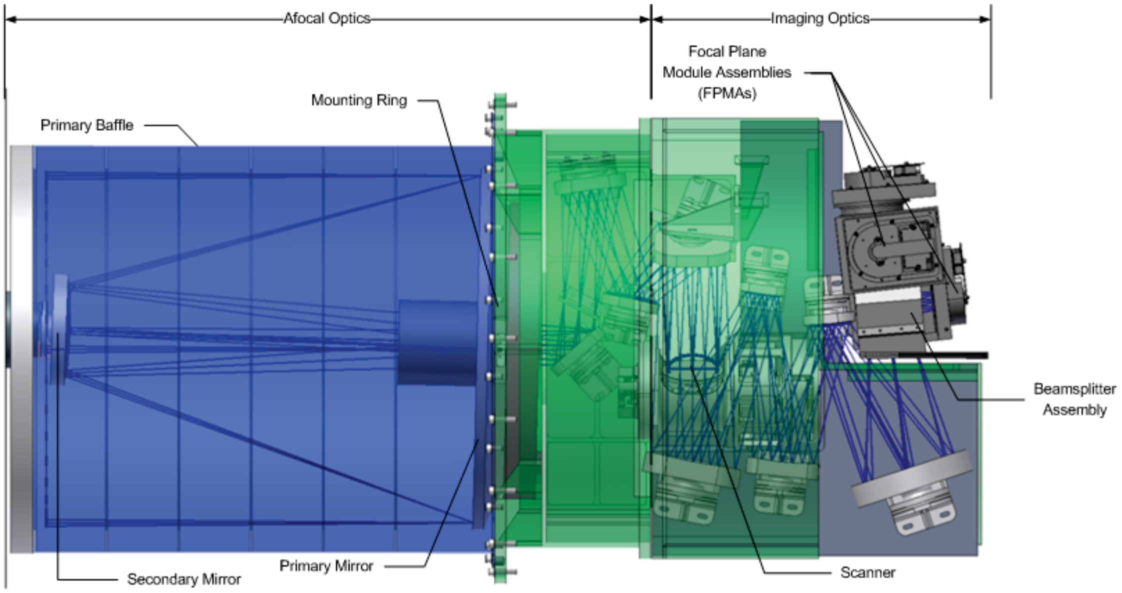

Figure 3.14: An illustration of WISE infrared space telescope (Image courtesy of NASA/JPL).

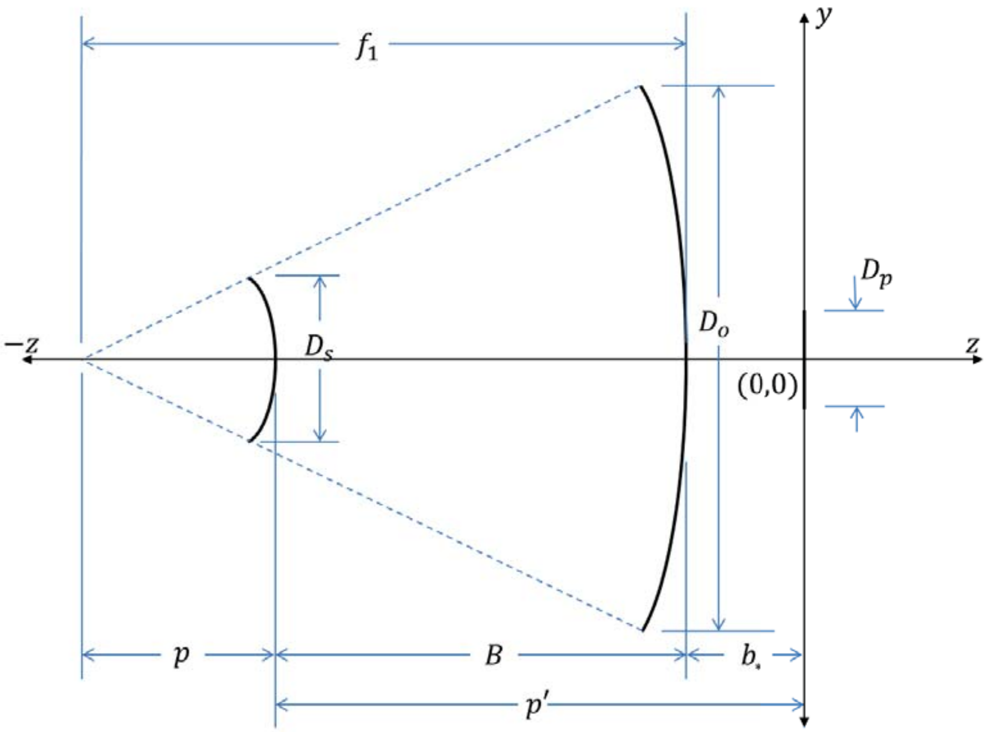

Figure 3.15: Classical Cassegrain telescope configuration [39].

The overall distance from the secondary mirror to the focal plane, also known as the secondary to Cassegrain focus p', follows directly from the primary focus, as follows:

$$p' = pM \tag{3.20}$$

From the Cassegrain focus, the mirror separation, B, is selected as

$$B = p' - b_* \tag{3.21}$$

Another very important part of the Cassegrain telescope design is the sizing of the secondary mirror. The secondary mirror diameter, D_s, can be determined as

$$D_s = \frac{pD_o}{f_1} + \frac{BD_p}{f_1 M} \tag{3.22}$$

where D_p is the image plane size. This correlates to the size of the imaging device, which is equivalent to the minimum dimension of the array.

With these parameters selected, the radius of curvature (ROC) is found for both the primary and secondary mirrors, as follows:

$$R_1 = 2f_1 \tag{3.23}$$

and

$$R_2 = \frac{2}{1/p - 1/p'} \tag{3.24}$$

where R_1 is the ROC for the primary mirror and R_2 is the ROC for the secondary mirror. By using the ROC of each mirror, the prescription for the two mirrors can be found as

$$z_1 = \frac{y_1^2}{2R_1} - b_* \tag{3.25}$$

$$z_2 = \frac{y_2^2/R_2}{1 + \sqrt{1 - (1 + b_2)(y_2/R_2)^2}} - (b_* + B) \tag{3.26}$$

and

$$b_2 = \frac{-4M}{(M-1)^2} - 1 \tag{3.27}$$

where z_1 and z_2 are face locations of the mirrors when the image plane array is at the origin of a measurement: $-D_o/2 \leq y_1 \leq -D_0/2$ and $-D_s/2 \leq y_2 \leq -D_s/2$. This is only valid for the case of a classical Cassegrain telescope.

When looking through a telescope, the magnification, primary mirror diameter, and image plane size (array size or eye pupil diameter) make a difference in the brightness of the image. The brightness coefficient takes into account the light grasp and magnification of the device to give the maximum amount of light that is illuminating the device, as follows:

$$k_{sb} = \frac{D_o}{MD_p}^{2} \tag{3.28}$$

A way to interpret this coefficient is to use the same telescope but different eye pieces to enlarge the image size at the entrance of the eye pupil. This spreads the same amount of light out onto a larger area, hence creating a dimmer object.

3.4.3 Signal-to-Noise Ratio

The IR detector array receives signals from an asteroid, and the sensor array wells are then filled. While the signal is obtained from the asteroid, the detector also has noise and dark current values, which is called the total detector noise. Since the frequencies of this noise are not known precisely, the signal-to-noise ratio (S/N) is to be estimated. Once the estimated value of the S/N reaches a mission selected value, the target object in question, here an asteroid, is said to be able to be detected. To simulate these values, approximation of blackbody radiation signal current and noise signal current are considered.

A step in approximating the asteroid signal requires the integration of Planck's law over the detectable wavelength band of the IR detector. Black body radiation for different temperature values is shown in Fig. 3.16. The form of Planck's law used here is a function of the wavelength. While there are multiple bands for the wavelengths, the focus here is on objects that are in the 250 Kelvin range. For this case, the wavelengths being used start at the Mid Infrared N band (7.5-14.5 μm) and extend to 16.5 μm, which is used for the W3 band of the WISE telescope. This gives the radiance of the asteroid with integration bounds as

$$L = \int_{\lambda_1}^{\lambda_2} \epsilon \frac{2hc}{\lambda^5} \frac{1}{\exp(\frac{hc}{k_B T_{ast} \lambda}) - 1} d\lambda \tag{3.29}$$

where h is Planck's constant, k_B is Boltzmann constant, and c is the speed of light.

Once the radiance is found, the irradiance on the detector can be calculated. This takes into account the solid angle subtended by a circular approximation of the asteroid. The irradiance is then given by

$$E = \frac{L \pi r_{ast}^2}{d_{ast}^2} \tag{3.30}$$

To calculate the signal current, the irradiance needs to be converted into a photon flux. This will compute the minimum amount of electrons passing through the aperture. The Wien's displacement law for finding the wavelength of peak emission is given by [49]

$$\lambda_{max} = b/T_{ast} \tag{3.31}$$

where λ_{max} is the maximum energy per photon, in Joules, and

$$\psi = \frac{hc}{\lambda_{max}} \tag{3.32}$$

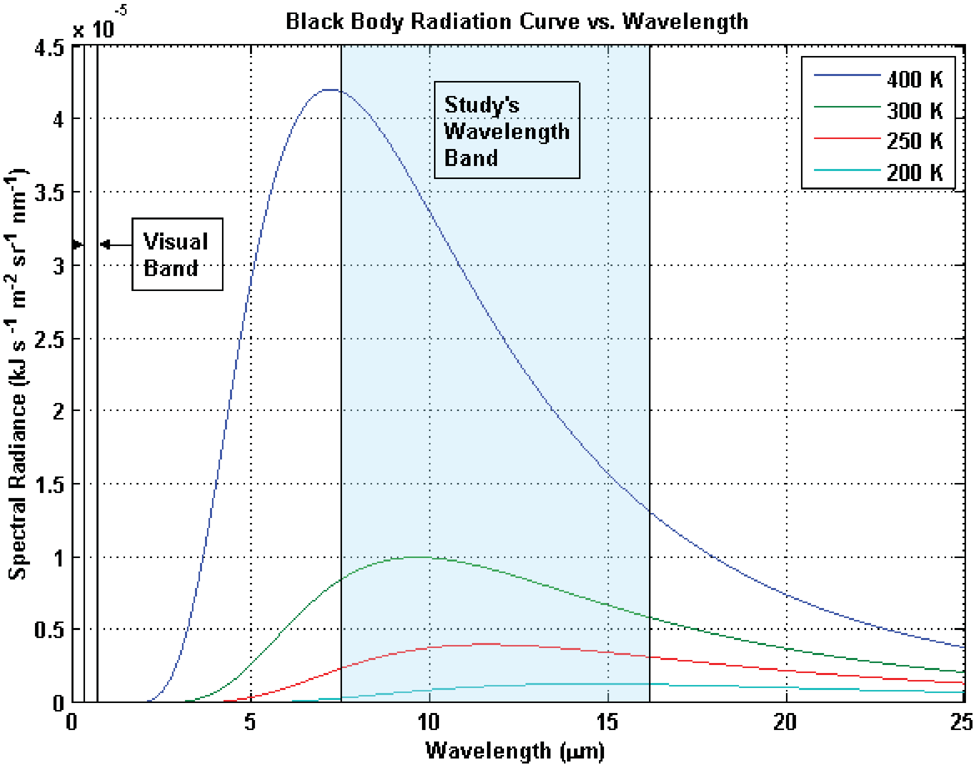

Figure 3.16: Black body radiation for different temperature values [38, 39].

where ψ is the maximum energy per photon at the desired wavelength.

The photon flux, which is the amount of photons passing through a unit area of 1 m^2, can be determined by dividing the irradiance by the maximum energy per photon at the desired wavelength. This gives the photon flux as

$$\Phi = \frac{E}{\psi} \tag{3.33}$$

By using telescope and detector array parameters, the photon flux is manipulated into the signal current, as follows [49]:

$$I_{signal} = k_{sb}\left(\frac{L\pi r_{ast}^{2}b}{d_{ast}^{2}hcT_{ast}}\pi \quad \frac{D_o}{2}\;^{2} \quad \tau_{optics}\right)q\eta G \tag{3.34}$$

which takes into account the object's solid angle, maximum frequency emission given by Wien's displacement law, and the effects of the surface brightness due to the optics. The variable τ_{optics} is estimated to be at 0.504 in [50]. This is assumed to be the transmission coefficient in the IR range as well. However, it would be advantageous to know the number of electrons being excited for a given amount of time and number of exposures. A new form of the above equation is given by

$$H_{signal} = k_{sb}\left(\frac{L\pi r_{ast}^{2}b}{d_{ast}^{2}hcT_{ast}}\pi \quad \frac{D_o}{2}\;^{2} \quad \tau_{optics}\right)\eta G N\tau_{int} \tag{3.35}$$

where N is the number of exposures and H_{signal} is given in number of electrons.

Noise Currents. One of the most important aspects of signal processing is the amount of noise in the system. If there is too much noise and the noise signal is not known, it would be virtually impossible to differentiate between correct or incorrect data. The following analysis incorporates four places where there could be unwanted current added to the system. This, for generality, will be called a noise current.

Dark current noise is assumed to follow Poisson statistics, therefore the current is given by the standard deviation of the form

$$I_{dark} = \sqrt{n_{e,d}n_{pix}q} \tag{3.36}$$

However, this does not take into account the number of exposures and exposure time. By looking at a Poisson process, the standard deviation is related to the duration of the total sampling. The dark current deviation can then be written in a slightly different form as

$$\sigma_{dark} = \overline{n_{e,d}n_{pix}N\tau_{int}} \tag{3.37}$$

where σ_{dark} is also given in number of electrons.

Much like the dark current noise, shot noise follows a Poisson process as well. This noise comes from the total number of detected photons, which are emitted by the target asteroid. The equation, incorporating the number of exposures and exposure time, is then given by

$$\sigma_{shot} = \overline{H_{signal}} \tag{3.38}$$

where σ_{shot} is given in the total number of electrons.

Johnson noise in the detector due to resistance of the material is described by

$$I_{Johnson} = \sqrt{\frac{2k_BT_d}{R_d\tau_{int}}} \tag{3.39}$$

and

$$R_d = \frac{\rho l_y}{l_xl_z} \tag{3.40}$$

A depiction of an array cell can be seen in Fig. 3.17. Again, the current needs to be changed into number of electrons and also with respect to the number of exposures and exposure duration. This would represent the standard deviation in number of electrons, using Poisson statistics, which then yields

$$\sigma_{Johnson} = \sqrt{\frac{2k_BT_dN\tau_{int}}{R_dq^2}} \tag{3.41}$$

Generation-Recombination Noise. Generation-Recombination noise is the result of generation and recombination of charged particles within the detector material. In [51], the following

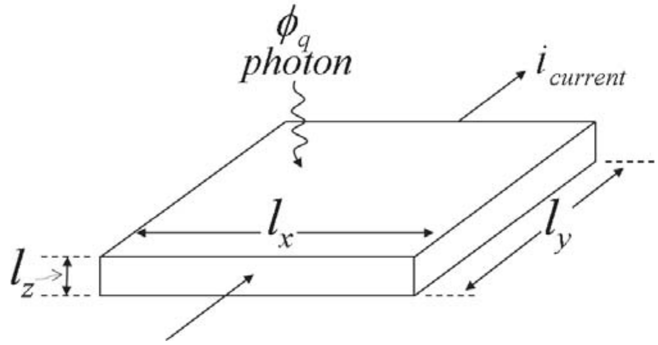

Figure 3.17: An IR detector array cell [38, 39].

equation is used to calculate the current generated in the sensor array:

$$I_{GR} = 2qG \quad \overline{\frac{\eta \Phi \tau_{optics} A_d}{2\tau_{int}}} \tag{3.42}$$

However, this is given in amperes and does not include the number of exposures. An alternate form is then found for Generation-Recombination deviation following a Poisson process. This form, in number of electrons, is given by

$$\sigma_{GR} = G \quad \overline{2\eta \Phi \tau_{optics} A_d N \tau_{int}} \tag{3.43}$$

S/N Calculation. A signal-to-noise ratio formula [51] is given by

$$S/N = \frac{\text{average number of photons from source}}{\text{standard deviation of the photon stream}} = \frac{\bar{n}}{\sigma} \tag{3.44}$$

The standard deviation can be written as the square root of the sum of the squares for each noise component. This can only be done due to each noise signal being uncorrelated. Also, by using H_{signal} as the average photons from the source, the signal-to-noise ratio can be written as

$$S/N = \frac{H_{signal}}{\overline{\sigma^2_{dark} + \sigma^2_{shot} + \sigma^2_{Johnson} + \sigma^2_{GR}}} \tag{3.45}$$

By factoring out the exposure time and number of exposures and also assuming no telescope variables, distances, or object parameters are changing, an alternate form of the above equation is given by

$$S/N = K \quad \overline{N\tau_{int}} \tag{3.46}$$

where K is a constant. This shows that the signal-to-noise ratio increases with the square root of the product of exposure time and number of exposures. More details on IR sensor characterization can be found in [51–53].

Table 3.2: NEOWISE IR telescope characterization [39].

Instrument Characteristics	Values	Asteroid Parameters	Values
F	1.35 m	T_{ast}	300 K
M	8	r_{ast}	125 m
D_o	0.4 m	d_{ast}	0.5 AU
η	0.7		0.9
G	6.83		
τ_{optics}	0.504		
N	200		
τ_{int}	8.8 sec		
$n_{e,d}$	5 e/pixel/sec		
n_{pix}	1024 $\times$1024 = 1,048,576 pixels		
R_d	5.00E04 Ω		
Pixel pitch	18 μm		
$\lambda_1,\ \lambda_2$	7.5, 16.5 μm		

3.4.4 NEOWISE IR Telescope

The fundamentals of a Cassegrain telescope and an IR sensor described in the preceding section has been applied to NEOWISE telescope in [39]. Table 3.2 summarizes the selection of IR sensor array and telescope parameters for NEOWISE.

3.4.5 HAIV IR Telescope

Sensor array data of the target is needed by the terminal guidance algorithm of the HAIV mission. This may require the object on the image plane to fill multiple pixels to ensure correct thrusting maneuvers for accurate targeting. Table 3.3 summarizes a baseline telescope design using similar parameters from Table 3.2. Note that a reference mission scenario considers the intercept of a 50-m diameter target at approximately 10-km/s closing speed. Due to such hypervelocity intercept, long exposure times and number of exposures must be kept at a minimum. A simple solution is to operate the device at its maximum data collection rate and use only one exposure. A typical high-speed digital single-lens reflex (DSLR) camera can reach frame rates of 1000 Hertz. Since video is not being recorded, shutter speed is taken to be 1/1000 of a second. These values are generated with the assumption of perfect focusing for the telescope. The pixel fill entry in Table 3.4 corresponds to the horizontal pixel illumination on the detector array. This assumes that the largest dimension of the asteroid is on horizontal axis without loss of generality.

A reference IR telescope configuration of the HAIV mission is illustrated in Fig. 3.18. This is a true scaled model where all dimensions are given in meters, and the origin of the axis is the

Table 3.3: HAIV IR telescope characterization [39].

Instrument Characteristics	Values	Asteroid Parameters	Values
F	8 m	T_{ast}	300 K
M	8	r_{ast}	25 m
D_o	0.4 m	d_{ast} at 2 hours	7.2E4 km
D_s	$\approx$ 0.050 m	d_{ast} at 60 sec	600 km
B	$\approx$ 0.88 m		0.9
b	0.08 m		
N	1		
τ_{int}	0.001 sec		
$n_{e,d}$	5e/pixels/sec		
n_{pix}	$1024 \times 1024 =$ $1,048,576$ pixels		
R_d	$5.00e04\,\Omega$		
Pixel pitch	18 μm		
$\lambda_1,\ \lambda_2$	7.5 , 16.5 μm		

Table 3.4: Performance of a reference IR telescope/seeker of the HAIV mission [39]

Parameters	Values
Geometric optics	
Pixel fill at 2 hours	$\approx$1.5
S/N at 2 hours	4.5E3
Geometric optics	
Pixel fill at 60 sec	$\approx$ 185
S/N at 60 sec	9.8E5

location of the image plane. The sun rays come from the negative optical axis, or with respect to the image, from the left. This reference design has been implemented into the terminal guidance simulation [39].

For the IR image rendering, the fictional face illumination can be described as

$$C_{IR,i} = k_{d_{IR}}(\vec{N}_i \cdot \vec{S}) + k_{a_{IR}} \tag{3.47}$$

where $k_{d_{IR}}$ represents the heating of the asteroid by the sun and $k_{a_{IR}}$ is the constant coefficient that corresponds to the core temperature of the asteroid. For both face coefficients, this model is very fast and can be computed completely in parallel for each face.

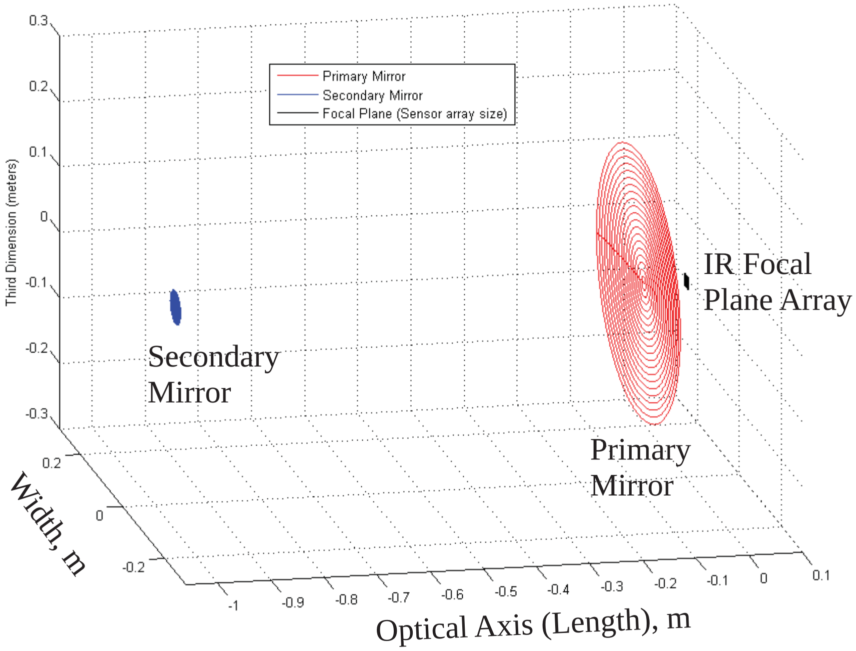

Figure 3.18: A reference Cassegrain IR telescope configuration for the HAIV mission [39].

3.5 Terminal Intercept Guidance with an IR Seeker

Impacting a small object at hypervelocity speeds will require a precision terminal guidance system. This section presents the terminal guidance simulation results using an IR camera system, including a reference HAIV telescope described in the previous section.

As mentioned previously, the pixel fill values selected were for a 50-m target asteroid. Simulated IR and visual images, of this small asteroid, were provided previously in Fig. 3.5. These images correspond to what is sensed at 60 seconds before impact for each camera (these images are cropped so that they can be seen better). It can be seen that there is a pink plus on each image. This mark is the targeted impact location of each sensor. These points are the COF of the IR image and the COB for the visual image.

A hybrid guidance scheme is examined for intercepting a small 50-m target asteroid in [39]. This scheme employs three pulses pre-scheduled at 6,300, 3,600, and 1,000 seconds before impact. After these trajectory correction maneuvers are completed, the system switches over to closed-loop PN guidance at the last 270 seconds before impact. In addition, there is no thrusting control when the flight time before impact is less than 60 seconds. The performance of the hybrid guidance scheme can be seen in Fig. 3.19. The PN guidance scheme performs better using an IR sensor. This is primarily due to the target COF location of the IR image being very close to the COM of the target asteroid.

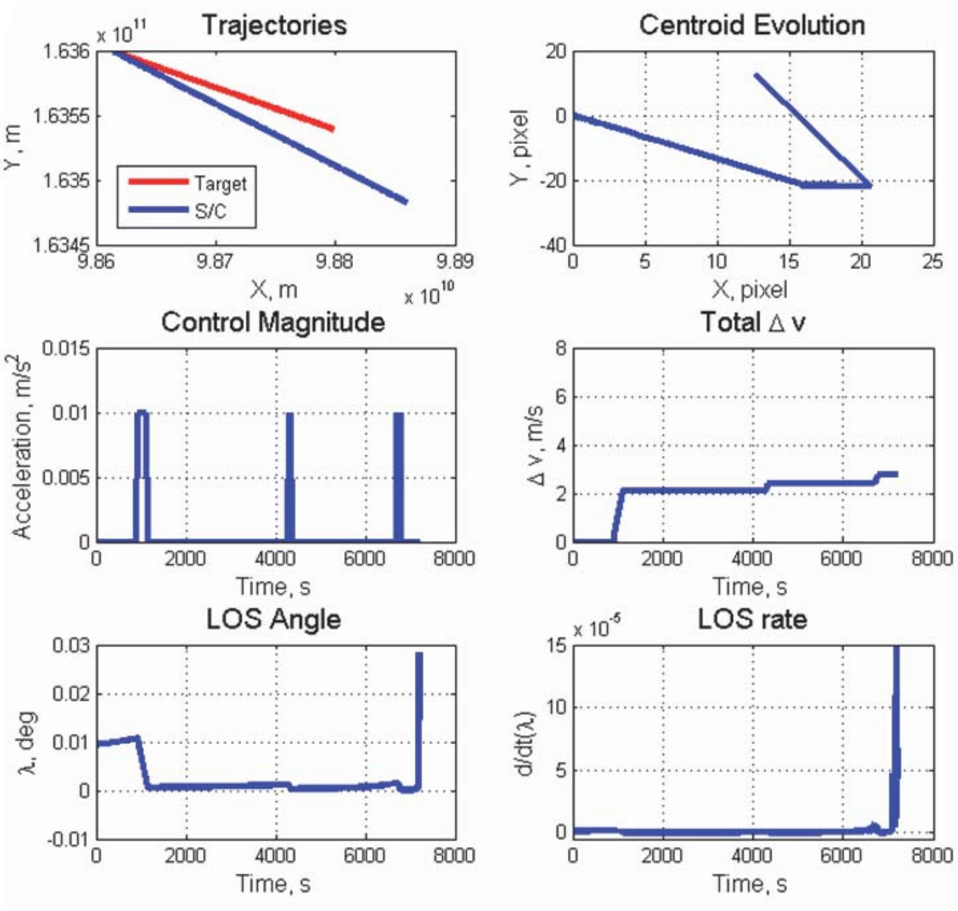

Figure 3.19: Terminal guidance simulation results for intercepting a 50-m target asteroid using an IR seeker [38, 39].

A Monte Carlo impact simulation was also conducted after the spacecraft separates at 60 seconds before impact. Approximately 98.5 percent of the fore bodies and 98.7 percent of the aft bodies impacted in the IR terminal guidance simulation. The impact distribution on a 50 m asteroid is provided in Fig. 3.20 where the fore body impacts are indicated in green and the aft body impacts are indicated in red. For such a small asteroid, a single kinetic-impactor or a nuclear contact burst may suffice in practice. However, the effects of separation dynamics uncertainty were examined via Monte Carlo simulations to assess the robustness of the two-body HAIV mission concept. In most cases, the aft body impacted the same area impacted ahead by its associated fore body even in the presence of separation dynamics uncertainty.

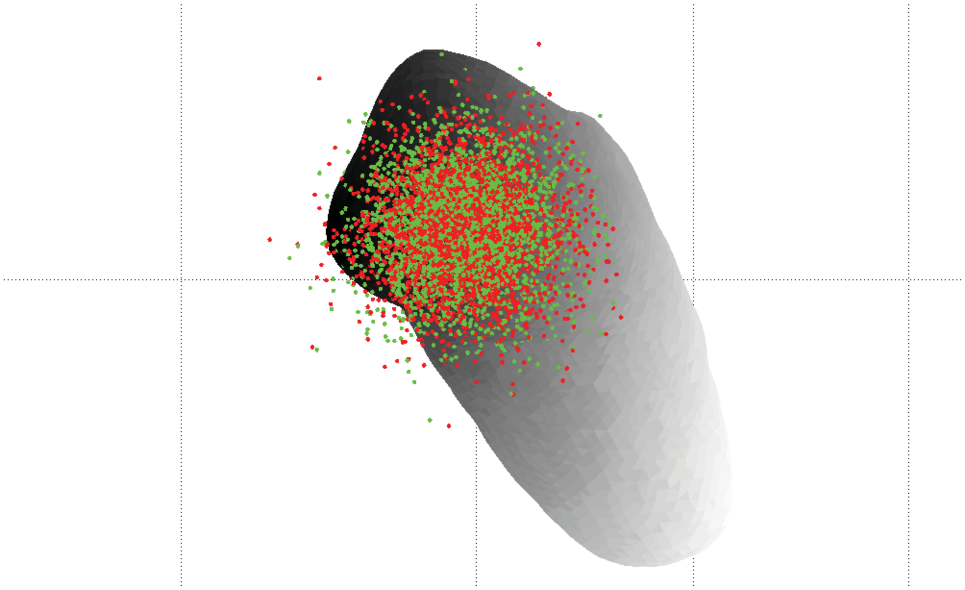

Figure 3.20: Monte Carlo simulation result for intercepting a 50-m target asteroid using an IR seeker [38, 39]. Note that in most cases, the aft body impacted the same area impacted ahead by its associated fore body even in the presence of separation dynamics uncertainty.

Chapter 4

Hypervelocity Kinetic Impact and Nuclear Subsurface Explosion: Modeling and Simulation

This chapter describes a unified modeling and simulation framework for investigating the mission effectiveness of the two-body HAIV (Hypervelocity Asteroid Intercept Vehicle) concept [17–19, 21, 22, 54, 55].

4.1 Introduction

The two-body HAIV mission concept overcomes key difficulties in coupling nuclear explosion energy into a target asteroid at high relative closing velocities of 5 to 30 km/s. The HAIV mission exploits a concept of blending a kinetic impactor and a nuclear subsurface explosion to mimic the behavior of a buried explosion, increasing energy coupling at least by an order of magnitude [12, 13]. A subsurface nuclear explosion has been known to be approximately 20 times more efficient than a surface contact burst [11]. To computationally validate such increase in energy-coupling efficiency, the HAIV mission concept is simulated using a Smoothed Particle Hydrodynamics (SPH) method adapted for high-speed, low-cost, implementation on Graphics Processing Units (GPUs). Both Tillotson and Jones-Wilkins-Lee (JWL) energy coupling models, that are often used by various hydrodynamic codes for simulating the effects of high-energy explosives, are also employed for the HAIV mission simulation study. ANSYS Autodyn commercial software is also used to further examine various energy-coupling models employed by hydrocodes.

Because the hypervelocity kinetic impact and nuclear subsurface explosion simulations rely heavily on energy transmission through shocks, the simulation research work conducted for the HAIV mission concept study in [17–19] exploited the Adaptive Smoothed Particle Hydrodynamics (ASPH) method for mitigating some of the computational and fidelity issues that arise in more complex, high-fidelity simulations. This simple approach is based on the research work of Owen et al. [20]. The propagation of the nuclear explosive shock can be seen in Fig. 4.1. The shock propagation process dissipates some energy due to interactions with the rebounding shock front. In the center area of deeper regolith, the seeding process naturally results in a much more porous material, absorbing energy from the shock. Upon reaching the second core at the far side, some large chunks escape the disruption process in some cases (even with lower material strengths). An improved ASPH code, implemented on a modern low-cost GPU desktop computer, has been developed for the HAIV mission study [17–19]. However, a more computationally efficient, modern GPU-based hydrocode needs to be further developed by incorporating more accurate physical models of a nuclear subsurface explosion [21, 22].

Initial simulation studies in [17] considered a spherical asteroid model, with the key limitations being the size of the target and a lack of a range of source energy input. With a new computational approach to the hydrodynamic simulations developed in [18, 19], a 2D inhomogeneous shape of user-selected characteristics, such as that shown in Fig. 4.2, was further examined. This model was also extended to general 3D shapes imported from a surface triangulation, such as the scaled shape model for 433 Eros shown in Fig. 4.2. This approach will allow us to consider much larger targets with increased resolution and a faster turnaround time, so the influence of more composition parameters can be investigated.

In contrast to the Weibull distribution used to seed implicit flaws in brittle materials in [17], an improved simulation code utilizes a tensor relationship for material characteristics and orientation [18, 19]. This allows for more realistic size and shape generation for asteroid fragments by treating damage as a local quantity (cracks) rather than a distributed state variable. One of the key limitations is that most proposed neighbor-finding methods for interpolation rely on complex logic and they are not suitable for efficient GPU implementation. Therefore, the addition of the third dimension makes this problem far more complex. A bin process used in previous SPH research is extended for the GPU computing platform. The study results in [18,19] showed that a large amount of data can be processed using GPU simulation. Initial work was focused mostly on prediction of relative impacting mass, but disruption at different times along a given orbit can have a large effect on the resulting shape of debris.

4.2 GPU-based ASPH Hydrocode Development

The methods used to generate the simulation models for studying the concept of blending a kinetic impact and a nuclear subsurface explosion are described. A brief discussion of the extensions from

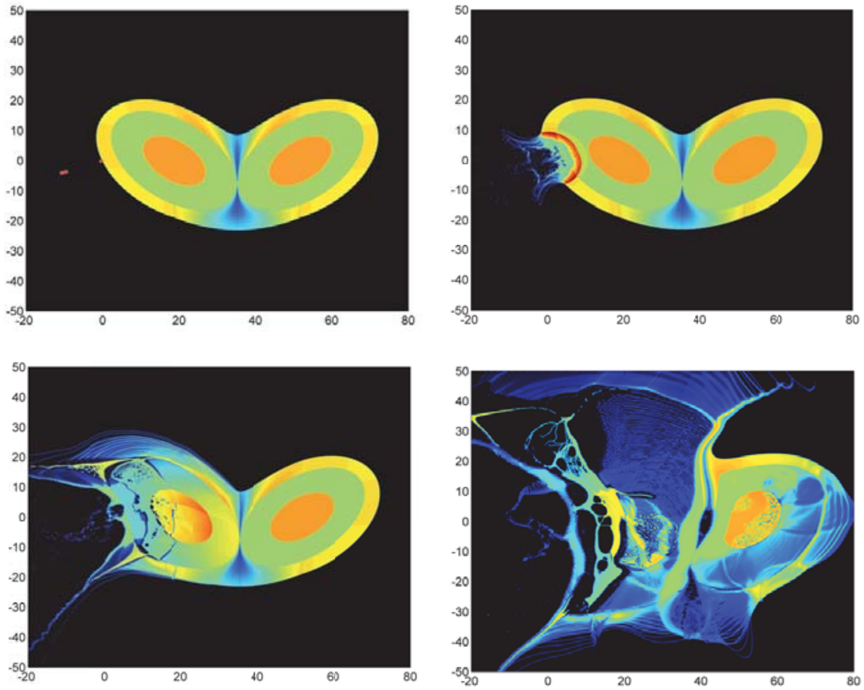

Figure 4.1: A 70-m asymmetric asteroid model disrupted by a 10-km/s kinetic impact and a subsequent 70-kt nuclear subsurface explosion of the HAIV system [17–19].

past work is also provided here, as well as new relationships for the ASPH hydrocode formulation and damage model. Any computer programs that model the behavior of fluid flow systems by breaking down the system into a three-dimensional array of cells and calculating the forces and other physical variables affecting each one are often called hydrocodes. The core SPH and ASPH concepts have been discussed in [17–19, 54] as applied to asteroid disruption modeling and simulation, which was built upon a wealth of past SPH literature and was programmed on the GPUs using the CUDA (Compute Unified Device Architecture) framework. CUDA is a parallel computing platform and programming model created by NVIDIA and implemented by the GPUs.

4.2.1 Adaptive Smoothed Particle Hydrodynamics (ASPH) Method

The hypervelocity impact and high-energy explosion simulations rely heavily on energy transmission through shocks. The ASPH modeling technique, developed by Owen et al. [20], to mitigate some of the computational and fidelity issues that arise in more complex simulations is briefly discussed herein.

The SPH method uses a kernel function that acts on a normalized position space. This smoothing kernel $W(\boldsymbol{\eta})$ is a function of the normalized position vector $\boldsymbol{\eta} = \mathbf{r}/h$, where $\mathbf{r}$ is the physical position vector and h is the isotropic smoothing length. To add a directional sense to ellipsoidal nodes, the ASPH method uses a symmetric, positive definite linear transformation $\mathbf{G}$ such that

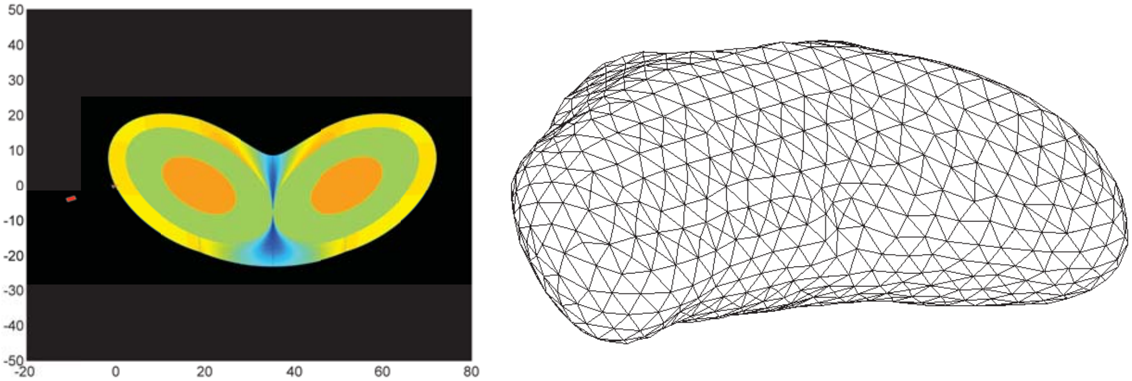

Figure 4.2: A 2D contact binary asteroid model developed for HAIV simulation studies and a surface triangulation of asteroid 433 Eros [18, 19].

$\boldsymbol{\eta} = \mathbf{G}\mathbf{r}$. Then, the kernel derivative becomes

$$\nabla W(\boldsymbol{\eta}) = \nabla W(\mathbf{G}\mathbf{r}) = \frac{\partial W(\mathbf{G}\mathbf{r})}{\partial \mathbf{r}} = \frac{\partial \boldsymbol{\eta}}{\partial \mathbf{r}} \frac{\partial W}{\partial \boldsymbol{\eta}} = \mathbf{G} \frac{\boldsymbol{\eta}}{\eta} \frac{\partial W}{\partial \eta} \tag{4.1}$$

The linear transformation tensor $\mathbf{G}$ (a 3 × 3 matrix for the 3D problem) is evolved as

$$\Delta \mathbf{G} = (\Delta \mathbf{R})\mathbf{G} - \mathbf{G}\boldsymbol{\sigma}\Delta t \;\; \text{or} \;\; \frac{D\mathbf{G}}{Dt} = \frac{D\mathbf{R}}{Dt}\mathbf{G} - \mathbf{G}\boldsymbol{\sigma} \tag{4.2}$$

where $D\mathbf{G}/Dt$ is the Lagrangian derivative of $\mathbf{G}$, $\Delta \mathbf{R}$ is an infinitesimal rotational transformation of the smoothing kernel, and $\boldsymbol{\sigma}$ is the deformation tensor that indicates how the velocity field varies spatially to first-order such that $\mathbf{v}(\mathbf{r} + d\mathbf{r}) \approx \mathbf{v}(\mathbf{r}) + \boldsymbol{\sigma} d\mathbf{r}$. We have $\sigma_{\alpha\beta} \equiv \partial v_\alpha / \partial r_\beta$ where (α, β) refer to spatial directions and

$$\boldsymbol{\sigma} = \begin{bmatrix} \sigma_{11} & \sigma_{12} & \sigma_{13} \\ \sigma_{21} & \sigma_{22} & \sigma_{23} \\ \sigma_{31} & \sigma_{32} & \sigma_{33} \end{bmatrix} = \begin{bmatrix} \partial v_x/\partial x & \partial v_x/\partial y & \partial v_x/\partial z \\ \partial v_y/\partial x & \partial v_y/\partial y & \partial v_y/\partial z \\ \partial v_z/\partial x & \partial v_z/\partial y & \partial v_z/\partial z \end{bmatrix}$$

A symmetrized kernel function W_{ij} is defined as

$$W_{ij} = \frac{1}{2}[W(\boldsymbol{\eta}_i) + W(\boldsymbol{\eta}_j)] \tag{4.3}$$

where

$$\boldsymbol{\eta}_i = \mathbf{G}_i \mathbf{r}_{ij}, \quad \boldsymbol{\eta}_j = \mathbf{G}_j \mathbf{r}_{ij}, \quad \mathbf{r}_{ij} = \mathbf{r}_i - \mathbf{r}_j \tag{4.4}$$

A smoothing process for the tensor $\mathbf{G}$ is then implemented after many time steps. This is done as a weighted average over the neighboring values to generate the new smoothing tensor $\mathbf{G}'$ as

$$\mathbf{G}' = |\mathbf{G}||\mathbf{C}_i|\mathbf{C}_i \tag{4.5}$$

where

$$\mathbf{C}_i = \frac{\sum_j \mathbf{G}_j^{-1} W_{ij}}{\sum_j W_{ij}} \tag{4.6}$$

To mitigate spurious shear viscosity that is introduced by the artificial viscosity Π_{ij}, a modification to Π_{ij} can be adopted as [20]:

$$\tilde{\Pi}_{ij} = \frac{1}{2}(f_i + f_j)\Pi_{ij} \tag{4.7}$$

where $\Pi_{ij} = (\Pi_i + \Pi_j)/2$ and

$$f_i = \frac{|\nabla \cdot \mathbf{v}_i|}{|\nabla \cdot \mathbf{v}_i| + |\nabla \times \mathbf{v}_i| + \epsilon c_i/h_i} \tag{4.8}$$

and c_i is the local speed of sound and ϵ is a small number chosen to prevent divergence [20].

4.2.2 Tensor Damage Model

In the initial SPH model used for the HAIV mission study, the behavior of the core material under high stress was governed by the activation of implicit flaws. These flaws are seeded in the representation particles using a Weibull distribution with a coefficient of around 4.2×10^{23} and an exponent between 6.2 and 9.5. Using a range of distribution exponents and strength properties allows us to examine the behavior of the core material with varying brittleness and material cohesion. This turns out to be very important for a contact binary system (Fig. 4.2), as strong core material absorbs energy from the disruption shock and can result in large remaining chunks of material. Smoothing lengths are chosen to allow for resolution of between 1 cm and 5 cm, which results in a hydrodynamic system of between 800,000 and 6,000,000 nodes. This system is scaled to be an ideal size for the GPU simulation programs developed for the HAIV mission study, maximizing both computational efficiency and simulation turnaround time.

Consequently, a damage model using a tensor variable is implemented. The details are the same as those used in the Spheral hydrocode, developed by Dr. Mike Owen at the Lawrence Livermore National Laboratory. A tensor damage variable per node is introduced in order to support directionality in the damage evolution. Cracks are allowed to open up in response to strain aligned perpendicularly to that direction, and there is substantially reduced crack growth in orthogonal directions to the strain. The tensor strain $\sigma_{\alpha\beta}$ used is the "pseudo plastic strain" of SolidSpheral [20], which evolves in time as

$$\frac{D\sigma_{\alpha\beta}}{Dt} = \frac{1}{G_s}\frac{DS_{\alpha\beta}}{Dt} \tag{4.9}$$

where $S_{\alpha\beta}$ is the traceless stress tensor and G_s is the shear modulus. The maximum damage allowed to accumulate in a volume then is computed as

$$\max\left(\frac{n_i}{n_i^{tot}}, \Delta_i\right) \tag{4.10}$$

where n_i is the number of active flaws, n^{tot} is the total number of flaws assigned to a particle, and Δ_i is the directional scalar damage.

4.2.3 Neighbor Finding Implementation

In order to speed up neighbor-finding calculations with the increased dimensionality, a tree data structure was used to superimpose a sparse physical grid on the data. This implementation is similar to several approaches used to simulate local gravity interactions in astrophysical simulations. First, the coordinate arrays are sorted and then an inverse map for the particle IDs into the sorted array is defined. Then, a partitioning of the sorted space is defined so that each grid box represents a nearly equal number of particles, and that all the particles in neighboring grid locations are no greater than the desired maximum of particle neighbors. This is a hard limit due to memory structure on the GPU data representation.

Each bin is assigned a list of particles in it. Then, a neighbor search for a particle limits itself to the particles in the nearby grid bins. With a well-defined number of particles per bin, this results in an implementation that scales linearly with number of particles. The main limitation is in the assignment of particle IDs to the bin and in the storage requirements for this connectivity information. However, storage added is small compared to the storage of neighbor IDs for each particle, and the sort and assignment can be done in parallel on the GPU. The power of this approach lies in how it scales with increased number of SPH interpolants. In addition to scaling superlinearly (compared to quadratic brute force calculations), the present approach uses the Thrust library to sort the position components of the particles in parallel. This eliminates a series of memory transfers with the host and keeps all data on the GPUs.

A subsequent group of GPU kernels establish pointers to the limits on the sorted array for which candidate neighbor particles may belong. This reduces the neighbor finding to an integer union calculation, which can be conducted as a logical (true/false) operation. Comparing the position of the sorted particle IDs with the limits allows for a simple yes/no decision on whether a proposed neighbor could be within the support of the interpolation function. Figure 4.3 gives a depiction of this process for each computing thread. Figure 4.4 shows the improvements of the present model over in-place neighbor calculations (also on the GPU). While dimensionality affects the speed-up, there are still substantial gains made over past implementations.

4.2.4 Grid Generation

An automatic grid generation for the SPH input conditions has been developed in [17–19]. This grid generation program requires a function for a piecewise-defined surface $z = F_i(x, y)$. The

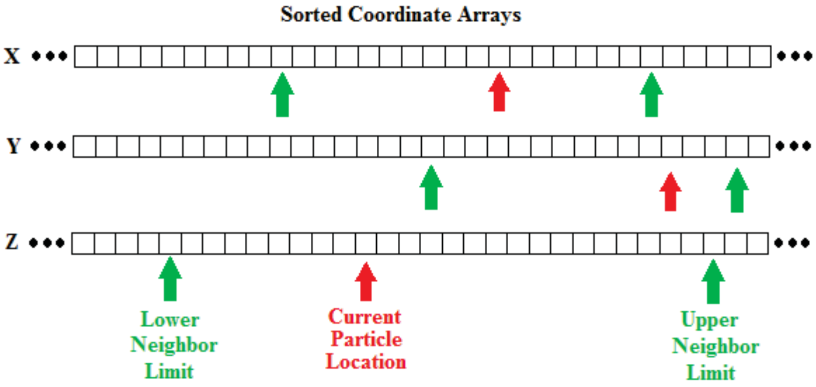

Figure 4.3: Description of sorted neighbor kernel process [18, 19].

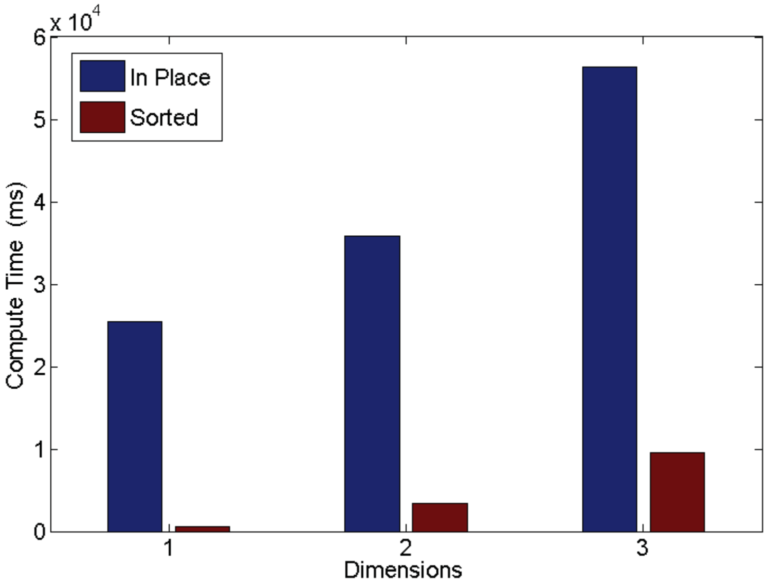

Figure 4.4: Neighbor search cost [18, 19].

pieces should not overlap, and the surfaces for $z > 0$ and $z < 0$ can be distinct. A uniform grid of points (x, y) are created and the initial conditions for the optimization are $(x_0, y_0, z_0) = (x, y, F(x, y))$. Then, updates to these positions are made to satisfy the local minimization problem of the form

$$\min \sum_j (r_{ij} - d)^2 \text{ subject to } z_i = F(x_i, y_i) \tag{4.11}$$

where d is the specified desired optimal separation, the sum is over the immediate neighbors, and r_{ij} is the distance between points i and j. This problem is solved independently for each point i. An iterative update scheme is converged until the boundary particles are seeded. Then, a uniform grid of interior particles is initialized. The positions of these points are similarly updated using an unconstrained minimization problem of the form

$$\min \sum_j L_{ij} \tag{4.12}$$

where L_{ij} is the Lennard-Jones potential defined as

$$L_{ij} = \epsilon \left[\left(\frac{r_m}{r_{ij}} \right)^{12} - 2 \left(\frac{r_m}{r_{ij}} \right)^{6} \right] \tag{4.13}$$

where ϵ is the depth of the potential well and r_m is the distance at which the potential reaches its minimum.

4.3 Energy-Coupling Models

4.3.1 Introduction

This section provides an extension to the hydrodynamic modeling and simulation work in [17–19], which used a GPU-accelerated 2D ASPH methodology. An explicit hydrodynamic software, called Autodyn by ANSYS, is also utilized for studying the efficiency of the HAIV mission concept in [18, 19, 21]. ANSYS Autodyn commercial software is a versatile explicit analysis/simulation tool for modeling the nonlinear dynamics of solids, fluids, gases and their interactions. ANSYS Autodyn provides both Lagrangian and Eulerian modeling frameworks in 2D and 3D, and it allows visualization of solutions in real time. In addition, a validated material library is included for accurate material properties. Autodyn also aids in simulation setup time by including geometry manipulation tools and built-in grid generators.

Another new approach, which utilizes high-order (order of accuracy 3rd or higher) numerical methods developed in computational fluid dynamics (CFD), is also employed for the HAIV

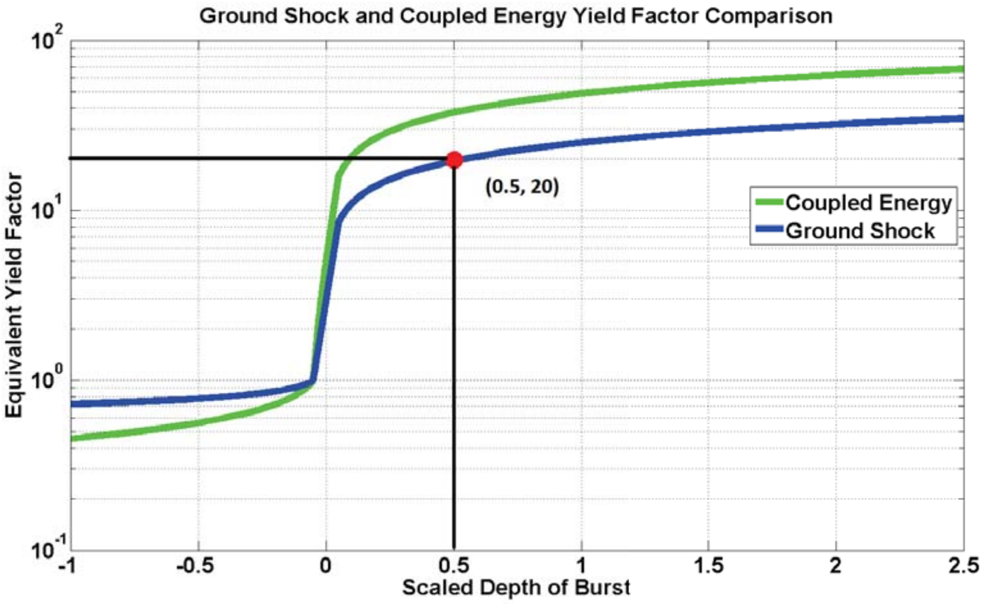

Figure 4.5: Subsurface explosion efficiency plot [11].

mission study in [21, 22]. The correction procedure via reconstruction (CPR) method, developed in [56] and extended in [57, 58], has been implemented and tested against both analytical and Autodyn solutions in one and two-dimensional blast wave problems. The data for material models was extracted from previous works of literature in the field and documentation provided by ANSYS. The explosive device chosen in most simulations is Trinitrotoluene (TNT). Energy coupling is modeled via two methods: Direct energy deposition and Jones-Wilkins-Lee (JWL) equation of state. The direct energy deposition model was initially used in the GPU-based SPH algorithm [17–19] and was implemented in Autodyn for comparison.

4.3.2 Energy Deposition Modeling

Upon specifying an yield for the NED payload (e.g., 100 kilotons), total energy of the device is calculated in Joules using the specific internal energy of TNT. The specific internal energy of nodes is then calculated by dividing the total energy by the nodal mass. The specific internal energy calculated is an input to the hydrocode simulation as an initial condition. This method produces an isotropic explosion, converting a fraction of its internal energy to kinetic energy, which will be coupled to the target body. Material properties are governed by Tillotson equation of state throughout the simulation for both target body and the explosive device. The Tillotson equation was also used in the GPU-based SPH algorithm [17–19].

A specific detonation mechanism (point source or line source) along with an initiation time governs the energy distribution and coupling. Rock material characteristic models, which encapsulate the brittle and rubble like nature, are implemented to further test the blast dynamics in [18, 19].

The research work in [18, 19, 21, 22, 55] attempted to verify the efficiency improvement factors of subsurface explosions over a surface blast. A 20 times efficiency factor, as indicated in Fig. 4.5, can be extracted from the study report entitled "Effects of Nuclear Earth-Penetrator and Other Weapons" published by National Research Council [11]. The scaled depth-of-burst (DOB) used in Fig. 4.5 is defined as

$$\text{Scaled DOB} = \frac{d}{Y^{1/3}} \tag{4.14}$$

where d is the buried depth in units of meters and Y is the NED yield in units of kt. The scaled DOB and the actual depth d are defined to be negative for explosions above the surface.

In Fig. 4.5, it can be seen that equivalent yield factors for coupled energy asymptotically approach 100 (i.e., as burial depth increases). For a generic 300-kt explosion at 3-m depth-of-burst (scaled DOB of 0.45), the ground-shock-coupling factor is about 20, which is equivalent to a contact burst of about 6.0 Mt [11]. According to the empirical curves presented in Fig. 4.5, subsurface detonations yield an increase to the energy coupling efficiency when compared to surface blasts. Validating the above mentioned efficiency factors will aid us in the design process when determining required impact velocity for the kinetic impactor and required mass of the detonation payload, thus improving overall mission efficiency. Energy coupling to the target object is determined by the following factors: material characteristics of the target, target resolution, blast modeling scheme and simulation framework (e.g., FEM/SPH), and buried depth of the explosive device.

The SPH method is a Lagrangian particle physics method, initially developed to solve astrophysics problems. It is formulated with the basic fluid dynamic equations smoothed over a kernel function W for a calculated or specified smoothing length. The kernel function, usually specified as a cubic spline, modifies the basic fluid dynamic equations via averaging to obtain the following conservation of momentum, energy and mass equations (the first equation defines the velocity vector):

$$\frac{D\mathbf{r}_i}{Dt} = \mathbf{v}_i \tag{4.15}$$

$$\frac{D\mathbf{v}_i}{Dt} = -\sum_{j=1}^{N} m_j \left(\frac{p_i}{\rho_i^2} + \frac{p_j}{\rho_j^2} + \Pi_{ij} \right) \nabla W_{ij} \tag{4.16}$$

$$\frac{DE_i}{Dt} = \frac{1}{2} \sum_{j=1}^{N} m_j \left(\frac{p_i}{\rho_i^2} + \frac{p_j}{\rho_j^2} + \Pi_{ij} \right) (\mathbf{v}_i - \mathbf{v}_j) \cdot \nabla W_{ij} \tag{4.17}$$

$$\frac{D\rho_i}{Dt} = \sum_{j=1}^{N} m_j (\mathbf{v}_i - \mathbf{v}_j) \cdot \nabla W_{ij} \tag{4.18}$$

$$\rho_i = \sum_{j=1}^{N} m_j W_{ij} \tag{4.19}$$

where $\mathbf{r}$ is the position vector, $\mathbf{v}$ is the velocity vector, p is the pressure, ρ is the density, m is the mass, Π is the artificial viscosity, E is the specific internal energy, and N is the total number of neighbors. Numerical integration of the above equations can be performed by using a leap frog or a Runge Kutta method. Autodyn also incorporates an adaptive time step calculation along with density limiters to ensure the robustness of the simulation. Smoothing length of the simulation is updated with each time step for faster and accurate results.

A multitude of material modeling options consisting of different equations of states, strength, and failure models need to be considered to capture the accurate material characteristics during the hypervelocity kinetic impact and nuclear subsurface explosion. The NED yield is modeled via TNT material properties. The JWL equation of state is specified for the explosive material, while the target is modeled by Tillotson equation of state. Capturing the material behavior is crucial, as these characteristics determine the failure method, particle velocities, and energy coupling factors.

4.3.3 Tillotson Equation of State

Material modeling of asteroids is an extremely complex problem. Asteroids consist of materials ranging from metals to gaseous compounds arranged in heterogeneous distributions. Structural integrity of an asteroid is also unknown as it may range from a solid to a shattered rubble pile held together by gravity. Most of the previous simulation work was done assuming homogeneous density layers. Initial material modeling used the Tillotson equation of state and a failure criterion based on Weibull distribution is introduced to initialize pre-shattered geometries in [18, 19].

The Tillotson equation of state predicts metallic material behavior during energy transfer modes. This equation defines material phase changes, compressions, and expansions based on energy transfer. The Tillotson equation of state is defined for four regions located to the right of the Hugoniot curve. Figure 4.6 depicts the four regions that define shock compression.

Within Region I, the material is represented in a compressed state. The vertical line extends up to 1,000 Mbar and the pressure is expressed as

$$p_1 = (a + \frac{b}{\omega_0})\eta\rho_0 E + A\mu + B\mu^2 \tag{4.20}$$

where a and b are material parameters, A denotes the bulk modulus, and B represents the compressive term. The specific internal energy E and the density ρ play a major role in determining the phase and pressure of the metallic material. Parameters η, μ, and ω_0 are defined as

$$\eta = \frac{\rho}{\rho_0} \tag{4.21a}$$

$$\mu = \eta - 1 \tag{4.21b}$$

$$\omega_0 = 1 + \frac{E}{E_0\eta^2} \tag{4.21c}$$

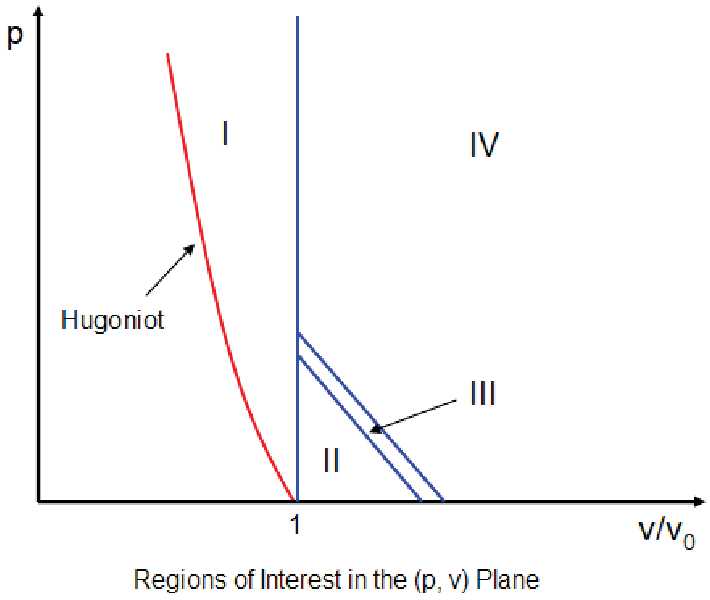

Regions of Interest in the (p, v) Plane

Figure 4.6: Tillotson equation of state (Image from ANSYS Autodyn manual 14.5).

where the reference or initial values are denoted by subscript 0.

Region II defines material characteristics under shock due to energy that is less than the sublimation energy. The pressure is then described as

$$p_2 = (a + \frac{b}{\omega_0})\eta\rho_0 E + A\mu \tag{4.22}$$

In Region III, the pressure is just the mean pressure between Regions II and IV, given by

$$p_3 = p_2 + \frac{(p_4 - p_2)(E - E_s)}{E_s' - E_s} \tag{4.23}$$

where E_s denotes sublimation energy of the material and E_s' represents the energy required for the material to expand as a gas.

The expansion phase of a shocked material is governed by Region IV with pressure expressed as

$$p_4 = a\eta\rho_0 E + \quad \frac{b\eta\rho_0 E}{\omega_0} + A\mu e^{\beta x} \quad e^{-\alpha x^2} \tag{4.24}$$

where $x = 1 - 1/\eta$ and (α, β) are material parameters for the Tillotson equation of state.

A Tillotson material model is an efficient method of modeling pre-shattered rubble piles. A linear relationship between a shock wave and particle velocities lays the foundation for this equation of state and it has provided results that agrees with laboratory experiments. This model was used to represent the particle distribution of the target asteroid in blast simulations and hypervelocity impacts in [18, 19].

Table 4.1: Properties of shock equation of state

Parameters	Definition	Water
ρ_0	Initial density	1,000 kg/m^3
c	Speed of sound	1.48 km/s
γ_0	Gruneisen coefficient	0.5
a	Volume correction coefficient	0.0
S_1	Fitting coefficient	2.56
S_2	Fitting coefficient	1.986
S_3	Fitting coefficient	1.2268

4.3.4 Shock Equation of State

The shock equation of state, which was developed using empirical relations and used by various hydrocodes, represents characteristics of underwater explosions. Properties of shock equation of state are given in Table 4.1, and the pressure is described as

$$p = \frac{\rho_0 c^2 \mu [1 + (1 - \gamma_0/2)\mu - \mu^2/2]}{[1 - (S_1 - 1)\mu - S_2 \mu^2/(\mu+1) - S_3 \mu^3/(\mu+1)^2]^2} + (\gamma_0 + a\mu)E \tag{4.25}$$

where $\mu = \rho/\rho_0 - 1$.

4.3.5 Jones-Wilkins-Lee (JWL) Equation of State

The JWL equation of state is based on various empirical relationships obtained from experiments conducted with high energy explosives such as TNT. Pressure of the explosive gas is given by

$$p = A(1 - \frac{\omega\eta}{R_1})e^{-R_1/\eta} + B(1 - \frac{\omega\eta}{R_2})e^{-R_2/\eta} + \omega\eta\rho_0 E \tag{4.26}$$

where A, B, R_1, R_2, and ω are coefficients obtained from experiments, η represents the density ratio between the gaseous products and original material, and E is the specific internal energy of the material, and ρ_0 is the initial density of the material. A graphical representation of the relationship between pressure and volume is given in Fig. 4.7. The JWL equation of state for TNT is also shown in Fig. 4.7, where the three terms of Eq. (4.26) are plotted along with total pressure.

4.4 GPU-based ASPH Hydrocode Simulations

GPU-based ASPH hydrocode simulations for disrupting an asymmetric asteroid model [18, 19] are described here. A description of the targets used for 2D and 3D analysis is also given. Explosion energy coupling sensitivity to both timing and location is examined. A comparison of the subsurface explosion to a surface contact burst is also discussed.

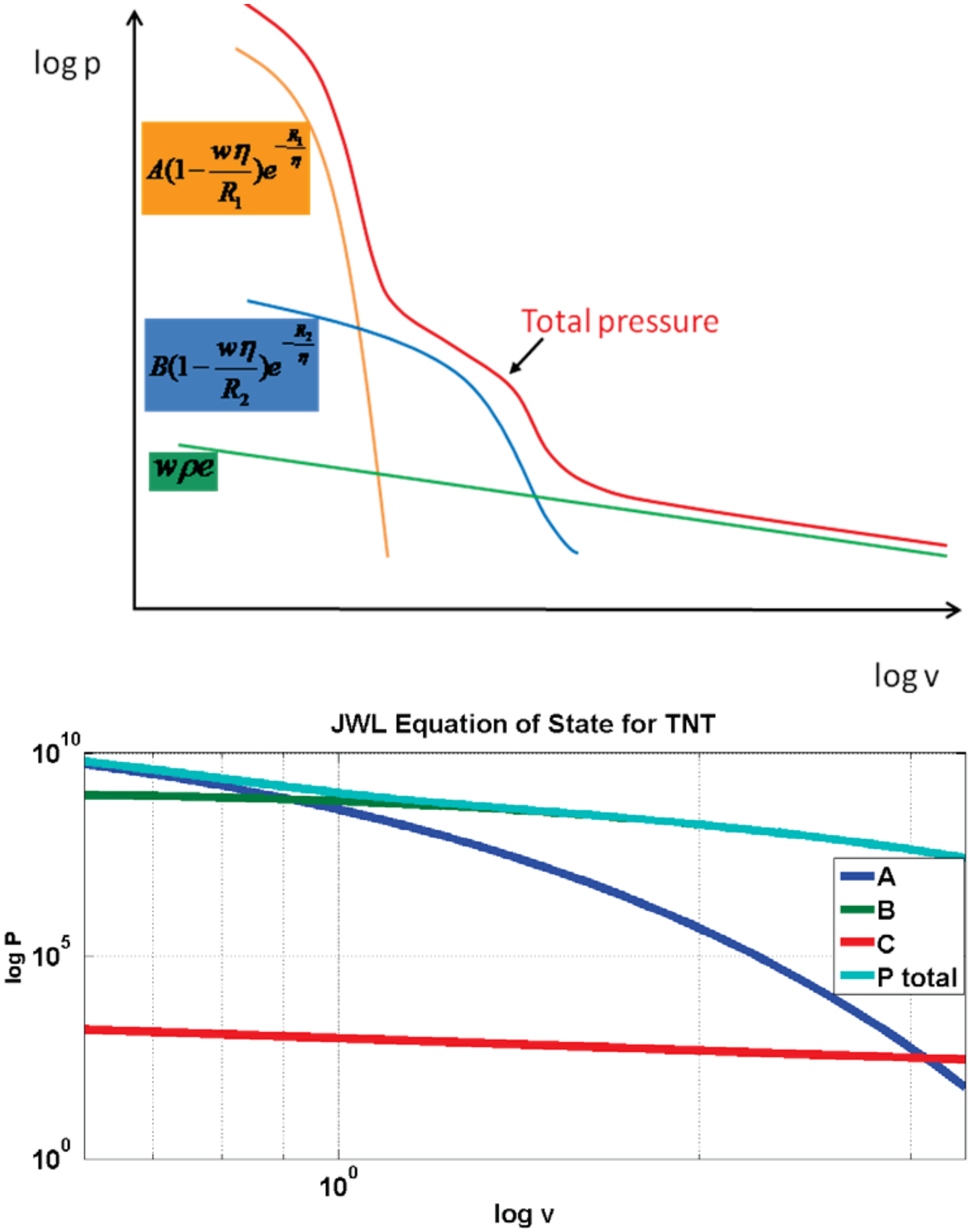

Figure 4.7: JWL equation of state: general equation of state (top) and TNT equation of state (bottom). Images from ANSYS Autodyn manual 14.5.

4.4.1 Disruption of an Asymmetric Asteroid Model

An asymmetric asteroid model developed for the HAIV mission study consists of a contact binary system with a rubble pile exterior, as shown in Fig. 4.2. With binary asteroids comprising about 16% of the known near-Earth asteroid population, an impactor mission faces an approximately 1 in 6 chance that the target it approaches will be a binary system. This is a characteristic that will be unable to be predicted ahead of time without radar observation, in the case of systems with close secondaries. It has been suggested that many irregularly shaped asteroids with unusual spin states could be contact binary (or multiple) systems. These types of systems would exhibit some of the same characteristics as monolithic rocks and as rubble piles. Furthermore, those asteroids identified as rubble piles could have large solid components beneath their regolith.

The two cores of the model shown in Fig. 4.2 are elliptical, with major and minor axes of 50 and 30 m, respectively. These cores have material properties similar to granite with a linear elastic-plastic strength model, and are canted by 45 degrees relative to the horizontal. There is a vertical line of symmetry, so the cores are mirror images of one another. A rubble regolith extends 2 m in depth vertically above each core, and is packed along lines of constant potential around the body, resulting in a maximum regolith depth of 14 m. These properties result in exterior dimensions of the target being approximately 76 $\times$ 42 m, as shown in Fig. 4.2. The inner half of each core has an initial bulk density of 2,630 kg/m^3, while the outer portion of the core is more porous material with an average bulk density of 1,910 kg/m^3. A linear model for material strength is used in this target with a yield strength of 14.6 MPa and a shear modulus of 35 MPa, resulting in a more granulated fragmentation and slower dispersion velocities. Real asteroid targets are expected to fall within the two extremes considered here, with variances for composition, distribution of mass, and orientation.

The nuclear explosion shock wave and the subsequent disruption of the target can be seen in Fig. 4.8. This process dissipates some energy due to interactions with the rebounding shock front. In the center area of deeper regolith, the seeding process naturally results in a much more porous material, absorbing energy from the shock. The new damage model allows for better tracking of crack propagation. Upon reaching the second core at the far side, some large chunks escape the disruption process in some cases (even with lower material strengths).

The overall velocity statistics for this case, which are the governing variables behind successful disruption, are similar to those an ideal cylindrical case. The histogram for radial dispersion velocities of the fractured particles is provided in Fig. 4.9. There is a mean dispersion velocity of approximately 350 m/s.

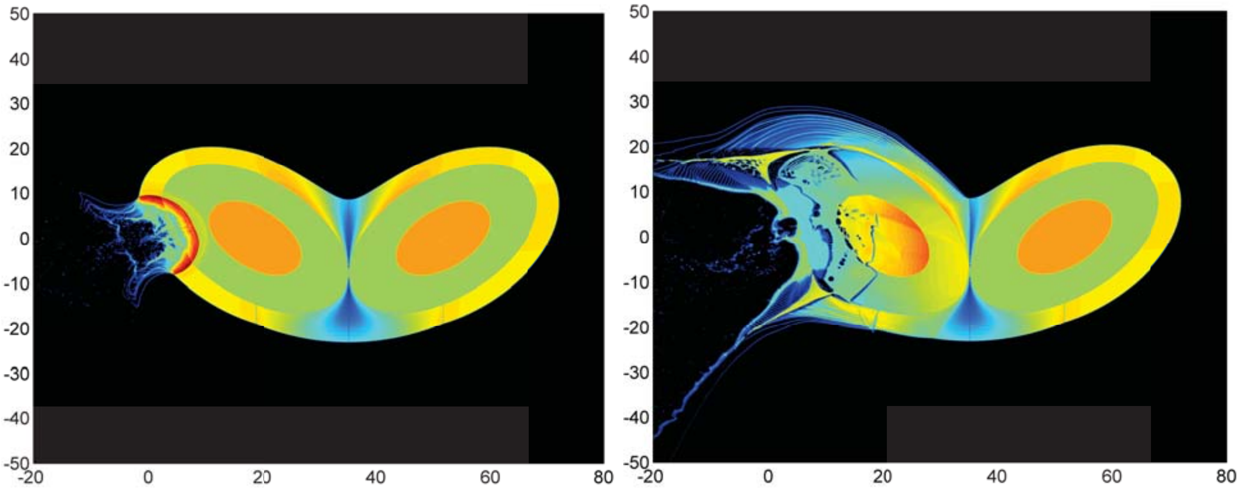

Figure 4.8: Asymmetric shock behavior and disruption process for a 70-m asymmetric asteroid [18, 19].

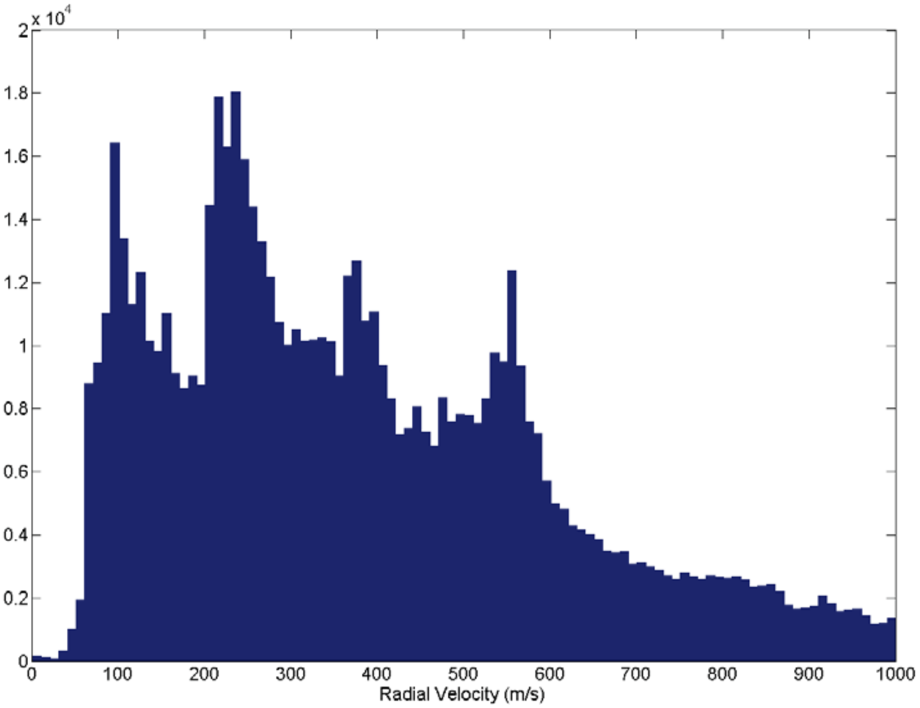

Figure 4.9: Radial dispersion velocity histogram [18, 19].

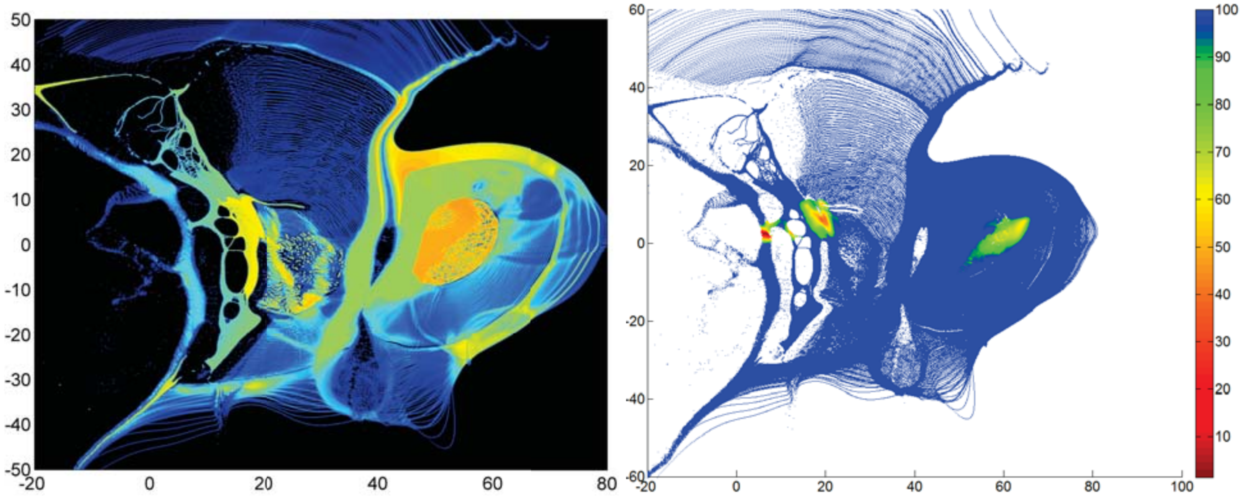

Figure 4.10: Final disruption of a target and location of slowest moving debris [18, 19]. The color bar indicates the relative dispersion velocity distribution of slowest debris in units of m/s.

There remains a high risk for this example of single largest chunks on the order of tens of meters. However, this material is highly stressed due to velocity gradients, and may be ripped apart in further time. The large velocity gradients and the location of the slowest debris can be observed in Fig. 4.10. Furthermore, these large chunks are still imparted substantial velocities from the blast of approximately 10 to 20 m/s, and have sufficient energy to disperse from the nominal impacting trajectory over tens of days. The color bar in Fig. 4.10 indicates the relative dispersion velocity distribution of slowest debris in units of m/s.

4.4.2 Subsurface Explosion Sensitivity Analysis

A series of sensitivity studies using a 2D-ASPH hydrocode have been conducted in order to identify mission critical information in [18, 19]. The tests incorporated a spacecraft model with a leading impactor and a follower body carrying a nuclear explosive device (NED) payload. A 70-m wide asteroid considered in the preceding section was used as a target. The first task was to study the NED detonation sensitivity in different locations inside a crater. Once the impactor creates a crater, the NED payload was guided to different locations of the crater to qualitatively identify the magnitude of the damage caused by the nuclear detonation. The second task was to study NED detonation sensitivity in a series of locations between above the surface and the bottom of the crater. Detonations were conducted below and under the surface level to observe damage. The final qualitative study was correlation between the crater size and the damage from the nuclear detonation. Particle dispersion and fragmentation were analyzed after detonating the NED payload in the bottom of the crater. Different sizes (widths) of intermediate crater formation were created by adjusting the distance between the impactor and the payload.

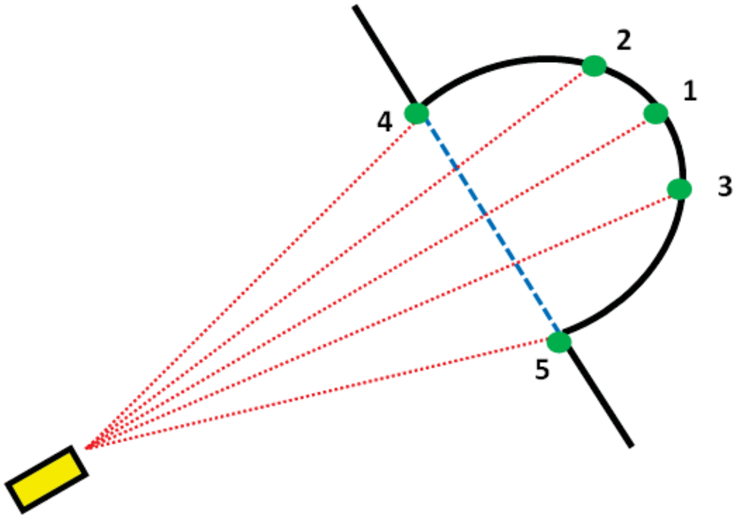

Figure 4.11: Subsurface explosion locations inside a crater, selected for a mission robustness/sensitivity evaluation study [18, 19].

Various test locations are depicted in Fig. 4.11. A 50-kt nuclear energy source was used for the various images in Fig. 4.12. Velocity magnitude of both impactor and the payload is 10 km/s at all times. The nuclear payload was detonated just before it starts to deform after contacting the surface. All the simulations were run for approximately 6-ms simulation time. The NED payload approaches the bottom of the crater, at which point the width of the crater is 6.4 m and the crater depth is 5.0 m. A shock propagation can be observed along with a destabilization of the surface layers and a layer near the core. In the final intermediate stage, more surface layers shows a shredding effect along with a density change in the middle layers. At test locations 2 and 3, the first image shows the front of the payload has begun to deform. This image was taken right before the payload was detonated. At 200 time steps, a smaller shock has started to propagate adjacent to the larger one which suggests that particles with high kinetic energy (from the NED payload) have taken some time to reach with that specific point. At the final intermediate stage, the smaller shock has merged into the larger one. More particles from the surface layer have been dispersed with the presence of a peeling effect compared to test location 1. Locations 2 and 3 show a symmetry in the results. This symmetry can be observed by comparing the two figures of intermediate steps after the NED payload detonation.

For test locations 4 and 5, the NED payload impacts the elevation of the ground at the top end of the crater. These locations also show the same kind of symmetry in simulation results. The location of the initial crater seemed to have moved through the particle distribution relative to the location of the explosion. Particle dispersion seems to be a lot less in these scenarios compared to other scenarios in the same intermediate crater formation time scale.

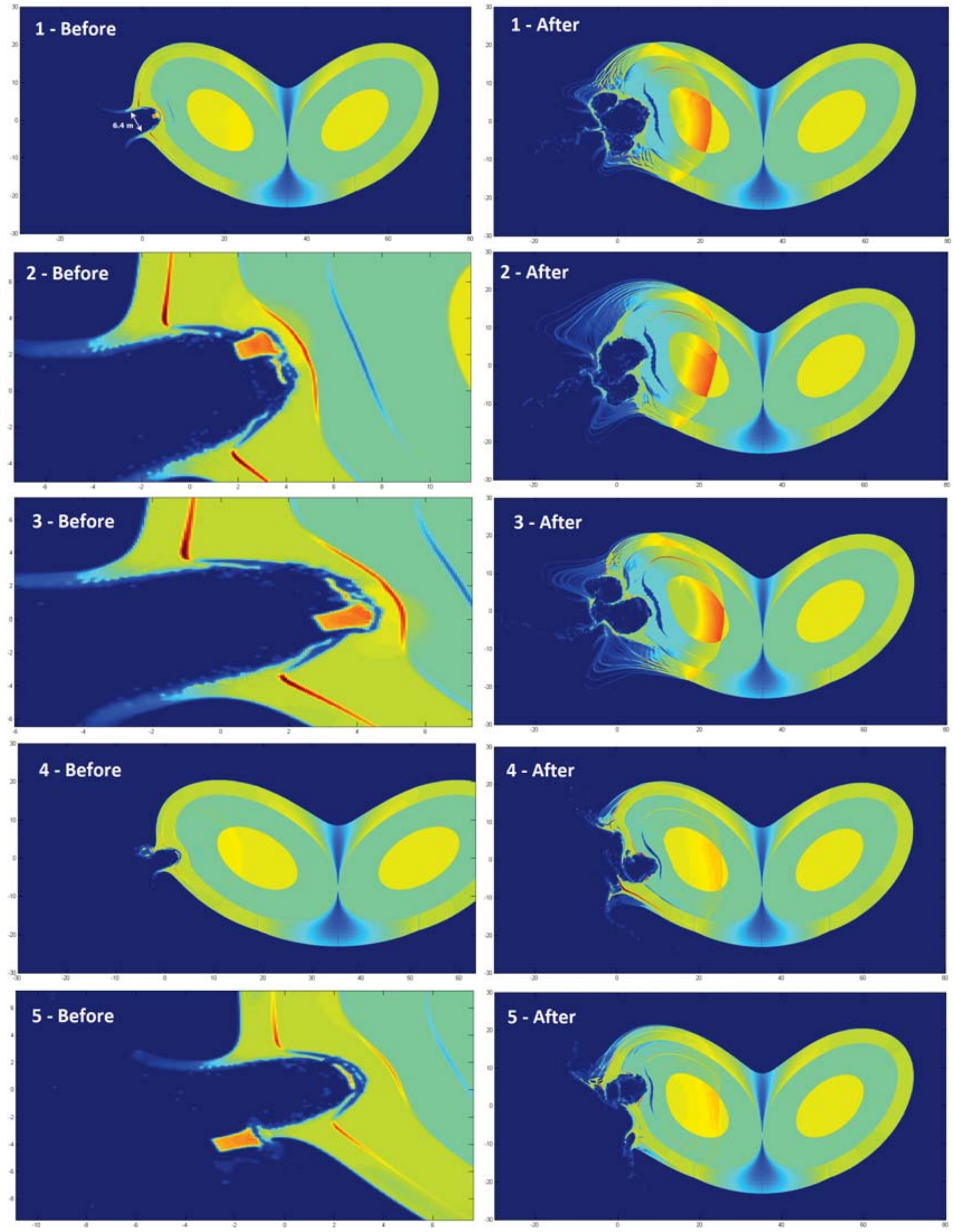

Figure 4.12: Simulation results for various subsurface explosion locations inside a crater [18, 19].

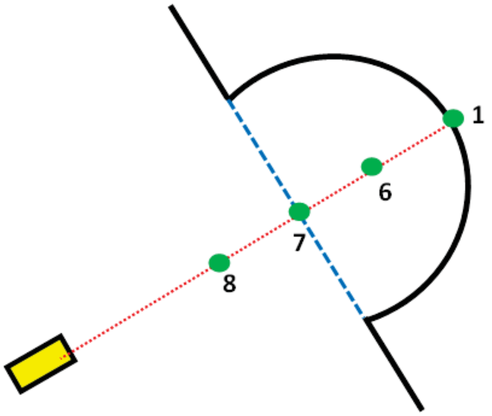

Figure 4.13: Explosion locations for examining the nuclear detonation timing sensitivity.

Other simulations were also conducted to identify which configuration of impactor-NED is more effective. The test considered an initial separation distance of 40 m between an NED payload and the impactor. Figure 4.13 shows possible NED detonation locations. The simulations were run for approximately 0.012 s. The location 1 is the nominal case of detonation at the bottom of the crater formed by the primary kinetic impactor. For the location 6, the NED payload was detonated as the front of the payload intersected with the initial surface height. This location is slightly below the surface at this time. Distance from crater bottom to payload is approximately 7 meters. The test point 7 was located slightly above the current surface line, and the bottom of the crater from the NED payload is about 9.5 m. The final test location 8 is approximately 15.75 m from the bottom of the crater. This case was run for about 10 ms. Before and after detonation images of these four different cases are shown in Fig. 4.14.

4.4.3 GPU-Accelerated Computations

GPU-accelerated computations employed for the HAIV mission study in [17–19] have resulted in orders of magnitude improvement in computational ability. Speed-up of the GPU-accelerated model compared to serial execution for the both target models has been demonstrated. While the 330,000 particles of the target model (Fig. 4.2) are limited mostly by computer communication bandwidth, the 3.1 million particles in the standoff model are limited by computational speed and memory bandwidth for the threads on the GPUs. A substantial speed-up improvement, from 53 to 358 times, is observed. New high-throughput neighbor-finding methods are suggested, using the GPU-acceleration technology of the current simulation tool. The hydrocode simulation models [17–19] employs a tensor relationship for material characteristics and orientation. This allows for more realistic size and shape generation for NEO fragments by treating damage as a local

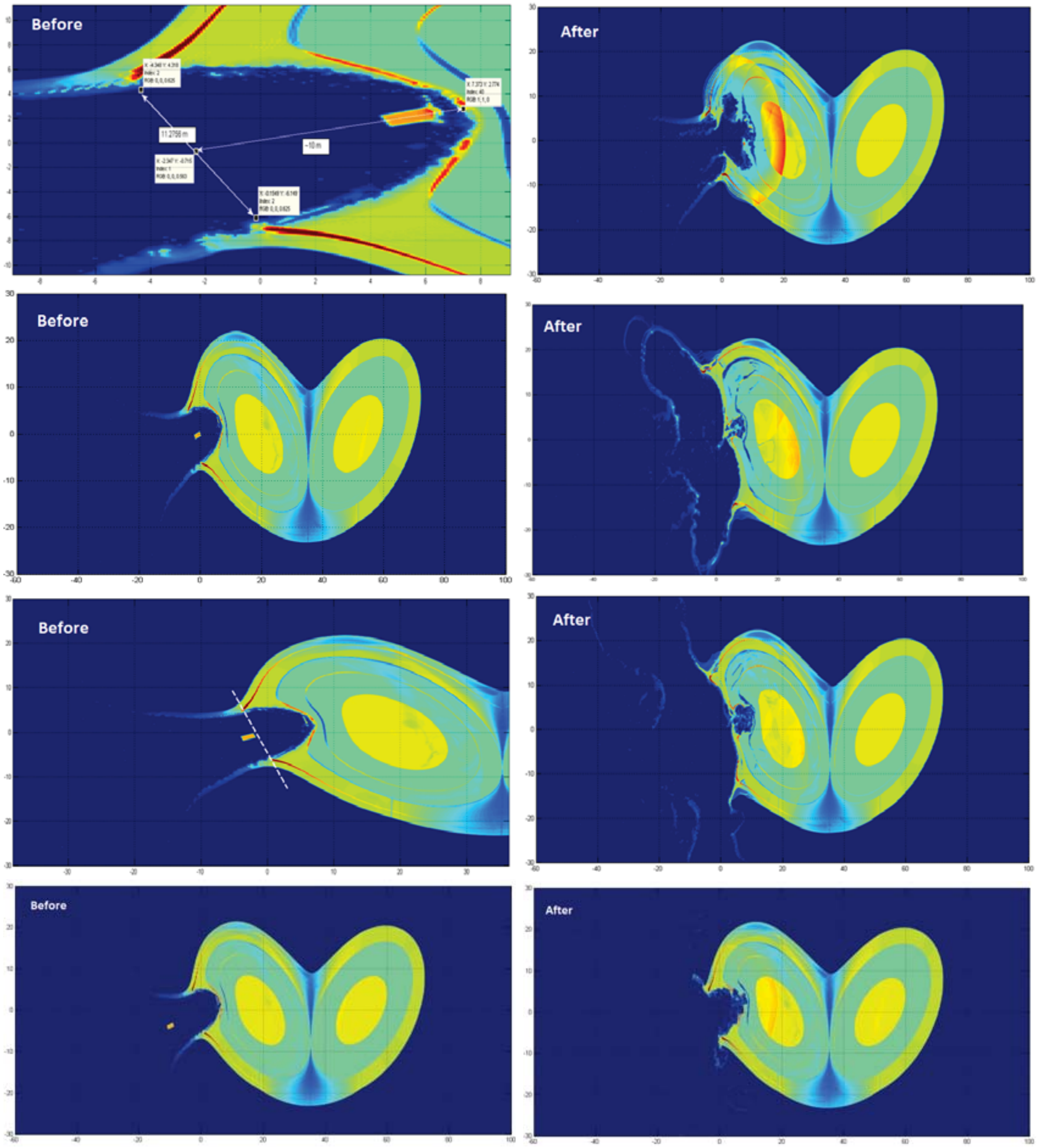

Figure 4.14: Simulation results for examining the nuclear detonation timing sensitivity [18, 19].

quantity (cracks) rather than a distributed state variable. GPU acceleration of the 3D model is up to 200 times on a single workstation, continuing a trend of increasing computational complexity while also increasing efficiency. This approach allows us to compute a range of values rather than monolithic single simulations. GPU technology provides a useful reduction in time-to-solution comparable to 30 similar CPU-only nodes (which would cost $4,000 each) in a $14,000 form factor, showing an 8.6 times improvement in cost-adjusted performance. Since a large amount of data can be processed using GPU simulations, the research work in [17–19] confirms that disruption at different times along a given orbit can have a large effect on the resulting shape of debris. This allows for a more clear set of objectives for HAIV mission design. Another new result is the availability of representative 3D fragment distributions. This will improve the trajectory of the desired hypervelocity intercept mission by allowing full degrees of freedom in choosing the approach asymptote.

4.5 Thermal Shield Analysis and Design

In this section, we briefly discuss the analysis and design of a thermal shield to protect the follower body carrying an NED payload from the heat flux radiated from the superheated particles of the crater. The superheated particles are caused by the initial kinetic collision between the target asteroid and the leading kinetic impactor. A computational procedure is developed to solve this thermal shield design problem with a range of assumptions. The procedure contains the following four steps [55]:

- Step 1 : Predict the temperature distribution of the crater
- Step 2 : Calculate the temperature distribution of the surface of the follower body
- Step 3 : Predict the temperature distribution inside the follower body
- Step 4 : Determine materials suitable to withstand extreme temperatures

4.5.1 Thermal Analysis Procedure

Step 1

For this initial step, a simple algorithm is developed, which utilizes the output from the GPU-accelerated ASPH simulations as well as the direct temperature output obtained using ANSYS Autodyn [21, 22]. Temperatures of all the particles are estimated as a secondary calculation by using the data gathered from an ASPH run. Internal energy E, density ρ and mass m are extracted from the output of ASPH simulations.

Temperature of the i^{th} particle is given by

$$T_{final} = T_{initial} + \frac{\Delta E}{\bar{C}_v} \tag{4.27}$$

where $\bar{C}_v$ is the heat capacity of a constant volume calculated using a weighted average of C_v and the density of asteroid material. Because the simulation assumes the mass to be constant before and after the initial collision, the conservation of mass can be applied as

$$\sum_{i=1}^{n} m_i = \text{Constant} \tag{4.28}$$

The conservation of mass can be rewritten assuming a constant volume V for each particle as

$$\sum_{i=1}^{n} \rho_i V = \sum_{i=1}^{n} m_i \tag{4.29}$$

Therefore, the volume of a particle can be redefined as

$$V = \frac{\sum_{i=1}^{n} m_i}{\sum_{i=1}^{n} \rho_i} \tag{4.30}$$

By using the Einstein equation for solids, we can express C_v for each particle as

$$C_v(i) = 3 N_i k_B \tag{4.31}$$

where k_B is the Boltzmann constant and

$$N_i = \frac{\rho_i V}{M} N_A$$

where M is the molar mass and N_A is the Avogadro's number. Finally, we have

$$\bar{C}_v = \frac{\sum_{i=1}^{n} \rho_i C_v(i)}{\sum_{i=1}^{n} \rho_i} \tag{4.32}$$

Various assumptions need to be made in order to make the calculation process simple and fast. The follower body is assumed to be made out of aluminum. Phase changes that occur in asteroid materials during the initial impact can be ignored. Initial temperatures of all the SPH nodes are set to zero while the temperature changes across the shock wave propagation are also ignored.

A preliminary temperature prediction for the newly generated crater of a 70-m asymmetric asteroid model is provided in Fig. 4.15. Superheated particles are concentrated on the bottom of

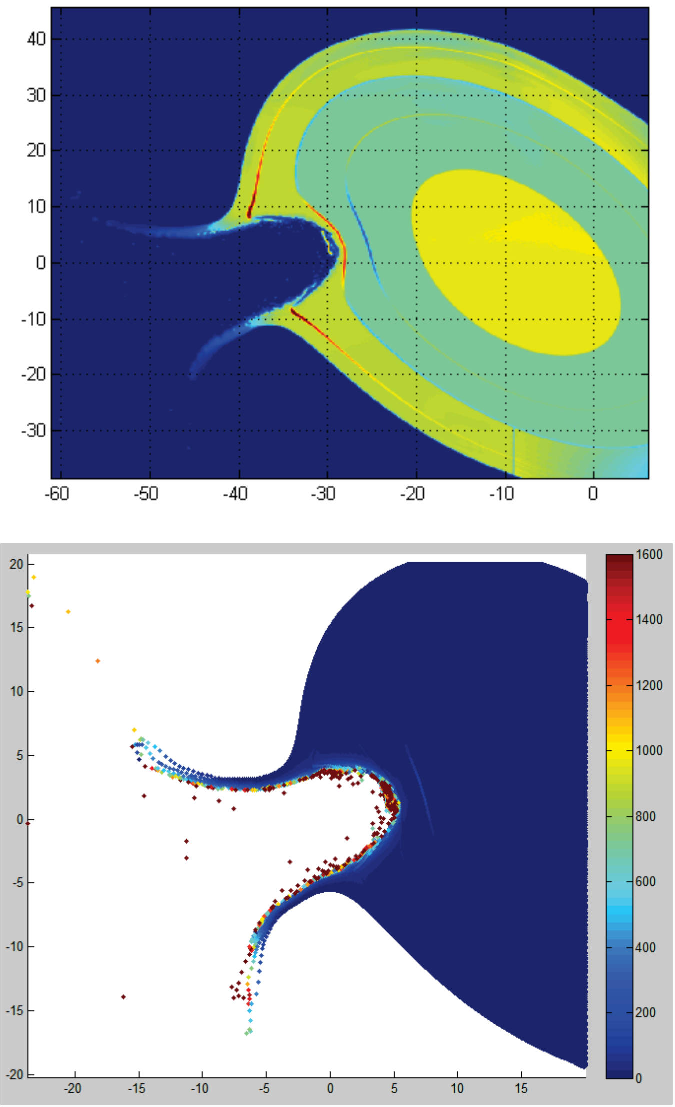

Figure 4.15: Nodal density (top) and temperature distribution in units of Kelvin (bottom).

the crater. They are also present inside the crater traveling at arbitrary directions which could potentially hit and damage the follower spacecraft or melt the NED payload upon contact, if the follower body is not properly protected by the Whipple shield. A special type of hypervelocity impact shield used to protect spacecraft from collisions with micrometeoroids and orbital debris with impact speed range of 3 to 18 km/s is called the Whipple shield.

Step 2

After the crater temperatures have been predicted, the view factors for each side of the follower spacecraft need to be calculated. The view factors are defined as groups of superheated particles in the crater which contributes to the heat flux for each side of the NED payload. A diagram in Fig. 4.16 shows the surface numbering for the spacecraft orientation with respect to the crater.

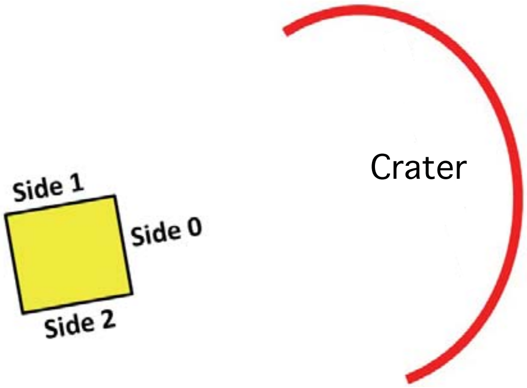

Figure 4.16: Surface numbering for the thermal analysis of a follower spacecraft carrying an NED.

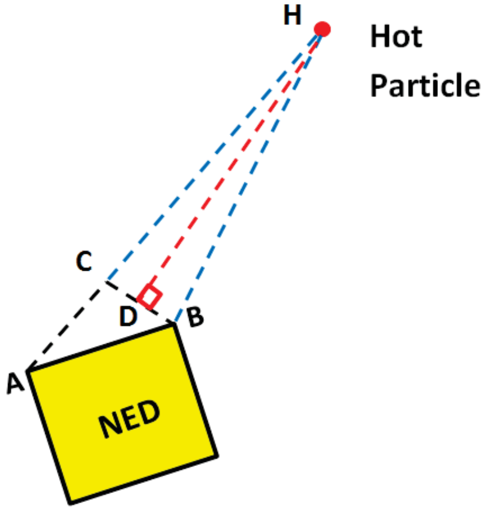

Figure 4.17: Solid angle calculation.

Once the view factors are determined, heat flux calculations can be performed using a steady-state thermal equilibrium assumption. In order to calculate the heat radiated from the crater and the heat absorbed by the aluminum spacecraft, solid angles Ω for each view factor are calculated.

Figure 4.17 illustrates how the heat is radiated to the side 2 of the spacecraft using the solid angle. The solid angle is defined as the angle created between each heated particle and the corresponding side of the follower body.

A 1-m width is assumed for the follower spacecraft. The distances indicated in blue (HC and HB) are equal in magnitude. If the length HD is defined as r and the length BC is defined as ℓ, the solid angle can be calculated as

$$\Omega = \frac{\ell}{r^2} \tag{4.33}$$

The thermal radiation emitted from the heated asteroid material and received by aluminum-walled spacecraft is calculated using the heat radiation transport theory. The temperature of each side of the NED payload is described as

$$\alpha_r \;{}_e\sigma \underset{i=1}{\overset{N}{}} (\Omega_i T_{e,i}^4) = \;{}_r\sigma T_r^4 \tag{4.34}$$

where α_r is the absorption coefficient of the spacecraft material, ${}_e$ is the emissivity of the heat flux emitter (superheated asteroid particles), ${}_r$ is the emissivity of the receiver (spacecraft wall), σ denotes the Stefan-Boltzmann constant, T_e is the temperature of the heat emitting node, T_r is the temperature on the surface of the spacecraft, and N is the number of superheated particles affecting each side of the follower spacecraft.

Step 3

Once the temperatures of the spacecraft walls are estimated for the steady-state condition, this information is fed to a heat diffusion model to evaluate the 2D temperature distribution inside the follower body for a time scale of a 1.0 millisecond assuming the leading impactor and the follower body are separated by a 10 m distance while traveling at 10 km/s. A simple explicit scheme is introduced to solve the thermal diffusion equation of the form

$$\frac{\partial T}{\partial t} - C\nabla^2 T = 0 \tag{4.35}$$

where T is the temperature representing the diffusing property for a material volume and C is the thermal conductivity. Once a Δx discretization and a Δt time step are specified, the stability criterion is given by

$$K = \frac{\alpha \Delta t}{\Delta x^2} \leq \frac{1}{2} \tag{4.36}$$

The explicit finite-difference representation of the discretized 1D equation is given by

$$T_i^{n+1} = T_i^n + K\left(T_{i+1}^n - 2T_i^n + T_{i-1}^n\right) \tag{4.37}$$

where the node index is denoted by i and the current time step is represented by n.

A simple validation is conducted to ensure the accurate implementation of the explicit scheme. The time dependent heat distribution is assumed as [55]:

$$T(x,t) = \sin \;\; \frac{\pi x}{L} \;\; e^{-\alpha\pi^2 t/L^2} \tag{4.38}$$

where L is the total length of the discretized length. Temperatures at $x = 0$ and $x = L$ boundaries are set to zero, while the initial temperature distribution across the length is given by

$$T(x) = \sin \;\; \frac{\pi x}{L} \tag{4.39}$$

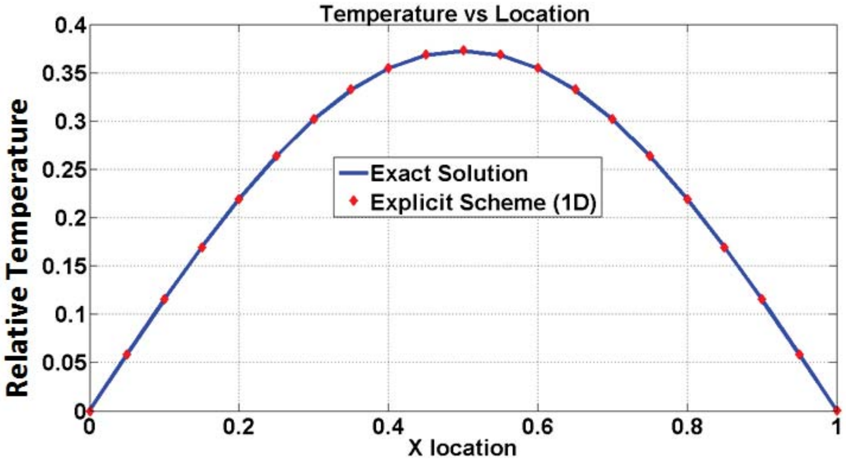

Figure 4.18: Heat diffusion validation result [55].

The constructed explicit scheme is run until $t = 1.0$ s and the results from both exact solution and the explicit scheme are compared in Fig. 4.18.

Figure 4.18 demonstrates the accuracy of implementation of the explicit solver scheme. The explicit scheme is computationally less expensive and stable. However obtaining solutions in high resolution grids requires decreasing the time step for a stable run. In order to increase the accuracy of thermal modeling, the explicit algorithm is extended to a 2D representation in [55], as follows:

$$T_i^{n+1} = T_i^n + K_x \;\; T_{i+1}^n - 2T_i^n + T_{i-1}^n \;\; + K_y \;\; T_{i+1}^n - 2T_i^n + T_{i-1}^n \tag{4.40}$$

where

$$K_x = \frac{\alpha \Delta t}{\Delta x^2} \leq 0.5; \quad K_y = \frac{\alpha \Delta t}{\Delta y^2} \leq 0.5 \tag{4.41}$$

This model is used in the radiation heat transfer algorithm, and the boundary conditions are determined by the temperatures of the outer walls of the follower body.

Step 4

After obtaining the temperature distribution inside the follower body, a thermal protection shield needs to be designed. As an initial step, a list of materials that can withstand extreme temperatures is prepared. Some of the materials identified as potential candidates for heat shields are provided in Table 4.2.

These materials are currently used in many extreme thermal applications ranging from turbine blades to re-entry heat shields where the materials are coated onto surfaces using industrial techniques. These coatings are applied to surfaces via a plasma gun and the ceramics such as Hafnium Oxide are never layered above a metallic layer as it may crack during expansion. The design

Table 4.2: Material properties [55]

Material	Conductivity W/(mK)	Melting point K	Boiling point K
Aluminum	237	933	2,797
Tungsten	173	3,695	5,828
Tantalum	57.5	3,290	5,731
Tantalum carbide	22	4,153	5,053
Graphite	5.7	4,000	4,500
Titanium	21.9	1,941	3,560
Hafnium oxide (ceramic)	23.0	3,030	5,673

requirement for the thermal shield may require a survival time of 1.0 millisecond. The initial iteration of the follower body utilizes a metallic thermal shield which will later be improved with more accurate temperature predictions

4.5.2 Improved Thermal Analysis Procedure

An improved thermal analysis procedure developed in [55] utilizes the temperature output from ANSYS Autodyn. A benchmark test case is constructed and solved using Autodyn where an aluminum impactor collides with a granite spherical target at 10 km/s. The follower vehicle is assumed to have a square cross section with temperature predictions obtained at x = -10.0 m as shown in Fig. 4.19. The initial setup of this test case is illustrated in Fig. 4.19.

View factors are calculated for each side (defined in Fig. 4.16). This determines the amount of superheated particles which affect each side of the follower body. Figure 4.20 shows how each region is defined and the locations of the superheated particles for each side. The temperatures below 1,500 K are omitted because the molten rock temperatures are above 1,500 K.

After obtaining the temperatures of the crater particles and determining particles each side of the follower body see (via view factors), the temperatures on each side are determined. The emissivity and absorptivity of aluminum are assumed as 0.02 and 0.08 respectively. Emissivity of granite is assumed as 0.45. The predicted temperatures are summarized in Table 4.3.

It is evident that Side 0 has the highest temperature as it directly faces the hot surface of the crater. Side 1 and Side 2 have identical temperatures. This is caused by the symmetry of the results and the symmetrical placement of the follower along the flight direction. Sides 1 and 2 experience a lower temperature than Side 0 as the number of particles affecting those sides is significantly lower than the particles affecting Side 0. Based on the temperatures predicted on the surface of the follower body, the temperature diffusion inside the follower body is computed as shown in Fig. 4.21.

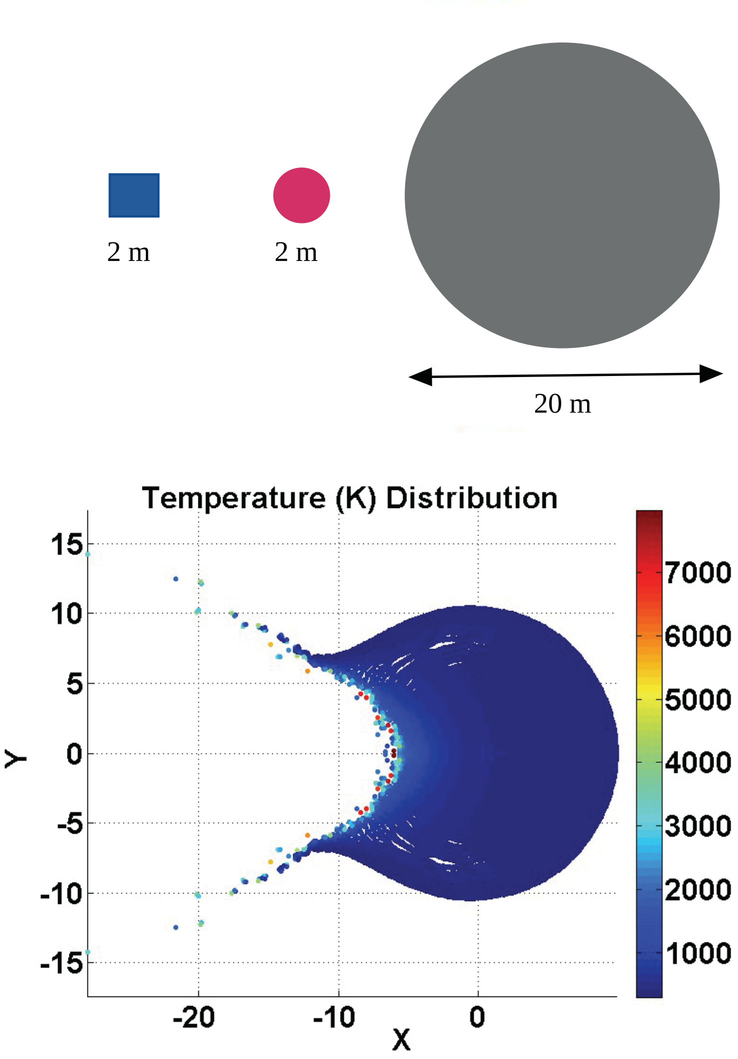

Figure 4.19: Thermal analysis test setup and temperature distribution in units of Kelvin.

According to materials provided in Table 4.2, it is proven that the aluminum wouldn't sustain these high temperatures as the shield reaches melting temperatures. A layer of tungsten is suggested to be sprayed on the aluminum to withstand the extreme temperatures that will be burned off as the follower body travels towards the crater. A 0.2 mm thick tungsten layer is suggested. This adds an additional mass of 50 kg to the mass of the follower body. This mass is subject to change with future research on lighter materials and more accurate temperature approximations.

4.6 Whipple Shield Analysis and Design

The Whipple shield is a special type of hypervelocity impact shield used to protect spacecraft from collisions with orbital debris and micrometeoroids for impact velocities of 3 to 18 km/s. A Whipple shield consists of a relatively thin outer bumper made from metal or composite (Nextel/Kevlar)

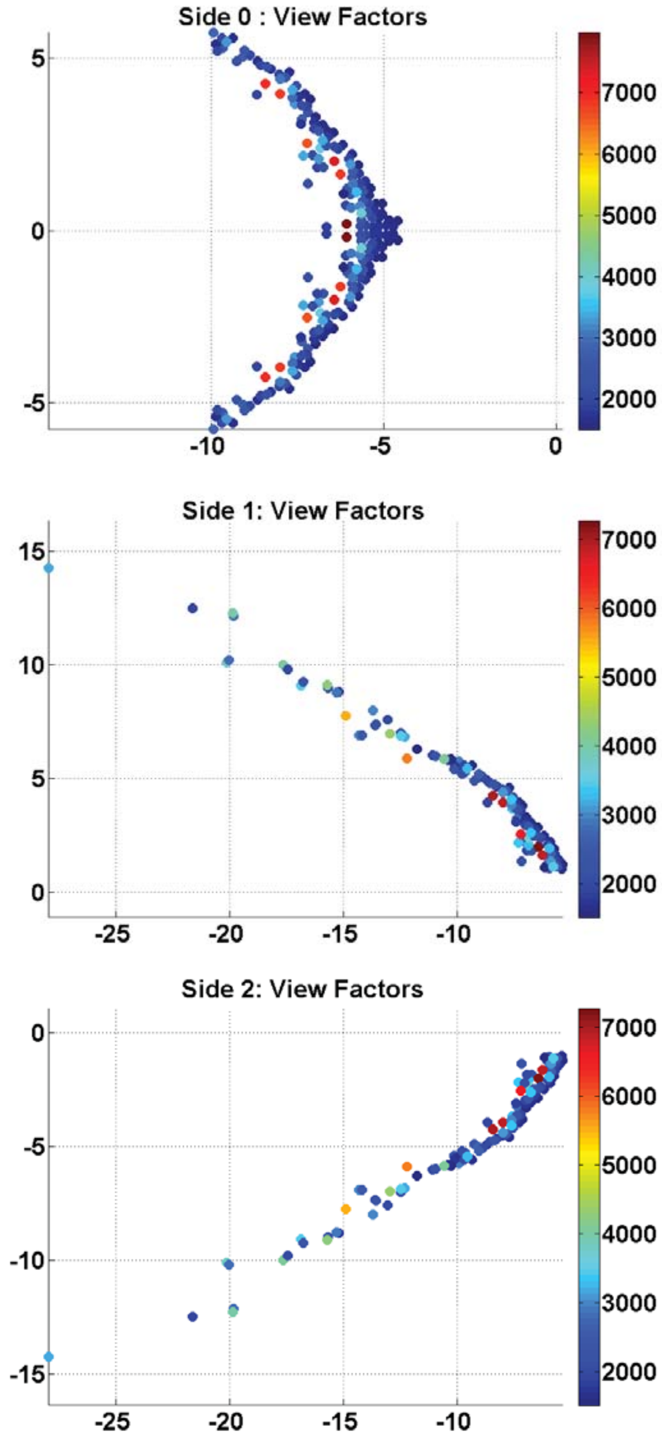

Figure 4.20: View factor calculations for each side of the follower body [55].

Table 4.3: Predicted temperatures of each side

Sides	Temperature (K)
Side 0	9,100
Side 1	6,592
Side 2	6,592

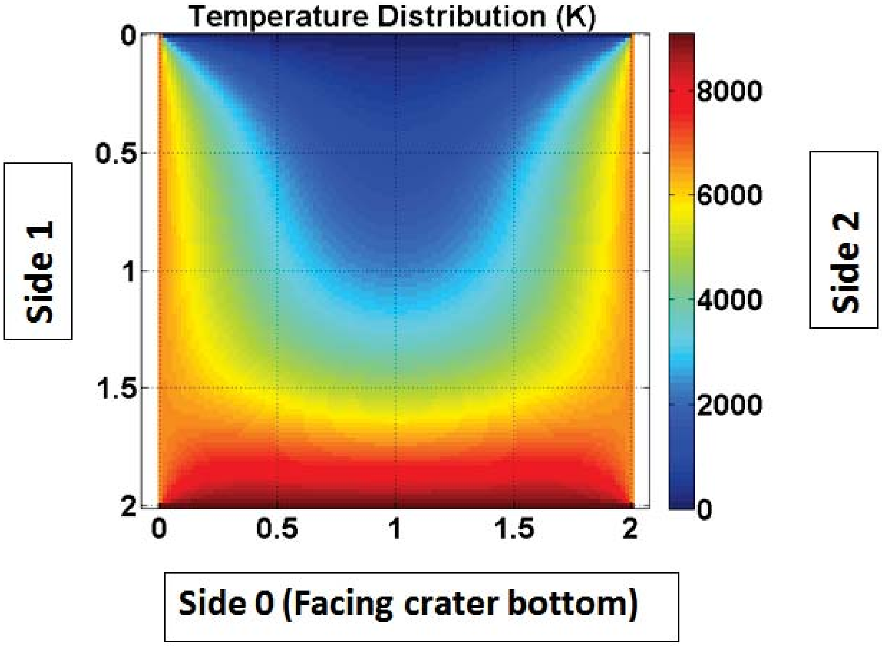

Figure 4.21: Temperature diffusion for an aluminum body [55].

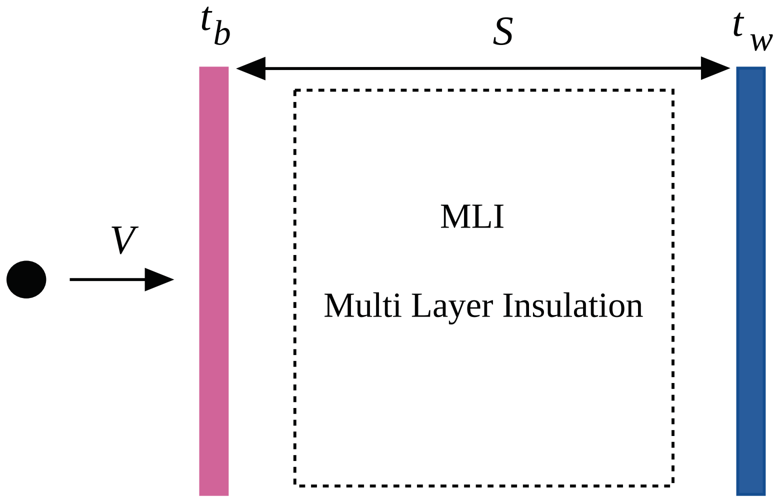

Figure 4.22: Whipple shield simulation setup.

placed some distance away from the inner wall of the spacecraft.

A typical simulation test setup for the Whipple shield is provided in Fig. 4.22. The MLI (Multi Layer Insulation) is often removed from the hypervelocity impact simulation setup. The front bumper shown in red has its thickness of t_b. The bumper comes into contact with meteoroid debris and other particles traveling at hypervelocity speeds. The wall of the spacecraft shown in blue has its thickness of t_w. The distance between the bumper and the wall is denoted by S.

Ballistic limit equations (BLE) define the threshold particle diameter that could cause perforation/spall of the inner wall. These equations do not always provide the correct predictions due to their empirical nature. These equations were constructed via analyzing data from various hypervelocity laboratory tests. The inaccuracies in predictions are caused by material defects, non-homogeneous density distributions and other failure modes. Ballistic limit equations are defined for 3 regions based on a material phase change and failure after the kinetic impact, as follows:

- Ballistic Phase ($V <$ 3.0 km/s): The projectile or the micrometeoroid debris penetrates without breaking into pieces. The maximum particle diameter d_c is described as

$$d_c = {\frac{t_w(\sigma/40)^{0.5} + t_b}{0.6(\cos\theta)^{5/3}\rho_w^{0.5}V^{2/3}}}^{\frac{18}{19}} \tag{4.42}$$

- Shatter Phase (3.0 km/s $< V <$ 7.0 km/s): The projectile breaks and creates an expanding debris cloud upon impacting the front bumper. The maximum particle diameter d_c is described as

$$\begin{aligned} d_c = & {\frac{t_w(\sigma/40)^{0.5} + t_b}{1.248(\cos\theta)^{5/3}\rho_w^{0.5}}}^{\frac{18}{19}}(1.75 - (V\cos\theta)/4) \\ & + [1.071 t_w^{2/3}\rho_P^{-1/3}\rho_b^{-1/9}S^{1/3}(\sigma/70)^{1/3}][(V\cos\theta)/4 - 0.75] \end{aligned} \tag{4.43}$$

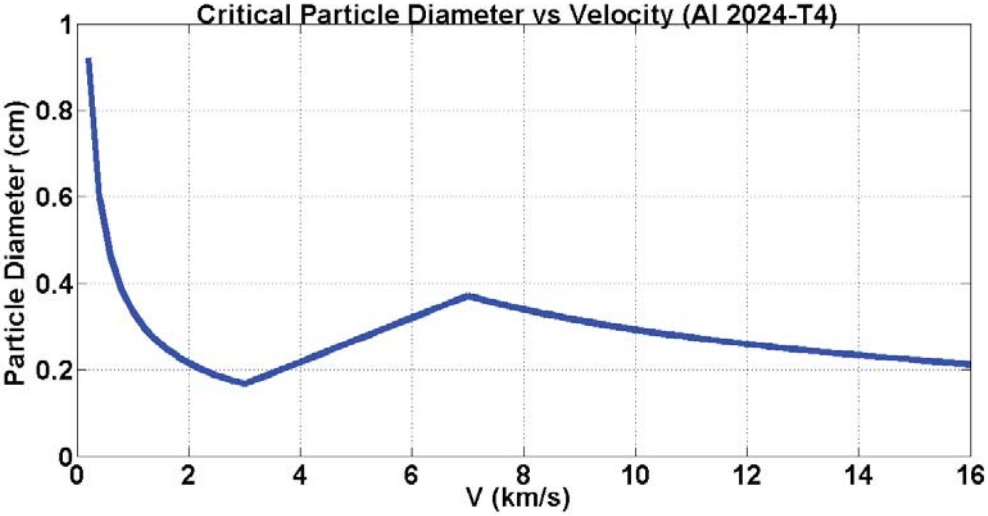

Figure 4.23: BLE curve [55].

- Melting Phase ($V > 7.0$ km/s): As the projectile hits the bumper, both materials will melt and vaporize due to the vast amounts of kinetic energy transfer. The maximum particle diameter d_c is described as

$$d_c = 3.918 t_w^{2/3} {\rho_w}^{-1/3} \rho_b^{-1/9} (V \cos\theta)^{-2/3} S^{1/3} (\sigma/70)^{1/3} \tag{4.44}$$

where ρ_b is the density of the bumper and ρ_w is the density of the wall, and σ is the rear wall yield stress, and θ is the he impact angle measured from an axis normal to the bumper shield. These equations were developed by the Hypervelocity Impact Technology Group at NASA Johnson Space Center.

A sample BLE curve is shown in Fig. 4.23 for a wall thickness of 0.16 cm and a bumper thickness of 0.16 cm. The shield is assumed to be constructed of aluminum alloy which has a yield stress of 37,000 psi. The separation between the wall and the bumper is 12.0 cm.

Figure 4.23 clearly indicates different traits for different velocity regions. The velocity region between 3 km/s and 7 km/s is seen to be linear. In an actual Whipple shield design process, this curve is used to make the following predictions:

- If the diameter of the debris (assuming spherical debris) exceeds the critical diameter for a given impact velocity V, this results in rear wall perforation.

- If the diameter of the debris is below the critical limit for a given impact velocity V, this ensures the safety of the rear wall (spacecraft wall). No material loss will be predicted.

To observe the trends in the BLE curves with varying parameters, the original wall thickness t_w is doubled and tripled. Increasing the wall thickness improves the structural integrity of the

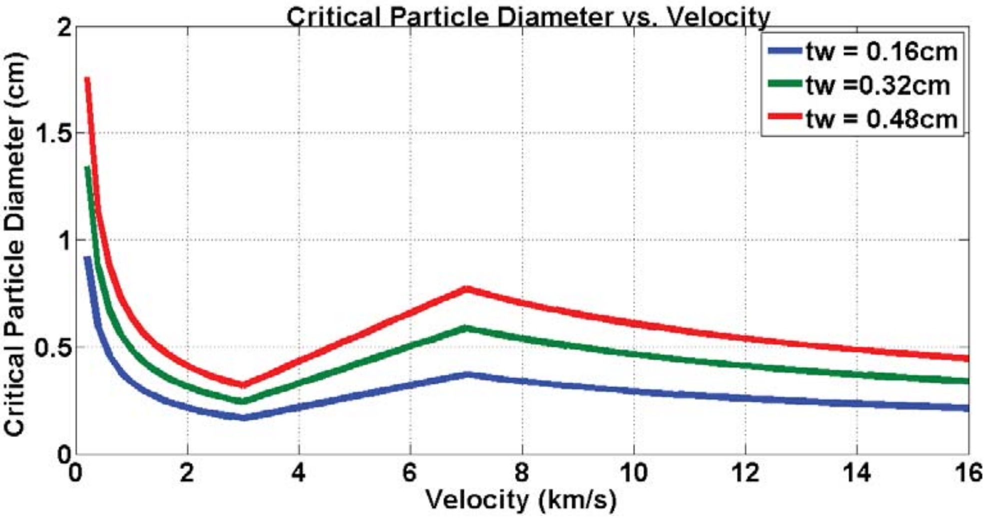

Figure 4.24: BLE curves for different wall thickness comparison [55].

spacecraft wall as fast moving debris has to penetrate more layers of the material. Therefore, an increase in critical particle diameter is bound to occur for each velocity. Figure 4.24 depicts change in critical diameter for different thicknesses (0.16, 0.32, 0.48 cm) of the rear wall. Critical diameter curves seem to have shifted upwards as the wall thickness increases. This qualitative trend validates the relationship between critical particle diameter (for a given velocity) requirement and the spacecraft wall thickness.

In order to utilize Autodyn 2D for the Whipple shield design, some results available in the literature are re-examined in [55]. The input parameters include a shock equation of state followed by strength modeling done using the Johnson-Cook strength model. The axial symmetry solver is used in this case to generate the results. A qualitative comparison is performed for solutions obtained at different times during the progression of the solution. The projectile has an impact velocity of 3.1 km/s colliding normally to the bumper shield. The bumper thickness is set to 2.0 mm. Both the bumper and the projectile are modeled using the SPH method which is also later coupled with a finite element approach that represents the spacecraft wall. The spacecraft wall is 10.0 mm thick and located 200 mm away from the bumper shield. The bumper and the rear wall are made out of Al 2024 while the projectile is constructed out of Al 1100. The input for the equation of state is given in Table 4.4 and Table 4.5.

A principal stress failure model is also incorporated with max tensile stress of 2.5 GPa and 1.0 GPa for Al 2024 and Al 1100, respectively. An erosion option is also turned on to counter any cell degeneration that exceeds an instantaneous geometric strain of 1.0. The rear wall has a fixed boundary condition at 73 mm from the radial locations. A set of qualitative solutions obtained during specific time instances are shown in Figs. 4.25 and 4.26.

Table 4.4: Shock EOS (Al-2024 and Al-1100) [55]

Parameters	Units	Values
Density (Al-2024/Al-1100)	kg/m^3	2785/2701
Bulk sound Speed	km/s	53.258
γ_0	Gruneisen coefficient	0.5
Particle shock velocity slope	N/A	1.338
Specific heat capacity	J kg^{-1}K^{-1}	875

Table 4.5: Johnson-Cook (Al-2024 and Al-1100) [55]

Parameters	Units	Values
Yield stress	GPa	0.265
Shear modulus	GPa	27.6
Hardening constant	GPa	0.426
Hardening exponent	N/A	0.34
Strain rate constant	N/A	0.015
Thermal exponent	N/A	1.0
Melting temperature	K	775

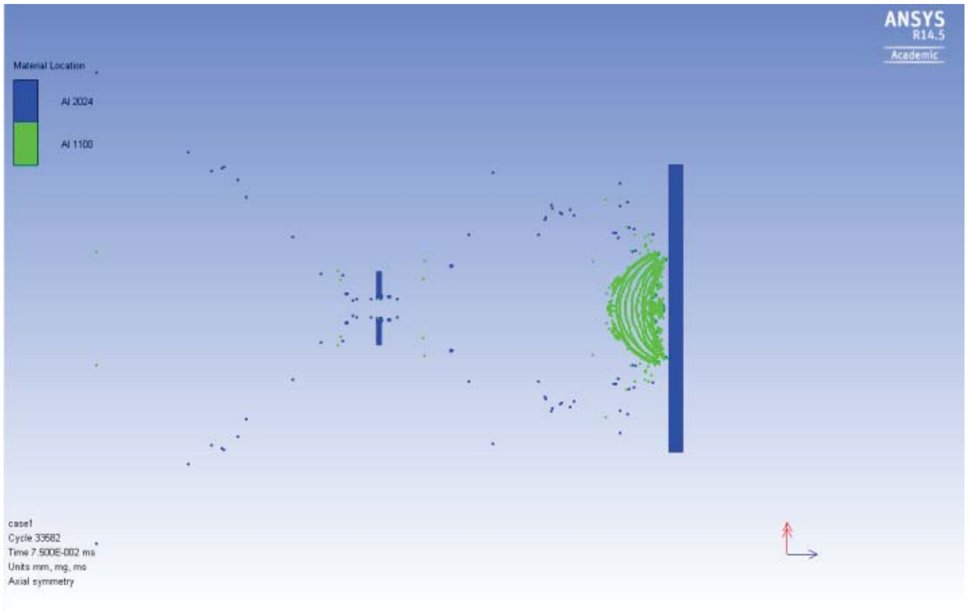

Figure 4.25: Nodal displacement 75μs [55].

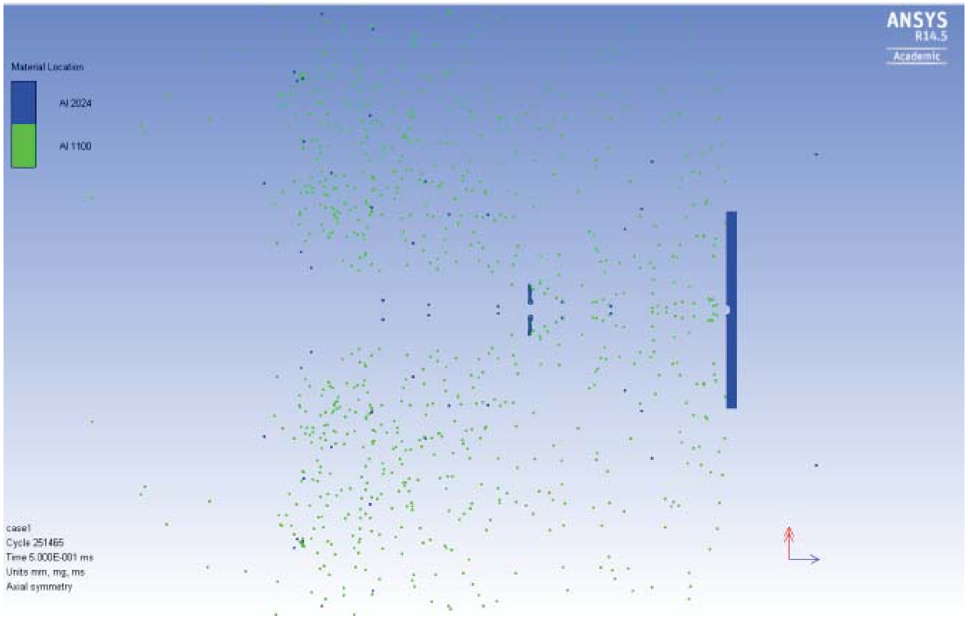

Figure 4.26: Nodal displacement 500μs [55].

In a qualitative comparison to the results presented in the literature, the Autodyn solutions show identical dispersion patterns. Both solutions suggest successful operation of the Whipple shield as the inner wall only got slightly dented by the impact. Slight changes in the debris cloud can be observed along with changes in deformation. These could be due to certain modifications the Autodyn solver underwent in the span of 10+ years since the recorded simulation.

The initial location of the impactor was not recorded in the literature work so I placed it 1 mm away from the bumper assuming the initial analyst tried to keep it close as possible to the bumper to avoid unnecessary simulation time. Geometrical trends observed in the debris cloud and the plate deformations seem to be accurate. Results were mirrored along x axis to obtain the axisymmetric solution of the simulation.

A series of test cases are simulated in order to validate the methodology developed in [55] using using Autodyn 2D and PAMSHOCK 3D. The complete test scenario is modeled by using the SPH method for Autodyn 2D and the PAMSHOCK model contained a rear wall that is modeled in FEM. A 3D Lagrangian-Lagrangian coupled system, which consists of a projectile that is modeled in SPH and two walls that obey solid mechanics in a FEM framework, is used in [55]. A shock EOS along with Johnson-Cook strength model is used in all these cases utilizing Al-2024 alloy for the bumper, wall and the projectile. Anticipated perforation results are tabulated in Table 4.6.

Perforation of the Whipple shield is denoted by ”P” and the No Perforation is denoted by ”NP” in column 6 of Table 4.6. These cases were run with axisymmetric solver. Each case consisted of a projectile and a bumper shield modeled in SPH along with a rear wall that is captured by a

Table 4.6: Whipple shield validation results [55]

Test No.	Velocity (km/s)	Projectile (mm)	t_b (mm)	t_w (mm)	Expected Result
EMI 19.0	3.31	5.0	1.6	3.2	NP
EMI 20.1	5.5	5.0	1.6	3.2	NP
EMI 21.0	7.2	5.0	1.6	3.2	NP
EMI 71.0	5.1	8.0	1.6	3.2	P

Lagrangian grid. Cells in the Lagrangian grid were set to deteriorate for a given effective plane strain. Qualitative results are shown in Fig. 4.27.

The cases seem to be producing the anticipated results. EMI 19, 20.1 and 21.0 have shown no perforation while EMI 71 is showing clear perforation. Even though the results accurately predict the perforation of a given case, it does not match up with the images provided in literature. This may be due to changes in the solver and different material parameters and options the authors have used in the process that were undocumented. These cases will be re-run in future to determine possible causes.

The Whipple shield of the HAIV may be constructed out of aluminum due to its strength. The Whipple shield will protect the spacecraft from debris traveling up to 10 km/s. The maximum diameter of the debris should be 5 mm. Once an algorithm that predicts the debris size is developed, a better estimation of the bumper and wall thickness required to protect the follower body can be obtained.

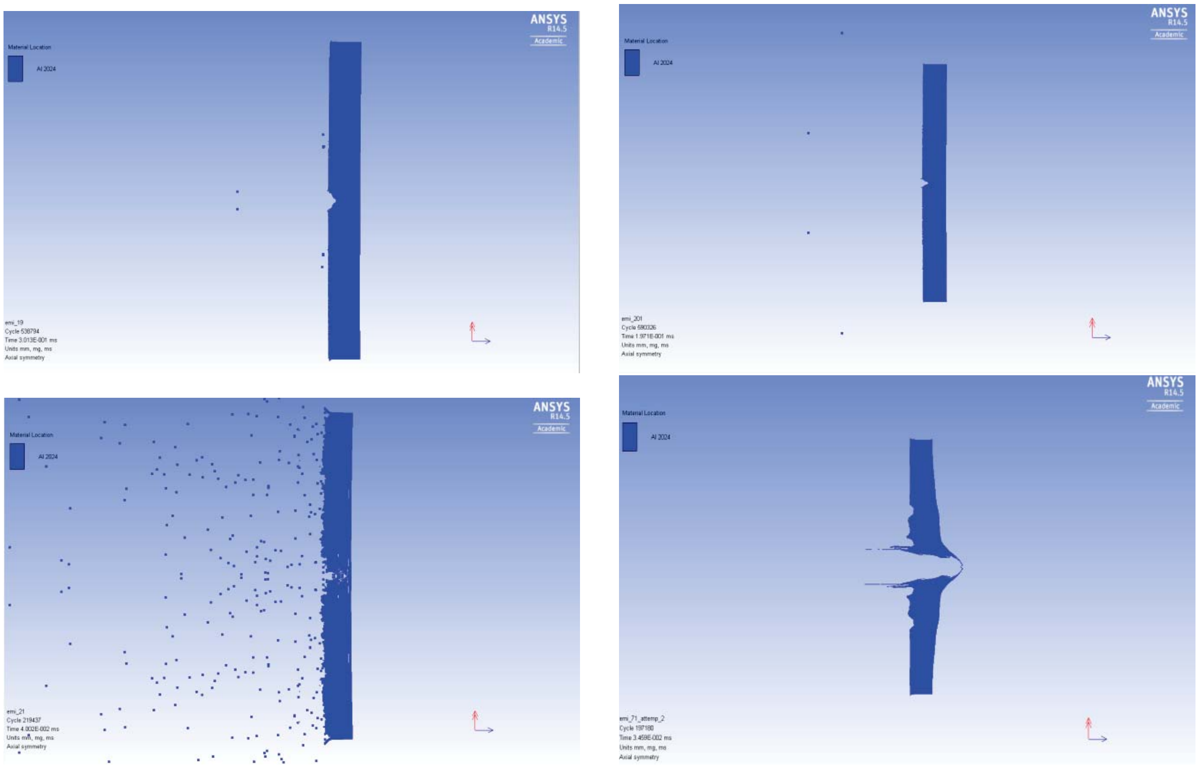

Figure 4.27: Preliminary simulation results of the Whipple shield for the HAIV mission study [55].

Chapter 5

Suborbital Intercept and Disruption of NEOs

In this chapter, we consider the HAIV (Hypervelocity Asteroid Intercept Vehicle) mission concept as applied to a probable worst-case situation for which a very late suborbital intercept/disruption mission becomes inevitable [59, 60]. The HAIV carries a nuclear explosive device for the purpose of optimally disrupting a target near-Earth object (NEO) into a very large number of small fragments. It is emphasized that an earlier interplanetary intercept/disruption, rather than a late suborbital intercept/disruption, should be preferred whenever possible, provided that we could have an earlier alert ($>$ 1 month) and an interplanetary launch vehicle that can be launched with a very short notice [61]. This chapter presents the initial conceptual consideration of suborbital intercept and disruption of small NEOs with very short warning times ($<$ 1 day). In such ultra-short warning time situations, when we don't have sufficient mission lead time to achieve large orbital dispersion of NEO fragments, full neutralization of the NEO impact threat is infeasible because most of the fragments will still strike Earth. However, if the NEO is fractured or fragmented into sufficiently small pieces prior to reaching Earth's atmosphere, each of those small pieces will break up sooner and the resulting airbursts will occur at safer (higher) altitudes. Thus, the objective of a suborbital NEO intercept and fragmentation mission is to reduce the probable impact damage of a Tunguska-like event (caused by $\sim$50 m NEO) to be no greater than the damage level of several Chelyabinsk-like events.

5.1 Introduction

Small NEOs (approximately 50–150 m in diameter) are far more numerous than larger NEOs. There are hundreds of thousands to millions of such small NEOs yet to be discovered [32]. Small NEOs, which are mostly asteroids rather than comets, are very faint in the night sky due to their small sizes, and are, therefore, difficult to discover far in advance of Earth impact. Furthermore, even small NEOs are capable of creating explosions with energies on the order of tens or hundreds of megatons.

One aspect of an initial conceptual study described in this chapter was to consider the development of incoming NEO response timelines, with an emphasis on assessing the minimum amount of warning for which a planetary defense mission could credibly be made ready and launched to intercept the target NEO. In this chapter, we consider ultra-short warning scenarios for which the incoming NEO is not detected until less than 24 hours before its Earth impact. The purpose of considering such an incredibly short warning times is to establish a lower bound for the warning time through investigation of such highly worst-case yet probable situations.

Such ultra-short warning scenarios are, in fact, realistic situations that will likely have to be dealt with in practice. At present we have no space-based NEO survey telescopes, despite the fact that scientists and engineers in the NEO community have repeatedly articulated the need for one [32]. The Jet Propulsion Laboratory (JPL) has proposed its NEOCam concept, while the B612 foundation is attempting to fund the development of its space-based Sentinel telescope spacecraft with private donations. A new ground-based telescope system, the Asteroid Terrestrial-impact Last Alert System (ATLAS), is currently under development and is scheduled to commence full-scale operations in early 2016. ATLAS should be able to provide approximately 3 weeks of warning for an incoming 140 m NEO, and 2 days of warning for an incoming 10 m NEO [62].

With only ground-based observation capabilities, we cannot observe NEOs in the sunward direction and are therefore blind to NEOs on such approach trajectories. This was demonstrated spectacularly by the impact and detonation of a $\sim$20 m NEO approximately 30 km above the city of Chelyabinsk in Russia on February 15, 2013. There was no warning of the NEO's approach, and its airburst detonation released approximately 500 kt of energy. The resulting shock wave shattered windows throughout the city, collapsed some building roofs, and injured approximately 1,500 people. Prior to this event, the NEO 2008 TC_3 was the first to be detected prior colliding with Earth. The approximately 4 m size NEO was detected approximately 20 hours before impacting the Earth and exploding high in the atmosphere over Sudan. The only other instance of a NEO being detected prior to Earth impact is the NEO designated 2014 AA, an approximately 2–4 m object that entered Earth's atmosphere approximately 21 hours after being discovered on January 1, 2014. Earth is typically struck by NEOs several meters in size a few times each year.

Even when NEOs are not approaching from the sunward direction, small NEOs (being very faint in the night sky due to their small size) are difficult to detect and so we may, therefore, have relatively little warning of the approach of a small NEO that is still sizable enough to cause damage to people and infrastructure on Earth's surface. Small ($<$ 150 m diameter) NEOs are far more numerous than larger NEOs, and so one of the most likely NEO threats we face is that posed by a 50–150 m diameter NEO on an Earth-impacting trajectory that is not detected until shortly (hours, days, or perhaps a few months) before Earth impact. The aforementioned Chelyabinsk impactor was only 18 m in diameter but delivered approximately 500 kt of energy. It detonated relatively high above the ground because of its very shallow atmospheric entry angle, but if it had entered at a steeper angle, the damage to the ground would have been much worse. Under some general assumptions for NEO density, impact velocity, impact angle, and atmospheric entry behavior, NEOs 20–85 m in diameter are expected to create 230 kt to 28 Mt airbursts, and NEOs 100–150 m in diameter are expected to impact the ground with energies between 47 and 159 Mt [63].

In this chapter we focus on a hypothetical assessment of what could be done to act against incoming NEOs with only a few hours or a few days of warning time, from the viewpoints of intercept trajectory design and launch vehicle payload capabilities. Current anti-ballistic missile (ABM) technology could be adapted for use against NEOs. The United States has deployed Ground Based Interceptor (GBI) missiles that are launched from silos and can intercept an enemy missile in the midcourse phase of flight with an Exoatmospheric Kill Vehicle (EKV) interceptor. SM-3 missiles have a similar capability and are designed to be launched from ships. The higher altitude and larger payload requirements for a suborbital NEO intercept are beyond current GBI missiles.

However, Intercontinental Ballistic Missiles (ICBMs), such as the Minuteman III, do have adequate launch mass capability. It is assumed that the Minuteman III based interceptor will be able to deliver a HAIV payload (described in Section 19.2) into a precision intercept trajectory against an incoming NEO. It is also assumed that the precision terminal intercept guidance will be provided by the HAIV itself (similar to the combined GBI/EKV system). In this chapter we will explore the performance of notional upgraded ICBMs to launch a HAIV system carrying a nuclear explosive device to intercept and disrupt a hypothetical incoming NEO at high altitudes (generally at least 2,500 km above Earth). It will be shown that suborbital NEO intercepts using Minuteman III or SM-3 IIA launch vehicles could achieve NEO intercept a few minutes prior to when the NEO would strike Earth. Any side effects caused by a nuclear explosion at an altitude of 2,500 km or higher as well as the rapid launch readiness of existing or upgraded ICBMs for a suborbital asteroid intercept with short warning times (e.g., 1 to 24 hrs) will need to be further studied.

5.2 An Optimum Suborbital Intercept Problem and Its Solutions

5.2.1 Problem Formulation

It is assumed that a NEO is on a hyperbolic approach trajectory with respect to the Earth. For a given hyperbolic NEO trajectory that intersects the Earth and a fixed launch site on Earth, the goal is to determine the optimal suborbital intercept trajectory. The performance of the missile is limited to its available total ΔV. The criterion for optimal intercept is defined as the maximum altitude of intercept from a fixed launch position on Earth. Because the NEO is on a hyperbolic Earth encounter trajectory, maximum altitude is equivalent to earliest intercept.

The NEO trajectory, interceptor trajectory, and positions on Earth's surface (of launch sites) are defined with respect to the ECI (Earth-Centered Inertial) reference frame, as shown in Fig. 5.1(a). The time, distance, and speed units used here are seconds (s), km, and km/s, respectively. For nomenclature purposes, a subscript T refers to the target NEO, and a subscript M refers to the interceptor missile.

The preliminary conceptual NEO intercept study conducted in [59,60] consists of the following assumptions:

- Orbital elements of the target NEO at acquisition are assumed to be exactly known;
- The interceptor missile begins its flight from a few known locations on Earth's surface (defined by longitude and latitude relative to the ECI frame);
- Each interceptor missile's performance is simply characterized by its available total ΔV;
- The Earth is assumed to be a rotating sphere with negligible atmosphere;
- Each missile launches from Earth's surface with a single impulse;
- Restricted two-body orbital dynamics are assumed.

For more rigorous intercept trajectory analysis and design, a multi-stage rocket model should be used. The burn time of an ideal optimal problem considered in [59, 60] is about 187 seconds while the total time of flight is 1,394 seconds.

Because the vectors are defined with respect to the ECI frame, it is not necessary to correlate the problem to a specific sidereal time. Instead, we assume that the prime meridian is aligned with the vernal equinox direction at the moment of interceptor launch. This makes it convenient to map

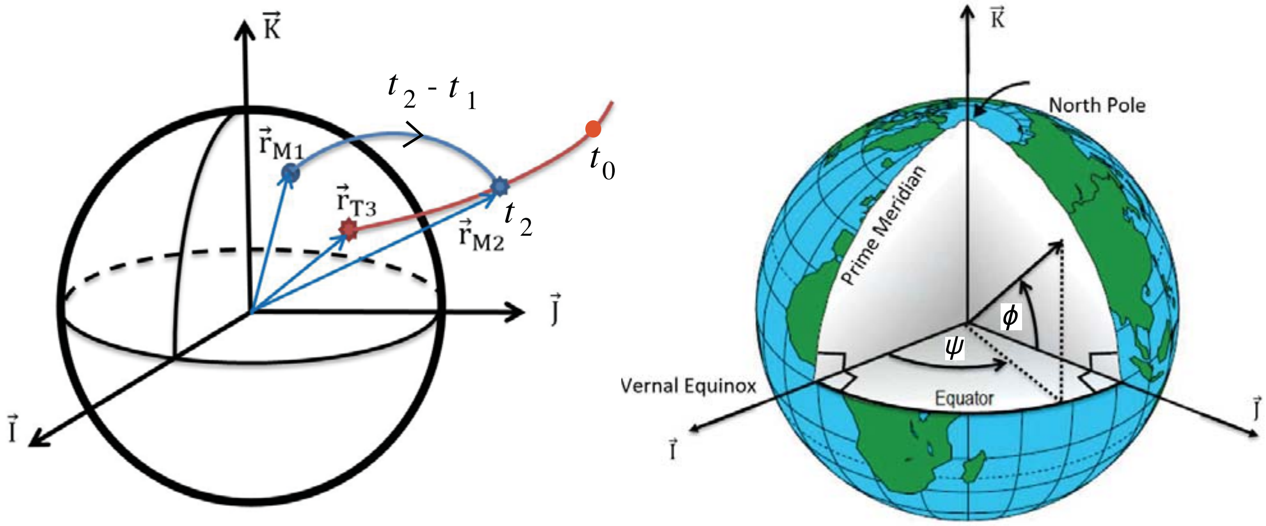

(a) ECI reference frame. (b) Earth's surface relative to ECI frame.

Figure 5.1: ECI reference frame [59, 60].

Table 5.1: Nomenclature for the key mission event time

Symbols	Definition
t_0	Time of target detection
t_1	Time of missile launch
t_2	Time of NEO intercept
t_3	Time of Earth impact
$t_2 - t_1$	Time of flight (TOF)
$t_3 - t_2$	Intercept-to-impact time (IIT)

the surface longitude to the ECI frame without having to calculate sidereal time. Figure 5.1(b) shows the orientation of the Earth's surface with respect to the ECI frame. The position vector of the Earth's surface is expressed as

$$\vec{r} = R_{\oplus}(\cos\psi\cos\phi\vec{I} + \sin\psi\cos\phi\vec{J} + \sin\phi\vec{K}) \tag{5.1}$$

where ψ is the longitude, ϕ is the latitude, $R_{\oplus}$ = 6,378.15 km is the radius of the Earth, and ($\vec{I}$, $\vec{J}$, $\vec{K}$) comprise a set of orthonormal basis vectors of the ECI frame.

The NEO intercept mission formulation can be considered to be independent of time. The timing of the major events such as target acquisition, missile launch, and intercept are all relative to an arbitrary time of impact. Each point in time is measured in seconds until impact. The times are identified using subscripts as described in Table 5.1.

A Fictional Target Trajectory

The NEO's trajectory, hyperbolic with respect to the Earth, is defined in terms of the geocentric orbital elements at the time of acquisition (i.e., when the NEO is detected and its state is known). The acquisition time is arbitrary for this problem, but we assume that at the time of acquisition the NEO is beyond the range of any missile but inside the Earth's gravitational sphere of influence ($\sim$1,000,000 km). For the example problem considered in [59,60], the target NEO orbit is designed such that it impacts the east coast of the United States with an incidence angle of 53.73° (measured from vertical) and an impact velocity of 14.933 km/s; these values are typical for Earth-impacting NEOs.

Orbital Trajectory Models

The interceptor missile and the NEO are treated as point masses for which the governing dynamics are simply given by

$$\dot{\vec{r}} = \vec{V} \tag{5.2}$$

$$\dot{\vec{V}} = -\frac{\mu \vec{r}}{r^3} \tag{5.3}$$

where $\vec{r}$ and $\vec{V}$ are the position and velocity vectors of the point mass, and μ is the gravitational parameter of Earth (3.986×10^5 km^3/s^2). The position and velocity are related to the semimajor axis of the orbit through the vis-viva equation and the equation of orbit, as

$$\frac{V^2}{2} - \frac{\mu}{r} = -\frac{\mu}{2a} \tag{5.4}$$

$$r = \frac{a(1-e^2)}{1 + e\cos\theta} \tag{5.5}$$

where a is the semimajor axis, e is the eccentricity, and θ is the true anomaly.

Optimization

The optimal suborbital intercept of a NEO from a fixed launch site is found by maximizing the altitude of intercept. The higher intercept altitude will minimize any effects on Earth due to the nuclear explosion and give fragments more time to disperse. The optimal orbit will utilize the full ΔV available to the missile, and account for the additional speed provided by the Earth's rotation. There are only two free variables that determine the suborbital trajectory: the intercept-to-impact time (IIT), $t_3 - t_2$ and the time-of-flight (TOF), $t_2 - t_1$ of the missile. It will be shown that there is a unique optimal solution for typical intercept scenarios.

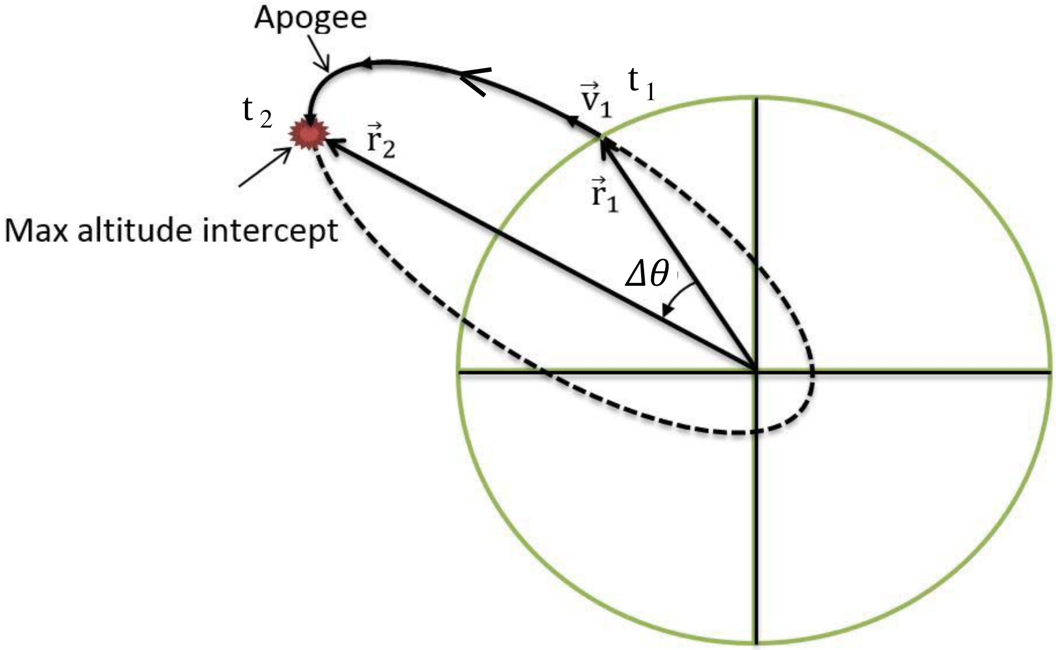

Figure 5.2: Optimal intercept orbital geometry [59, 60].

Accounting for the Rotation of Earth

The Earth's eastward rotation essentially provides a ΔV boost to the interceptor, allowing it to reach a higher altitude. The speed at the equator is estimated as

$$V_E = \frac{2\pi R}{24 \times 3,600} = 0.4638 \text{ km/s} \tag{5.6}$$

The speed of the Earth's surface in the ECI frame is dependent only on the latitude and longitude of the launch site. The inertial velocity vector of the launch site, $\vec{V}_L$ is the found as

$$\vec{V}_L = V_E(-\sin\psi\cos\phi\vec{I} + \cos\psi\cos\phi\vec{J}) \tag{5.7}$$

The velocity vector due to rotation at the launch site, $\vec{V}_L$, is added to the burn-out velocity vector of the booster, $\vec{V}_{bo}$, to obtain the initial velocity vector of the interceptor missile, $\vec{V}_1$, as

$$\vec{V}_1 = \vec{V}_{bo} + \vec{V}_L \tag{5.8}$$

Determining Target NEO Position and Velocity as a Function of Time

The position of the NEO in the ECI frame must be known at any given point in time. From the orbital elements of the NEO at the acquisition point, the initial perifocal frame position and velocity vectors, $\vec{r}_1$ and $\vec{v}_1$, are calculated and transformed into the ECI frame. For a given time-of-flight

(TOF) of the NEO, the position at that time can be found by solving Kepler's hyperbolic TOF equation of the form

$$\text{TOF} = t_2 - t_1 = \sqrt{-\frac{a^3}{\mu}}\left[(e\sinh H_1 - H_1) - (e\sinh H_2 - H_2)\right] \tag{5.9}$$

where H is the hyperbolic eccentric anomaly related to the true anomaly (θ) as

$$\tanh\frac{H_i}{2} = \sqrt{\frac{e-1}{e+1}}\tan\frac{\theta_i}{2} \tag{5.10}$$

Using the known positions of the launch site and the NEO at a given time t_2 (the time of intercept), along with the missile TOF, the required initial velocity vector for the missile can be found by solving Lambert's problem discussed in Chapter 16.

5.2.2 Intercept Trajectory Optimization

The solver used to find the optimal solution is the `fmincon` function available in the MATLAB Optimization Toolbox. The `fmincon` is a constrained nonlinear multivariable minimization routine. There are two independent variables involved: the TOF and the intercept-to-impact (IIT). Both variables are given upper and lower bounds to keep the solver from testing unreasonable points. An interior set point is chosen within the search window as the starting point. A constraint is placed on the solution such that the required ΔV is not permitted to exceed the maximum ΔV available to the missile. The NEO's altitude decreases monotonically with time because the NEO is on a hyperbolic trajectory with respect to the Earth. Thus, maximizing IIT is equivalent to maximizing intercept altitude. A graphical representation of an example search window is presented in Fig. 5.3. Each of the contours is a line of constant ΔV required for intercept. For each ΔV curve, there is one TOF at which TOI is a maximum. This is the unique solution point for the ΔV at which intercept altitude is maximized. The locus of the optimal altitude intercepts is shown on the graph, as well as the set of intercepts for which the interceptor reaches the target NEO at apogee. It is interesting to note that the optimal intercept solution follows a nearly linear trend.

5.2.3 Suborbital Intercept Examples

Several example intercept scenarios and solutions are presented herein. For these examples, the NEO is discovered heading toward the east coast of the United States less than 11 hours before impact. The orbital elements of the target NEO are provided in Table 5.2. Interceptors based on the Minuteman III and the SM-3 Block IIA will be launched from silos at Minot Air Force Base (AFB), North Dakota. The maximum intercept altitude for each vehicle will be compared. Because

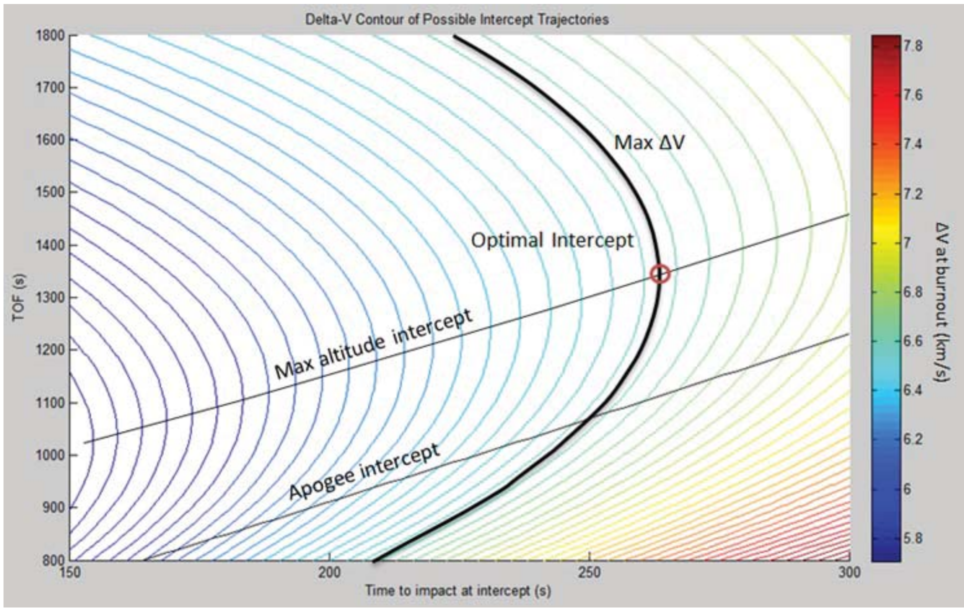

Figure 5.3: ΔV contour across interceptor launch window [59, 60].

Table 5.2: Target orbital elements

Orbital elements	Values
a	$-4,067$ km
e	2.154
i	59°
Ω	256°
ω	100°
θ_0	243.4°

the smaller SM-3 can be launched from a ship, an SM-3 will be launched from a position in the Gulf of Mexico. This is intended to show how positioning the launch site directly beneath the NEO's path can increase the intercept altitude.

Interceptor Characteristics

The Minuteman III and SM-3 Block IIA are assumed to have a ΔV capability of 6.6 km/s and 5.5 km/s at burnout, respectively. Estimate of SM-3 Block IIA performance is obtained from [64]. Estimate of Minuteman III performance is obtained from [65, 66]. They are launched from a silo field in North Dakota with coordinates 48.5° N, 101.4° W. For clarity, these interceptors will be referred to as interceptors A and B, respectively. Interceptor C will be a SM-3 Block IIA launched from a ship located at 25° N, 90° W.

Table 5.3: Optimal intercept parameters [59, 60]

Interceptor	A	B	C
Missile	Minuteman III	SM-3 IIA	SM-3 IIA
ΔV (km/s)	6.6	5.5	5.5
Launch site	48.5°N 101.5°W	48.5°N 101.5°W	25°N 90°W
Intercept altitude (km)	2,625	1,269	2,044
Intercept closing speed (km/s)	14.2	14.4	13.7
Time-of-flight (s)	1,341	971	817
Intercept-to-impact time (s)	264	133	209

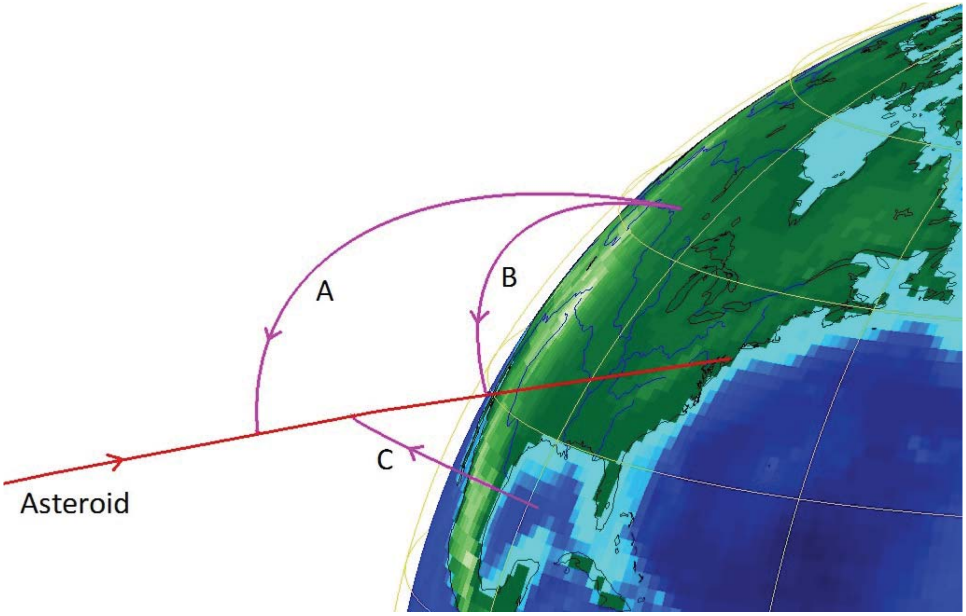

Figure 5.4: Ideal optimal intercept trajectories [59, 60].

Interceptor A reaches the highest intercept altitude of 2,625 km. Both of the smaller SM-3 missiles are able to achieve intercept, but at lower altitudes. Details of the intercept results are presented in Table 5.3. Figure 5.4 shows the NEO's path and the three interception trajectories relative to Earth. Interceptor C is launched from a point nearly directly beneath the NEO's path and, therefore, can reach a higher intercept than the same vehicle launched from further away. Due to the unpredictable nature of NEO impacts, however, it would not always be practical to move the launch site on short notice or have many launch sites around the country. Increasing the ΔV performance of the booster vehicle is much more effective, as will be discussed presently. The Minuteman III has 16.7% higher ΔV than the SM-3 used in this example, yet it can achieve intercept at 50% higher altitude when launched from the same location at the same target.

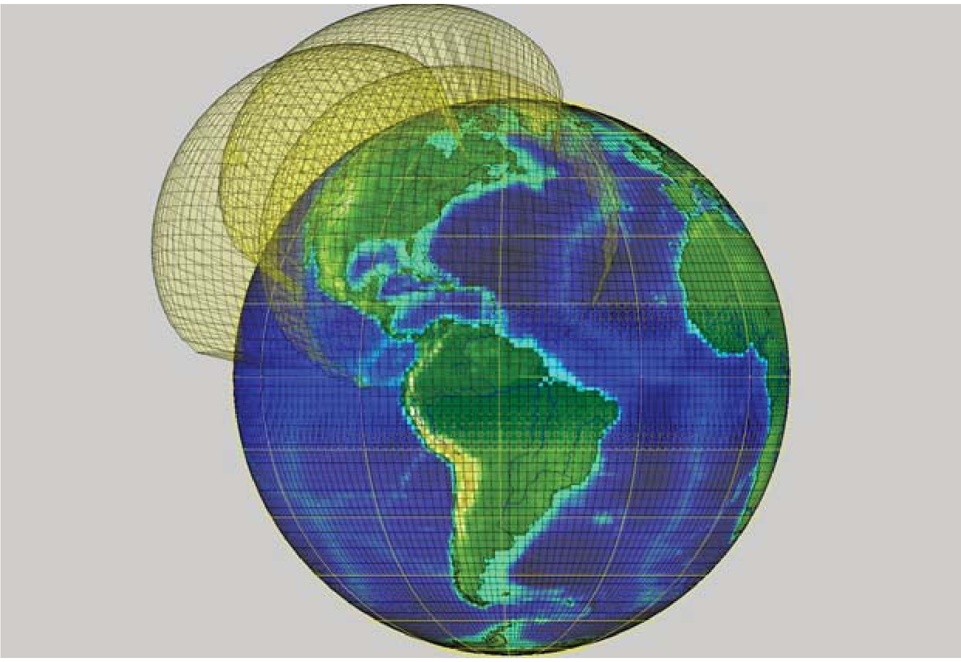

Figure 5.5: Notional planetary defense domes for the United States [59, 60].

Planetary Defense Domes

For the purposes of planetary defense planning it is important to choose launch sites that maximize coverage of critical areas. The Minuteman III has sufficient range to protect most of North America if the silo location is chosen carefully. Assuming that intercept must occur above 1,000 km altitude to be reasonably safe, Fig. 5.5 shows example defense coverage areas for the following three launch sites: Minot AFB in North Dakota, Vandenberg AFB in California, and Cape Canaveral in Florida.

All of these sites are already used for testing/deployment of missiles, and together they create a fairly even spread of coverage across the entire continent. It should be noted that a simplified model was used to compute the defendable area for each site. The domes in Fig. 5.5 are terminated at the apogee of the interceptor, creating a more conservative estimate of their range. The actual useful range of each missile site is thus larger than shown in Fig. 5.5.

5.2.4 Late Intercept Solutions

After the optimal launch time for a certain target and interceptor configuration has passed, it is still possible to achieve intercept, albeit at a lower altitude. The launch time window for post-optimal solutions is bounded by the optimal launch time and the latest possible launch time for which intercept is still possible. The latter bound is equivalent to the minimum-TOF ballistic trajectory between the launch site and the target impact site. For every post-optimal launch time, t_1, there is

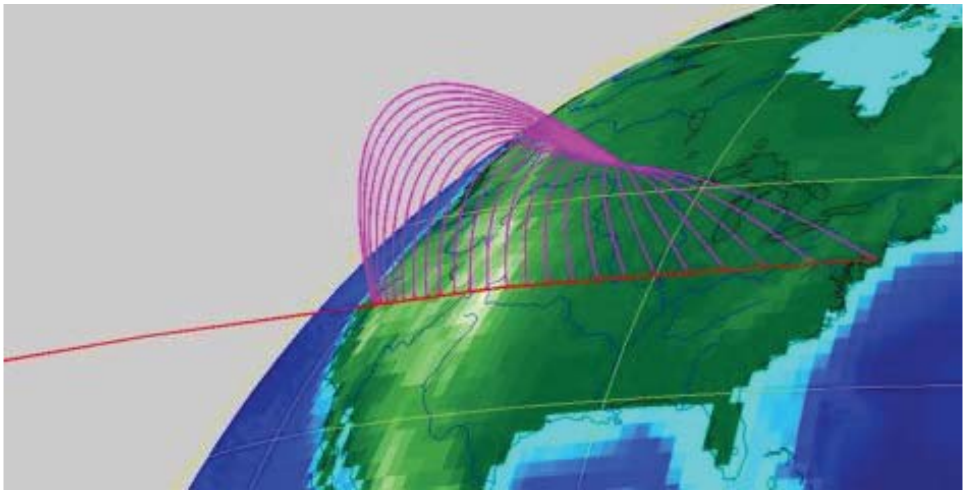

Figure 5.6: Late intercept trajectories [59, 60].

a unique intercept trajectory that maximizes altitude. It can be shown that the maximum altitude possible for intercept decreases monotonically with later t_1. Therefore, the best time to launch after the optimal t_2 has passed is as soon as possible. Because t_1 is considered fixed for each trajectory calculation, we must vary TOF to obtain the earliest possible intercept. Figure 5.6 shows a sampling of post-optimal trajectories. The leftmost trajectory is the optimal solution, and the rightmost trajectory is the "last chance" solution.

5.3 Higher ΔV Interceptors

Interceptors with higher ΔV performance are summarized in Table 5.4. Firstly, the Minotaur V launch vehicle with five solid fueled stages can launch a 300 kg payload with a ΔV of 9.5 km/s. This is much greater than the Minuteman III considered earlier, however the Minotaur V must be assembled on a launch pad and cannot be launched from a silo. The second case to consider is a fictional booster vehicle that can deliver the interceptor to nearly the moon's mean orbit radius of 384,000 km. The NEO's trajectory and launch site are kept the same as in the previous example.

It should be noted that the fictional booster approaches a parabolic escape orbit, although it remains a suborbital trajectory. Because of this, the results are very sensitive to small changes in ΔV. The Minotaur V can reach the NEO at an altitude nearly 5 times higher than the Minuteman III, and the intercept altitude increases exponentially with increasing launch ΔV. The time of flight is a limiting factor here. For the case of the fictional booster, intercept occurs 10 hours before impact, but the interceptor must be launched nearly 5 days before impact. The important point illustrated by these examples is that a small improvement in ΔV leads to a proportionately

Table 5.4: Higher ΔV intercept scenarios [59, 60]

Vehicles	Minotaur-V	Fictional Booster
ΔV (km/s)	9.5	11.12
Launch site	48.5°N 101.5°W	48.5°N 101.5°W
Intercept altitude (km)	15,101	393,620
Time-of-flight (s)	5,779	414,030
Time-of-flight	1.6 hrs	4.79 days
Intercept-to-impact time (s)	1,388	38,623

Table 5.5: Non-ballistic missile options [59, 60]

Vehicles	Stages	Country	Platform	Payload to LEO (kg)
Minotaur I	4	US	Launch Pad	580
Minotaur IV	4	US	Launch Pad	1,735
Minotaur V	5	US	Launch Pad	532 (GTO)
Pegasus	3	US	Air Launch	443
Shavit	3	Israel	Launch Pad	350
Start-1	4	Russia	Launch Pad	532
Taurus/Antares	4	US	Launch Pad	1,320

large increase in intercept altitude. The ΔV improvement can be achieved by using a larger booster or reducing the payload mass.

Although the Minuteman III is the primary example considered, it does not represent the only viable option for last-minute suborbital asteroid interception. This section looks at some of the alternatives provided in Tables 5.5 and 5.6. The list is limited to active or recently deactivated boosters that can launch at least a 300 kg payload into LEO, and large ICBMs. Liquid fueled launch vehicles are excluded from the list, as they require a more complicated and time-consuming fueling procedure that may not be compatible with a short warning launch. It is important to note that if there is enough time to assemble a large rocket on a pad before launching the interceptor, sending the interceptor into a parking orbit will generally be more effective than a purely suborbital intercept mission.

Both conventional launch vehicles and ballistic missiles are listed in Tables 5.5 and 5.6, along with a comparison of performance. An estimate of the payload to LEO is given for each launch vehicle, and an estimate of the burnout velocity and throw weight is given for the ballistic missiles. While not specific to a suborbital intercept mission with a 300 kg payload, these numbers provide a rough comparison of performance between the vehicles.

Table 5.6: Ballistic missile options [59, 60]

Vehicles	Stages	Country	Platform	Burnout Velocity (km/s)	Throw-Weight (kg)
Minuteman III	3	US	Silo	6.6	1,150
Peacekeeper	4	US	Silo	6.7	3,950
Trident II	3	US	Submarine	6.3	2,800
R-36	3	Russia	Silo	∼7.0	8,800
GBI	4	US	Silo	6.0	∼100
SM-3	4	US	Ship	5.5	∼100

5.4 Practical Issues and Future Research Work

5.4.1 Fragmentation and Airbursts

For any scenario in which suborbital intercept is the only option, it is unlikely that such an intercept will result in complete neutralization of the NEO. In such close proximity to the Earth, most, if not all, fragments will still strike the Earth. Similarly, any attempt to completely disrupt a large NEO would require a prohibitively large nuclear payload that would itself be dangerous to the Earth. For those reasons, the method of defense described herein is only effective against smaller (50–150 m) NEOs. In the scope of the problem considered herein, however, we have assumed that large NEOs are more likely to be discovered relatively far in advance of their Earth impact dates; consequently, small NEOs are the most probable threat and are, therefore, focused on in this paper. NEOs much smaller than 50 m may break up in the atmosphere, depositing at most a shower of less dangerous fragments. However, the events at Tunguska in 1908 and Chelyabinsk in 2013 both provide evidence that large airbursts over land are capable of causing significant damage. On the other hand, a fragmented or fractured asteroid will tend to break up at a higher altitude, which would limit the damage caused by low-altitude airbursts.

5.4.2 EMP (Electromagnetic Pulse) Effects

The United States and former USSR both experimented with high-altitude (400 to 500 km) nuclear detonations during the 1960s. The EMP effects have been identified from such nuclear detonations However, it is expected that smaller yields and sufficiently higher altitudes ($>$ 2,500 km) may limit the EMP effects on the ground. Additionally, we may be able to appropriately shape an NED explosion such that most of the explosion energy is directed toward the target NEO and away from the Earth. However, the possible EMP effects on both the ground and Earth-orbiting satellite infrastructure must be investigated further.

5.4.3 Launch Vehicle Mission Planning Issues

The entire ascent flight of a launch vehicle from lift-off to the final target point in space basically consists of two phases: the atmospheric (or endoatmospheric) ascent and the vacuum (or exoatmospheric) ascent. Most launch vehicles are operated in open-loop guidance mode (but, obviously, in closed-loop flight control mode) during the atmospheric ascent flight. That is, launch vehicle guidance commands for achieving optimal flight trajectories are pre-computed in pre-mission planning. They are updated using the day-of-launch wind profile prior to launch, loaded into the launch vehicle guidance computer, and then used as pre-programmed guidance commands in actual ascent flight. Trajectory optimization tools are used to pre-compute optimal ascent trajectories for various flight conditions and path constraints.

Once a launch vehicle reaches an altitude of approximately 50 km or above, where the atmospheric effects can be ignored, the vehicle is then operated in closed-loop guidance mode for its exoatmospheric ascent. For example, the Space Shuttle was operated in open-loop ascent guidance mode for the powered first stage (ascent flight with the solid rocket boosters). The powered second stage (after solid rocket booster jettison) utilized a closed-loop guidance algorithm for its exoatmospheric ascent.

The open-loop guidance during the atmospheric ascent is not capable of autonomously adapting to significant off-nominal flight conditions. Pre-mission planning for generating optimal ascent trajectories has been known to be an extremely time-consuming and labor-intensive process. Consequently, rapid generation of optimal ascent trajectories and autonomous/adaptive closed-loop atmospheric ascent guidance have been a research topic of practical interest for many decades [67–71]. Advanced ascent guidance technology needs to be further developed for operationally responsive launch vehicles required for planetary defense with very short warning times ($<$ 24 hours).

5.4.4 Future Research Work

As described previously, the primary purpose of the research work of [59, 60] described in this section is to begin understanding the most rapid launch response that might be possible against an incoming NEO, from an ideal trajectory optimization perspective. However, the investigation undertaken towards that end has also led us to identify an array of topics that ought to be pursued in future work, if further development of the suborbital NEO intercept mission concept is pursued. The following is a summary of the key future work items identified in [59, 60]:

- NED yield sizing for properly fragmenting 50–150 m NEOs of various types, structures, etc.

- Limiting cases for the sizes/types of NEOs for which a suborbital disruption attempt would be likely to be effective in reducing the negative effects on Earth. That is, if the incoming NEO is larger than a certain size, it may be that a disruption attempt would not be effective, produce an undesirable outcome, or require an NED that is too energetic to detonate near Earth.

- Examination of all effects on Earth (and Earth-orbiting satellite infrastructure) due to NED detonation at altitudes of 2,500 km or higher.

- How quickly a dedicated launcher (e.g., silo-based) could actually be made ready for deployment during a very short warning time incoming NEO scenario, accounting for all logistical and programmatic factors.

- Precision guidance for ascent and the terminal phase of intercept. As noted in the results presented herein, the velocity of the interceptor relative to the NEO at intercept is on the order of 14 km/s, which poses a very challenging hypervelocity guidance, navigation, and control problem, especially when aiming at a relatively small NEO.

- Effects of realistic navigation and orbit determination errors (e.g., unavoidable errors in knowledge of the NEO's orbit and knowledge of the interceptor's state as a function of time).

- Assessment of NEO intercept performance achieved when the interceptor begins in Earth orbit rather than on Earth's surface.

- Analysis of the minimum time required (starting from NEO threat detection/confirmation) to prepare an interceptor for launch via a spacecraft launch vehicle (instead of a silo-based booster), including interceptor vehicle development/preparation, testing, launch vehicle preparation and integration, etc. This analysis would be timely and interesting, because typical spacecraft development schedules require 4 to 6 years from the start of development until launch.

5.5 ATLAS (Asteroid Terrestrial-impact Last Alert System)

Although this chapter has focused on a suborbital intercept/fragmentation of an asteroid with such very short warning times of 1 to 24 hrs, the mission effectiveness of the proposed HAIV system can be further enhanced by exploiting an asteroid warning system, which is being developed at the University of Hawaii with $5 million funding from NASA [62].

Once this system, called the ATLAS (Asteroid Terrestrial-impact Last Alert System), becomes fully operational in early 2016, it is expected that it will offer a one-week warning for a 45-m asteroid and three weeks for a 140-m asteroid. Provided that such one-week warning from the ATLAS can be assured, a target asteroid ($>$ 45 m) can be intercepted and disrupted far outside of Earth's gravitational field and consequently, by avoiding a troublesome suborbital intercept. It is emphasized again that a suborbital intercept may become inevitable for the probable situations with ultra-short warning times of only 1 to 24 hrs.

Chapter 6

Close Proximity Dynamics and Control Around Asteroids

The NIAC Phase 2 study was focused on the HAIV concept for hypervelocity intercept missions. However, the close proximity dynamics and control problem of spacecraft orbiting around irregular-shaped asteroids has also been briefly examined for the design of an observer satellite mission orbiting around a target asteroid [72–74]. The study results described in this chapter will be applicable to NASA's Asteroid Redirect Mission as well as future asteroid exploration missions. The gravitational fields of small bodies are not uniform due to irregular shapes and non-homogeneous mass distribution. Perturbation forces can be strong enough to destabilize orbital motion of spacecraft about irregular-shaped asteroids. Various gravitational field models, such as a polyhedron model, a spherical harmonics expansion, and an inertia dyadic gravitational model, are described for the purposes of close proximity dynamics and control analysis/simulation. A state-feedback control scheme, augmented by disturbance accommodation control (DAC) filters, is introduced for maintaining stable, close proximity orbital motion with little propellant expenditure. However, this proposed control scheme exploiting the DAC filtering concept requires an accurate gravitational field measurement or estimation and spacecraft's relative state vector information.

6.1 Introduction

Unlike with larger bodies such as planets, the dynamical environment around small bodies such as asteroids and comets can be difficult to characterize. The gravitational fields are not uniform due to irregular shapes and non-homogeneous mass distribution, and perturbation forces such as solar radiation pressure can be strong enough to destabilize an orbit around an asteroid. There has been much research devoted to finding open-loop solutions to stable orbits about small bodies, but the solutions prove to be highly sensitive to the initial conditions.

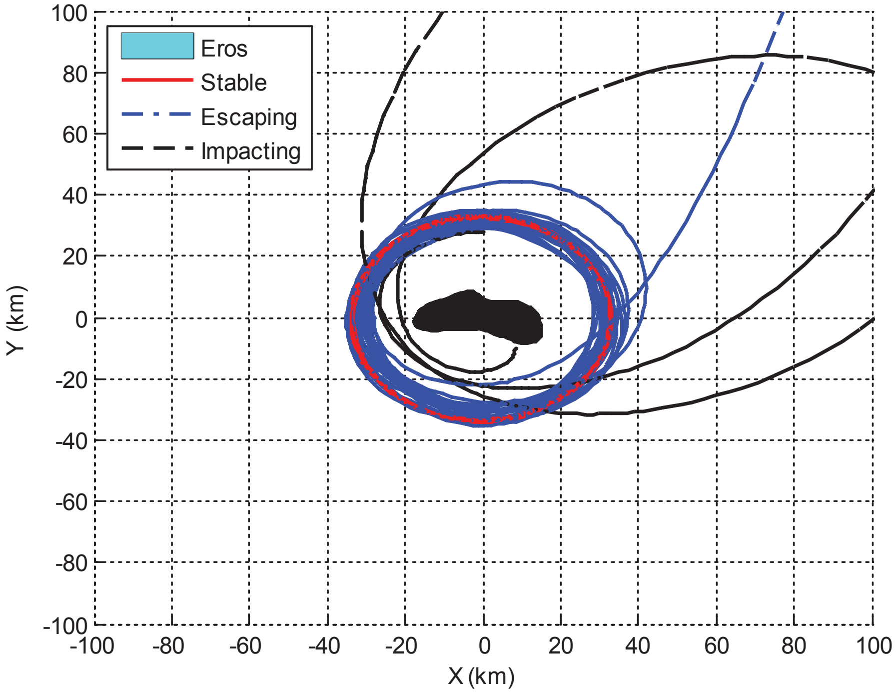

Figure 6.1: Various orbits around asteroid 433 Eros [72–74].

To enable future asteroid exploration missions, a thorough understanding is required of the dynamical environment around such irregular-shaped asteroids. Relevant perturbation forces in close proximity operations include the non-uniform gravitational field of the asteroid caused by a non-homogenous mass distribution and solar radiation pressure. The individual or combined effects of these forces have been shown to destabilize orbits, and can cause the spacecraft to impact or escape the asteroid [75, 76]. One proposed solution is to hover above the body as was done in the JAXA Hayabusa mission to Itokawa [77, 78]. Hovering about a fixed-point above the asteroid, though, would only be appealing if it was desired to land at a particular point on the body. The propellant required could also lead to shorter mission durations, which would limit the scientific return.

In an effort to avoid the requirements of stationkeeping or hovering, there has been much research devoted to open-loop solutions of orbits about asteroids and comets and their stability bounds [75, 79–86]. While it is possible to find orbits that remain stable for great lengths of time, Fig. 6.1 shows how three different orbits with similar initial conditions about asteroid 433 Eros can produce radically different results. The coordinate system (X, Y, Z) used in Fig. 6.1 is an inertial (non-spinning) reference frame fixed at the center of mass of Eros with the positive Z-axis along the north pole spin axis. The spin period of Eros is 5.27 hrs. A sample orbit begins at a radius of 32.9 km along the inertial X-axis with a velocity equal to that of the local circular. After

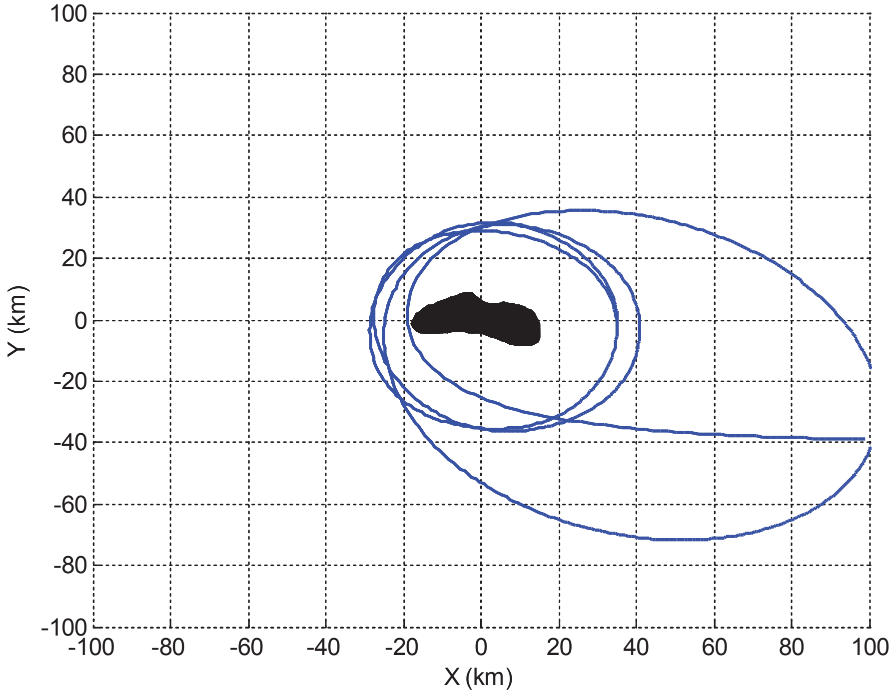

Figure 6.2: A stable orbit in Fig. 6.1, but resulting in an escape due to an orbit injection error of 5 percent in the velocity [72–74].

numerically simulating the orbit for over a week, it is observed that it remains in a quasi-stable orbit around the body, as can be seen in Fig. 6.1. The second sample orbit has a radius of 32.8 km also at the local circular velocity, but is shifted 45° from the X-axis. Here the orbit remains about the body for over a week before finally escaping. The third sample orbit begins at a radius of 27.85 km along the inertial Y-axis with the local circular velocity. The orbit first travels far away from the body twice before impacting. Even though stable orbits can be found, Fig. 6.2 shows how an orbit injection error of 5 percent in the velocity is enough to destabilize the orbit, and cause the spacecraft to escape the body. Given the sensitivity of the dynamic environment at asteroids and comets to initial conditions, it is not practical to rely entirely upon open-loop solutions to keep a spacecraft in orbit about such an irregular-shaped body for close proximity mission operations.

In this chapter, the gravitational forces of a polyhedron shape model derived by Werner and Scheeres [87], a 15^{th} order harmonic expansion [88], and an inertia dyadic gravitational model [89] are compared, and used in a state-feedback control scheme to command an arbitrary orbit about the asteroid 433 Eros. The concept of disturbance accommodation control (DAC) filtering, extensively discussed in [90–95], is applied in an iterative manner to allow the spacecraft to deviate from the reference trajectory and follow a periodic solution of the nonlinear equations of motion, as was proposed for the fuel-efficient halo orbit control in [95]. The DAC filtering application not only reduces the amount of ΔV required but also guarantees the spacecraft will remain in orbit about the asteroid for any arbitrary reference orbit.

6.2 Gravitational Models of an Irregular-Shaped Asteroid

This section presents the gravitational force equations of three different gravitational field models.

6.2.1 Spacecraft's Equation of Motion

Consider a right-handed (x, y, z) coordinate system that is fixed to the rotating asteroid body. This body-fixed reference frame, with a set of basis vectors $\{\vec{i}, \vec{j}, \vec{k}\}$, aligns the positive x-axis along the asteroid's prime meridian and the positive z-axis along the north spin pole. It is assumed that the asteroid spins about the z-axis with an angular velocity vector $\vec{\omega} = \omega\vec{k} = \omega\vec{K}$ where $\vec{K}$ is a unit vector along the Z-axis of an inertial (non-spinning) frame (X, Y, Z) with a set of basis vectors $\{\vec{I}, \vec{J}, \vec{K}\}$. The spacecraft position vector from the center of mass of an asteroid is then expressed as

$$\vec{r} = x\vec{i} + y\vec{j} + z\vec{k} = X\vec{I} + Y\vec{J} + Z\vec{K} \tag{6.1}$$

and we have

$$\begin{bmatrix} x \\ y \\ z \end{bmatrix} = \begin{bmatrix} \cos\omega t & \sin\omega t & 0 \\ -\sin\omega t & \cos\omega t & 0 \\ 0 & 0 & 1 \end{bmatrix} \begin{bmatrix} X \\ Y \\ Z \end{bmatrix} \tag{6.2}$$

The equation of motion of a spacecraft orbiting around an asteroid is simply described by

$$\left.\frac{d^2\vec{r}}{dt^2}\right|_I = \left.\frac{d^2\vec{r}}{dt^2}\right|_B + 2\vec{\omega} \times \left.\frac{d\vec{r}}{dt}\right|_B + \dot{\vec{\omega}} \times \vec{r} + \vec{\omega} \times (\vec{\omega} \times \vec{r}) = \vec{g} + \vec{u} \tag{6.3}$$

$$\left.\frac{d\vec{r}}{dt}\right|_B = \dot{x}\vec{i} + \dot{y}\vec{j} + \dot{z}\vec{k} \tag{6.4a}$$

$$\left.\frac{d^2\vec{r}}{dt^2}\right|_B = \ddot{x}\vec{i} + \ddot{y}\vec{j} + \ddot{z}\vec{k} \tag{6.4b}$$

6.2.2 Polyhedron Gravitational Model

The polyhedron gravitational model can be advantageous when the gravitating body has a complex, irregular shape. Although computationally slower than using a spherical harmonics expansion model, the polyhedron model is valid anywhere around the body, whereas the spherical harmonics expansion is only valid outside of a circumscribing sphere. Here we describe the equations used to simulate the gravitational filed of a polyhedron model, which assumes a constant density. The

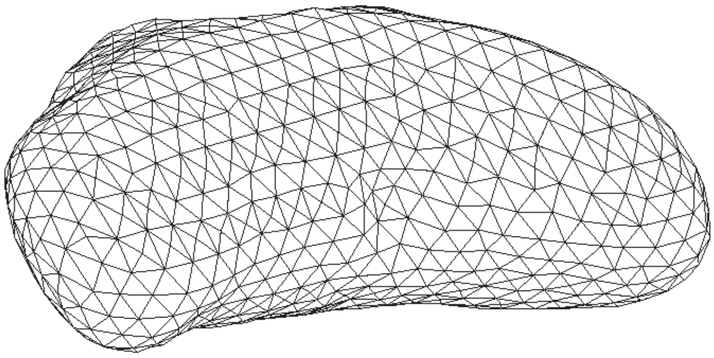

Figure 6.3: Illustration of a triangulated shape model of asteroid 433 Eros.

polyhedron shape model of asteroid Eros [96–98] uses triangular facets as illustrated in Fig. 6.3. The complete derivation of the polyhedron gravity model is given by Werner and Scheeres [87].

The gravitational potential function of a polyhedron shape model is described as [87]

$$U = \frac{1}{2}G\rho \underset{e\in edges}{\quad} L_e\vec{r}_e \cdot \tilde{E}_e \cdot \vec{r}_e - \frac{1}{2}G\rho \underset{f\in facets}{\quad} \omega_f\vec{r}_f \cdot \tilde{F}_f \cdot \vec{r}_f \tag{6.5}$$

where G is the universal gravitational constant, ρ is the constant density, $\vec{r}_e$ is a vector from a point in space to an edge, $\vec{r}_f$ is a vector from a point in space to facet on the polyhedron, $\tilde{E}_e$ is an edge dyadic, L_e is a dimensionless per-edge factor, $\tilde{F}_f$ is a facet dyadic, and ω_f is a dimensionless per-facet factor. Furthermore, we have

$$\tilde{E}_e = \vec{n}_A\vec{n}^A_{21} + \vec{n}_B\vec{n}^B_{12} \tag{6.6}$$

$$\tilde{F}_f = \vec{n}_f\vec{n}_f \tag{6.7}$$

where $\vec{n}_f$, $\vec{n}_A$, and $\vec{n}_B$ are outward facing unit normal vectors, and $\vec{n}^A_{21}$ and $\vec{n}^B_{12}$ are outward facing edge unit normal vectors. These unit vectors are shown in Fig. 6.4. For a coordinate system, whose origin lies within the polyhedron, the outward facing normal vectors can be determined as

$$\vec{n}_f = (\vec{r}_2 - \vec{r}_1) \times (\vec{r}_3 - \vec{r}_2) = \vec{r}_1 \times \vec{r}_2 + \vec{r}_2 \times \vec{r}_3 + \vec{r}_3 \times \vec{r}_1 \tag{6.8}$$

where $\vec{r}_1$, $\vec{r}_2$, and $\vec{r}_3$ are vectors from the origin to each of the three vertices that define the triangular facet, and $\vec{n}_f$ is the facet normal vector.

In computer modeling applications, the vertices that define each facet are stored in a matrix using either a clockwise or counterclockwise rotation. The rotation direction refers to the direction around the facet we would have to travel to find next vertex point. Equation (6.8) assumes a

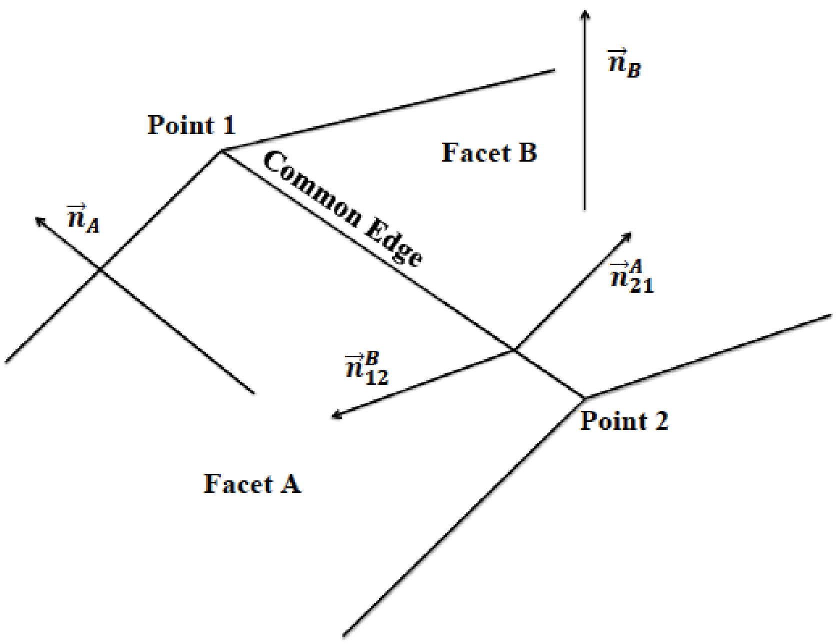

Figure 6.4: Illustration of the various normal vectors employed in formulating the polyhedron gravitational model [87],

counterclockwise rotation. For clockwise rotation storage, simply multiply the equation by -1. The outward facing edge normal vectors, also assuming a counterclockwise rotation, are

$$\vec{n}^f_{ij} = (\vec{r}_j - \vec{r}_i) \times \vec{n}_f \tag{6.9}$$

The dimensionless factors L_e and ω_f are then given by

$$L_e = \ln \frac{r_i + r_j + e_{ij}}{r_i + r_j - e_{ij}} \tag{6.10}$$

$$\omega_f = 2\tan^{-1} \quad \frac{\vec{r}_i \cdot \vec{r}_j \times \vec{r}_k}{r_i r_j r_k + r_i(\vec{r}_j \cdot \vec{r}_k) + r_j(\vec{r}_k \cdot \vec{r}_i) + r_k(\vec{r}_i \cdot \vec{r}_j)} \tag{6.11}$$

where $\vec{r}_i$, $\vec{r}_j$, and $\vec{r}_k$ are vectors from the field point to one of the three vertices on the triangular facet, (r_i, r_j, r_k) are the magnitudes of the vectors, and e_{ij} is the length of the edge connecting $\vec{r}_i$ and $\vec{r}_j$. Note that per facet, there is one value of ω_f and three values of L_e (one for each edge).

The gradient vector of the potential described by Eq. (6.5) is expressed as

$$\nabla U = -G\rho \underset{e\in edges}{\quad} L_e \tilde{E}_e \cdot \vec{r}_e + G\rho \underset{f\in facets}{\quad} \omega_f \tilde{F}_f \cdot \vec{r}_f \tag{6.12}$$

This also leads to a simple method for determining whether or not a field point is outside of the polyhedron by evaluating the Laplacian of the potential as

$$\nabla^2 U = -G\rho \underset{f\in facets}{\quad} \omega_f \tag{6.13}$$

The sum of ω_f goes to zero when the field point is located outside of the polyhedron, and 4π inside the polyhedron. This is particularly helpful in knowing during a simulation whether or not a spacecraft remained in orbit about a body, or crashed into the surface without requiring much additional computation. Equation (6.13), however, will not provide any information if the spacecraft escaped the gravitational field of the body. This can only be determined by analyzing the results after a simulation.

6.2.3 Spherical Harmonics Expansion Model

A classical approach to gravitational force modeling is to use spherical harmonics. However, this spherical harmonics gravity model is only valid outside of the minimum circumscribing sphere around the body. The potential function in spherical harmonics is expressed as a double summation involving the associated Legendre polynomials $P_{n,m}$ and the harmonic coefficients $C_{n,m}$ and $S_{n,m}$, as follows [88]:

$$U(r,\lambda,\phi) = \frac{\mu_\otimes}{r} \overset{\infty}{\underset{n=0}{}} \overset{n}{\underset{m=0}{}} \frac{R_\otimes}{r}^{\,n} P_{n,m}(\sin\phi)\{C_{n,m}\cos(m\lambda) + S_{n,m}\sin(m\lambda)\} \tag{6.14}$$

$$P_{n,m}(\sin\phi) = \frac{1}{2^n n!}(1-\sin^2\phi)^{m/2}\frac{d^{n+m}}{d(\sin\phi)^{n+m}}(\sin^2\phi - 1)^n \tag{6.15}$$

where $\mu_\otimes$ is the gravitational parameter of an asteroid, $R_\otimes$ is the reference radius of the circumscribing sphere of an asteroid body, r is the radial position, λ is the longitude, and ϕ is the latitude. As can be seen in Fig. 6.5, the position vector of a spacecraft can be expressed as

$$\vec{r} = x\vec{i} + y\vec{j} + z\vec{k} = r\vec{e}_r \tag{6.16}$$

and the basis vectors $\{\vec{e}_r, \vec{e}_\lambda, \vec{e}_\phi\}$ of the spherical coordinates are related to $\{\vec{i}, \vec{j}, \vec{k}\}$ as

$$\begin{bmatrix} \vec{e}_r \\ \vec{e}_\lambda \\ \vec{e}_\phi \end{bmatrix} = \begin{bmatrix} \cos\phi\cos\lambda & \cos\phi\sin\lambda & \sin\phi \\ -\sin\lambda & \cos\lambda & 0 \\ -\sin\phi\cos\lambda & -\sin\phi\sin\lambda & \cos\phi \end{bmatrix} \begin{bmatrix} \vec{i} \\ \vec{j} \\ \vec{k} \end{bmatrix} \tag{6.17}$$

It should be noted that all $S_{n,0}$ equal zero and $C_{0,0}$ is one. Should the coordinate system have its origin at the attracting body's center of mass, the coefficients $C_{1,0}$, $C_{1,1}$, and $S_{1,1}$ are all zero. For our purposes we will use the more general case described by Eq. (6.14) to calculate the gradient of the potential in spherical coordinates before converting to a cartesian coordinate system to determine the gravitational acceleration vector, as follows:

$$\begin{aligned} \vec{g} &= g_x\vec{i} + g_y\vec{j} + g_z\vec{k} && \text{(6.18a)} \\ &= \frac{\partial U}{\partial r}\vec{e}_r + \frac{1}{r\cos\phi}\frac{\partial U}{\partial \lambda}\vec{e}_\lambda + \frac{1}{r}\frac{\partial U}{\partial \phi}\vec{e}_\phi && \text{(6.18b)} \end{aligned}$$

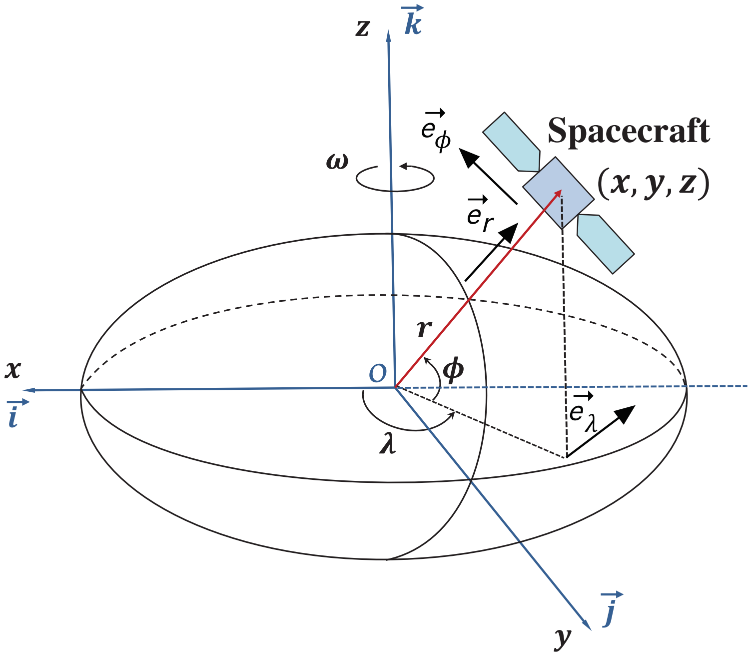

Figure 6.5: Illustration of the spherical coordinate system (r, λ, ϕ) with a set of basis vectors $\{\vec{e}_r, \vec{e}_\lambda, \vec{e}_\phi\}$ relative to the body-fixed reference frame (x, y, z) with a set of basis vectors $\{\vec{i}, \vec{j}, \vec{k}\}$.

where

$$\frac{\partial U}{\partial r} = -\frac{\mu_\otimes}{r^2}\sum_{n=0}^{\infty}\sum_{m=0}^{n}\left(\frac{R_\otimes}{r}\right)^n (n+1)P_{n,m}(\sin\phi)\{C_{n,m}\cos(m\lambda) + S_{n,m}\sin(m\lambda)\}$$

$$\frac{\partial U}{\partial \lambda} = \frac{\mu_\otimes}{r}\sum_{n=0}^{\infty}\sum_{m=0}^{n}\left(\frac{R_\otimes}{r}\right)^n mP_{n,m}(\sin\phi)\{S_{n,m}\cos(m\lambda) - C_{n,m}\sin m\lambda\}$$

$$\frac{\partial U}{\partial \phi} = \frac{\mu_\otimes}{r}\sum_{n=0}^{\infty}\sum_{m=0}^{n}\left(\frac{R_\otimes}{r}\right)^n \{P_{n,m+1}(\sin\phi) - m\tan\phi P_{n,m}(\sin(\phi)\}\{C_{n,m}\cos(m\lambda) + S_{n,m}\sin(m\lambda)\}$$

and the gravitational acceleration vector components can then be converted from the spherical coordinates to the body-fixed frame as follows:

$$\begin{bmatrix} g_x \\ g_y \\ g_z \end{bmatrix} = \begin{bmatrix} \cos\phi\cos\lambda & -\sin\lambda & -\sin\phi\cos\lambda \\ \cos\phi\sin\lambda & \cos\lambda & -\sin\phi\sin\lambda \\ \sin\phi & 0 & \cos\phi \end{bmatrix} \begin{bmatrix} \partial U/\partial r \\ (r\cos\phi)^{-1}\partial U/\partial\lambda \\ r^{-1}\partial U/\partial\phi \end{bmatrix} \tag{6.19}$$

The preceding derivations of the spherical harmonics expansion model are applicable only in the case when the harmonic coefficients are not normalized. Often the coefficients are given as normalized values to avoid numerical difficulties associated with the gravitational coefficients that may become very small as the degree and order get large. In some computers, this would introduce truncation errors and thus the normalization becomes necessary to prevent inaccuracy. A common method of normalization is described as [88]

$$\Pi_{n,m} = \quad \overline{\frac{(n+m)!}{(n-m)!k(2n+1)}} \tag{6.20}$$

$$k = 1 \quad \text{if} \quad m = 0$$

$$k = 2 \quad \text{if} \quad m \neq 0$$

$$\bar{S}_{n,m} = \Pi_{n,m} S_{n,m} \qquad \bar{C}_{n,m} = \Pi_{n,m} C_{n,m} \qquad \bar{P}_{n,m} = P_{n,m}/\Pi_{n,m} \tag{6.21}$$

It is important to remember to normalize the Legendre polynomials as well when using normalized coefficients because their product must remain the same (i.e. $\bar{C}_{n,m}\bar{P}_{n,m} = C_{n,m}P_{n,m}$ and $\bar{S}_{n,m}\bar{P}_{n,m} = S_{n,m}P_{n,m}$). Normalized spherical harmonic coefficients up to the sixth order and degree for asteroid Eros are provided in Table 6.1.

6.2.4 Inertia Dyadic Gravitational Model

Now we derive a gravitational force model involving asteroid's inertia dyadic (or inertia matrix) as described in [89]. For a continuous rigid body, the gravitational force acting on a point-mass spacecraft can be expressed as

$$\vec{F} = -Gm \quad \vec{p}(\vec{p} \cdot \vec{p})^{-3/2} \rho dV \tag{6.22}$$

where G is the universal gravitational constant, ρ is asteroid's density, $\vec{p}$ is the position vector of a spacecraft of mass m from a point P of the asteroid body, as illustrated in Fig. 6.6.

From Fig. 6.6, we have $\vec{p} = \vec{r} + \vec{R}$ and $\vec{F}$ is then expressed as

$$\vec{F} = -Gm \quad (\vec{R} + \vec{r})(R^2 + 2\vec{R} \cdot \vec{r} + r^2)^{-3/2} \rho dV \tag{6.23}$$

where $R = |\vec{R}|$ and $r = |\vec{r}|$. This equation can be rearranged as

$$\vec{F} = -\frac{Gm}{R^2} \quad \frac{\vec{R}}{R} + \frac{\vec{r}}{R} \quad 1 + 2\frac{\vec{R}}{R} \cdot \frac{\vec{r}}{R} + \frac{r^2}{R^2} \quad ^{-3/2} \rho dV \tag{6.24}$$

which is then expressed as

$$\vec{F} = -\frac{Gm}{R^2} \quad (\vec{a}_1 + \vec{q})(1 + 2\vec{a}_1 \cdot \vec{q} + q^2)^{-3/2} \rho dV \tag{6.25}$$

where $\vec{a}_1 = \vec{R}/R$ is a unit vector along $\vec{R}$, $\vec{q} = \vec{r}/R$, and $q = |\vec{q}|$.

Assuming that $(2\vec{a}_1 \cdot \vec{q} + q^2) < 1$ and using the binomial series expansion of the form

$$(1+x)^n = \overset{\infty}{\underset{k=0}{\quad}} \frac{n!x^k}{(n-k)!k!} = 1 + nx + \frac{1}{2!}n(n-1)x^2 + \frac{1}{3!}n(n-1)(n-2)x^3 + \cdots \tag{6.26}$$

Table 6.1: Normalized spherical harmonic coefficients up to the sixth order and degree [98]

Order	Degree	$\bar{C}_{n,m}$	$\bar{S}_{n,m}$
0	0	1	0
1	0	0	0
	1	0	0
2	0	–0.05246	0
	1	0	0
	2	0.08240	–0.02811
3	0	–0.00141	0
	1	0.00406	0.00337
	2	0.00177	–0.00070
	3	–0.01042	–0.01207
4	0	0.01293	0
	1	–0.00010	0.00014
	2	–0.01747	0.00463
	3	–0.00030	–0.00012
	4	0.01746	–0.00911
5	0	0.00066	0
	1	–0.00276	–0.00122
	2	–0.00078	–0.00038
	3	0.00458	0.00354
	4	0.00050	–0.00070
	5	–0.01021	–0.00584
6	0	–0.00498	0
	1	–0.00002	–0.00012
	2	0.00654	–0.00119
	3	0.00029	0.00007
	4	–0.00565	0.00177
	5	–0.00049	0.00005
	6	0.00508	–0.00160

we rewrite Eq. (6.25) as

$$\vec{F} = -\frac{Gm}{R^2} \quad (\vec{a}_1 + \vec{q}) \quad 1 - \frac{3}{2}(2\vec{a}_1 \cdot \vec{q} + q^2) + \frac{15}{8}(4(\vec{a}_1 \cdot \vec{q})^2 + 4q^2\vec{a}_1 \cdot \vec{q} + q^4) - \frac{105}{48}(8(\vec{a}_1 \cdot \vec{q})^3 + 12q^2(\vec{a}_1 \cdot \vec{q})^2) + \cdots \quad \rho dV \tag{6.27}$$

Ignoring terms of q^3 and higher, we obtain

$$\vec{F} = -\frac{Gm}{R^2} \qquad \vec{a}_1 \quad 1 - \frac{3}{2}(2\vec{a}_1 \cdot \vec{q} + q^2) + \frac{15}{2}(\vec{a}_1 \cdot \vec{q})^2 \quad + \vec{q}\,(1 - 3\vec{a}_1 \cdot \vec{q}) \quad \rho dV \tag{6.28}$$

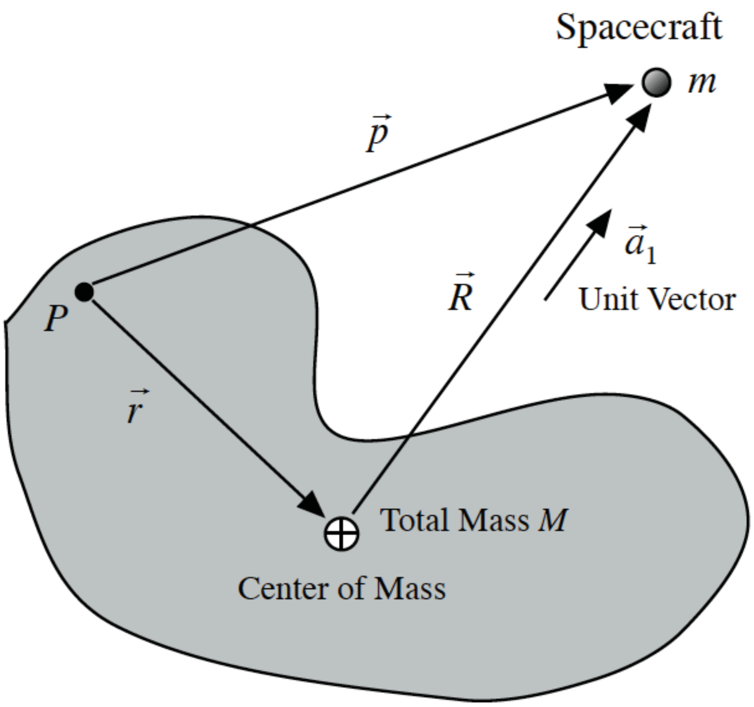

Figure 6.6: Illustration of various position vectors used in deriving an inertia dyadic gravity model.

Replacing $\vec{q}$ with $\vec{r}/R$ and using $\quad \vec{q}\rho dV = 0$, we obtain

$$\vec{F} = -\frac{GMm}{R^2}\vec{a}_1 + \frac{3Gm}{2R^4} \quad \vec{a}_1 \quad r^2\rho dV - 5\vec{a}_1\vec{a}_1 \cdot \quad \vec{r}\vec{r}\rho dV \cdot \vec{a}_1 + 2 \quad \vec{r}\vec{r}\rho dV \cdot \vec{a}_1 \tag{6.29}$$

where $M = \quad \rho dV$ is the total mass of the asteroid.

The inertia dyadic of a rigid-body asteroid is defined as

$$\tilde{J} = \quad (r^2\tilde{I} - \vec{r}\vec{r})\rho dV \tag{6.30}$$

where $\tilde{I}$ denotes the unit dyadic. The trace of the inertia dyadic $\tilde{J}$ can then be expressed as

$$tr(\tilde{J}) = tr \quad r^2\tilde{I}\rho dV \quad - tr \quad \vec{r}\vec{r}\rho dV \quad = \quad 3r^2\rho dV - \quad r^2\rho dV = 2 \quad r^2\rho dV \tag{6.31}$$

and Eq. (6.30) can be rewritten as

$$\vec{r}\vec{r}\rho dV = \tilde{I} \quad r^2\rho dV - \tilde{J} = \frac{1}{2}tr(\tilde{J})\tilde{I} - \tilde{J} \tag{6.32}$$

Substituting Eq. (6.32) into Eq. (6.29), we obtain

$$\vec{F} = -\frac{GMm}{R^2} \quad \vec{a}_1 + \frac{1}{MR^2} \quad \frac{3}{2} \quad tr(\tilde{J}) - 5\vec{a}_1 \cdot \tilde{J} \cdot \vec{a}_1 \quad \vec{a}_1 + 3\tilde{J} \cdot \vec{a}_1 \tag{6.33}$$

where M is the mass of the attracting asteroid body, m is the spacecraft mass, R is the distance to the spacecraft from the asteroid center of mass, $\vec{a}_1$ is a unit vector along $\vec{R}$.

Finally, we have the inertia dyadic gravitational force model expressed as

$$\vec{F} = -\frac{GMm}{R^2}[\vec{a}_1 + \vec{f}^{(2)}] \tag{6.34}$$

where

$$\vec{f}^{(2)} = \frac{1}{MR^2} \quad \frac{3}{2} \quad tr(\tilde{J}) - 5\vec{a}_1 \cdot \tilde{J} \cdot \vec{a}_1 \quad \vec{a}_1 + 3\tilde{J} \cdot \vec{a}_1 \tag{6.35}$$

In general, we have

$$\vec{F} = -\frac{GMm}{R^2} \quad \vec{a}_1 + \overset{\infty}{\underset{i=2}{}} \vec{f}^{(i)} \tag{6.36}$$

where $\vec{f}^{(i)}$ is a collection of terms of the *i*th degree in $|\vec{r}|/R$ [89].

The inertia dyadic of a rigid body is often expressed as [89, 90]

$$\tilde{J} = \quad \vec{b}_1 \quad \vec{b}_2 \quad \vec{b}_3 \quad \begin{bmatrix} J_1 & 0 & 0 \\ 0 & J_2 & 0 \\ 0 & 0 & J_3 \end{bmatrix} \begin{bmatrix} \vec{b}_1 \\ \vec{b}_2 \\ \vec{b}_3 \end{bmatrix} \tag{6.37}$$

where $\{\vec{b}_1, \vec{b}_2, \vec{b}_3\}$ is a set of basis vectors for the principal axes of inertia of a rigid body and (J_1, J_2, J_3) are the principal moments of inertia. We can also employ a set of basis vectors $\{\vec{i}, \vec{j}, \vec{k}\}$ and the principal moments of inertia (J_x, J_y, J_z). The trace of the inertia dyadic $\tilde{J}$ is then expressed as

$$tr(\tilde{J}) = \vec{b}_1 \cdot \tilde{J} \cdot \vec{b}_1 + \vec{b}_2 \cdot \tilde{J} \cdot \vec{b}_2 + \vec{b}_3 \cdot \tilde{J} \cdot \vec{b}_3 = J_1 + J_2 + J_3 \tag{6.38}$$

Similarly, the unit dyadic is expressed as

$$\tilde{I} = \quad \vec{b}_1 \quad \vec{b}_2 \quad \vec{b}_3 \quad \begin{bmatrix} 1 & 0 & 0 \\ 0 & 1 & 0 \\ 0 & 0 & 1 \end{bmatrix} \begin{bmatrix} \vec{b}_1 \\ \vec{b}_2 \\ \vec{b}_3 \end{bmatrix} = \vec{b}_1\vec{b}_1 + \vec{b}_2\vec{b}_2 + \vec{b}_3\vec{b}_3$$

and we have the trace of the unit dyadic as $tr(\tilde{I}) = 3$.

The basis vectors $\{\vec{b}_1, \vec{b}_2, \vec{b}_3\}$ of the body-fixed reference frame are related to a set of basis vectors $\{\vec{a}_1, \vec{a}_2, \vec{a}_3\}$, as follows:

$$\begin{bmatrix} \vec{b}_1 \\ \vec{b}_2 \\ \vec{b}_3 \end{bmatrix} = \begin{bmatrix} C_{11} & C_{12} & C_{13} \\ C_{21} & C_{22} & C_{23} \\ C_{31} & C_{32} & C_{33} \end{bmatrix} \begin{bmatrix} \vec{a}_1 \\ \vec{a}_2 \\ \vec{a}_3 \end{bmatrix} \tag{6.39}$$

or

$$\begin{bmatrix} \vec{a}_1 \\ \vec{a}_2 \\ \vec{a}_3 \end{bmatrix} = \begin{bmatrix} C_{11} & C_{21} & C_{31} \\ C_{12} & C_{22} & C_{32} \\ C_{13} & C_{23} & C_{33} \end{bmatrix} \begin{bmatrix} \vec{b}_1 \\ \vec{b}_2 \\ \vec{b}_3 \end{bmatrix} \tag{6.40}$$

where $C_{ij} = \vec{b}_i \cdot \vec{a}_j$ are the direction cosines, and we have

$$\vec{a}_1 = C_{11}\vec{b}_1 + C_{21}\vec{b}_2 + C_{31}\vec{b}_3$$

which is to be used to replace $\vec{a}_1$ in Eqs. (6.34) and (6.35) by $\{\vec{b}_1, \vec{b}_2, \vec{b}_3\}$, if needed.

Using the inertia dyadic expressed as

$$\begin{aligned} \tilde{J} = &\quad \vec{a}_1 \quad \vec{a}_2 \quad \vec{a}_3 \quad \begin{bmatrix} C_{11} & C_{21} & C_{31} \\ C_{12} & C_{22} & C_{32} \\ C_{13} & C_{23} & C_{33} \end{bmatrix} \begin{bmatrix} J_1 & 0 & 0 \\ 0 & J_2 & 0 \\ 0 & 0 & J_3 \end{bmatrix} \begin{bmatrix} C_{11} & C_{12} & C_{13} \\ C_{21} & C_{22} & C_{23} \\ C_{31} & C_{32} & C_{33} \end{bmatrix} \begin{bmatrix} \vec{a}_1 \\ \vec{a}_2 \\ \vec{a}_3 \end{bmatrix} \\ = &\quad \vec{a}_1 \quad \vec{a}_2 \quad \vec{a}_3 \quad \begin{bmatrix} J_{11} & J_{12} & J_{13} \\ J_{21} & J_{22} & J_{23} \\ J_{31} & J_{32} & J_{33} \end{bmatrix} \begin{bmatrix} \vec{a}_1 \\ \vec{a}_2 \\ \vec{a}_3 \end{bmatrix} \end{aligned} \tag{6.41}$$

where J_{ij} are the time-varying moments and products of inertia, we obtain the inertia dyadic gravitational force model as [89]

$$\vec{F} = -\frac{GMm}{R^2} \quad \vec{a}_1 + \frac{3}{MR^2} \quad \frac{1}{2}(J_{22} + J_{33} - 2J_{11})\vec{a}_1 + J_{12}\vec{a}_2 + J_{13}\vec{a}_3 \tag{6.42}$$

where

$$\begin{aligned} J_{22} + J_{33} - 2J_{11} &= J_1(1 - 3C_{11}^2) + J_2(1 - 3C_{21}^2) + J_3(1 - 3C_{31}^2) \\ J_{12} &= J_1 C_{12} C_{11} + J_2 C_{22} C_{21} + J_3 C_{32} C_{31} \\ J_{13} &= J_1 C_{13} C_{11} + J_2 C_{23} C_{21} + J_3 C_{33} C_{31} \end{aligned}$$

6.2.5 Comparison of Gravitational Models

When simulating an asteroid's gravitational field, the polyhedron shape model requires noticeably more computation time than either the spherical harmonic expansion or the inertia dyadic models. This comes from the fact that the polyhedron model sums contributions from each facet and facet edge. Reasonably accurate models will require at least several thousand facets as opposed to a 15^{th} order harmonic expansion, which sums 136 elements, or the inertia dyadic gravitational model, which sums elements equal to the selected order.

These gravity models are applied to asteroid 433 Eros. In Table 6.2, some key physical parameters of Eros, including its inertia matrix data required for the dyadic inertia gravity model, are provided. The measured center of mass is very close to the center of mass estimated assuming a uniform internal structure [96–98]. This results in a near constant density, which is required for the polyhedron gravity model. Eros is also a prime example of an asteroid with a very irregular shape with the largest dimension being more than twice as long as the smallest dimension.

Figure 6.7 plots the strength of the gravitational field around asteroid 433 Eros using these three models. As the magnitude of the gravitational acceleration is rather weak, the log of this acceleration is used for graphical illustration. Away from the surface of the body, both the polyhedron shape model and the harmonic expansion exhibit almost identical results with the inertia dyadic

Table 6.2: Characteristics of asteroid 433 Eros [96–98]

Physical Parameters	Values		
Semi (x, y, z) axis	(16.7, 8.6, 6.3) km		
Bulk density	2.67 g/cm^3		
$\mu_{\otimes} = GM$	4.463e-4 km^3/s^2		
Rotation period	5.27 hours		
(J_2, J_3) coefficients	(0.0525, 0.0014)		
Inertia matrix			
$J_{xx} \quad J_{xy} \quad J_{xz}$	1.117e23 kg·m^2	6.232e22 kg·m^2	–2.257e20 kg·m^2
$J_{yx} \quad J_{yy} \quad J_{yz}$	6.232e22 kg·m^2	4.793e23 kg·m^2	–2.589e19 kg·m^2
$J_{zx} \quad J_{zy} \quad J_{zz}$	–2.257e20 kg·m^2	–2.589e19 kg·m^2	4.978e23 kg·m^2
Normalized inertia matrix			
$J_{xx} \quad J_{xy} \quad J_{xz}$	16.709 km^2	9.319 km^2	–0.034 km^2
$J_{yx} \quad J_{yy} \quad J_{yz}$	9.319 km^2	71.669 km^2	–0.004 km^2
$J_{zx} \quad J_{zy} \quad J_{zz}$	–0.034 km^2	–0.004 km^2	74.443 km^2

model having the same trend but slightly different magnitudes. Nearer to the surface, the inertia dyadic model starts to exhibit a relatively strong gravitational field as opposed to the polyhedron shape model. This difference with the inertia dyadic model is likely due to the low order used to calculate the gravitational force (only the $\vec{f}^{(2)}$ term is included). Of note as well is that the further away from the gravitating body, the more closer each model becomes to a simple point mass approximation. For orbits closer to the body, the non-uniform effects are more apparent, and diverge from the point mass approximation.

Figure 6.8 focuses on the surface gravitational acceleration computed from the polyhedron shape model. Consistent with the gravity field from Fig. 6.7, the gravitational force is relatively strong in the middle of the shape and decreases towards the far ends.

6.3 Close Proximity Dynamics and Fuel-Efficient Orbit Control

6.3.1 Close Proximity Orbital Dynamics

Several illustrative orbits around asteroid Eros were previously shown in Fig. 6.1, which demonstrate how three different orbits with similar initial conditions about asteroid 433 Eros can produce radically different results. The first sample orbit begins at a radius of 32.9 km along the inertial X-axis with a velocity equal to that of the local circular and it remains in a quasi-stable orbit around the body, as can be seen in Fig. 6.1. The second sample orbit has a radius of 32.8 km also at the local circular velocity, but is shifted 45° from the X-axis. This orbit remains about the body for

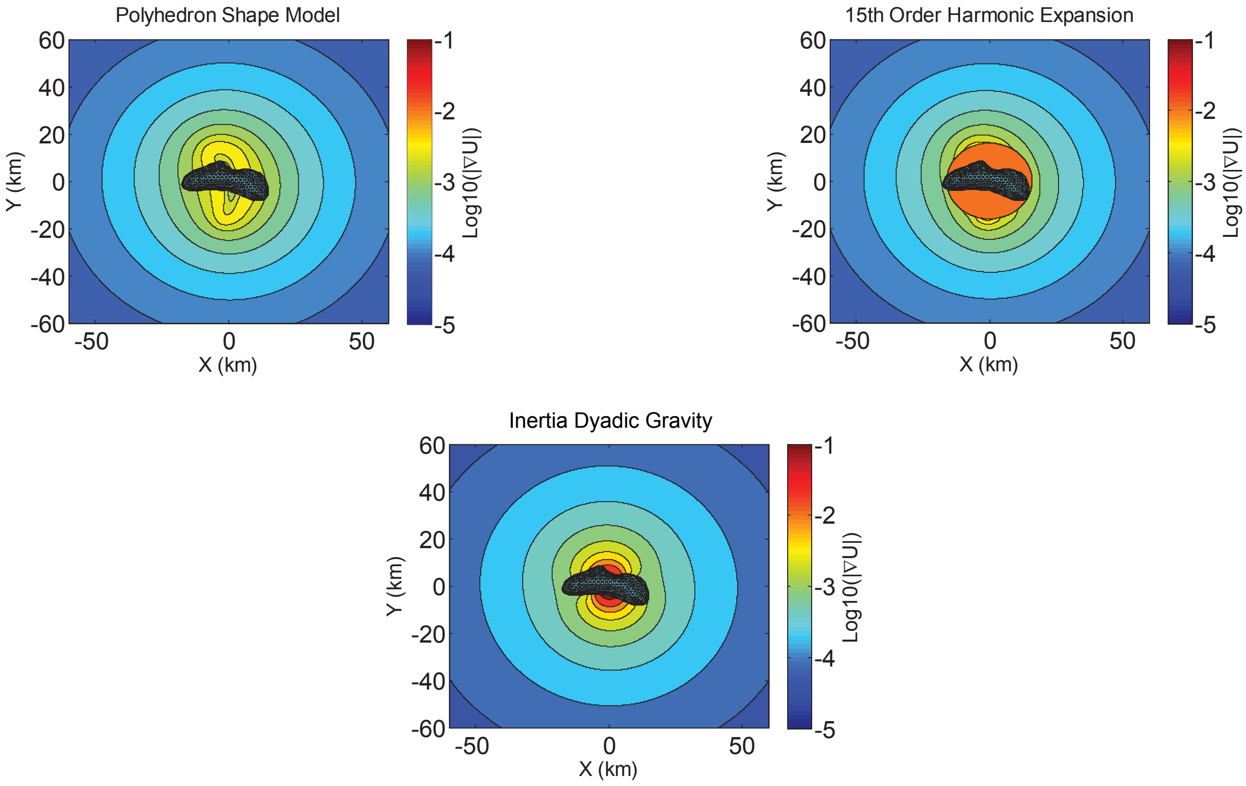

Figure 6.7: Gravity field comparisons of the three gravitational models [72–74].

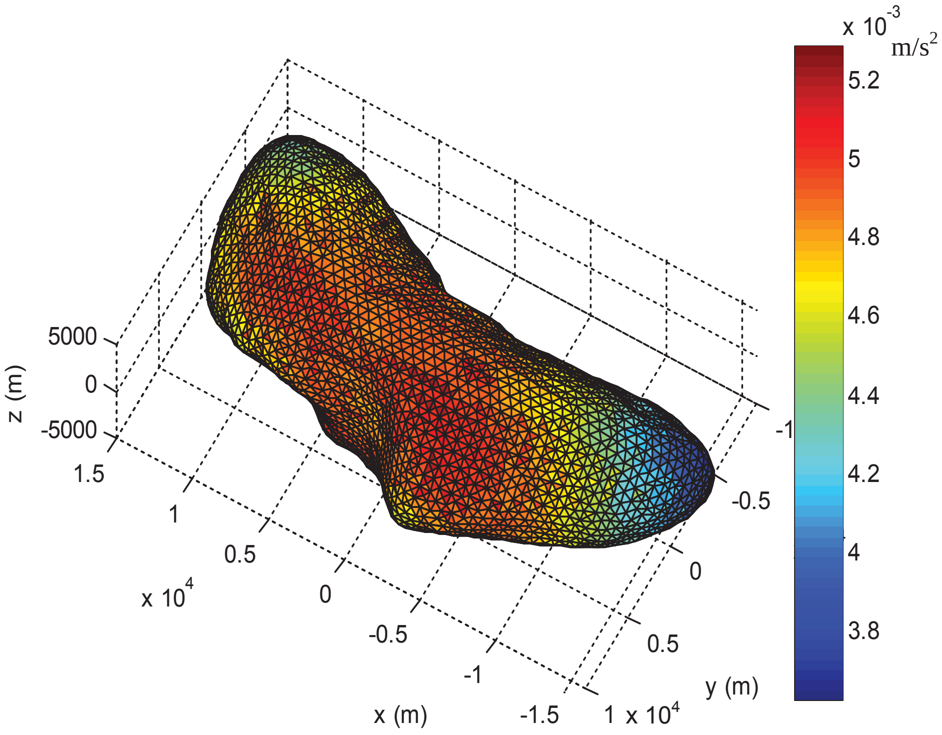

Figure 6.8: Surface gravitational acceleration distribution obtained using the polyhedron shape model of asteroid Eros [72–74].

over a week before finally escaping. The third sample orbit begins at a radius of 27.85 km along the inertial Y-axis with the local circular velocity. The orbit first travels far away from the body twice before impacting. Given the sensitivity of the dynamic environment at asteroids and comets to initial conditions, it is not practical to rely entirely upon open-loop solutions to keep a spacecraft in orbit about such an irregular-shaped body for close proximity mission operations.

6.3.2 Fuel-Efficient Close Proximity Orbit Control

Disturbance Accommodation Control (DAC) Concept

Given various models of the gravitational field of an asteroid body, we now consider feedback control of orbital motion of a spacecraft around an irregular-shaped asteroid assuming that the orbital position and velocity of the spacecraft relative to the COM of an asteroid are available for the close proximity operations. However, it is emphasized that an accurate estimation or measurement of spacecraft's orbital position and velocity relative to the asteroid's COM is not a trivial problem.

For a state-feedback control logic design, we first express the equations of motion in state-space form. As the gravitational terms are highly nonlinear and unknown, they are considered as disturbance acceleration $\mathbf{w}$ for a simple dynamical model of the form:

$$\dot{\mathbf{x}}_p = \mathbf{A}_p \mathbf{x}_p + \mathbf{B}_p \mathbf{u} + \mathbf{w} \tag{6.43}$$

$$\mathbf{x}_p = \begin{bmatrix} X \\ Y \\ Z \\ \dot{X} \\ \dot{Y} \\ \dot{Z} \end{bmatrix}, \quad \mathbf{u} = \begin{bmatrix} u_x \\ u_y \\ u_z \end{bmatrix}, \quad \mathbf{A}_p = \begin{bmatrix} 0 & 0 & 0 & 1 & 0 & 0 \\ 0 & 0 & 0 & 0 & 1 & 0 \\ 0 & 0 & 0 & 0 & 0 & 1 \\ 0 & 0 & 0 & 0 & 0 & 0 \\ 0 & 0 & 0 & 0 & 0 & 0 \\ 0 & 0 & 0 & 0 & 0 & 0 \end{bmatrix}, \quad \mathbf{B}_p = \begin{bmatrix} 0 & 0 & 0 \\ 0 & 0 & 0 \\ 0 & 0 & 0 \\ 1 & 0 & 0 \\ 0 & 1 & 0 \\ 0 & 0 & 1 \end{bmatrix}$$

where $\mathbf{x}_p$ is the plant state vector, $\mathbf{u}$ is the control acceleration vector expressed along the inertial (non-spinning) reference frame (X, Y, Z).

Disturbance-rejection or disturbance accommodation control (DAC) concept discussed in [8, 91–95] is a technique which can be used to reduce the control effort in the presence of persistent disturbances. It works by eliminating parts of the control acceleration, and allows the spacecraft to follow a trajectory that is closer to a natural periodic solution of the nonlinear equations of motion, as demonstrated for numerous spacecraft dynamics and control problems in [8, 91–95]. As we are forcing the spacecraft to follow a particular reference orbit, the nonlinear gravitational effects can cause constant or periodic disturbances, which require a higher control magnitude to cancel out. Since these disturbances cannot be accurately modeled beforehand, we use an iterative method for designing a disturbance accommodation control (DAC) filters. This method allows the spacecraft to deviate from the reference trajectory and follow one that requires less ΔV.

When first orbiting the gravitating body with only standard proportional-derivative (PD) type control, there exist certain frequency components in the control acceleration. These frequency components can be found by examining an FFT (Fast Fourier Transform) plot of the control commands along each axis. Once the spectral components have been identified, we can design disturbance accommodation control (DAC) filters of the form

$$\ddot{\alpha}_i + \omega_{xi}^2 \alpha_i = u_x \tag{6.44a}$$

$$\ddot{\beta}_i + \omega_{yi}^2 \beta_i = u_y \tag{6.44b}$$

$$\ddot{\gamma}_i + \omega_{zi}^2 \gamma_i = u_z \tag{6.44c}$$

where ω_{xi}, ω_{yi}, and ω_{zi} represent the *i*th frequency component in each axis. For constant disturbances, the filters take the form of

$$\dot{\tau}_x = u_x \tag{6.45a}$$

$$\dot{\tau}_y = u_y \tag{6.45b}$$

$$\dot{\tau}_z = u_z \tag{6.45c}$$

The DAC filter can include as many frequencies as are present in the FFT plots. The DAC filters can then be described in state space form as

$$\dot{\mathbf{x}}_d = \mathbf{A}_d \mathbf{x}_d + \mathbf{B}_d \mathbf{u} \tag{6.46}$$

where $\mathbf{x}_d$ is the DAC filter state vector. It should be noted that if a frequency or bias component is not used during the iteration, the corresponding filter state is not included in $\mathbf{x}_d$. The disturbance filter in Eq. (6.46) can then be augmented to the plant model in Eq. (6.43), as follows:

$$\begin{bmatrix} \dot{\mathbf{x}}_p \\ \dot{\mathbf{x}}_d \end{bmatrix} = \begin{bmatrix} \mathbf{A}_p & 0 \\ 0 & \mathbf{A}_d \end{bmatrix} \begin{bmatrix} \mathbf{x}_p \\ \mathbf{x}_d \end{bmatrix} + \begin{bmatrix} \mathbf{B}_p \\ \mathbf{B}_d \end{bmatrix} \mathbf{u} + \begin{bmatrix} \mathbf{w} \\ 0 \end{bmatrix} \tag{6.47}$$

For a combined system described by Eq. (6.47), the control can be expressed as

$$\mathbf{u} = -\mathbf{K} \begin{bmatrix} \mathbf{x}_p - \mathbf{x}_r \\ \mathbf{x}_d \end{bmatrix} \tag{6.48}$$

where $\mathbf{K}$ is the control gain matrix to be determined and $\mathbf{x}_r$ is an initial periodic reference state vector [8, 91–95]. One way to find this gain matrix is to use a linear quadratic regulator (LQR) method. The LQR method finds an optimal $\mathbf{K}$ that minimizes the following performance index

$$J = \frac{1}{2} \int_0^\infty (\mathbf{x}^T \mathbf{Q} \mathbf{x} + \mathbf{u}^T \mathbf{R} \mathbf{u}) dt \tag{6.49}$$

where $\mathbf{Q}$ and $\mathbf{R}$ are the weighting matrices (to be properly chosen). An optimal control gain matrix $\mathbf{K}$ can be easily obtained by Matlab's LQR command.

In an iterative design, spectral components are identified and added to the DAC filter states in Eq. (6.46) each time the control is updated. Care must be taken, though, in selecting $\mathbf{Q}$ and $\mathbf{R}$ during these updates as the same weighting matrices might not be valid with the new system, or the choice for $\mathbf{Q}$ and $\mathbf{R}$ may cause the closed-loop system performance and stability to be unsatisfactory. These iterations are necessary as suppressing frequency components in the control can result in different frequency components appearing in the control. Normally these frequency components are some integer combination of the body spin rate and the orbit frequency. After several iterations, optimal DAC filters can be designed that results in a drastic reduction of ΔV, as demonstrated in [72–74].

Closed-Loop Control Evaluation of Gravitational Models

The gravity models described in Section 6.2 have been computationally tested in [72–74] for orbital motion simulation of a spacecraft around asteroid 433 Eros, one of the largest near-Earth asteroids. We use this real asteroid because the assumption of constant density in the polyhedron gravity model derivation holds true, as the measured center of mass of Eros is very close to center of mass assuming a uniform internal structure. Eros is also a prime example of an asteroid with a very irregular shape. Eros has an elongated shape with the largest dimension being more than twice as long as the smallest dimension, and there is also a large concavity near the middle.

A 35 km radius prograde orbit with PD control in the XY-plane is first examined using the inertia dyadic gravity model (with only the $\vec{f}^{(2)}$ term), a 15^{th} order harmonics expansion, and a 2^{nd} order harmonics expansion. As can be seen in Fig. 6.9, there is a slight magnitude difference in the X- and Y-directions between the 15^{th} order expansion and the other two models. There is a much larger distinction in the Z-direction, but since the control accelerations in this direction are an entire order of magnitude smaller than in the X- or Y-direction, these variations are hardly noticeable. In fact, integrating these control accelerations for the one-week proximity operation period results in a ΔV of 20.6 m/s for the inertia dyadic model, 21.37 m/s for the 15^{th} order expansions, and 20.42 m/s for the 2^{nd} order expansion, which are all within 1 m/s of each other. However, the close proximity operation around a large asteroid requiring such excessive ΔV is impractical.

Similar to the FFT plots in Fig. 6.10, there is little difference between the three models in the X- and Y-direction, but a noticeable difference in the Z-direction. There is virtually no difference between the inertia dyadic model and a 2^{nd} order harmonic expansion. They are both capable

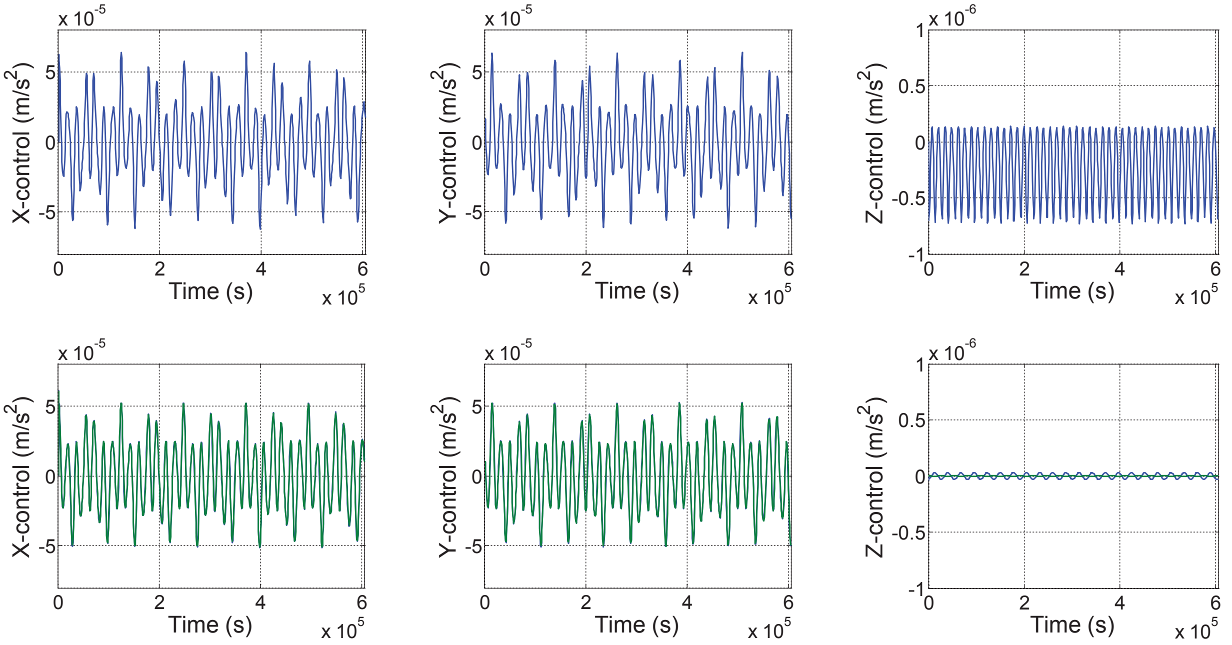

Figure 6.9: Control acceleration histories for the 15^{th} order expansion, 2^{nd} order expansion, and inertia dyadic models. The 15^{th} order is plotted on the top and both the 2^{nd} order and inertia dyadic models are overlayed on the bottom.

of being utilized to find the three major frequencies present, but leave out the smaller, higher frequencies noticeable with the higher order expansion. It is highly likely that including terms of a sufficiently high order in $\vec{f}^{(i)}$ would be capable of simulating these smaller frequency components.

Next we will further examine five different orbiting scenarios: a prograde and retrograde orbit in the XY-plane, a 45° inclined orbit, a polar orbit, and hovering in the body-fixed reference frame. In each of these scenarios, the spacecraft will follow a 35 km radius circular reference orbit with PD control before DAC filters are added. It is unlikely that a realistic mission would follow an orbit that is so close to an asteroid, but the irregularities in the gravity field are stronger and more noticeable the closer the spacecraft comes to the body. Being able to orbit closer to the asteroid is not without its advantages, though, as scientists can observe the object in greater detail. For our purposes, it is assumed that all of the states of a spacecraft can be measured for feedback control and the thrusters are capable of producing the required control accelerations. All models assume an asteroid density of 2.67 g/cm^3 and rotation period of 5.27 hours, and the spherical harmonics uses a reference radius of 16 km. The shape model, spherical harmonic coefficients, and the inertia dyadic are downloaded from NASA's website of shape and gravity models produced by the NEAR Shoemaker mission [98].

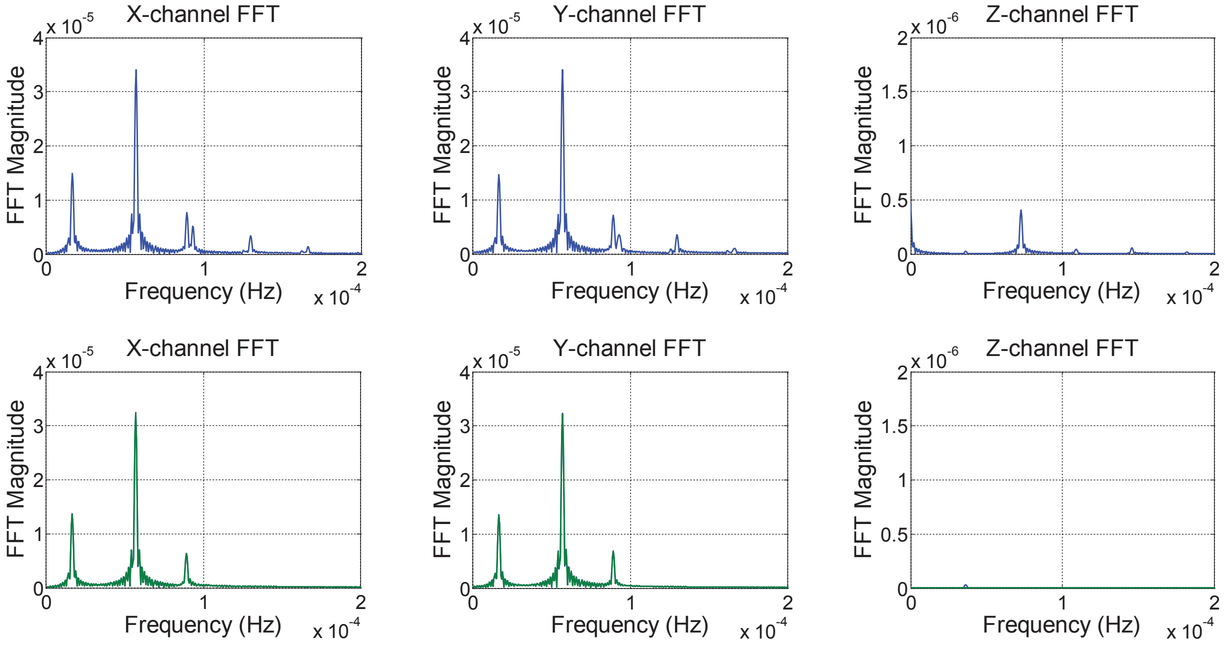

Figure 6.10: FFT plots for the 15^{th} order expansion, 2^{nd} order expansion, and moments of inertia models. The 15^{th} order is plotted on the top and both the 2^{nd} order and inertia dyadic models are overlayed on the bottom.

XY-Plane Prograde Orbit

Consider a prograde orbit in the XY-plane about the asteroid. The orbit begins on the X-axis at the local circular velocity. The resulting orbits of PD control and DAC filtering are given in Figs. 6.11. A comparison between the polyhedron model and the harmonics model results show very little difference in the X- and Y-control and a slight bias difference in the Z-control. Integrating these control accelerations of the PD control results in a ΔV of 21.13 m/s per week with the polyhedron model and 21.37 m/s with the harmonics model. The spectral components of the control accelerations have five noticeable peaks in the X- and Y-control and two in the Z-control, similar to Fig. 6.10. For the X and Y FFTs, the two highest peaks correspond to the orbit frequency and twice the asteroid rotation frequency minus three times the orbit frequency. The control accelerations of DAC filtering decrease to near zero, and the bias in both Z-controls was completely eliminated. Both gravity models resulted in a new ΔV requirement of 0.13 m/s per week.

XY-Plane Retrograde Orbit

Consider the same orbit, except retrograde instead of prograde. Such a retrograde orbit is known to be stable. Adding PD control results in an identical ΔV requirement as the prograde case. This would not be obvious by comparing the control acceleration histories. The Z-axis controls for both retrograde and prograde have about the same amplitude, but the retrograde control oscillates at a

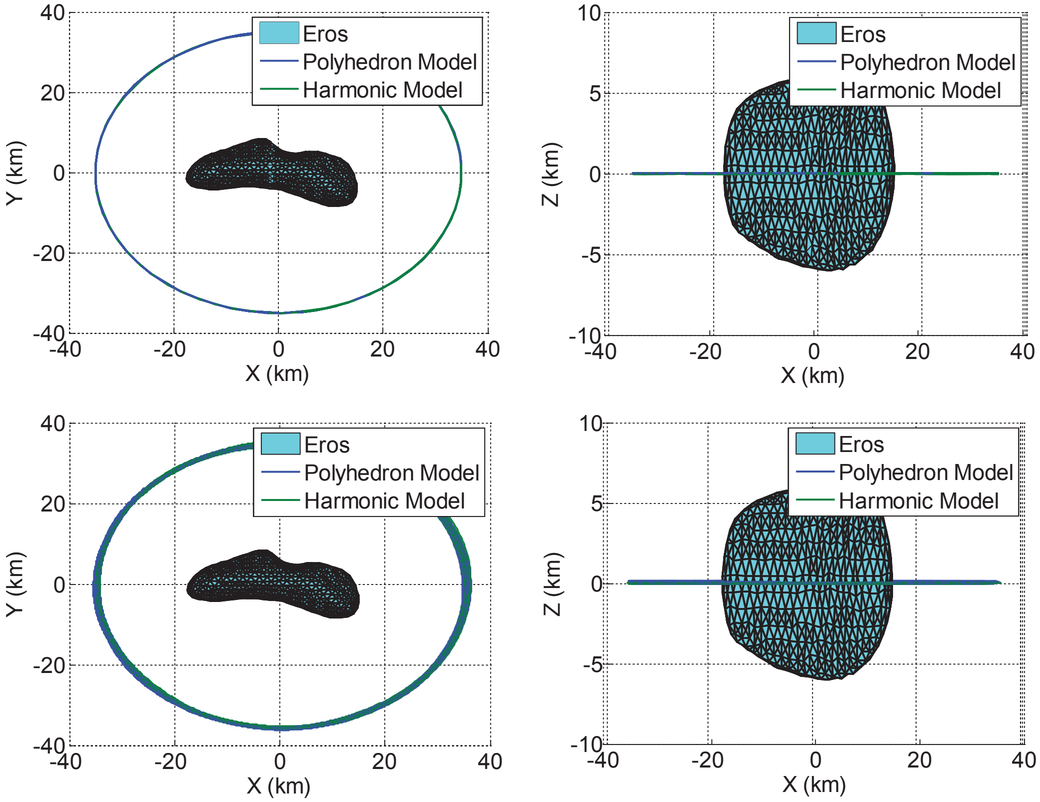

Figure 6.11: 35 km prograde orbits with PD control (top) and with DAC filters (bottom).

higher frequency. On the other hand, the X- and Y-controls for both cases differ greatly from one another both in shape and frequency. This is also reflected in the FFT plots as the prograde orbit has less peaks present (5 noticeable peaks in the X and Y as opposed to 6). The largest peak for the retrograde orbit also occurs at a higher frequency than the prograde orbit for each axis control. DAC filtering of these frequencies resulted in a new ΔV requirement of 0.134 m/s per week for the polyhedron model and 0.15 m/s for the harmonic model. In practice, no control will be required for such a retrograde orbit.

45° Inclined Orbit

Consider an inclined orbit by 45 degrees. When left uncontrolled, an orbit of this type will naturally precess about the asteroid. Adding PD control will prevent this precession from happening at the expense of a ΔV of 17.65 m/s per week for the polyhedron model and 17.59 m/s for the harmonics model. In this case, the control accelerations along each axis exhibit the same frequency peaks in the FFT plots, though not necessarily with the same magnitude. Filtering these frequencies allows the spacecraft to be controlled, while also precessing as it would naturally about the asteroid as shown in Fig. 6.12. After applying DAC filters to all the frequency components of the control accelerations shown in Fig. 6.13, the control accelerations became to nearly zero, as can be seen

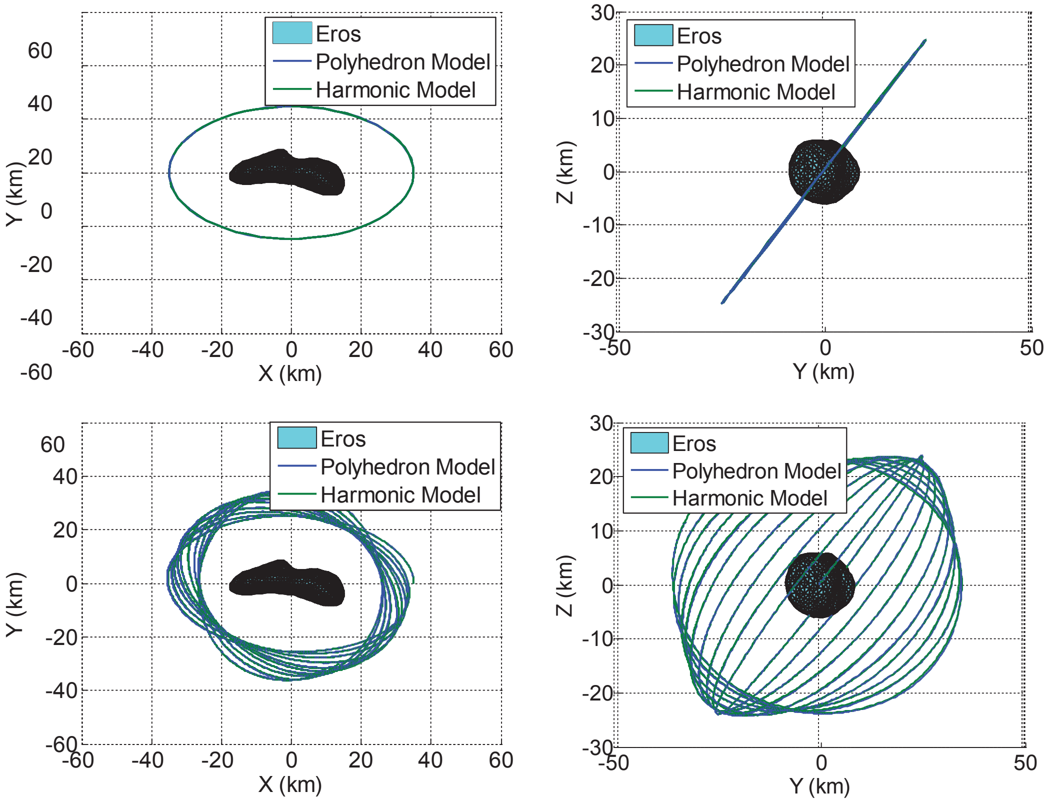

Figure 6.12: 35 km inclined orbits with PD control (top) and DAC filters (bottom).

in Fig. 6.14. The ΔV requirement is reduced to 0.123 m/s per week for the polyhedron model and 0.135 m/s per week for the harmonic model.

Polar Orbit

Perhaps the most useful orbit to have, in terms of scientific return, would be a polar orbit. Whereas an orbit in the XY-plane would be limited to only viewing parts of the surface in the plane, a polar orbit would be able to view the entire surface due to the spin of the asteroid. For PD control, the most irregular control acceleration history out of the four scenarios has been observed. Despite being the most irregular, this orbit requires the least amount of control effort before applying DAC filters. The polyhedron model requires 16.85 m/s of ΔV per week, and the harmonic model requires 16.36 m/s. Applying DAC filters to each of the frequencies present reduces the ΔV per week to 0.112 m/s for the polyhedron model and 0.13 m/s for the harmonics model.

Center-of-Mass Offset

Thus far we have assumed that the asteroid's center of mass (COM) is known with a large degree of accuracy. We now assume a large COM location estimation error of one kilometer along the Z-axis. The spacecraft is then controlled to follow a 35 km radius circular orbit around this estimated

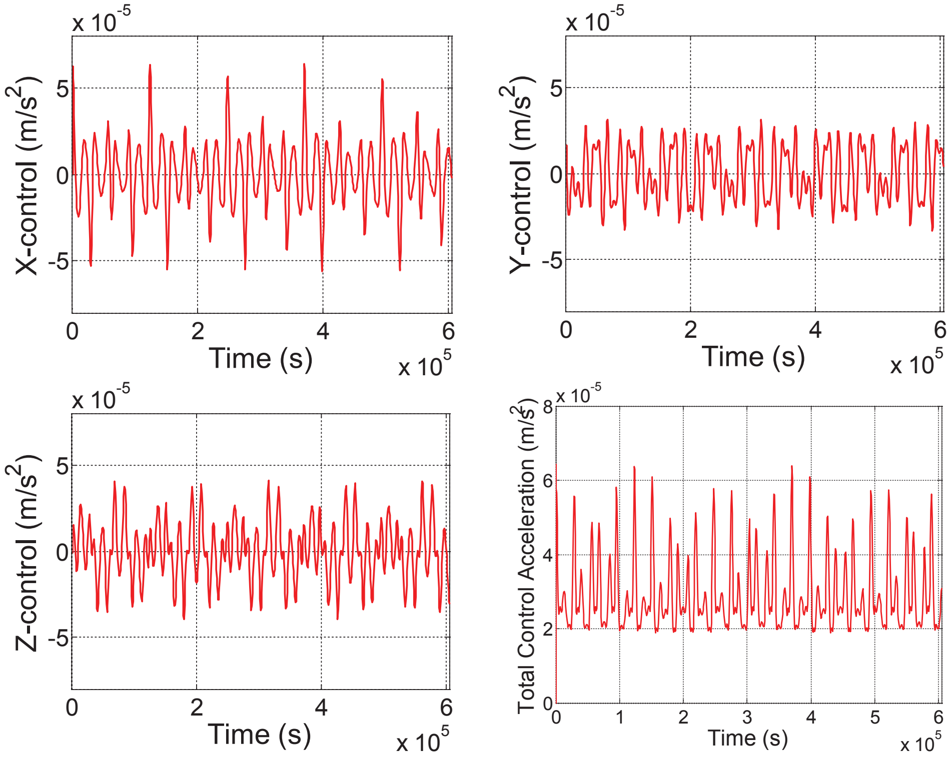

Figure 6.13: Inclined orbit control acceleration histories with PD control.

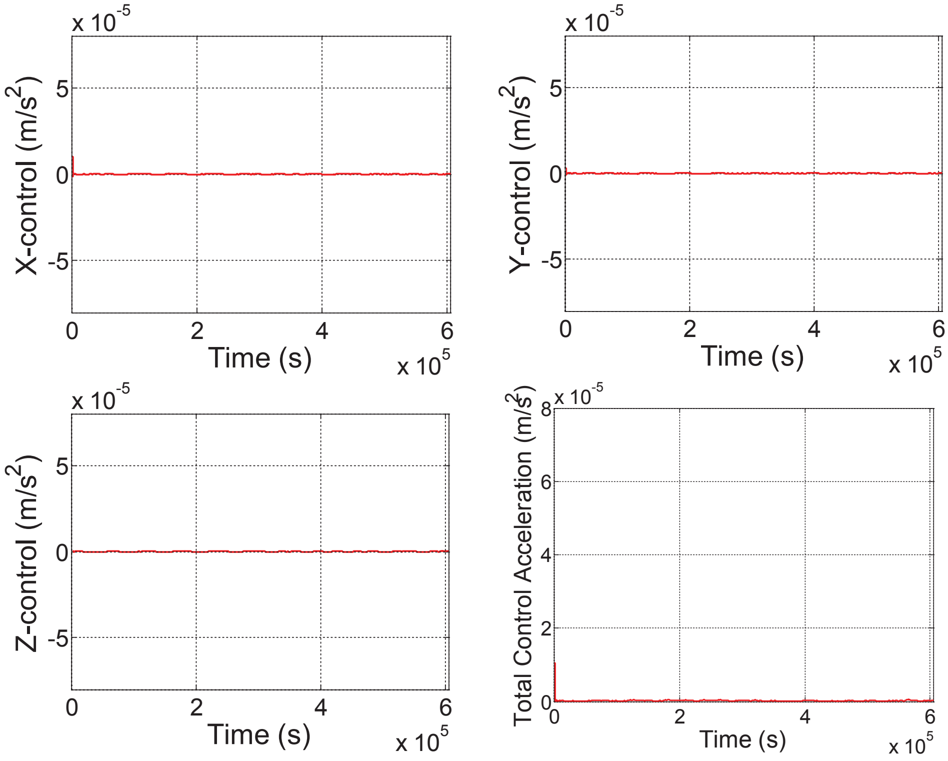

Figure 6.14: Inclined orbit control acceleration histories with DAC filters.

COM. After the frequencies from the FFT plots of the control inputs have been identified and DAC filtering has been implemented, the spacecraft oscillates naturally around the true COM with a ΔV requirement of 0.13 m/s per week.

Body-Frame Hovering

The last scenario is a hovering control in the body-fixed reference frame. Hovering in this case entails finding a reference orbit which has the same period as the asteroid's rotation rate. For 433 Eros, the reference circular orbit with the appropriate period is slightly under 16 km in radius. This can be problematic as some dimensions of Eros can also approach 16 km in radius. Thus, in order to simulate this hovering case, the spacecraft will have to orbit in areas where the asteroid's radius is significantly smaller such as along the y-axis. Here we place the spacecraft along the positive y-axis. As the orbit is slightly under 16 km, only the polyhedron and inertia dyadic models can be used due to the inherent limitation of a spherical harmonics expansion model at and below its circumscribing sphere's radius. Since the inertia dyadic model has been shown to be similar to a second-order harmonic expansion, the polyhedron model will be used to obtain more accurate results. Figure 6.15 shows the results of hovering with PD and DAC filtering in the body-fixed frame. Maintaining the orbit with PD control requires an excessive amount of fuel at 199 m/s per week. Here the DAC filters achieve the best reduction yet to 0.5 m/s per week. The large ΔV requirement for PD control appears to be due to the assumed initial position not being close enough to the actual 1:1 orbit as we see the spacecraft position drift significantly in the positive x-direction when DAC filters are added.

The control scheme described in this section relies on being able to accurately determine a spacecraft's position and velocity state vector with respect to the asteroid's center of mass. The state vector is assumed to be known exactly in order to verify the validity of this approach. Future research needs to integrate state estimation using a combination of optical cameras and a 3D Flash LIDAR.

6.4 Summary

The orbital motions around small bodies are sensitive to the initial conditions and the gravitational environment. Although there has been much study and effort devoted to finding open-loop solutions of stable orbits in such an environment, it is not guaranteed that the spacecraft will always be successfully placed into such stable trajectories around irregular-shaped asteroids. This chapter has demonstrated that any of three different gravity models could be used to accurately simulate

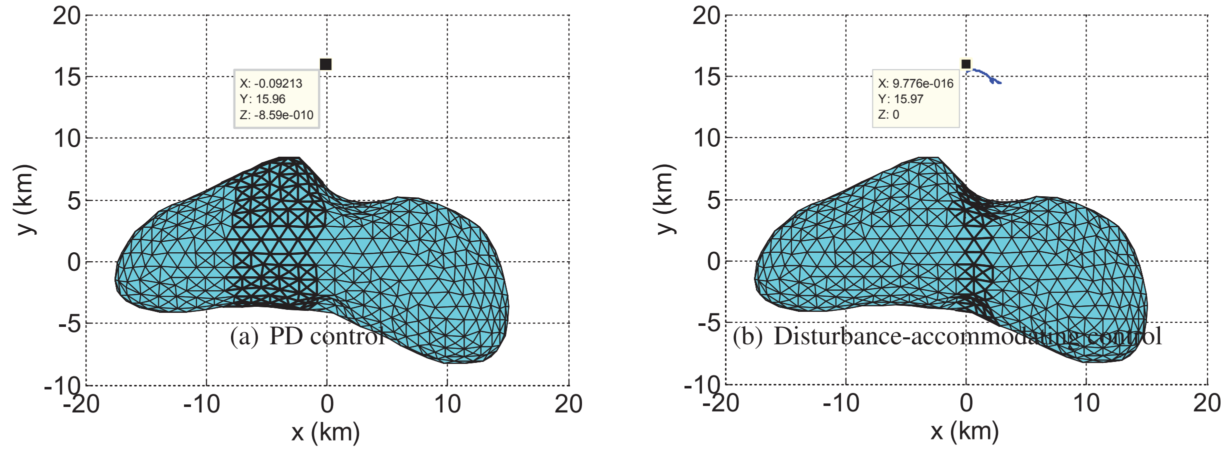

(a) PD control

(b) Disturbance-accommodating control

Figure 6.15: Hovering scenario with PD control and DAC filters.

an asteroid's gravitational field. A simple feedback control combined with disturbance accommodation control (DAC) filtering was studied to ensure the spacecraft remains in a stable orbit about a body with very little control effort. Another advantage to this control scheme is that, unlike open-loop solutions, prior knowledge of the body is not required. This is due to the fact that only the control acceleration history is required to know at what frequencies the DAC filters should be tuned. However, there are two major drawbacks of the proposed DAC application. They are: (i) the need of accurate relative navigation information with respect to the asteroid's COM and (ii) the identification of gravitational perturbation frequency components.

References

[1] Gehrels, T. (Ed.), *Hazards Due to Comets and Asteroids,* The University of Arizona Press, Tucson, AZ, 1994.

[2] Dearborn, D., "21st Century Steam for Asteroid Mitigation," AIAA-2004-1413, *2004 Planetary Defense Conference: Protecting Earth from Asteroids*, Orange County, CA, Feb. 23-26, 2004.

[3] Adams, R. et al., *Survey of Technologies Relevant to Defense from Near-Earth Objects*," NASA-TP-2004-213089, NASA MSFC, July 2004.

[4] Belton, M., Morgan, T., Samarasinha, N., and Yeomans, D. (Eds.), *Mitigation of Hazardous Comets and Asteroids,* Cambridge University Press, 2005.

[5] Lu, E. and Love, S., "Gravitational Tractor for Towing Asteroids," Nature 438, November, 2005, pp. 177-178.

[6] *2006 Near-Earth Object Survey and Deflection Study,* Final Report, NASA HQ, PA&E, December 28, 2006.

[7] Barbee, B. W. and Fowler, W. T., “Spacecraft Mission Design for the Optimal Impulsive Deflection of Hazardous Near-Earth Objects (NEOs) Using Nuclear Explosive Technology,” Planetary Defense Conference, Washington DC, March 5-8, 2007

[8] Wie, B., “Dynamics and Control of Gravity Tractor Spacecraft for Asteroid Deflection,” *Journal of Guidance, Control, and Dynamics*, Vol. 31, No. 5, 2008, pp. 1413-1423.

[9] Kaplinger, B., Wie, B., and Basart, J., “A Preliminary Study on Nuclear Standoff Explosions for Deflecting Near-Earth Objects,” *Proceedings of the 1st IAA Planetary Defense Conference*, Granada, Spain, April 27-30, 2009.

[10] *Defending Planet Earth: Near-Earth Object Surveys and Hazard Mitigation Strategies*, Report No. 0-309-14968-1, National Research Council, The National Academies Press, 2010.

[11] *Effects of Nuclear Earth-Penetrator and Other Weapons*, National Research Council, The National Academies Press, 2005.

[12] Wie, B., “Hypervelocity Nuclear Interceptors for Asteroid Disruption,” *Acta Astronautica*, Vol. 90, 2013, pp. 146-155.

[13] Pitz, A., Kaplinger, B., Vardaxis, G., Winkler, T., and Wie, B., “Conceptual Design of a Hypervelocity Asteroid Intercept Vehicle (HAIV) and Its Flight Validation Mission,” *Acta Astronautica*, Vol. 94, 2014, pp. 42-56.

[14] Vardaxis, G. and Wie, B., “Near-Earth Object Intercept Trajectory Design for Planetary Defense,” *Acta Astronautica* Vol. 101, 2014, pp. 1-15.

[15] Barbee, B., Wie, B., Mark, S., and Getzandanner, K., “Conceptual Design of a Flight Demonstration Mission for a Hypervelocity Asteroid Intercept Vehicle,” *Acta Astronautica*, Vol. 106, 2015, pp. 139-159.

[16] Wagner, S., Pitz, P., Zimmerman, D., and Wie, B., “Interplanetary Ballistic Missile (IPBM) System Architecture Design for Near-Earth Object Threat Mitigation,” IAC-09.D1.1.1, *60th International Astronautical Congress*, October 2009.

[17] Kaplinger, B., Wie, B., and Dearborn, D., “Nuclear Fragmentation/Dispersion Modeling and Simulation of Hazardous Near-Earth Objects,” *Acta Astronautica*, Vol. 90, 2013, pp. 156-164.

[18] Kaplinger, B. and Wie, B., “GPU Accelerated 3-D Modeling and Simulation of a Blended Kinetic Impact and Nuclear Subsurface Explosion,” IAA-PDC13-04-06, *2013 IAA Planetary Defense Conference*, April 2013.

[19] Kaplinger, B., Setzer, C., Premaratne, P., Wie, B., “GPU-Accelerated 3D Modeling and Simulation of a Blended Kinetic Impact and Nuclear Subsurface Explosion,” AIAA-2013-4548, presented at AIAA Guidance, Navigation, and Control Conference, Boston, MA, August 19-22, 2013.

[20] Owen, J. M., Villumsen, J. V., Shapiro, P. R. and Martel, H., “Adaptive Smoothed Particle Hydrodynamics: Methodology II,” *The Astrophysical Journal Supplement Series*, No. 209, 1998, pp. 116-155.

[21] Premaratne, P., Zimmerman, B., Setzer, C., Harry, J., and Wie, B., “Nuclear Explosion Energy Coupling Models for Optimal Fragmentation of Asteroids,” AAS 14-285, AAS/AIAA Space Flight Mechanics Meeting, Santa Fe, NM, Jan 27-30, 2014.

[22] Zimmerman, B. and Wie, B., “Computational Validation of Nuclear Explosion Energy Coupling Models for Asteroid Fragmentation,” AIAA-2014-4146, *AIAA/AAS Astrodynamics Specialist Conference*, San Diego, CA, August 4-7, 2014.

[23] Kaplinger, B., Wie, B., and Dearborn, D., “Earth-Impact Modeling and Analysis of a Near-Earth Object Fragmented and Dispersed by Nuclear Subsurface Explosions,” *The Journal of the Astronautical Sciences,* Vol. 59, Issue 1-2, January 2014, pp. 101-119.

[24] Megan, B., Dearborn, D., and Schultz, P., “Limits on the Use of Nuclear Explosives for Asteroid Deflection,” *Acta Astronautica*, Vol. 90, 2013, pp. 103-111.

[25] Kubitschek, D. G.,“Impactor Spacecraft Targeting for the Deep Impact Mission to Comet Tempel 1,” AAS 03-615, *AAS/AIAA Astrodynamics Specialist Conference*, Big Sky, Montana, August 3-7, 2003.

[26] “Deep Impact Launch,” Press Kit, NASA, January 2005.

[27] Frauenholz, R. S., Bhat, R. S., Chesley, N., Mastrodemos, N., Owen Jr., W. M., and Ryne, M. S., “Deep Impact Navigation System Performance,” *Journal of Spacecraft and Rockets*, Vol. 45, No. 1, 2008, pp. 39-56.

[28] Wagner, S., Wie, B., and Barbee, B., “Target Selection for a HAIV Flight Demo Mission,” IAA-PDC13-04-08, *3rd IAA Planetary Defense Conference*, Flagstaff, AZ, April 15-19, 2013. To appear in *Acta Astronautica*.

[29] Carnelli, I., Galvez, I., and Izzo, D., “Don Quijote: A NEO Deflection Precursor Mission,” NASA Near-Earth Object Detection and Threat Mitigation Workshop, 2006.

[30] Galvez, A. and Carnelli, I., “ESA’s Don Quijote Mission: an Opportunity for the Investigation of an Artificial Impact Crater on an Asteroid,” *25th International Symposium on Space Technology and Science*, 2006.

[31] Cano, J., Sanchez, M., and Carnelli, I., “Mission Analysis for the Don Quijote Phase-A Study,” *Proceedings of the 20th International Symposium on Space Flight Dynamics*, 2007.

[32] Barbee, B. W., Mink, R. G., Adamo, D. R., and Alberding, C. M., “Methodology and Results of the Near-Earth Object (NEO) Human Space Flight (HSF) Accessible Targets Study (NHATS),” *Advances in the Astronautical Sciences*, Volume 142, Univelt, Inc., San Diego, CA, 2011, pp. 613-632.

[33] Wagner, S., "Automated Trajectory Design for Impulsive and Low-Thrust Interplanetary Missions Analysis," Ph.D. Thesis, Department of Aerospace Engineering, Iowa State University, December 2014.

[34] Wagner, S. and Wie, B., "Hybrid Algorithm for Multiple Gravity-Assist and Impulsive ΔV Maneuvers," submitted to *AIAA Journal of Guidance, Control, and Dynamics*, 2014.

[35] Hawkins, M, Pitz, A., Wie, B., and Gil-Fernández, J.,"Terminal-Phase Guidance and Control Aanlysis of Asteroid Interceptors," AIAA-2010-8348, *AIAA Guidance, Control, and Navigation Conference*, Toronto, Canada, August 2-5, 2010.

[36] Hawkins, M., Guo, Y., and Wie, B., "Spacecraft Guidance Algorithms for Asteroid Intercept and Rendezvous Missions: A Review," *International Journal of Aeronautical and Space Sciences*, Vol. 13, 2012, pp. 345-360.

[37] Lyzhoft, J., Hawkins, M., Kaplinger, B., and Wie, B., "GPU-Based Optical Navigation and Terminal Guidance Simulation of a Hypervelocity Asteroid Impact Vehicle (HAIV)," AIAA-2013-4966, AIAA Guidance, Navigation, and Control Conference, Boston, MA, August 19-22, 2013.

[38] Lyzhoft, J., Groath, D., and Wie, B., "Optical and Infrared Sensor Fusion for Hypervelocity Asteroid Intercept Vehicle," AAS 14-421, AAS/AIAA Space Flight Mechanics Meeting, Santa Fe, NM, Jan 27-30, 2014.

[39] Lyzhoft, J. and Wie, B., "IR Telescope and Sensor Characterization for Hypervelocity Asteroid Intercept Guidance," AIAA-2014-4299, AIAA/AAS Astrodynamics Specialist Conference, San Diego, CA, August 4-7, 2014.

[40] Gil-Fernández, J., Panzeca, R., and Corral, C., "Impacting Small Near Earth Objects," *Advances in Space Research*, Vol. 42, No. 8, October 2008, pp. 1352-1363.

[41] Gil-Fernández, J., Cadenas-Gorgojo, R., Priet-Llaons, T., and Graziano, M., "Autonomous GNC Algorithms for Rendezvous Missions to Near-Earth Objects," AIAA-2008-7087, AIAA/AAS Astrodynamics Specialist Conference and Exhibit, Honolulu, HI, 2008.

[42] Zarchan, P., *Tactical and Strategic Missile Guidance*, Vol. 219, Progress in Astronautics and Aeronautics, 6th Edition, AIAA, 2012.

[43] Guo, Y., Hawkins, M., and Wie, B., "Applications of Generalized Zero-Effort-Miss/Zero-Effort-Velocity (ZEM/ZEV) Feedback Guidance Algorithm," *Journal of Guidance, Control, and Dynamics*, Vol. 36, No. 3, 2013, pp. 810-820.

[44] Guo, Y., Hawkins, M., and Wie, B., "Waypoint-Optimized Zero-Effort-Miss/Zero-Effort-Velocity (ZEM/ZEV) Feedback Guidance for Mars Landing," *Journal of Guidance, Control, and Dynamics*, Vol. 36, No. 3, 2013, pp. 799-809.

[45] Raugh, A. C. "NEAR Collected Shape and Gravity Models," NEAR-A-5-COLLECTED-MODELS-V1.0. April 19, 2002.

[46] Thomas, P. C., et al, "Eros: Shape, Topography and Slope Processes" Icarus, Volume 155, 2002, pp. 18-37.

[47] Gouraud, H. "Continuous Shading of Curved Surfaces," IEEE Transactions on Computers, Volume C-20 (6), 1971, pp. 623-629.

[48] Wright, E. L. et al., "The Wide-Field Infrared Survey Explorer (WISE): Mission Description and Initial On-Orbit Performance," *The Astronomical Journal*, Vol. 140, No. 6, 2010, pp. 1868.

[49] Rieke, J. H., *Detection of Light: from the Ultraviolet to the Submillimeter*, Cambridge University Press, New York, 1994, pp. 56.

[50] Schott, J. R., *Remote Sensing: The Image Chain Approach*, Oxford University Press, New York, 1997, pp. 184.

[51] Dereniak, E. L. and Boreman, G. D., *Infrared Detectors and Systems*, John Wiley & Sons, New York, 1996, Chapter 5.

[52] Morin, F. J., Miata, J. P., "Electrical Properties of Silicon Containing Arsenic and Boron," *Physical Review*, Vol. 96, No. 1, 1954, pp. 28-35.

[53] Schneider, H. and Liu, H. C., *Quantum Well Infrared Photodetectors*, Springer-Verlag, Berlin, Heidelberg, New York, 2007.

[54] Kaplinger, B., "Physical Modeling and High-Performance GPU Computing for Characterization, Interception, and Disruption of Hazardous Near-Earth Objects," Ph.D. Thesis, Department of Aerospace Engineering, Iowa State University, May 2013.

[55] Premaratne, P., "Nuclear Subsurface Explosion Modeling and Hydrodynamic Fragmentation Simulation of Hazardous Asteroids," M.S. Thesis, Department of Aerospace Engineering, Iowa State University, May 2014.

[56] Huynh, H. T., "A Flux Reconstruction Approach to High-Order Schemes Including Discontinuous Galerkin Methods," AIAA 2007-4079, 2007.

[57] Wang, Z. J., "Spectral (Finite) Volume Method for Conservation Laws on Unstructured Grids: Basic Formulation," *Journal of Computational Physics* , *178*, 210–251, 2002, pp. 210-251.

[58] Zimmerman, B. J. and Wang, Z. J., "The Efficient Implementation of Correction Procedure Via Reconstruction with GPU Computing," AIAA 2013-2692, 2013.

[59] Hupp, R., DeWald, S., and Wie, B., "Suborbital Intercept and Fragmentation of Asteroids with Very Short Warning Time," AAS 14-281, *AAS/AIAA Space Flight Mechanics Meeting*, Santa Fe, NM, Jan 27-30, 2014.

[60] Hupp, R., DeWald, S., Wie, B., and Barbee, B., “Mission Design and Analysis for Suborbital Intercept and Fragmentation of an Asteroid with Very Short Warning Time,” AIAA 2014-4460, *AIAA/AAS Astrodynamics Specialist Conference*, San Diego, August 2014.

[61] Melamed, N., McVey, J. P., Mayberry, J. P., “Expeditious Response to a Short Warning NEO Impact Threat,” Presented at 2013 IAA Planetary Defense Conference, April 15-19, 2013, Flagstaff, AZ.

[62] http://fallingstar.com/how_atlas_works.php, last accessed 2014-10-28.

[63] http://en.wikipedia.org/wiki/Impact_event, last accessed on 2014-10-28.

[64] http://www.fas.org/pubs/pir/2011winter/2011Winter-Anti-Satellite.pdf, last accessed on 2014-10-28.

[65] http://www.fas.org/nuke/guide/usa/icbm/lgm-30_3.htm, last accessed on 2014-10-28.

[66] http://www.astronautix.com/lvs/mineman3.htm, last accessed on 2014-10-28.

[67] Hanson, J. M., Shrader, M.,W., and Cruze, C. A., “Ascent Guidance Comparisons,” *The Journal of the Astronautical Sciences,* Vol. 43, No. 3, 1995, pp.‘307-326. Also, NASA-TM-112493.

[68] Dukeman, G. A., “Atmospheric Ascent Guidance for Rocket-Powered Launch Vehicles,” AIAA 2002-4559, August 2002.

[69] Picka, B. A. and Glenn, C. B., “Space Shuttle Ascent Flight Design Process Evolution and Lessons Learned,” AIAA 2011-7243, 2011.

[70] Lu, P., Griffin, B., Dukeman, G., and Chavez, F., “Rapid Optimal Multiburn Ascent Planning and Guidance,” *Journal of Guidance, Control, and Dynamics*, Vol. 31, No. 6, 2008, pp. 1656-1664.

[71] Chavez, F. and Lu, P., “Rapid Ascent Trajectory Planning and Closed-Loop Guidance for Responsive Launch,” RS7-2009-1004, *7th Responsive Space Conference*, April 27-30, 2009, Los Angeles, CA.

[72] Winkler, T., Hawkins, M., Lyzhoft, J., and Wie, B., “Fuel-Efficient Feedback Control of Orbital Motion Around an Irregular-Shaped Asteroid,” AIAA-2012-5044, AIAA Guidance, Navigation, and Control Conference, August 2012.

[73] Winkler, T. and Wie, B., “Optical Navigation and Fuel-Efficient Orbit Control Around an Irregular-Shaped Asteroid,” AIAA-2013-5117, AIAA Guidance, Navigation, and Control Conference, August 2013.

[74] Winkler, T., “Fuel-Efficient Feedback Control of Orbital Motion around Irregular-Shaped Asteroids,” M.S. Thesis, Department of Aerospace Engineering, Iowa State University, May 2013.

[75] Scheeres, D. J., “Orbital Mechanics About Small Bodies,” *Acta Astronautica*, Vol. 27, 2012, pp. 1-14.

[76] Scheeres, D. J., “Close Proximity Dynamics and Control about Asteroids,” *Proceedings of 2014 American Control Conference*, June 4-6, 2014, Portland, Oregon, pp. 1584-1595.

[77] Broschart, S. B. and Scheeres, D. J., “Control of Hovering Spacecraft Near Small Bodies: Application to Asteroid 25143 Itokawa,” *Journal of Guidance, Control, and Dynamics*, Vol. 27, No. 2, 2005, pp. 343-354.

[78] Kawaguchi, J., “Hayabusa, Summary of Guidance, Navigation and Control Achievement in its Proximity Phase,” AIAA-2006-6533, *Astrodynamics Specialist Conference*, August 2006.

[79] Scheeres, D. J., “Dynamics About Uniformly Rotating Tri-Axial Ellipsoids: Applications to Asteroids,” *Icarus*, Vol. 110, 1994, pp. 225-238.

[80] Scheeres, D. J., Ostro, S. J., Hudson, R. S., and Werner, R. A., “Orbits Close to Asteroid 4769 Castalia,” *Icarus*, Vol. 121, 1996, pp. 67-87.

[81] Scheeres, D. J., Williams, B. G., and Miller, J. K., “Evaluation of the Dynamic Environment of an Asteroid: Applications to 433 Eros,” *Journal of Guidance, Control, and Dynamics*, Vol. 23, 2000, pp. 466-475.

[82] Hu, W. and Scheeres, D. J., “Numerical Determination of Stability Regions for Orbital Motion in Uniformly Rotating Second Degree and Order Gravity Fields,” *Planetary and Space Science*, Vol. 52, 2004, pp. 685-692.

[83] Hu, W. and Scheeres, D. J., “Periodic Orbits in Rotating Second Degree and Order Gravity Fields,” *Chinese Journal of Astronomy and Astrophysics*, Vol. 8, No. 1, 2008, pp. 108-118.

[84] Scheeres, D. J., “Satellite Dynamics About Small Bodies: Averaged Solar Radiation Pressure Effects,” *Journal of the Astronautical Sciences*, Vol. 47, No. 1, 1999, pp.‘25-46.

[85] Scheeres, D. J. and Marzari, F., “Spacecraft Dynamics in the Vicinity of a Comet,” *Journal of the Astronautical Sciences*, Vol. 50, No. 1, 2002, pp. 35-52.

[86] Scheeres, D. J., Miller, J. K., and Yeomans, D. K., “The Orbital Dynamics Environment of 433 Eros: A Case Study for Future Asteroid Missions,” InterPlanetary Network Progress Report 42-152, 2003, pp. 1-26.

[87] Werner, R. A. and Scheeres, D. J., “Exterior Gravitation of a Polyhedron Derived and Compared with Harmonic and Mascon Gravitation Representations of Asteroid 4769 Castalia,” *Celestial Mechanics and Dynamical Astronomy*, Vol. 65, 1997, pp. 313-344.

[88] Vallado, D. A., *Fundamentals of Astrodynamics and Applications*, Third Edition,” Microcosm Press, 2007, Chapter 8.

[89] Kane, T. R., Likins, P. W., and Levinson, D. A., *Spacecraft Dynamics*, McGraw-Hill Book Company, 1983, Chapter 2.

[90] Wie, B., *Space Vehicle Dynamics and Control*, Second Edition, AIAA, 2008, Chapters 2 and 6.

[91] Wie, B., "Active Vibration Control Synthesis for the COFS (Control of Flexible Structures) Mast Flight System," *Journal of Guidance, Control, and Dynamics*, Vol. 11, No. 3, 1988, pp. 271-276.

[92] Wie, B., Byun, K.-W., Warren, W. Geller, D., Long, D., and Sunkel, J., "New Approach to Momentum/Attitude Control for the Space Station," *Journal of Guidance, Control, and Dynamics*, Vol. 12, No. 5, 1989, pp. 714-722.

[93] Wie, B. and Gonzalez, M., "Control Synthesis for Flexible Space Structures Excited by Persistent Disturbances," *Journal of Guidance, Control, and Dynamics*, Vol. 15, No. 1, 1992, pp. 73-80.

[94] Wie, B., Liu, Q., and Bauer, F., "Classical and Robust H_∞ Control Redesign for the Hubble Space Telescope," *Journal of Guidance, Control, and Dynamics*, Vol. 16, No. 6, 1993, pp. 1069-1077.

[95] Cielaszyk, D. and Wie, B., "New Approach to Halo Orbit Determination and Control," *Journal of Guidance, Control, and Dynamics*, Vol. 19, No. 2, 1996, pp. 266-273.

[96] Miller, J. K. et al. "Determination of Eros Physical Parameters for Near Earth Asteroid Rendezvous Orbit Phase Navigation," AAS 99-463, *AAS/AIAA Astrodynamics Specialist Conference*, 1999.

[97] Miller, J. K. et al., "Determination of Shape, Gravity, and Rotational State of Asteroid 433 Eros," *Icarus*, Vol. 155, 2002, pp. 3-17.

[98] "NEAR-A-5-COLLECTED-MODELS-V1.0," http://sbn.psi.edu/pds/resource/nearbrowse.html.